

University of Nottingham
UK | CHINA | MALAYSIA

FLUID FLOW AND ACOUSTIC ABSORPTION IN POROUS METALLIC STRUCTURES USING NUMERICAL SIMULATION AND EXPERIMENTATION

By

ABDULRAZAK JINADU OTARU
MEng (Hons)

Thesis submitted to the University of Nottingham for the degree of Doctor of Philosophy

Department of Mechanical, Materials and Manufacturing Engineering, the University of Nottingham, United Kingdom

September 2018

ABSTRACT

The need to cut down vibration and minimize back pressure wave in a loudspeaker has led to the choice of artificially-made metallic foam structure due to its important low weight, recyclable, stiffness, high surface area, and longer active product life for money. Commercially available highly porous metallic structures are known to be poor sound absorber but there is a possibility that if they can be made by interacting with the shapes and structural properties of this material, they could be made useful. Currently available poroacoustic models needed to describe the sound absorption behaviour of porous materials point out the permeability of this structure as the key parameter driving this behaviour. Knowing this parameter through experimentation or prediction is imperative to the design of material with novel attributes for this process.

Pore-level numerical simulation of fluid flow through low-density “bottleneck-type” structures using tomography images of the “real” structures and “unconventional” sphere-packing models have been used herein to account for this permeability with reasonable fit to experimental data of airflow measured across these structures. This parameter was observed to be dependent on the structural parameters of the porous medium and most importantly, its pore diameter openings. Theoretical models to account for flow behaviour of this structure at low and high fluid velocities were proposed. Optimal values of structural parameters needed for the design of “bottleneck-type” structure for efficient sound absorption were achieved for a hardbacked and airgap simulation.

DEDICATION

To the memory of my mum (Mrs. Habibat Otaru); my brother (Mr. Onimisi Jinadu Otaru); and my sister (Ms. Zulaihat Jinadu Otaru). May their gentle souls continue to rest in peace (Amin!!!).

ACKNOWLEDGMENTS

Primarily, I would like to thank my supervisors: Prof. Herve P. Morvan (Thermofluids and CFD, Technology Strategy Manager-CTO Office at Rolls-Royce and Honorary Professor, The University of Nottingham, UK), Prof. Andrew R. Kennedy (Materials and Novel Manufacturing, Chair in Advanced Manufacturing, Lancaster University, UK) and Assoc. Prof. Kathy Simmons (Thermofluids and CFD, The University of Nottingham, UK) for their supervision, encouragement, and guidance throughout the course of this research.. Hat tip to my internal examiner, Prof. Steve Pickering (Thermofluids, Head of Mechanical, Materials and Manufacturing Engineering, The University of Nottingham, UK) for his thorough criticism and examination of this work in all stages of my annual presentations.

I am indebted to the University of Nottingham (Dean of Engineering Research Scholarship for International Excellence), Petroleum Technology Development Fund, Bowers and Wilkins Group and Simpleware Ltd for the provision of funds, equipment, materials, licenses and technical support needed for the successful completion of this research project. Gratitude to Zeno Karl Schindler Foundation, Switzerland for creating a conducive platform for me in developing an interest in scientific research through the award of its ZKSF Master Thesis Grant in 2012.

I would like to thank Sarah-Jean Baptiste, Mattia Cobianchi, Martial Rousseau, Solomon Idiyang, Hannah Constantin, Rory Screaton, Hatem Oun, John Hinchcliffe, Buss Thomas, Christopher Fox, Akinola Adeniyi, Nigel Sykes, Max Mason, Martin Corfield, Patel Uresha and Thiago De Carvalho for their

invaluable assistance. Staff, friends, and colleagues at the University of Nottingham for whom I am thankful are Boudhika Hewakandamby, Ado Mohammed, Clare Hollingworth, Abdulsalam Aliyu, Nawar Kadeer, Ezekiel Agunlejika, Julie Harrison, Happiness Ijeje, Helen Giberson, Ebiundu Komonibo, Matt Neville, Peter Atagher, Laura Sun, Valentine Anyawu, Ruth Anderson, Jabir Sani Maihula, Dafne Gaviria, Bashir Rumah, Hala Dhowre, Tunji Owoseni, Marina-Eirini Mitrousi, Fatai Akande, Maha Nsaif, Idongesit Peter, Sofia Catalucci, Umaru Musa, Carmel Leah Howe, Omar Rajab, Ahmed Ibrahim, Hadrian Moran, Suleiman Usman and Sabrin Samad.

I wish to thank my parents and siblings; my in-laws; my uncle (Dr. Musa Suberu Otaru) and his family; extended family members, friends and well-wishers for their support and encouragement during this project. To my beautiful and adorable wife (Mrs. Fatima Zahra Abubakar-Otaru), you are a wonderful woman. Thanks for been there all through, and to my son (Faaz-AJ Otaru), you are a gift from Allah (SWT). Together, we pulled this through.

Lastly, to my creator; the only one; the omnipotence; the provider; the giver and the forgiver; the master of the day of reckoning; originator of the heavens and planets. When He decree a matter, He only says to it, “Be”, and it is (Quran 2:117). I am indeed grateful to you for sparing my life throughout this journey. “Which of your favours will I deny?” my Lord. May you continue to bless me and my family, long life, sound health, wisdom, wealth and prosperity (Amin!!!).

TABLE OF CONTENTS

ABSTRACT i

DEDICATION ii

ACKNOWLEDGMENTS iii

TABLE OF CONTENTS v

NOMENCLATURE ix

LIST OF FIGURES xvi

LIST OF TABLES xxx

ACTIVITIES xxxiii

CHAPTER 1 1

INTRODUCTION 1

1.1 Fluid Flow through Porous Metallic Structures 4

1.2 Sound Pressure Waves through Porous Metallic Structures 8

1.3 Research aim and objectives 10

1.4 Themes Needing Further Study 11

1.5 Thesis Plan 12

CHAPTER 2 16

LITERATURE REVIEW AND GOVERNING EQUATIONS 16

2.1 Metallic Foam 16

2.1.1 Metal foam processing 17

2.1.1.1 Hydro/Alcan 18

2.1.1.2 Alporas 19

2.1.1.3. Gasar 19

2.1.1.4 Foaminal/Alulight 20

2.1.1.5 Formgrip/Foamcast 21

2.1.2 Replication casting processes using packed beds of salt 21

2.1.3 Space fillers 23

2.2 Fluid Flow 24

2.2.1 Continuity and momentum equations 25

2.3 Pore-scale and Fluid Models 27

2.3.1 Darcy's Law 28

2.3.2 Brinkmann equation 30

2.3.3 Darcy-Dupuit-Forchheimer Model 31

2.3.4 Permeability estimation for non-Darcy regime 33

2.3.5 Reynolds number for porous media flow 34

2.3.6 Boundary conditions 36

2.4 Sound and Acoustic 39

2.4.1 Helmholtz wave equation 40

2.4.2 Acoustic absorption 41

2.4.3 Techniques for enhancing acoustic absorption 43

2.5 Poroacoustic parameters 46

2.5.1 Static airflow resistivity 48

2.5.2 Open porosity 49

2.5.3 High-frequency limit of dynamic tortuosity 50

2.5.4 Viscous and thermal characteristic lengths 52

2.6 Acoustic porous media models 56

2.6.1 Primeval models 57

2.6.2 Visco-inertial and thermal effects using Johnson et al acoustic models 60

2.6.3 Wilson model 62

2.7 Separating low and high frequencies regime in a porous absorber 64

2.8 Multiscale Asymptotic Modelling Approach 67

2.9 Summary 69

CHAPTER 3 71

THE PERMEABILITY OF VIRTUAL MACROPOROUS STRUCTURES GENERATED BY SPHEREPACKING MODELS: COMPARISON WITH ANALYTICAL MODELS 71

3.1 Summary 71

3.2 Introduction 71

3.3 Image Processing and representative volume 74

3.4 Simulation 80

3.5 Results and discussion 82

3.6 Extension to binary-sized structures 85

3.7 Conclusions 99

CHAPTER 4 100

MEASUREMENT AND NOVEL SIMULATION OF AIRFLOW THROUGH POROUS ALUMINIUM FOAM STRUCTURES WITH SPHERICAL CELLS 100

4.1 Summary 100

4.2 Introduction 101

4.3 Specimen manufacture and characterization 106

4.4 Meshing and CFD simulation 109

4.5 Experimental measurement of pressure drop 112

4.6 Results and discussion 115

4.6.1 Structural characterization 115

4.6.2 Experimental measurement of airflow through Al structure. 120

4.6.2.1 Test on documented foam samples and repeatability analysis 120

4.6.2.2 Reynolds number and Friction factor relation 123

4.6.2.3 Experimental measurement of air pressure drop 127

4.6.3 CFD simulation of airflow through Al structures using X-ray CT images of the “real” structure. 132

4.6.4 Comparison with CFD simulation of airflow through "virtually-derived" macroporous spherical structures. 138

4.6.5 Modelling challenges associated with X-ray CT computation..... 142

4.6.6 Extension to "semi-virtual" CT structures 145

4.7 Conclusions..... 154

CHAPTER 5..... 156

NUMERICAL SIMULATION OF PRESSURE WAVE ACROSS "BOTTLENECK-TYPE" POROUS STRUCTURES..... 156

5.1 Summary..... 156

5.2 Introduction..... 156

5.3 Structural characterization 161

5.4 Simulation procedure..... 166

5.5 Model validation 169

5.6 Discussion of results..... 176

5.7 Optimization and sensible application of "bottleneck" structures 184

5.8 Erosion and dilation effects using the sphere-packing model 192

5.9 Conclusions..... 194

CHAPTER 6..... 196

CONCLUSIONS AND FUTURE WORK 196

Statement of Originality 197

REFERENCES..... 198

APPENDICES..... 229

APPENDIX I: FLOW AND IMAGE DATA FOR AIRFLOW THROUGH POROUS METALLIC STRUCTURES. 229

APPENDIX II: IMAGES, TABLES, AND FIGURES ON SOUND ABSORPTION BEHAVIOUR OF POROUS STRUCTURES 241

APPENDIX III: KOZENY CONSTANT OF SPHERICAL STRUCTURES GENERATED BY SPHERE-PACKING MODELS 256

NOMENCLATURE

Symbols /Abbreviations	Meaning	Units
2D	Two-dimensional	[-]
3D	Three-dimensional	[-]
A	Viscous term Ergun coefficient	[-]
$	Dollars	[-]
APMR	Acoustic of porous materials recipes	[-]
A_p	Peak of absorption	[-]
Al	Aluminium	[-]
CT	Computerized tomography	[-]
r_c	Capillary radius	[m]
r_p	Pore radii	[m]
r_w	Pore openings	[m]
D_p	Pore diameter sizes	[m]
D_w	Pore diameter openings	[m]
$\emptyset$	Porosity	[-]
P_i	Infiltration pressure	[bars]
θ	Wetting angle	[-]
D_p	Pore diameter sizes	[m]
D_w	Pore diameter openings	[m]
σ_{xy}	Surface tension	[$N.m^{-1}$]
k_0	Permeability	[m^2]
R_{eD}	Pore diameter-based Reynolds number	[-]

R_{eK}	Permeability-based Reynolds number	[-]
f_F	Fanning friction factor	[-]
A_c	Normal incidence absorption coefficient	[-]
NaCl	Sodium chloride	[-]
$NaAlO_2$	Sodium aluminate	[-]
LCS	Lost carbonate sintering	[-]
CFD	Computational fluid dynamics	[-]
RCP	Replication casting process	[-]
PPI	Pores per inch	[inch]
BC	Boundary condition	[-]
Q	Monopole source term	[$N.m^{-3}$]
Q	Dipole source term	[s^{-2}]
A_f	Average pore area	[m^2]
A_T	Total cross-sectional area	[m^2]
v_s	Superficial fluid inlet velocity	[$m.s^{-1}$]
v_p	Pore fluid inlet velocity	[$m.s^{-1}$]
V	Volume	[m^3]
ρ	Density	[$kg.m^{-3}$]
T	Time	[sec]
C	Form drag	[m^{-1}]
C_F	Forchheimer coefficient	[-]
C	Speed of sound	[$m.s^{-1}$]
K	Wave number	[$rad.m^{-1}$]
F	Frequency	[Hz]
I_a	Sound intensity absorber	[$W.m^{-2}$]

I_i	Incident sound intensity	[W.m^{-2}]
W	Wavelength	[m]
Z	Specific acoustic surface impedance	[N.m^{-3}]
Z_c	Characteristic impedance	[N.m^{-3}]
G	Rigidity modulus	[Pa]
τ_{xy}	Shear strain	[N.m^{-2}]
γ_{xy}	Shear strain	[rad]
F	Body force	[N]
K	Bulk modulus	[Pa]
τ	Dynamic tortuosity	[-]
σ	Airflow resistivity	[Pa.s.m^{-2}]
ʌ	Viscous characteristic length	[m]
$\bar{\text{ʌ}}$	Thermal characteristic length	[m]
k_0'	Static thermal permeability	[m^2]
τ_0	Static viscous tortuosity	[-]
τ_0'	Static thermal tortuosity	[-]
L	Structural length	[m]
μ	Fluid dynamic viscosity	[Pa.s]
F_r	Formation resistivity factor	[-]
R	Complex acoustic resistance	[N.m^{-3}]
X	Complex acoustic acceptance	[N.m^{-3}]
P_0	Static air pressure	[Pa]
P_m	Skeletal frame pressure	[Pa]
L_m	Specific frame thickness	[m]

S	Coupling coefficient	[-]
v_m	Solid material velocity	[m.s^{-1}]
v_0	Air velocity	[m.s^{-1}]
C_0	Steady shape factor	[-]
C_D	Dynamic shape factor	[-]
V_c	Complex specific volume	[m^3]
β_w	Complex compressibility	[Pa^{-1}]
S_x	Bessel function	[-]
P	Ambient pressure	[Pa]
γ	Specific heat ratio	[-]
k_T	Thermal conductivity	[w.m^{-1}.K^{-1}]
ρ_c	Complex density	[kg.m^{-3}]
N_{pr}	Prandtl number	[-]
δ_{vor}	Vorticity-mode boundary layer thickness	[m]
δ_{ent}	Entropy-mode boundary layer thickness	[m]
τ_{vor}	Vorticity-mode relaxation time	[sec]
τ_{ent}	Entropy-mode relaxation time	[sec]
σ_{FB}	The ratio of the structural surface area to bulk volume (specific surface)	[m^{-1}]
σ_{FF}	The ratio of the structural surface area to the structural surface area (specific surface)	[m^{-1}]
DEM	Discrete element modelling	[-]
μCT	Micro-computerized tomography	[-]
JCA	Johnson-Champoux-Allard	[-]
DB	Delany-Bazley	[-]

DBM	Delany-Bazley-Mikki	[-]
JCAL	Johnson-Champoux-Allard-Lafarge	[-]
JCAPL	Johnson-Champoux-Allard-Prides-Lafarge	[-]
RVE	Representative volume element	[-]
LPV	Linear pressure variation boundary condition	[-]
ISW	Impermeable side wall boundary condition	[-]
SSW	Solid sidewall boundary condition	[-]
δ_v	Viscous boundary layer thickness	[m]
δ_t	Thermal boundary layer thickness	[m]
w_v	Viscous characteristic length	[m]
w_t	Thermal characteristic length	[m]
C_p	Specific heat capacity at constant pressure	[KJ.kg^{-1}.K^{-1}]
C_v	Specific heat capacity at constant volume	[KJ.kg^{-1}.K^{-1}]
d_i	Microscopic variation unit cell length	[m]
D	Macroscopic variation unit cell length	[m]
MAM	Multiscale asymptotic modelling	[-]
R	Gas constant	[KJ.kg^{-1}.K^{-1}]
T_0	Air temperature	[K]
T	Temperature	[K]
λ	Bulk viscosity	[Pa.s]
L-S	Mixed-sized packings of small in large sized particles	[-]
L-L	Monosized packings of large-sized particles	[-]
S-S	Monosized packings of small-sized particles	[-]

S-L	Mixed-sized packings of large in small-sized particles	[-]
MTU	Micro-computed tomography of monosized structures	[-]
MTN	Micro-computed tomography of mixed-sized structures	[-]
DU	Discrete element packings of monosized structures	[-]
DN	Discrete element packings of mixed-sized structures	[-]
NU	Nottingham University	[-]
ΔH	Head loss	[-]
IP	Image processing	[-]
BM	Bottleneck model	[-]
LHS	Left-hand side	[-]
∇P	Pressure drop per unit length	[$Pa.m^{-1}$]
PTFE	Polytetrafluoroethylene	[-]
DPI	Digital pressure indicator	[-]
P_0	Absolute pressure	[bars]
P_R	Reference pressure	[bars]
SEM	Scanning electron microscope	[-]
RCM	Recemat	[-]
NCX	Nickel-chrome extra strong	[-]
R.D	Relative density	[-]
FD	Fluid domain	[-]
PS	Porous structure	[-]
PMS	Perfectly matched layer	[-]

NRC	Noise reduction coefficient	[-]
f_{peak}	The frequency of peak absorption	[Hz]
Hw	Half-band width	[Hz]
SAA	Sound absorption average	[-]
TH	Theoretical	[-]

LIST OF FIGURES

Fig.		Page No.
1.1	Acoustical effects in loudspeaker design and to the right are the 25-ultimate audiophile speaker produced by Bowers and Wilkins ($60,000/pair).	1
1.2	Images of close (a) and open (b) celled metallic foam structures (Zhou, 2006).	3
1.3	Geometry and notations of connecting spheres.	6
2.1	Samples of porous metallic foam structures made by (**a**) Foaming of Melts by Gas Injection (Hydro/Alcan) [adapted from Prakash et al., 1995] (**b**) Foaming of Melts with Blowing Agents (Alporas) [adapted from Ma and Song, 1993] (**c**) Solid-Gas Eutectic Solidification (Gasar) characterized by largely elongated pore structures [adapted from Shapovalov, 1998] (**d**) Foaming of Powder Compacts (Foaminal/Alulight), steel/aluminium foam/steel sandwich [adapted from Baumgartner et al., 2000] and (**e**) Two samples of aluminium/silicon carbide foam made by Foaming of Ingots Containing Blowing Agents (Formgrip/Foamcast) [adapted from Gergely and Clyne, 2000].	18
2.2	Routes for space-holding methods of metal foams production (Bram, et al., 2000).	22
2.3	Plots of pressure drop per unit length ($Pa.m^{-1}$) across 10 and 40PPI porous metallic structures against superficial air inlet velocity ($m.s^{-1}$) adapted from Dukhan, 2013.	34
2.4	Reducing high sound wave with an acoustic material (Bies and Hassan, 2009).	43
2.5	Plots of measured sound absorption coefficient of Polyurethane foam at airgap of 0, 5, 10, 15, 20 & 25mm (Muhammed et al., 2013).	46
2.6	Plots of measured hardbacked and 10mm airgap sound absorption coefficient of “bottleneck-type” porous aluminium foam structure against Frequency (Hz) (Lu and He, 2000).	46

2.7	Schematic representation of the growing complexity of motionless skeleton of (a) straight cylindrical pores (b) slanted cylindrical pores (c) non uniform sections and (d) non-uniform sections with possible constrictions regarding the microstructure of the porous materials and the number of poroacoustic models needed to describe its sound absorption behaviour (http://apmr.matelys.com/index.html).	47
2.8	Schematic view of viscous and thermal characteristics length (Olny and Panneton, 2008).	53
2.9	A 4-microphone, AFD 1200-AcoustiTube® - measuring setup with sample holding section (adapted from AFD Analysis software 1201 user guide) used to estimate the tortuosity, static thermal permeability, viscous and thermal characteristics length.	55
2.10	Frequency-dependent visco-inertia dissipation mechanism.	65
2.11	Frequency-dependent thermal dissipation mechanism.	65
3.1	An optical micrograph left of a porous sample made by vacuum casting using near-spherical NaCl (Langston and Kennedy, 2014) and right, an X-Ray CT (μCT) image showing the typical pore connectivity.	72
3.2	Two-dimensional (2D) and three-dimensional (3D) images of the virtual porous structure for pore sizes 2.0-2.5mm and 10μm capillary radius.	75
3.3	The plot of percentage fluid volume in metal foams (%) against cubic strut thickness (mm) for determination of representative volume element.	76
3.4	Three-dimensional (3D) Images of the internal morphology of virtual structures with 2mm mono-sized spherical for 10, 30, 45 and 80μm capillary radius.	77
3.5	Two-dimensional (2D) Images of the DEM virtual structures of uniform (2mm) pore sizes for a 10 and 80μm capillary radius.	77
3.6	Images of DEM structure and RVE for different capillary radii (left) 10μm and (right) 80μm.	78
3.7	Plots of isotropic and flow directional representation of permeability to pore size ratio, k_0/Dp^2 [-] and against the dimensional flow length to pore size ratio (L/Dp) [-] for a virtual DEM spherically celled structure (pore size, 2mm, and capillary radius, 10μm).	79

3.8	Plots of porosity (%) and a specific surface (mm^{-1}) against the dimensional flow length to pore size ratio (L/Dp) [-] for a virtual DEM spherically celled structure (pore size, 2mm, and capillary radius, 10μm).	79
3.9	Two-dimensional images of meshed "bottleneck" zone of "virtual" porous structures for different capillary radii (left) 10μm and (right) 80μm.	81
3.10	Representations of flow behaviour (surface fluid velocity scale and streamline for a $2\mu m.s^{-1}$ pore inlet velocity, v_p) on 2D DEM mono-sized slices for different capillary radii (left) 10μm and (right) 80μm [*Numerical scales unit for the legends measured in* $m.s^{-1}$].	82
3.11	The influence of normalized capillary radius on the ratio of CFD to modelled permeability.	83
3.12	The influence of normalized capillary radius on the ratio of structural parameters.	84
3.13	Plots of mean window radius, r_w, (μm) against capillary radius, r_c, (μm) for a mono-sized (2.0-2.5mm) and binary-sized (25vol%S) DEM packings.	86
3.14	Plots of unidirectional permeability $k_0/10^{-09}m^2$ against mean window radius (μm) for mono-sized (DU) and 25vol%S mixed-sized (DN) structures and their images for a 10 and 80μm capillary radii.	86
3.15	Three-dimensional (3D) numerically simulated velocity (top) and pressure (bottom) profile plots for water flow across the monosized (2.0-2.5mm) virtually-packed structures for a pore inlet velocity of $2.5mm.s^{-1}$ [*Numerical scales unit for the legends measured in* $m.s^{-1}$ *and Pa both for the velocity and pressure plots respectively*].	88
3.16	Three-dimensional (3D) numerically simulated velocity (top) and pressure (bottom) profile plots for water flow across the 25vol%S mixed-sized virtually-packed structures for a pore inlet velocity of $2.5mm.s^{-1}$ [*Numerical scales unit for the legends measured in* $m.s^{-1}$ *and Pa both for the velocity and pressure plots respectively*].	89
3.17	Plots of unit pressures pressure drop ($Pa.m^{-1}$) against superficial fluid (water) velocity ($mm.s^{-1}$) for the monosized and 25vol%S mixed-sized DEM structures at Darcy regime.	91
3.18	Plots of unit pressures pressure drop ($Pa.m^{-1}$) against superficial fluid (water) velocity ($mm.s^{-1}$) for the monosized	91

	and 25vol%S mixed-sized DEM structures at Darcy-Forchheimer regime.	
3.19	Representations of flow behaviour (surface fluid velocity scale and streamline for a 2.5mm.s^{-1} pore inlet velocity, v_p) on 2D DEM binary-sized (6.25 vol%S) slices for different capillary radii (left) 20μm and (right) 80μm [*Numerical scales unit for the legends measured in m.s^{-1}*].	93
3.20	Representations of flow behaviour (surface fluid velocity scale and streamline for a 2.5mm.s^{-1} pore inlet velocity, v_p) on 2D DEM binary-sized (12.5 vol%S) slices for different capillary radii (left) 20μm and (right) 80μm [*Numerical scales unit for the legends measured in m.s^{-1}*].	93
3.21	Representations of flow behaviour (surface fluid velocity scale and streamline for a 2.5mm.s^{-1} pore inlet velocity, v_p) on 2D DEM binary-sized (18.25 vol%S) slices for different capillary radii (left) 20μm and (right) 80μm [*Numerical scales unit for the legends measured in m.s^{-1}*].	93
3.22	Representations of flow behaviour (surface fluid velocity scale and streamline for a 2.5mm.s^{-1} pore inlet velocity,v_p) on 2D DEM binary-sized (25.0 vol%S) slices for different capillary radii (left) 20μm and (right) 80μm [*Numerical scales unit for the legends measured in m.s^{-1}*].	94
3.23	Representations of flow behaviour (surface fluid velocity scale and streamline for a 2.5mm.s^{-1} pore inlet velocity,v_p) on 2D DEM binary-sized (31.2 vol%S) slices for different capillary radii (left) 20μm and (right) 80μm [*Numerical scales unit for the legends measured in m.s^{-1}*].	94
3.24	Representations of flow behaviour (surface fluid velocity scale and streamline for a 2.5mm.s^{-1} pore inlet velocity,v_p) on 2D DEM binary-sized (37.5 vol%S) slices for different capillary radii (left) 20μm and (right) 80μm [*Numerical scales unit for the legends measured in m.s^{-1}*].	94
3.25	Representations of flow behaviour (surface fluid velocity scale and streamline for a 2.5mm.s^{-1} pore inlet velocity,v_p) on 2D DEM binary-sized (50 vol%S) slices for different capillary radii (left) 20μm and (right) 80μm [*Numerical scales unit for the legends measured in m.s^{-1}*].	95
3.26	Representations of flow behaviour (surface fluid velocity scale and streamline for a 2.5mm.s^{-1} pore inlet velocity,v_p) on 2D DEM binary-sized (100 vol%S) slices for different capillary radii (left) 20μm and (right) 80μm [*Numerical scales unit for the legends measured in m.s^{-1}*].	95

3.27	Plots of coordination number, N_C, against percentage various (0-50vol%) addition of binary-sized spherical packings for a 10μm capillary radius.	96
3.28	Plots of Darcian permeability, $k_0/10^{-09}m^2$, against percentage various (0-50vol%) addition of binary-sized spherical packings for capillary radius between 10-80μm.	96
4.1a	An Xradia-500 Microscope instrument used for capturing 2D CT slices of the porous metallic foam structures.	107
4.1b	Two-dimensional slices of foam structure having 0 (left), 72.96 (centre) and 100 vol percent threshold limit.	108
4.2	Two-dimensional (2D) images indicating a linear tetrahedral mesh growth from the re-entrant edge and the bottleneck regions of structures with the highest (left) and lowest (right) pressure differential.	111
4.3	Plots of pressure drop ratio [-] against mesh density/Mcells showing the effect of mesh structure to capture flow information on the "bottleneck" and pore region of Al porous structure with spherical cells [*Numerical scales unit for the legends measured in* $m.s^{-1}$].	111
4.4	Schematic representation of air flow measurement.	113
4.5	Inlet pressure-voltage calibration a digital pressure indicator (DPI 601).	114
4.6	An optical microscope images of foam structures cast with salts with particle sizes (left) X1/1.0 – 1.4mm and (right) Z1/2.0-3.15mm structures both produced at 0.9 bar.	117
4.7	An optical microscope images of Y1 and Y4 foam structures particle size range 2.0-2.5mm.	117
4.8	Scanning electron microscope (SEM) images of salts used for the casting process for particle sizes 1.0-1.4mm (left), 2.0-2.5mm (middle) and 2.5-3.15mm (right).	117
4.9	A two-dimensional model contour of porous Al structure taken from CT images for the highest Y1 (left) and lowest Y4 (right) pressure differentials.	118
4.10	Three-dimensional X-ray CT (left) and DEM (right) images of structural domains representative Y1 structures.	119

4.11	X-ray CT images of Inconel 450μm foam structure and a plot of pressure drops per unit length ($Pa.m^{-1}$) against superficial air inlet velocity ($m.s^{-1}$) for the structure.	120
4.12	Experimental pressure drop per unit length ($Pa.m^{-1}$) against air superficial inlet velocity ($m.s^{-1}$) for a repetitive test on aluminium foam sample Z1 (2.5-3.15mm).	122
4.13	Experimentally reduced pressure drop ($Pa.s.m^{-2}$) against air superficial inlet velocity ($m.s^{-1}$) for a repetitive test on aluminium foam sample Z1 (2.5-3.15mm).	122
4.14	Plots of dimensionless Fanning friction factor (f) against pore diameter-based Reynolds number (Re_D) for airflow through the lowest window-sized (Z1) porous Al foam structure.	124
4.15	Plots of dimensionless Fanning friction factor (f_F) against pore diameter-based Reynolds number (Re_D) for airflow through the lowest window-sized (X1) porous Al foam structure.	126
4.16	Plots of dimensionless Fanning friction factor (f_F) against pore diameter-based Reynolds number (Re_D) for airflow through the largest window-sized (Y4) porous Al foam structure.	126
4.17	Plots of measured pressure drop per unit length ($Pa.m^{-1}$) against superficial air inlet velocity ($m.s^{-1}$) six foam structures.	128
4.18	Plots of reduced pressure drop per unit length ($Pa.m^{-1}$) against superficial air inlet velocity ($m.s^{-1}$) six foam structures.	128
4.19	The relationship between pressure differential (bar) and the ratio of window to pore sizes [-] for the cast samples.	131
4.20	Normalised pressure drop [-] for 10 mm thick samples, plotted against superficial flow velocity.	133
4.21	Two-dimensional (2D) velocity profile plots for flow (left to right) through "virtually-created" porous samples Y1 (top) and Y4 (bottom) for an inlet pore velocity of 1m s^{-1} [*Numerical scales unit for the legends measured in* $m.s^{-1}$].	135
4.22	Graph of measured and modelled (using X-ray CT images) pressure drops per unit thickness ($Pa.m^{-1}$) against superficial air inlet velocity ($m.s^{-1}$).	137

4.23	Three-dimensional (3D) velocity magnitude profile plots computed using X-ray CT images of the "real" structure (top, Ø=75.2%, D_w=741μm & D_p=2.0-2.5mm) and DEM "virtual" macroporous spherical structures (bottom, Ø=74.7%, D_w=731μm & D_p =2.0-2.5mm) of similar RVE three dimensional spaces (8x8x8 mm^3) for a pore inlet velocity of 3.35mm.s^{-1} (left) and 1.25m.s^{-1} (right) [*Numerical scales unit for the legends measured in m.s^{-1}*].	139
4.24	Graph of measured and modelled (using X-ray CT and DEM images) pressure drops per unit thickness (Pa.m^{-1}) against superficial air inlet velocity (m.s^{-1}) for Y1-Y4 structures.	140
4.25	Plots of the ratio of measured to CFD modelled (X-ray CT and DEM) unit pressure drop [-] against superficial air inlet velocity (m.s^{-1}) for Y1 and Y4 structures.	141
4.26	Two-dimensional (2D) velocity profile plots for flow (left to right) through porous samples Y1 (left) and Y4 (right) for an inlet pore velocity of 1m s^{-1} [*Numerical scales unit for the legends measured in m.s^{-1}*].	142
4.27	Two-dimensional (2D) visualization of the actual three-dimensional (3D) CT volume of the velocity (left) and pressure drop (right) distribution for flow through porous samples Y1 (top) and Y4 (bottom) for air superficial inlet velocity of 1m s^{-1} [*Numerical scales unit for the legends measured in m.s^{-1} and Pa for the velocity and pressure plots respectively*].	144
4.28	Two-dimensional (2D) CT model contour fluid domain matrices (top) and three-dimensional (3D) CT RVE skeletal phases (bottom) for lowest porosity structure, Y3 (left) and after structural erosion of 1- (center, Y31) and 2- (right, Y32) pixels removed from the skeletal phase for 8.5mm flow thickness.	146
4.29	Plots of simulated pressure drop per unit length (Pa.m^{-1}) against superficial air inlet velocity (m.s^{-1}) for semi-virtual structures (structural domain erosion, 1-5 pixel removed) using CT images compared with simulations for near-equivalent "real" samples.	148
4.30	Two-dimensional (2D) visualization of the actual three-dimensional (3D) CT volume of the velocity (top) and pressure drop (bottom) distribution for flow through porous samples Y3 (left) and after structural erosion of 1- (centre, Y31) and 2- (right, Y32) pixels removed from the skeletal phase of the microstructure for superficial air inlet velocity	148

	of 1m s^{-1} [*Numerical scales unit for the legends measured in* $m.s^{-1}$ *and Pa for the velocity and pressure plots respectively*].	
4.31	Dimensionless plots of permeability-structural parameters of the porous structures using CT images of Y's and fluid domain dilated structures.	150
4.32	Graph of the viscous and inertial terms of the porous structure using the CT images of the Y's and fluid domain dilated structures.	150
4.33	Plots of permeability inverse (m^{-2}) against structural parameters (m^{-2}) of the porous structure using the CT images of the Y's and fluid domain dilated structures.	152
4.34	The plot of the natural log of Form drag coefficient (m^{-1}) against natural log of structural parameters (m^{-1}) of the porous structure using the CT images of the Y's and fluid domain dilated structures.	152
5.1	Plots of normal incidence absorption coefficient against frequency for a 25mm hard-backed glass wool fiber material (GWF, 98.7% porosity) by Kino and Ueno, 2008; 25.5mm hard-backed melamine foam (MF, 99.3% porosity) by Kino and Ueno, 2008; 10mm hard-backed nickel-chrome extra strong (NCX2733, 90.94% porosity) by Lautensack and Kabel, 2009; 23.31mm hardbacked porous sintered fiber metal (SFM, 90.94% porosity) by Bo and Tianning, 2009; 11.2mm hard-backed porous metal sponge 450 by Hinze and Rosler, 2014 and 20mm hard-backed open-celled aluminium foam structures with spherical cells presented by Li et al. 2014, (AL Foam, 60% porosity).	160
5.2	Digital microscope photograph of (a) Glass wool fiber material (GWF) by Kino and Ueno 2008 (b) Melamine foam (MF) by Kino and Ueno 2008 (c) Photographic cross-section of Porous sintered fiber metal structures (SFM) by Bo and Tianning, 2009 (d) Typical pore morphology of aluminium foam structure with spherical cells by Li et al., 2014 (e) 3D reconstructed X-ray CT image of nickel-chrome (NCX2733) extra strong structure by Lautensack and Kabel, 2009 and (f) 3D reconstructed X-ray CT image of porous metal sponge 450 by Hinze and Rosler, 2014.	160
5.3	Graphical representation of natural log of dynamic tortuosity ($ln\tau$) against natural log of packing density (porosity, $\emptyset$) using analytically predicted values reported by Du Plessis and Fourier, 2002 (Tortuosity factor, n is 0.552, shape factor, C_o is 0.35 with a very good fit $R^2 = 0.999$).	165

5.4	A two-dimensional geometry of a hardbacked porous structure in an impedance tube.	167
5.5	A 2D (a) and 3D half-tube (b & c) model representations of total acoustic pressure (Pa) computed for 25mm hardbacked glass wool fiber computed using Johnson-Champoux-Allard model [*Numerical scales unit for the legends measured in Pa]*.	169
5.6	Vertical-axis, is a 2D and horizontal, is a 3D value of computed normal incidence absorption coefficient for a 25mm hardbacked glass wool fiber material using Johnson-Champoux-Allard model for the frequency of 100-6500Hz.	169
5.7	Plots of measured (literature) and simulated (current) normal incidence absorption coefficient against frequency (Hz) for (a) hardbacked glass wool fiber (b) hardbacked melamine foam (c) hardbacked porous sintered fiber metal and (d) airgap or cavity behind the porous sintered fiber metal.	171
5.8	Plots of measured (Hinze and Rosler, 2014) and simulated (current) normal incidence absorption coefficient of hard-backed porous metal sponge 450 and 800 against frequency (500-7500Hz) at different structural thicknesses.	173
5.9	Plots of measured (Li et al., 2014, structure B) and modelled (current) normal incidence absorption coefficient (*Ac*) against Frequency (100-6500Hz) for a hard-backed 20mm thick aluminium foam structure (Tortuosity, $\tau = 1.867$) with spherical cells.	174
5.10	Plots of 20mm thick hardbacked numerically simulated normal incidence absorption coefficient (*Ac*) against frequency (Hz) using structural parameters of the theoretically predicted (TH) and "virtually-created" monosized "bottleneck" structures having a similar capillary radius of 80μm and different pore sizes, 1, 2 and 3mm.	178
5.11	Plots of 20mm thick hardbacked numerically simulated normal incidence absorption coefficient (*Ac*) against frequency (Hz) using structural parameters of the "virtually-created" monosized "bottleneck" structures having similar pore sizes of 2mm and different capillary radius of 10, 30, 45 & 80μm.	178
5.12	Plots of 20mm thick hardbacked numerically simulated normal incidence absorption coefficient (*Ac*) against frequency, Hz using structural parameters of selected "virtually-created" monosized "bottleneck" structures	179

	having different pore sizes and capillary radius but similar pore openings.	
5.13	Plots of 20mm thick hardbacked numerically computed normal incidence sound absorption coefficient against frequency (Hz) using structural parameters of X, Y and Z samples obtained from X-ray CT images of the real sample.	183
5.14	Plots of 20mm thick hardbacked numerically computed normal incidence sound absorption coefficient against frequency (Hz) using structural parameters of the Y samples (2.0-2.5mm) obtained from X-ray CT images of the "real" sample and "virtually-created" sphere-packing models.	184
5.15	Plots of 20mm thick hardbacked normal incidence absorption coefficient against frequency (Hz) for structures with constant window to pore size ratio (r_w/r_p-0.15), for different pore sizes (Dp=200, 1400 and 3000μm) and different porosities, 56, 68 & 80%.	187
5.16	Graphical representations of acoustic properties of numerically simulated "bottleneck-type" structures against permeability for pore sizes between 200 and 3000μm.	188
5.17	Plots of 20mm thick hardbacked numerically simulated and measured (Li, Zhendong and Han, 2014) normal incidence absorption coefficient against frequency (Hz) for optimised "bottleneck-type" monosized structures and commercially used soundproofing glass wool fiber (Kino & Ueno, 2008), melamine foam (Kino and Ueno, 2008) and porous sintered fiber metal (Bo and Tianning, 2009).	189
5.18	Plots of hardbacked numerically simulated normal incidence absorption coefficient against frequency (Hz) for optimized C2 structure for thicknesses between 5 and 40mm.	191
5.19	Plots of noise reduction coefficient (*NRC*) against structural thickness (mm) for 20mm thick hardbacked, 10, 25 and 50mm airgap behind (BHD) and between (BTW) two 10mm optimized C2 structures.	191
4.1A	Mesh structure and streamline velocity plots for Y1 structure at 1.5x res/6.75Lmin and 1.3 Growth rate for a superficial inlet velocity of 2.369 $m.s^{-1}$ [*Numerical scales unit for the legends measured in $m.s^{-1}$]*.	233
4.2A	Mesh structure and streamline velocity plots for Y1 structure at 2.1x res/6.75Lmin and 1.3 Growth rate for a superficial inlet velocity of 2.369 $m.s^{-1}$ [*Numerical scales unit for the legends measured in $m.s^{-1}$]*.	233

4.3A	Mesh structure and streamline velocity plots for Y1 structure at 2.7x res/6.75Lmin and 1.2 Growth rate for a superficial inlet velocity of 2.369 $m.s^{-1}$ [*Numerical scales unit for the legends measured in $m.s^{-1}$]*.	234
4.4A	Mesh structure and streamline velocity plots for Y1 structure at 2.7x res/6.75Lmin and 1.3 Growth rate for a superficial inlet velocity of 2.369 $m.s^{-1}$ [*Numerical scales unit for the legends measured in $m.s^{-1}$]*.	234
4.5A	Mesh structure and streamline velocity plots for Y1 structure at 5x res/6.75Lmin and 1.2 Growth rate for a superficial inlet velocity of 2.369 $m.s^{-1}$ [*Numerical scales unit for the legends measured in $m.s^{-1}$]*.	235
4.6A	Mesh structure and streamline velocity plots for Y1 structure at 5x res/6.75Lmin and 1.3 Growth rate for a superficial inlet velocity of 2.369 $m.s^{-1}$ [*Numerical scales unit for the legends measured in $m.s^{-1}$]*.	235
4.7A	Left-right: 3D velocity profile plots and 2D (YZ, ¼, ½ & ¾) section of computed airflow across foam structure Y1 at 1.0m/s superficial inlet velocity (pore inlet velocity, v_p, in this case, is 1.418m/s calculated using the foam porosity, 70.5%).	236
4.8A	Left-right: 3D velocity profile plots and 2D (YZ, ¼, ½ & ¾) section of computed airflow across foam structure Y1 at 1.516 $m.s^{-1}$ superficial inlet velocity (pore inlet velocity, v_p, in this case, is 2.150m/s calculated using the foam porosity, 70.5%) [*Numerical scales unit for the legends measured in $m.s^{-1}$]*.	236
4.9A	Left-right: 3D pressure profile plots and 2D (YZ, ¼, ½ & ¾) section of computed airflow across foam structure Y1 at 1.0$m.s^{-1}$ superficial inlet velocity (pore inlet velocity, v_p, in this case, is 1.418m/s calculated using the foam porosity, 70.5%) [*Numerical scales unit for the legends measured in Pa]*.	238
4.10A	Left-right: 3D pressure profile plots and 2D (YZ, ¼, ½ & ¾) section of computed airflow across foam structure Y1 at 1.516$m.s^{-1}$ superficial inlet velocity (pore inlet velocity, v_p, in this case, is 2.150m/s calculated using the foam porosity, 70.5%) [*Numerical scales unit for the legends measured in Pa]*.	238

4.11A	A 2D contour fluid phase and 3D RVE structural phase of Y1 structure for (Left) no fluid phase dilation and (Right) 1-pixel addition to the fluid phase.	238
4.12A	A 2D contour fluid phase and 3D RVE structural phase of Y1 structure for (Left) 2-pixel addition and (Right) 3-pixel addition to the fluid phase.	238
4.13A	A 2D contour fluid phase and 3D RVE structural phase of Y1 structure for (Left) 3-pixel addition and (Right) 4-pixel addition to the fluid phase.	239
4.14A	A 2D contour fluid phase and 3D RVE structural phase of Y2 structure for (Left) no fluid phase dilation and (Right) 1-pixel addition to the fluid phase.	239
4.15A	A 2D contour fluid phase and 3D RVE structural phase of Y2 structure for (Left) 2-pixel addition and (Right) 3-pixel addition to the fluid phase.	240
4.16A	A 2D contour fluid phase and 3D RVE structural phase of Y3 structure for (Left) no fluid phase dilation and (Right) 1-pixel addition to the fluid phase.	240
4.17A	A 2D contour fluid phase and 3D RVE structural phase of (Left) Y3 structure for 2-pixel addition to the RVE fluid phase and (Right) Y4 structure with no fluid phase dilation.	241
4.18A	A 2D contour fluid phase and 3D RVE structural phase of Y4 structure for (Left) 1-pixel addition and (Right) 2-pixel addition to the fluid phase.	241
5.1A	A 2D fluid phase model contour and 3D structural phase of DEM virtual structure of 1mm pore sizes and capillary radius of 10μm for a (left) No structural erosion, DU1-10, and (right) 1-pixel, DU1-E1, removed from the structural phase.	248
5.2A	A 2D fluid phase model contour and 3D structural phase of DEM virtual structure of 1mm pore sizes and capillary radius of 10μm for a (left) 2-pixel, DU1-E2, and (right) 3-pixel, DU1-E3, removed from the structural phase.	249
5.3A	A 2D fluid phase model contour and 3D structural phase of DEM virtual structure of 1mm pore sizes and capillary radius of 10μm for a (left) 4-pixel, DU1-E4, and (right) 5-pixel, DU1-E5, removed from the structural phase.	249
5.4A	A 2D fluid phase model contour and 3D structural phase of DEM virtual structure of 1mm pore sizes and capillary radius of 10μm for a (left) 1-pixel, DU1-D1, and (right) 2-pixel, DU1-D2, added to the structural phase.	250

5.5A	A 2D fluid phase model contour and 3D structural phase of DEM virtual structure of 2mm pore sizes and capillary radius of 10μm for a (left) No structural erosion, DU2-10, and (right) 1-pixel, DU2-E1, removed from the structural phase.	250
5.6A	A 2D fluid phase model contour and 3D structural phase of DEM virtual structure of 2mm pore sizes and capillary radius of 10μm for a (left) 2-pixel, DU2-E2, and (right) 3-pixel, DU2-E3, removed from the structural phase.	251
5.7A	A 2D fluid phase model contour and 3D structural phase of DEM virtual structure of 2mm pore sizes and capillary radius of 10μm for a (left) 4-pixel, DU2-E4, and (right) 5-pixel, DU2-E5, removed from the structural phase.	251
5.8A	A 2D fluid phase model contour and 3D structural phase of DEM virtual structure of 2mm pore sizes and capillary radius of 10μm for a (left) 1-pixel, DU2-D1, and (right) 2-pixel, DU2-D2, added to the structural phase.	252
5.9A	A 2D fluid phase model contour and 3D structural phase of DEM virtual structure of 3mm pore sizes and capillary radius of 10μm for a (left) No structural erosion, DU3-10, and (right) 1-pixel, DU3-E1, removed from the structural phase.	252
5.10A	A 2D fluid phase model contour and 3D structural phase of DEM virtual structure of 3mm pore sizes and capillary radius of 10μm for a (left) 2-pixel, DU3-E2, and (right) 3-pixel, DU3-E3, removed from the structural phase.	253
5.11A	A 2D fluid phase model contour and 3D structural phase of DEM virtual structure of 3mm pore sizes and capillary radius of 10μm for a (left) 4-pixel, DU3-E4, and (right) 5-pixel, DU3-E5, removed from the structural phase.	253
5.12A	A 2D fluid phase model contour and 3D structural phase of DEM virtual structure of 3mm pore sizes and capillary radius of 10μm for a (left) 1-pixel, DU3-D1, and (right) 2-pixel, DU3-D2, added to the structural phase.	254
5.13A	Plots of normal incidence absorption coefficient against frequency (Hz) for structures with constant porosity (56%), different pore sizes (rp=100, 700 and 1500μm) and three different windows to pore ratio (r_w/r_p=0.15, 0.45 and 0.30).	255
5.14A	Plots of normal incidence absorption coefficient against frequency (Hz) for structures with constant window to pore ratio (r_w/r_p-0.30), for different pore sizes rp=100, 700 and 1500μm) and for different porosities (Ø=56, 68 & 80%).	255

5.15A	Plots of normal incidence absorption coefficient against frequency (Hz) for structures with constant porosity (80%), different pore sizes (r_p=100, 700 and 1500μm) and three different windows to pore ratio (r_w/r_p =0.15, 0.45 and 0.30).	256

LIST OF TABLES

Table		Page No.
2.1	Summary of common boundary conditions for fluid flow (Hesketh, 2008).	37
2.2	Acoustic porous media models	64
2.3	Estimation of viscous and thermal boundary layer thickness.	66
3.1	Structural and flow data for DEM and μCT mono-sized, L-L, and mixed-sized, L-S, structures.	92
4.1	Measured and X-ray CT structural parameters of the porous Al structure.	116
4.2	X-ray CT and DEM based structural parameters of Y1 and Y4 structures.	120
4.3	Measured and X-ray CT structural parameters of the porous Al structure.	136
4.4	X-ray CT and DEM based flow parameters of Y1 and Y4 structures.	140
4.5	Structural and flow data for the real, Y3 & Y4 and eroded (Y1i) CT structures.	147
4.6	A tabular representation of proposed models and their applications	153
5.1	Structural parameters of Al structures with spherical cells in Li, Zhendong & Han 2014.	166
5.2	Structural (literature) and acoustic (current) data for non-spherical cell structures.	170
5.3	Measured (Li et al., 2011) and predicted (current) sound absorption coefficient of aluminium foam structure with spherical cells (Ø~65%) at 500, 1000 and 2000Hz.	175
5.4	Measured (Li, Zhendong & Han, 2014) and predicted structural of Al structures with spherical cells.	176
5.5	Structural parameters and acoustic properties of DEM monosized (1, 2 & 3mm) spherical structures.	177

5.6	Structural and acoustic parameters of porous structures with spherical cells (X, Y, and Z) characterized using CT images and DEM.	182
5.7	Structural and acoustic properties of "bottleneck-type" porous structures for the window to pore ratio for 0.15, 0.30 and 0.45 and porosities, 56, 68 and 80%.	185
5.8	Structural and acoustic properties of numerically simulated and measured "bottleneck-type" porous structures and commercially used non-spherical porous soundproofing materials.	189
4.1A	Experimental data of pressure drop per unit length (Pa/m) over foam structures X, Y, and Z.	230
4.2A	X-ray CT (μCT) and DEM computed values of pressure drops per unit length (Pa/m) for X, Y, and Z foam structures.	230
4.3A	X-ray CT (μCT) computed pressure drops per unit length for Y1 and Y1i dilated structures (RVE cubic flow length ~ 8.8mm).	231
4.4A	X-ray CT (μCT) computed pressure drops per unit length for Y2, Y3, Y4 and Y2i, Y3i and Y4i dilated structures (RVE cubic flow length ~ 8.5mm).	231
4.5A	Structural and flow data for Y1, Y2, Y3 and Y4 and Y1i, Y2i, Y3i and Y4i dilated structures.	232
5.1A	A tabular representation of the measured (Lu & He, 2000) and simulated (current) sound absorption coefficient at 500, 1000 and 1600Hz for a 20mm thick hardbacked and airgap aluminium foam structures with spherical cells.	242
5.2A	A tabular representation of predicted (Lu & He, 2000) and simulated (current) noise reduction coefficient and absorption peak for a 20mm thick hardbacked aluminium foam structures with spherical cells.	243
5.3A	Structural parameters and acoustic properties of DEM monosized (1, 2 & 3mm) spherical structures.	244
5.4A	Structural parameters and acoustic properties of DEM mixed-sized (S-S and L-L) spherical structures.	244
5.5A	Structural and acoustic parameters of porous structures with spherical cells (X, Y, and Z) characterized using CT images and DEM.	245

5.6A	Structural and acoustic properties of “bottleneck-type” porous structures for the window to pore ratio for 0.15, 0.30 and 0.45, pore diameter sizes between 200 and 3000µm and porosities, 56, 68 and 80%.	245
5.7A	A tabular representation of macroscopic data of actual eroded and dilated DEM structural phase for 1, 2 and 3mm.	247

ACTIVITIES

Published papers

- **Otaru, A.J.** & Kennedy, A.R. (2016), The Permeability of Virtual Macroporous Structures Generated by Sphere-Packing Models: Comparison with Analytical Models, *Scripta Materialia*, Vol 124, Pp 30-33. (Elsevier, current impact factor is 3.747) https://doi.org/10.1016/j.scriptamat.2016.06.037

- **Otaru, A.J.,** Morvan, H.P. & Kennedy, A.R. (2018), Measurement and Simulation of Pressure Drop across Replicated Microcellular Aluminium in the Darcy-Forchheimer Regime, *Acta Materialia*, Vol 149, Pp 265-275. (Elsevier, current impact factor is 6.036) https://doi.org/10.1016/j.actamat.2018.02.051

- **Otaru, A.J.,** Morvan, H.P. & Kennedy, A.R. (2018), Modelling and Optimisation of Sound Absorption in Replicated Microcellular Metals, *Scripta Materialia*, Vol 150, Pp 152-155 (Elsevier, current impact factor is 3.747) https://doi.org/10.1016/j.scriptamat.2018.03.022

Conferences

- **Otaru, A.J.** & Kennedy, A.R. & Morvan, H.P. (2015), Microscale Simulation of Single-Phase Flow in Porous Media: A Run-through of Kozeny Mathematical Assertion, *IMA conference for Numerical Methods for Simulation*, 1-4 September 2015 at the Mathematical Institute, University of Oxford.

- **Otaru, A.J.** & Kennedy, A.R. & Morvan, H.P. (2016), Discrete Element Modelling and Micro-Computed Tomography Pore-Scale Hydrodynamic Behaviour of Open-Cell Foam, International Conference of Nigerian Students in Diaspora, ICONS 10-12th June 2016, De MontFort University, Leicester.

Courses and training attended during this research are listed below:

- Creating a Poster in PowerPoint.

- How to use the University of Nottingham HPC.

- Introduction to MATLAB for Engineers.
- Academic Writing: Grammatical Accuracy.
- Body Language: The Silent Communication Tool.
- Introduction to Database Design.
- Simpleware Webinar
- COMSOL Multiphysics Webinar and Workshop
- Small Group Teaching
- Presentation Skills: An Introduction to Public Speaking.
- Lecturing for Learning.
- Foundation for Teaching in Higher Education
- Preparation to Teach in Higher Education.
- Three times field trip to Bowers and Wilkins Group, West Sussex, UK.
- Participated in the teaching and demonstration of CFD lab-Advanced Transport Phenomena using COMSOL Multiphysics 5.0™.
- Participated in the teaching and demonstration of Aircraft Propulsion System using GasTurb 11.

CHAPTER 1

INTRODUCTION

This research focuses on fluid flow and acoustic absorption in porous metallic structures using numerical simulation and experimentations. Its aim is to understand the pressure drop behaviour of such structures and their response when subjected to the propagation of pressure waves at waffling frequencies; to consider embedding such knowledge in the design of poroacoustic metallic materials to replace those conventionally used in cabinets of high-end loudspeakers.

Such an approach will help provide a heat sink for drive unit motor by absorbing radiation from the rear of the loudspeaker transducer. Such a configuration and material could also cut vibration in a speaker more than half, help minimize back pressure wave from the drive motor unit and increase design flexibility. Fig 1.1 (middle) presents a schematic representation of back pressure waves from the drive motor unit to the cabinet of the loudspeaker.

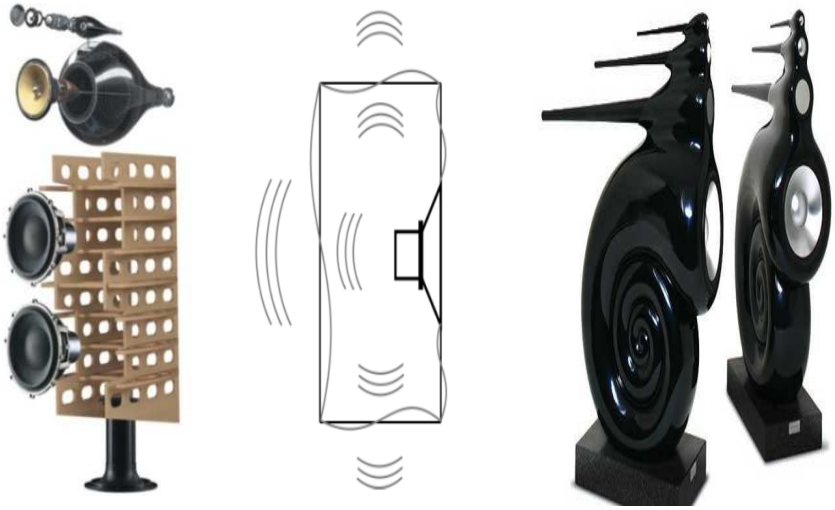


Fig 1.1. Acoustical effects in loudspeaker design and to the right are the 25-ultimate audiophile speaker produced by Bowers and Wilkins ($60,000/pair).

Acoustic foams are used as soundproofing to assist in minimizing reflections and reverberation, in music rooms, studios, and cinemas. Synthetic fibers such as kevlar, polyester, polyurethane, melamine, polyethylene or polypropylene are known conventional porous materials used to absorbed pressure waves. These materials absorb most sound energy striking them and reflect very little (Jorges and Malcom, 2010). This type of fibrous material is made from high-temperature extrusion and industrial processes based on synthetic chemicals (petrochemical source). Their carbon footprint is quite significant, and the industrial process to make them contributes to the release of some greenhouse gasses like methane, carbon dioxide and sulfur dioxide (Ballagh, 1996 and Zulkifli, 2008).

Natural fibers (wool, cotton, asbestos, fur felt, hemp, and flax) are generally porous and can absorb sound both at low and high frequencies (Kino & Ueno, 2008). They are biodegradable, inexpensive, and environmentally friendly but their low strength, softness, decrease in absorption potential over time (Deng, et al., 2008) and damages caused to the respiratory system, human skin, eye and other health-related issues (Ou, 1997) are of concern, leading to a limited usage of such material.

Lu and He (2000), Li et al. (2014), and Bo and Tianning (2009) have shown that the broadband characteristics of noise reduction can be achieved through open-celled metallic foam structures (Fig 1.2) which have earned numerous attentions resulting from increased worldwide technological research and development. They are expensive to produce but are environmentally friendly, easily recycled, have high durability and resistance, are less harmful, reduce vibration effects and have longer active product life for money.

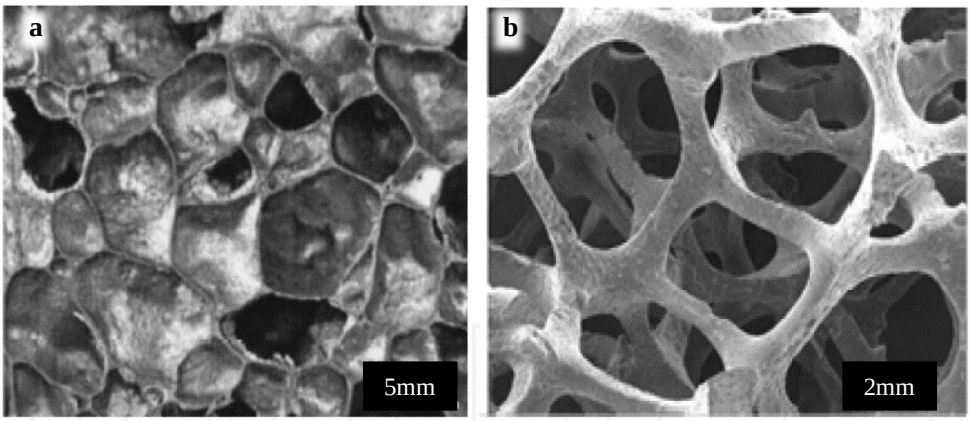


Fig 1.2. Images of close (a) and open (b) celled metallic foam structures (**adapted from Zhou, 2006**).

Relatable experimental and predictive studies conducted in this field (Lafarge et al., 1984, Mikki, 1990, Prides et al., 1993, Wilson, 1993, Ashby et al., 1999, Lu and He, 2000, Kino and Ueno, 2008, Muhammed et al., 2013, and Li et al., 2014) have all described the characteristic sound absorption behaviour of porous materials as a function of structural properties and most importantly, the permeability of the porous medium. Knowing or measuring and predicting the permeability of these ultralight and self-supporting structures (porous metals) is essential to the design and optimisation of enhanced materials (with novel attributes) capable of cutting down vibration in speakers.

In the light of these, a preliminary review of the fluid flow and acoustic absorption in porous metallic structures is presented below to identify the gap in research in the literature.

1.1 Fluid Flow through Porous Metallic Structures

Understanding the behaviour of fluid flow through porous metallic structures (nickel, steel, titanium, copper, and aluminium) is quite important in the design of porous material for engineering applications. Unlike flow through packed beds where the permeation of fluid is mainly dictated by their void spaces (interstices), flow through open-celled metallic foams as described in Habisreuther et al. (2009) is rendered more complex by the opening of their interconnecting pores or “windows”. This interconnection in porous metallic structures enables their high porosity, permeability, large foam surface area per unit bulk volume and good thermal conductivity (Dukhan et al., 2014) and has made it beneficial for their use as pressure reduction and heat transfer devices (Ranut et al., 2013).

The ratio of the fluid volume occupied by the continuum fluid phase to the total volume of this porous body, or the interconnected pore fluid volume to the total bulk volume of the porous medium has a significant influence on the flow behaviour of this structure. Also, the size of the pores and connectivity (openings) between connecting pores of open-celled foam dictates its flow behaviour and can be controlled by simply varying the size of salt granules (space holder or porogens) and infiltration pressure used during metal foam preparation (Kennedy, 2012). The size of the salt beads is a representation of the pores occupied by fluid in metal foam while the volume fraction is dictated by their packing through the addition or removal of beads during packing (Jinnapat and Kennedy, 2012). The degree of infiltration into the spaces between the beads, which is a function of infiltration pressure difference used, causes

significant changes in the connectivity of the metal matrix which is negative of the spatial arrangement of the beds (Langston and Kennedy, 2014).

Realistic manipulation of foam structures through hole-drilling, mechanical compression and rolling (Lu et al., 1999) to change their microstructure represents a high-priced approach and further complicates the skeletal configuration of foam matrix (Hetu et al., 2013). Moreover, foam measurements using an optical microscope techniques that measure cell diameter, “strut” length, “window” thickness, cell volume and many other features (Rhodes, 1980, and Richardson and Nandra, 1986) have been in use to reveal structural information of the material needed for a specific application.

Measuring foam features manually using the traditional optical microscope technique is time-consuming, limited to capturing only surface information and often requires destruction of the foam sample because of its complicated three-dimensional (3D) structure (Montming et al., 2004). These parameters are difficult to measure using this traditional technique which has been mostly adopted in medical and engineering research.

X-Ray computerized microtomoghraphy (μCT) is used in several applications ranging from material research (Watson et al. 2006, and Fularia et al., 2007) to reverse engineering of complex parts with precision. Pore-level characterization and computation of fluid through an open-celled foam on a representative micro-geometry have been presented by several researchers using a more realistic and high-resolution two-dimensional X-ray CT images (Petrasch et al. 2006, Narsilio, et al. 2009 and De Carvalho, et al., 2017). Magnetic resonance imaging (MRI) or micro-computed tomography provides a more visceral assessment and characterization of foam structures (Bodla et al., 2010) but represents an

expensive approach and modelling results often deviate from reality when it comes to low-resolution images (Peng, et al. 2012).

Simple permeability models for laminar flow have been developed by Despois and Mortenson (2005), and Furman et al. (2013) which could assist with the design of "bottleneck-type" porous metallic structures to meet the requirements for specific applications. Both approaches use the same premise, considering the window between the pores to be a "bottleneck" to the flow through the structure. The models consider different particle contact cases like loose packing (Furman et al. 2013) and packing enhanced through compaction (Despois and Mortenson, 2005) with different approaches to including contributions from the window size (r_w) and coordination number (N_C). The model to predict the permeability according to Furman et al. (2013) is presented in Eq. (1.1) where $\emptyset$ is the porosity, N_C the coordination number, r_w the window radius and r_p the radius of the pore or pore radii (Fig 1.3).

$$k_0 = N_C \frac{\emptyset r_w^3}{6\pi r_p} \quad \text{Where} \quad N_C = \frac{4-\emptyset+\sqrt{2+7\emptyset+\emptyset^2}}{2(1-\emptyset)} \tag{1.1}$$

$$r_w = \sqrt{(r_c + r_p)^2 - r_p^2} - r_c \quad \text{Where } r_c = \frac{2\sigma_{xy}}{P_i} cos\theta \tag{1.2}$$

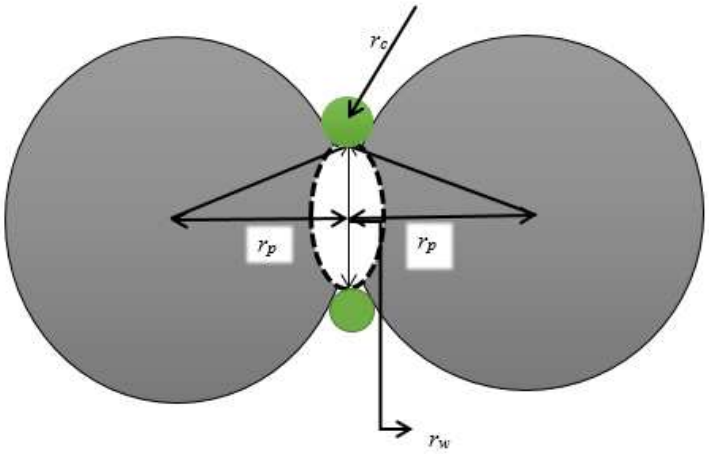


Fig 1.3. Geometry and notations of connecting spheres.

The coordination number was defined as a function of the packing fraction (also shown in Eq. 1.1) and the window sizes connecting two spheres within the porous matrix was considered in Asmar et al. (2002) to be a function of pore radii (r_p) and the degree of liquid foam infiltration pressure (Pi) measured by capillary radius (r_c) Eq 1.2. The extent to which an applied infiltration pressure, P_i, (used during realistic casting of metal foams) drives liquid metals into the void of packed beds is theoretically considered (Langston & Kennedy, 2014) to be a function of its capillary radius, r_c, surface tension, σ_{xy}, and wetting angle, θ, (Eq 1.2) with established wetting data of Al-NaCl available in the literature. This approach (Eq 1.2) involves measuring the liquid driving pressure necessary to balance the Laplace pressure (Yuan & Lee, 2013). These models are limited to predicting the coordination number and permeability (viscous term) of porous Al foam structure made by packed beds of near-spherical porogens but do not account for the inertial terms (away from Darcy).

Total control of pore sizes, packing density, and connectivity of the virtually-created "bottleneck-type" structures in Langston and Kennedy, 2014 could assist in providing alternative and economical ways of predicting the flow behaviour of open-celled structures made by replication-casting processes. This study considers production, characterization and realistic measurement of the pressure drop developed across "bottleneck-type" celled porous aluminium structures for different packing densities, pore sizes, and interstices. A computational fluid dynamics (CFD) approach is considered using sphere-packing models (discrete element modelling) and X-Ray computerized micrograph (μCT) of the "real" structure for the reconstruction of the three-dimensional micro-geometrical representative matrix based on the required pore volume (porosity).

1.2 Sound Pressure Waves through Porous Metallic Structures

Noise and vibration improvement control devices are of utmost importance and constitute a major environmental and safety component in the automotive, building, aeronautical, construction and many engineering industries (Chang-Young and Michael, 2009).

Close-celled metallic foams (Fig 1.2) are characterized by infinite air flow resistivity (ratio of fluid dynamic viscosity to permeability) and are generally termed as poor sound absorbers (Utsuno et al. 1989 and Lu & He, 2000). The open-celled (Fig 1.2) metallic foam structure is composed of one or more solid phases and a gaseous phase. The gaseous phase allows fluids to flow or offers compressibility while the solid phases provide geometrical architecture, strength, thermal conductivity, electrical conductivity, magnetic shielding and most importantly is in its provision for an acoustic barrier (Zhao, 2013). In this case, viscous (windows) and thermal (pores) losses predominate sound energy-dissipation mechanisms when compared to the minimal contributions made by Helmholtz resonators, structural vibration and vortex shedding (Lu et al. 1999). Though metal foams are quite expensive their ability to be recycled make them economically well-disposed of and would serve as an efficient absorber if it is enhanced. A possible way-out through this is the utilization of porous media models and structural variation during foam making processes (Kennedy, 2012).

Theoretical and experimental works in this area have shown the feasibility of using aluminium foam structure with open and semi-open cells for acoustic absorption application. Lu & He (2000), measured the static airflow resistivity and sound absorption coefficient for cellular metals with semi-open cells having different packing densities, pore sizes, and openings. Han et al. (2003) showed

that the Al foam samples with a small nominal pore size (500µm) exhibit the best absorption peak when there is no air gap and predominantly Helmholtz resonant absorption in the presence of air gap. The influence of pore sizes, porosity and foam layer thickness on the acoustic performance of porous steel samples manufactured by a lost carbonate sintering process were further substantiated in Lu et al. (2009). A simple tortuosity calculation method based on diffusivity transport in porous systems was proposed by Weisberg (1963), Ho and Streider (1982), and Matyka et al. (2008), in application to porous matrix of stochastically overlaying spherical structures and Zielinski (2013), provides an inverse approach for characterizing acoustic parameters.

Despite the unique and combined characteristics of low weight, high stiffness, low moisture absorption and excellent fire resistance of these materials enabling their suitability for high impact applications, the sound absorption behaviour of commercially used open-celled porous metallic structures were generally considered poor when compared to the performance of hard-backed fibrous materials especially at the region of ⅓ octave frequencies (≤2.0kHz). Enhancing the sound absorptive performance of these structures reported in Lu, Hess and Ashby (1999) can be done through hole-drilling or rolling and prearrangement of space fillers during processing; insertion of appropriate air gap (Lu and He, 2000, Bo and Tianning, 2009, and Muhammed et al., 2013) which predominantly becomes Helmholtz resonance absorption (Han et al, 2003) and increased porous layer thickness (Yeh et al., 1995, and Liu and Chen, 2014).

Previous experimental studies by this group have shown that the packing of porogens or salt beads to make metal foam (Jinnapat and Kennedy, 2010 and

Kennedy, 2012) has significant influence on structural variation, permeability, and other macroscopic parameters of an open-celled foam structure. A discrete element modelling approach (Asmar et al., 2002) linking the capillary interaction between connecting pores and connectivity was further substantiated in relation to its effects on the permeability (Otaru and Kennedy, 2016) and packing density of a near-spherical packed structures with its inverse imitating the structural domain of porous metal foam produced by sintering dissolution (SDP) process of packed beds of near-spherical porogens. This part of the study presents a theoretical and multiscale characterization of the non-acoustical macroscopic parameters and pressure wave simulation through macroporous "bottleneck-type" structures for a frequency range between 100 and 6500Hz. The aim is to attain the best and optimum inherent structural parameters leading to the design of "bottleneck-type" materials capable of absorbing sound pressure waves and to significantly eliminate resonance (structural vibration) and damping effects (dissipation of sound energy to heat energy) through application and alteration of metal foam microstructural arrangement during processing.

1.3 Research aim and objectives

The research is aimed at studying the fluid flow behaviour and acoustic absorption in porous metallic structures leading to the acquisition of knowledge needed in the design of an efficient sound absorbing materials with novel features. The following steps considered as research objectives are listed below.

- Predicting the structural and flow parameters of porous metallic structures using sphere-packing models with monosized cells.

- Extending the sphere-packing models to binary-sized structures to enhance our understanding of the effects of microstructural changes.
- Precision tests on air pressure drop measurements across these structures and CFD simulations using sphere-packing models, tomography and "structurally-adapted" tomography images.
- Pressure wave simulation across these structures using geometrically reconstructed three- and two-dimensional impedance tube.

1.4 Themes Needing Further Study

What is known on measurement and modelling of fluid flow and acoustic absorption in porous media published in the literature were reviewed and put together in Chapter 2. There are still areas where our understanding of the process is lacking.

To begin with, the application of this sphere-packing model (DEM) to mimic and quantify flow behaviour and the regime of manifestation of a more complicated porous metallic structure has been limited to flow developed across packed beds. Researchers in this field have focused more on realistic measurement, analytical predictions, and pore-level numerical simulation adopting the high-priced X-ray computerized tomography-based technique. The sphere-packing (DEM) approach is essential for a preliminary understanding of microstructural variation and its influence on the flow performance of "bottleneck-type" structures produced by negative-pressure infiltration process even in the paucity of experimental data.

Secondly, the models considered in Despois and Mortenson (2005) and Furman et al. (2013) only considered flow developed across the "real" bottleneck-type structures in the Darcy regime (very low velocities); theoretical models to predict the flow behaviour of these materials away from Darcy has not been considered. This is well captured in the main chapters using the computed flow data of the sphere-packing models (DEM) and "structural-adapted" tomography images (μCT) of the "real" structures.

Lastly, Zielinski (2013) is the only author to have proposed inverse identification techniques to characterize macroscopic parameters of a porous structure using measured values of effective density and bulk modulus. Many acousticians have published numerous articles in relation to measurement and simulation of acoustic pressure waves through open and semi-open structures. Further survey is required in the use of DEM and μCT approach in accounting for the interdependent and indispensable non-acoustical macroscopic parameter and the application of combined Helmholtz linear acoustic and poroacoustic models to predict its normal incidence sound absorption coefficient (A_c) of porous Al foams structures. Hence, the fundamental aim of this research is to enhance our understanding of the microstructural effects on the flow and acoustic behaviour of porous metal structures.

1.5 Thesis Plan

Chapter 1 of this thesis gives a background touch of the research topic as well as a summary of fluid flow and acoustic absorption through metallic foam structure. The aim and objectives of the thesis were also presented.

The fundamental models that fortify all the work carried out in this thesis are presented in **Chapter 2**. The continuity, momentum equations and various fluid models substantiated in the literature are reported in this Chapter. Pore-scale numerical simulation technique, flow patterns and the regime of manifestation were also presented in this Chapter. Lastly, the Helmholtz wave equation, sound absorption models, microstructural effects and Helmholtz resonant absorption in relation to the acoustic of the microstructure are presented as well.

Chapter 3 presents a numerical simulation of fluid flow through macroporous structures generated by sphere-packing models for varied pore sizes, interstices, packing densities and pore openings. This represents an underpinning to the modelling aspect of this work using pore-scale techniques. A detailed procedure of image processing and segmentation, representative volume element generation, mesh scale dependence study and characterization of this structure are presented in this Chapter. The permeability of monosized sphere packed structures with realistic measurement of water flow through “real” structure using falling head permeameter measurement was verified in this Chapter. Lastly, an extension to binary-sized structures was considered to vary widely the packing density and structural parameters of the virtual porous materials. The effects of capillary variation and coordination number of the spherical packed structures were studied for 0-100vol% addition of smaller sized structures into the larger sized packed structures.

Chapter 4 presents structural characterization, measurement and numerical simulation of air flow through "bottleneck-type" Al foam structures for varied porosities, pore sizes, and interstices. The application of Darcy-Weisbach approach on repetitively measured data of unit pressure drops to fully understand the airflow behaviour and regime of manifestation based on their pore diameter-based Reynold number (R_{eD}) and Fanning friction factor (f_F) was considered in this Chapter. Numerical approaches involving the use of tomography images (X-ray CT) and sphere-packing models (DEM) coupled with computational fluid dynamics (CFD) were used to quantify the pressure drop across these structures. Both measured and predicted values of the permeability and Form drag were obtained by fitting the unit pressure drops and superficial velocity to the Hazen-Dupuit-Forchheimer model for unidirectional flow of air. Lastly, analytical models for the viscous and inertial terms as a function of the structural parameters of the material through structural dilation of the CT structures to create semi-virtual structures were considered.

Chapter 5 presents a numerical simulation of the pressure waves across macroporous "bottleneck-type" structures. Firstly, the correlation between 2D and 3D numerical simulation were considered and put to test the application of the various poroacoustic models to predict the measured normal incidence absorption coefficient (A_c) of cellular structures based on its structural properties and theoretical models available in the literature. Wilson's model developed for structures with circular and triangular pores to simulate pressure wave through the virtual macroporous structures for pore diameter sizes (1, 2 and 3mm) and frequencies ranging between 100 and 6500Hz was considered. The key

parameters dictating the sound absorption coefficient of the porous material were identified and a sensible optimization of the structures was considered to help eliminate resonance and damping effects. Lastly, the application of back cavity or air gap (Helmholtz resonance absorption) and increased porous layer thickness to improve the absorption properties of the material were presented.

The importance of the key results obtained from the preceding Chapters and recommendations for further study were presented in **Chapter 6**.

CHAPTER 2

LITERATURE REVIEW AND GOVERNING EQUATIONS

In this chapter, an all-important review of the existing literature relating to fluid flow and acoustic absorption in porous structures is presented, with emphasis on porous aluminium structures made by negative-pressure infiltration of packed beds of salts. An introduction to metal foam and its processing is given. Secondly, literature findings on fluid flow and porous media models, Navier-Stokes equation, pore level techniques, permeability estimation for Darcy and non-Darcy flow regime are presented. Lastly, the acoustics of porous structures and parameters influencing the sound absorption of this porous materials are introduced.

2.1 Metallic Foam

A metal foam is a near-net or sponge-like shape cellular structure consisting of a solid matrix (usually aluminium, titanium, nickel, steel, copper or nickel-chromium alloy) with air-filled sealed (close-celled) or interconnecting (open-celled) pores comprising a significant amount of the volume. The high values of packing density or porosity between 75-95% (air-filled) and pore sizes between 0.2-5.0mm of metallic foams contribute significantly to their defining characteristics of high surface area and ultralight materials enabling their usefulness for high pressure and temperature applications (Jorge and Malcom 2010). If a metal can be made pressed or sintered, there is every possibility that it could be made porous and the resulting effect is a change in its microstructure (Kennedy, 2012) to produce open-celled foams. Micrographs of these foam structures have been introduced in Fig 1.2 of the preceding chapter.

2.1.1 Metal foam processing

The interconnecting pores or pore openings in porous metallic structures are generally considered as an open volume within the matrix network and allow the uniform length of passages and distribution (Ashby and Tianjian, 2003). The consideration of these pore openings during metallic foam manufacturing process is largely dependent on their applications. Examples of these applications include filters for high-temperature gas and fluid filtration, energy absorbers/package, heat exchanger, vibrational control, lightweight structure, mechanical damping (Ashby et al., 2006) and most importantly herein, is the open-celled foams for acoustic absorption.

Cellular metals are categorized into different type largely dependent on their manufacturing routes leading to their differences in structural morphology and porosity of the materials. Examples of these porous metallic foams are Hydro/Alcan, Alporas, Formgrip/Foamcast, Gasar and Foaminal/Alulight (Banhart, 2001, and Smith et al., 2012). Processing of these foams can achieve either by powder-technology (Alulight) or melt processes (Hydro/Alcan, Alporas, Formgrip/Foamcast, and Gasar). All these processes mentioned have their shortcomings in either the achievement of highly irregular or sponge-like structures with a wide pore-sizes distribution or limited levels of porosity. Images of these foams indicating the structural morphology (pore sizes distribution and openings) are presented in Fig 2.1.

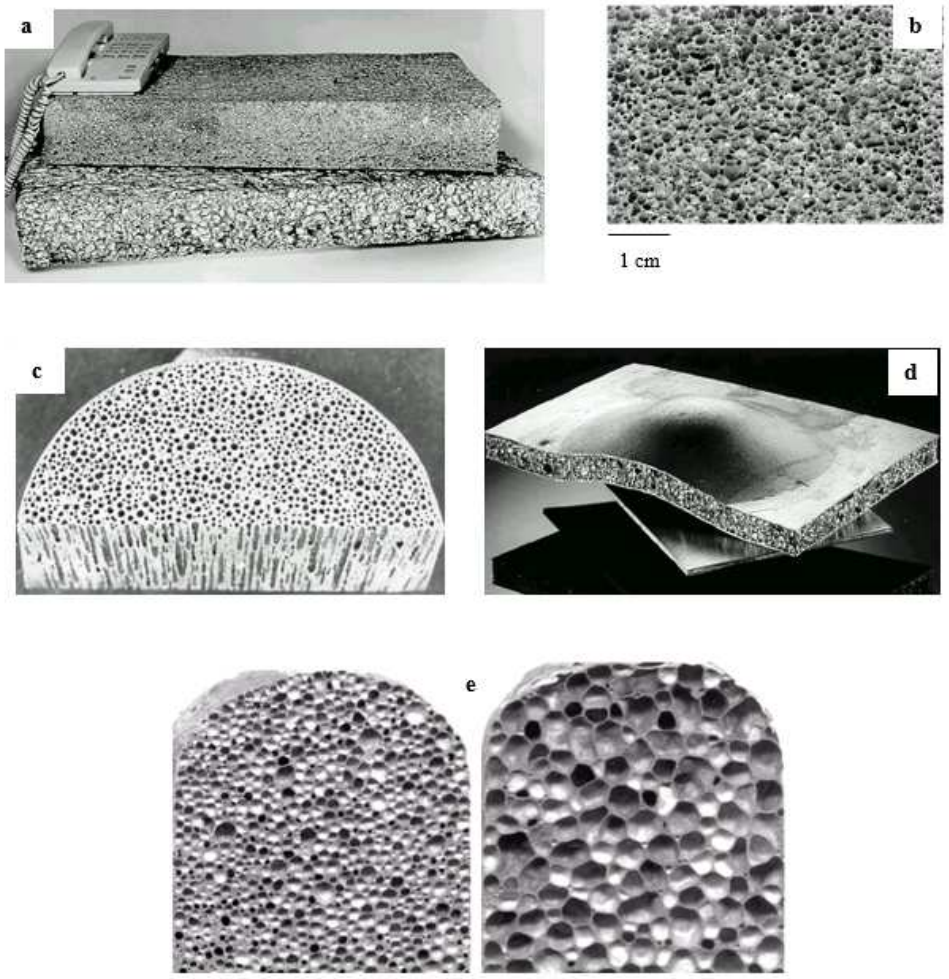


Fig 2.1. Samples of porous metallic foam structures made by (**a**) Foaming of Melts by Gas Injection (Hydro/Alcan) [**adapted from Prakash et al., 1995**] (**b**) Foaming of Melts with Blowing Agents (Alporas) [**adapted from Ma and Song, 1993**] (**c**) Solid-Gas Eutectic Solidification (Gasar) characterized by largely elongated pore structures [**adapted from Shapovalov, 1998**] (**d**) Foaming of Powder Compacts (Foaminal/Alulight), steel/aluminium foam/steel sandwich [**adapted from Baumgartner et al., 2000**] and (**e**) Two samples of aluminium/silicon carbide foam made by Foaming of Ingots Containing Blowing Agents (Formgrip/Foamcast) [**adapted from Gergely and Clyne, 2000**].

2.1.1.1 Hydro/Alcan

The Hydro/Alcan foam is produced by gas injection of liquid melts (Kenny, 1996). The first step in the process is the preparation of aluminium melt followed by the enhancement of the melt viscosity with the addition of either carbide, aluminium-oxide or magnesium oxide particles. Various alloys of aluminium can be used for this process but care should be taken to ensure uniform

distribution of the viscosity enhancement particles. Rotating impeller or vibrating nozzles are used to inject gases (air, nitrogen, argon) into the melt and consequently generates uniform bubbles in the melt. The presence of particles in the melts makes the foam relatively stable and can be pulled off the liquid surface with the help of conveyor belts. Upon cooling and solidification, the resulting composite is a low-density near-net shaped metal matrix as shown by Fig 2.1a.

2.1.1.2 Alporas

Unlike the Hydro/Alcan foam produced by the gas injection process, the Alporas type of cellular metal is produced by the addition of blowing agents to the melt (Asholt, 1999). The first step in this process is the addition of calcium metal to an aluminium melt (680^{o}C). The presence of this calcium metal increases the viscosity of the melt upon stirring and at this extreme operating temperature, calcium oxide (CaO), calcium aluminium oxide ($CaAl_2O_4$) are formed. After achieving the desired melt viscosity (usually increasing by a factor of up to five), 1.6wt% titanium oxide (TiH_2) is added as the blowing agent which releases hydrogen gas into the liquid melt. At constant pressure, the melt gradually expands and fills the vessel and upon cooling, the liquid melt turns into a solid porous metallic sponge as shown in Fig 2.1b (Ma and Song, 1998).

2.1.1.3. Gasar

The Gasar type of porous metallic structure is formed by solid-gas eutectic solidification process. The word “Gasar” refers to gas-reinforcement and particularly describes porous metallic structure made by solid-gas eutectic solidification (Shapovalov, 1998). This approach exploits the fact that a homogeneous melt charge with hydrogen can be achieved by the melting of

metals in a hydrogen atmosphere at an extremely high pressure typically, up to 50 atm. At low temperature, a heterogeneous two-phase system is formed as a result of the eutectic transition of the melt. The topology (geometrical representation) of this material is largely controlled by the hydrogen content, chemical composition of the melt, the rate of heat removed and pressure over the liquid melt. Fig 2.1c presents the Gasar foam structure characterized by obvious non-uniform pore-size distribution resulting from coalescence and the concurrent growth of small (10μm diameter) to large (10mm diameter) pores within the metal matrix.

2.1.1.4 Foaminal/Alulight

The Foaminal/Alulight foam is made via foaming of powder compacts (Baumgartner et al., 2000). The manufacturing processes begin with the embodiment of blowing agents into metal powder (aluminium, zinc, brass, tin, gold, lead, and alloys) followed by compaction to yield a dense nearly-finished product. The metal powders could be in the form of alloy powders or elementary metal powders. Rod-extrusion, or powder rolling, isostatic or uniaxial compression are known compaction methods adopted in this technological routes of foam processing. Secondly, heat treatment at an extremely high temperature (near the melting point of porous materials) helps to decompose the evenly distributed blowing agents thereby releasing gas and forces the melt to expand significantly. Though, the extent of the melt expansion is largely dependent on the melting temperature and precursor size from a few seconds to several minutes. Fig 2.1d presents a highly porous “Alulight” aluminium foam sandwiched between two metal face sheets bonded together with an adhesive.

2.1.1.5 Formgrip/Foamcast

The term Formgrip/Foamcast is an acronym for reinforced metals by gas release in precursor (Banhart, 2006). This type of porous metallic structures is made by foaming of Ingots containing blowing agents. The term Ingot refers to metal typically oblong in shape. Unlike the metal powder compaction process, this type of foam is made by the modification of powder-compact melting process through the homogeneous addition of TiH_2 particles into an aluminium melt. In this case, the melt is quickly cooled down below the melting point of the material after mixing to avoid premature hydrogen evolution. The delay in the decomposition of the earlier routes (Alulight) is attributable to the fact that an oxide barrier is formed on each particle of TiH_2 resulting from the heat treatment process (Gergely and Clyne, 2000). Fig 2.1e present images of porous metallic structures made by the Formgrip process.

2.1.2 Replication casting processes using packed beds of salt.

Controlling the pore-volume and sizes of metal foams is crucial during manufacturing processes. The best and most economical way to this problem will be the incorporating a volume of sacrificial space fillers (Kennedy, 2012). This is a manufacturing route in which a liquid metal (material) is poured into a mould consisting of hollow spheres of the desired shape and then allowed to solidify after mixing before compaction (Fig 2.2). The porous hollow sphere is removed by dissolution in warm water or thermal degradation to leave porosity (Zhao and Sun, 2001).

This replication process of manufacturing light-weight porous metal foams for engineering applications described in (Kennedy, 2012) can be done by casting liquid metals around organic or inorganic hollow spheres (packed beds of salts or porogens) of low density or by introducing this sphere into a metallic melt. Inorganic fillers materials are fired clay pellets loose sand pellets, foamed glass sphere, loose bulks of expanded clay granules (Rehder, 1983) while polymer spheres are classified as organic space fillers and can be used as space holder if the solidification of the melt is sufficiently fast (Banhart and Baumeister, 1998). Continuous pores are connected together with touching spheres to allow the flow of fluid from one side to another. The resulting interconnection of these pores has overall effects on the acoustical parameters (porosity, tortuosity, airflow resistivity, specific surface) of metal foams and it absorption potential.

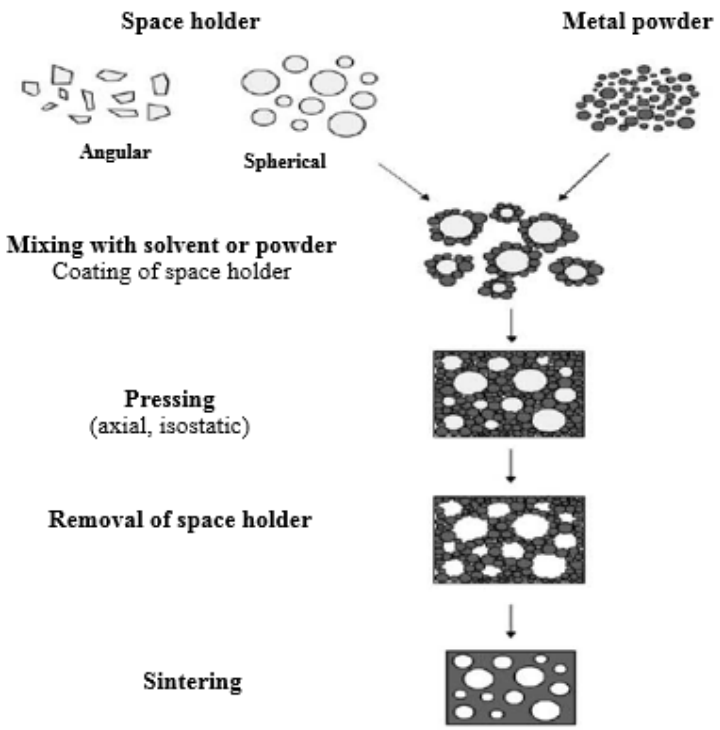


Fig 2.2. Routes for space-holding methods of metal foams production (**adapted from Bram, et al., 2000**).

Preheating of the bulk of space holders is employed during metal foams processing to avoid premature solidification of the melt especially at low infiltration pressure or high heat capacity of the material (Banhart and Baumeister, 1998). The space holding methods has the advantage that the morphology of the pore sizes can be manipulated through the sizes of the space holders and has overall effects on the foam porosity by controlling space holder volume fraction.

2.1.3 Space fillers

The use of water-soluble salts as space fillers is commercially known. Typical examples of these space fillers are sodium chloride (NaCl) and sodium aluminate ($NaAlO_2$). Numerous advantages like low cost, free of toxicity, and fast dissolution in water are associated with the use of NaCl as favoured space-holder (Wang et al., 2011).

The sodium chloride (melting point - 800^oC) is a favoured space holder in the replication casting process (RCP) and dissolves rapidly in water while $NaAlO_2$ is often considered for higher (1800^oC) melting processes (Ashby, Evans and Kennedy, 2006). Precaution should be taken to ensure that complete dissolution of salt in warm water is carried out to avoid limited pore spaces for absorption (Kennedy, 2012). Carbamide particles, ammonium bicarbonate particles, magnesium granules and potassium carbonate particles are also used as fillers. The potassium carbonate particles are used in the lost carbonate sintering (LCS) process because of its high melting (901^oC) point (Zhao, 2013). One of the advantages of Mg is its low boiling point (1107^oC) and its complete immiscibility with metals (Banhart, 2001). The high cost of space fillers may

deter manufacturers from this process, but regular pore structure and control of pore size give a good foam structure for any engineering application.

2.2 Fluid Flow

The part of fluid mechanics that deals primarily with fluid dynamics is termed fluid flow (Michael, 2006). Fluids are categorized into gases and liquids and when subjected to a motion of unbalanced forces it is called fluid flow. A typical example of this is the flow of water or oil from an overhead tank. The superficial flow velocity (v_s) of the fluid is very high in the top and low at the bottom of the tank with unbalanced gravitational force (g) enabling continuous flow of fluid.

The defining characteristics of this fluid mirror its properties and how it moves. These properties can be compressible (fractional change in volume due to density variation at different temperature especially for gases) or incompressible (no change in volume especially for water), steady (time-dependent) or unsteady (time-independent), rotational or non-rotational, viscous (shear stress directly proportional to fluid velocity) or non-viscous, Newtonian (viscous stress linearly proportional to local strain rate) or have ability to resist deformation by tensile or shear stress known as a non-Newtonian fluid (Rao, 2007). The numerical study of this fluid flow is known as computational fluid dynamics (CFD) and is well adopted in the field of science and engineering to mimic flow behaviour even in the paucity of experimental or measured data. The study of fluid flow is governed by the equation of continuity and momentum or Navier-Stokes equation.

2.2.1 Continuity and momentum equations

The generalized form of the continuity equation for fluid flow in the three-dimensional Cartesian coordinate system (typically, in the x, y, and z Cartesian coordinate) reported in Versteeg and Malasekara (2007), is represented Eq 2.1 for all directions and when considering one direction, Eq 2.2 holds.

$$\frac{\partial \rho}{\partial t} = -(\nabla . \rho v) \tag{2.1}$$

$$\frac{\partial \rho}{\partial t} + \rho \frac{\partial v_x}{\partial x} = 0 \tag{2.2}$$

Reported in Versteeg and Malasekara (2007), the generalized form of Navier-Stokes equation relates the rate of momentum increase per unit volume as a function of the rate of momentum addition by convection per unit volume $[\nabla \rho . v . v]$, the rate of momentum addition by molecular transport per unit volume $[\nabla \mathrm{p}] - [\nabla \tau]$, and external force on fluid per unit volume $[\rho g_i]$ as shown in Eq 2.3. Also, the shear stress component (τ) in Eq 2.3 can be expressed in terms of fluid viscosity (μ) and velocity (v) and Eq 2.4 holds for a constant density (ρ) and viscosity (μ).

$$\frac{\partial}{\partial t} \rho . v = -[\nabla \rho . v . v] - [\nabla \mathrm{p}] - [\nabla \tau] + [\rho \mathrm{gi}] \tag{2.3}$$

$$\rho \left(\frac{\partial v}{\partial t} + (v . \nabla) v \right) = -\nabla p + \mu \nabla^2 v + \rho g_i \tag{2.4}$$

The negative sign is an indication that fluid flows in the direction of pressure drop. The non-linear partial differential and time-dependent Eq 2.4 is often solved using commercial CFD software installed in a computer to find a numerical solution at a finite number of points or mesh or grid or discretization. This equation (Eq 2.4) described the motion of fluid substances and it arises

from the application of Newton's second law of fluid motion with the assumption that the sum of a proportional gradient of velocity (diffusing viscous term) and a pressure term described the stress (CMI, 2014).

$$\rho\left(\frac{\partial v}{\partial t} + v.\nabla v\right) = -\nabla p + \nabla.T + F \qquad 2.5$$

The term $-\nabla P$ is the gradient of pressure, v is the fluid velocity, ρ is the fluid density, μ is the fluid dynamic viscosity, p is the pressure, T is the component of total stress tensor with an order two, F is the body force (per unit volume) acting on the fluid and the del operator is represented as ∇. The equation can be defined for compressible or incompressible flow and for a horizontal flow or against gravitational effect Eq 2.4 is reduced to Eq 2.5.

$$\rho\left(\frac{\partial v}{\partial t} + (v.\nabla)v\right) = -\nabla p + \mu\nabla^2 v \qquad 2.5$$

At very low or creeping superficial fluid velocity, the rate of pressure drop in a unit length is linearly proportional to fluid velocity and the Navier-Stokes equation reduces to the Stokes equation and is stated below;

$$\rho\left(\frac{\partial v}{\partial t} + (v.\nabla)v\right) = 0, 0 = -\nabla P + \mu\nabla^2 v + \rho g_i \qquad 2.6$$

Eq 2.6 is often solved computationally when the fluid velocity is relatively small or within Darcy regime of laminar flow of fluid. Also, for inviscid fluids or highly viscous and sticky fluids where shear stress ($[\nabla .\tau] = 0$) or velocity at the surface is zero ($v = 0$), the Euler equation (Eq 2.7) is solved. Against gravitational effects (g = 0), the Navier-Stokes equation reduces to;

$$\rho\left(\frac{\partial v}{\partial t} + (v.\nabla)v\right) = -\nabla P + \rho g_i \qquad 2.7$$

2.3 Pore-scale and Fluid Models

The modelling of fluids across a porous medium involves solving the Navier-Stokes equation (Eq 2.3) at macroscopic or microscopic level. The treatment of foam as a homogeneous medium by neglecting small-scale details is associated with a volume averaging or macroscopic approach (Ranu et al., 2013) while the determination of macroscopic parameters used to depict the dynamic behaviour of fluid flow in porous media based on the micro-geometry (representative volume element) of the system by capturing small-scale details is described as pore-scale or microscopic approach (Peng et al., 2012). The microscopic approach is more suitable in describing the macroscopic parameters (permeability, porosity, tortuosity and foam surface area per unit bulk volume) of a porous medium because of its ability to capture detailed information of the porous matrix. Having knowledge of the fluid properties (fluid density and dynamic viscosity), porosity, porous body layer or thickness one can use the pore-scale numerical approach to describe the fluid flow at various velocities to estimate the pressure drop within the porous body (Bodla et al., 2002, Narsilio, et al., 2009, Peng et al., 2012, and De Carvalho et al., 2014).

The estimated or computed values of pressure drops are used to account for the permeability term of porous structures, and inertial term, in the case of high-velocity flow. Several equations have been developed to mimic the behaviour of fluid in the pore region and are listed below.

- Darcy's Law: Describes low-velocity flows of one or more fluids, where the pressure is the major driving force.
- The Richard's Equation: Governs the wetting and driving of rocks or soil.

- The Fracture Flow is a variant of Darcy's law that defines the flow along the interior boundaries representing fractures within a porous (or solid) medium.
- The Brinkmann equation is for porous media high-velocity flows but in the Laminar region ($1<Re<10$).
- The free and porous media flow combines free flow adjacent to the porous domain.
- The Laminar flow and creeping flow use the Navier-Stokes equations to describe free flows within a river or well.

Listed above are often derived from the Navier-Stokes equations (Eq 2.3) governing fluid flow.

2.3.1 Darcy's Law

Darcy's law states that the velocity field of fluid flow in a porous medium is determined by the gradient of pressure, the structure of the porous medium (permeability and porosity) and fluid viscosity (Whitaker, 1986). The law was put together by Henry Darcy based on series of experimental trials (Darcy, 1856). The net flux across a face of porous surface is mathematically expressed as $v_s = -\frac{k_o}{\mu}(\nabla p + \rho g \nabla D)$ 2.8

where u, k_o, μ, p, ρ, g and ∇D are the Darcy velocity (or specific discharge vector m/s), permeability of the porous medium (m^2), dynamic viscosity (Pa.s), fluid's pressure (Pa), fluid density (kg/m^3), magnitude of gravitational acceleration (m/s^2) and unit vector in the direction over which the gravity acts respectively. In other to turn of the gravity effects, the elevation D in Whitaker,

(1986) was set to zero and the resulting equation is given in Eq 2.9. Also, models can define the capacity to transmit flow using hydraulic conductivity (K, m/s) given by Eq 2.10.

$$v_s = -\frac{k_o}{\mu} * \nabla p \text{ where } v_p = {}^{v_s}/_{\emptyset} \quad 2.9$$

$$v_s = -\frac{K}{\rho g}(\nabla p + \rho g \nabla D) \text{ where } \frac{k_o}{\mu} = -\frac{K}{\rho g} \quad 2.10$$

The hydraulic conductivity K (m/s) represents both fluid and the solid matrix while the permeability is a property of the porous matrix only. The pressure *p* can also be expressed in term of the hydraulic head, *H*, pressure head H_p, and elevation head, *D* as described in Eq 2.11. The elevation head, *D* denotes the direction over which g acts. The hydraulic head is equal to the pressure head only when a gravity effect is insignificant, and *D* is set to zero. When defined as vertical elevation, the vertical gradient in *D* equals one and the horizontal gradient in *D* equals zero. Similarly, the average linear velocity (also termed the seepage velocity) within a given pore space is defined by Eq 2.10 as a function of the superficial fluid velocity (v_s) and porosity ($\emptyset$) of the porous medium.

$$H_p = \frac{p}{\rho g} = H - D \quad 2.11$$

In summary, the Henry Darcy's law interface built into commercial CFD packages (COMSOL Multiphysics, Ansys Fluent, and Simpleware) can be used to model single (relevant to this work for low velocity flows and to be discussed later) and multiphase flows across porous structures. The Darcy's law interface combines Darcy's law with continuity equation; it is used to simulate fluid flow through interstices in a porous medium. It is also used to simulate flow for which pressure gradient is the major driving force and highly influenced by the

frictional resistance within the pores. It can also be used to model media where porosity and permeability are very small or low-velocity flow (COMSOL Multiphysics, 2015 user guide).

2.3.2 Brinkmann equation

The Brinkmann equation is used to compute pressure fields and fluid velocity of single-phase flow in porous media at high velocity in the laminar flow regime. Fluid with varying density of Mach number below 0.3 is included. The fluid viscosity can also vary, for example, to describe non-Newtonian fluids. The Mach number is defined as the ratio of fluid velocity to speed of sound (Nield and Bejan, 1992).

Fast-moving fluids in porous media with kinetic potential from pressure, gravity and fluid velocity to drive the flow is described using Brinkmann equations. The physics interface in commercial CFD packages uses Darcy's law to describe the dissipation of kinetic energy by viscous shear, similar to Navier-Stokes equations. This physics interface is well suited for transitions from slow flow in porous media described by Darcy's law and fast flow in channels governed by Navier-Stokes equations (Le Bars and Worster, 2006). The modelling of non-Newtonian fluids, like the flow of oil from a reservoir to a well-perforation, hyperbolic zone near a river can be described by the coupling of Brinkmann and Navier-Stokes also known as Stokes-Brinkmann equation.

The Brinkmann equation of flow in porous media is formed from the combination of the continuity equation and the momentum equation described below:

$$Q_{br} = \frac{\partial}{\partial t}(\rho\emptyset) + \nabla.(\rho v) \quad 2.12$$

$$\frac{\rho}{\emptyset}\left(\frac{\partial v}{\partial t} + (v.\nabla)\frac{v}{\emptyset}\right) = -\nabla p + \nabla.\left[\frac{1}{\emptyset}\left\{\mu(\nabla v + (\nabla v)^T) - \frac{2}{3}\mu(\nabla.v)I\right\}\right] - \left(k_o{}^{-1}\mu + \frac{Q_{br}}{\emptyset^2}\right)v + F \quad 2.13$$

where μ is the dynamic viscosity of the fluid in kg/m.s; v is the velocity vector in m/s; ρ is fluid density in kg/m^3; p is the pressure measured in *Pa*; $\emptyset$ is porosity (0 – 1); k_o is permeability tensor of the porous medium; the mass sink or mass source is Q_{br} measured in kg/m^3.s; and the force term F (kg/m^2.s^2) accounts for the influence of gravity and other volume forces. The mass source (Q_{br}), accounts for the mass creation and mass deposit within the domains. Zero velocity is assumed for the mass exchange. It is important to understand that Eq 2.12 is the continuity expression for a compressible flow. For an incompressible flow with constant density, Eq 2.12 reduces Eq 2.14.

$$Q_{br} = \rho\nabla.v \quad 2.14$$

2.3.3 Darcy-Dupuit-Forchheimer Model

It is important for us to note that Henry Darcy's empirical model in Eq 2.9 expresses the volumetric flow rate of fluid flow in porous media as a function of pressure gradient and fluid properties (permeability and fluid viscosity). His expression is valid for fluid flow in the Darcy region of laminar flow and shows a linear relationship between flow rate and pressure drop in a porous medium. Deviation from this Darcy's law (*Re* > 1) is caused by either high fluid velocity, molecular, non-Newtonian fluid or ionic effects is termed the non-Darcy flow.

Experimental studies on flowing gas across packed beds of coal at high velocity performed by Philippe Forchheimer in 1901 observed the non-linearity between the fluid flow rate and the driving pressure gradient. Inertia effects caused by the non-linear increase in turbulence in the fluid flow rate become significant at this high velocity in the porous medium (Bejan, 1984). An inertia effect also known as the Forchheimer term and is added to Darcy's empirical equation (Eq 2.9) to account for this non-linearity as shown in Eq 2.15-2.17.

$$-\frac{\partial p}{\partial x_i} = \frac{\mu}{k_o} v_s + \rho \mathrm{C} v_s^2 \qquad 2.15$$

$$-\frac{\partial p}{\partial x_i} = \nabla p = \frac{\mu}{k_o} v_s + \rho \frac{C_F}{\sqrt{k_o}} v_s^2 \qquad 2.16$$

$$v_s = \frac{A_f}{A_T} v_p = \emptyset v_p \text{ and } \nabla P = \frac{\mu}{k_o}\frac{A_f}{A_T} v_p + \rho \frac{C_F}{\sqrt{k_o}} \left(\frac{A_f}{A_T} v_p\right)^2 \qquad 2.17$$

The term k_o is the permeability of the porous medium, A_f is the average pore area, A_T is the total cross-sectional area in a direction of flow (x, y, or z), C is the inertial factor or Form drag coefficient (measured in m^{-1} or ft^{-1}), ρ is the fluid density flowing through the porous medium, C_F is the Ergun's or Forchheimer coefficient, v_s is the inlet superficial velocity and v_p is the pore or modified inlet velocity based on the porosity of the foam microstructure or void fraction in the case of flow description in packed beds of particle. Acceleration and deceleration effects on the fluid as it travels through the tortuous flow path of the porous medium can result in higher fluid velocity resulting in inertial losses. Thus, the Forchheimer term accounts for this.

2.3.4 Permeability estimation for non-Darcy regime

Estimation of permeability for flow in the Darcy regime is done using Eq 2.9 by plotting the unit pressure drop (∇p) against superficial velocity (v_s). For the Darcy-Forchheimer or non-Darcy regime, the determination of permeability and inertial factors for flow through porous structure, a second-order polynomial is used to fit the pressure-velocity data; this is then compared to the Darcy-Dupuit-Forchheimer model (Eq 2.15). Fig 2.3 presents the pressure drop per unit thickness (Pa.m^{-1}) against superficial velocity (m.s^{-1}) of air flow through an open-celled (10 and 40 pore per inch) metallic foams for porosities of 92.9 and 93.8% respectively (Dukhan, 2013). Using the value of air viscosity of 1.8205 x 10^{-5} Ns.m^{-2} and air density 1.2041kg.m^{-3} at 20^{o}C, the permeability (k_o), Form drag (C) and Forchheimer constant (C_F) computed for the 10PPI foam using Eq 2.15 are 3.17 x 10^{-7}m^2, 87.2m^{-1} and 0.049 whilst that of the 40PPI foam are 1.73 x 10^{-7}m^2, 128.4m^{-1} and 0.05 indicating a stronger dependence of pressure drops on the microstructural arrangement of the porous material.

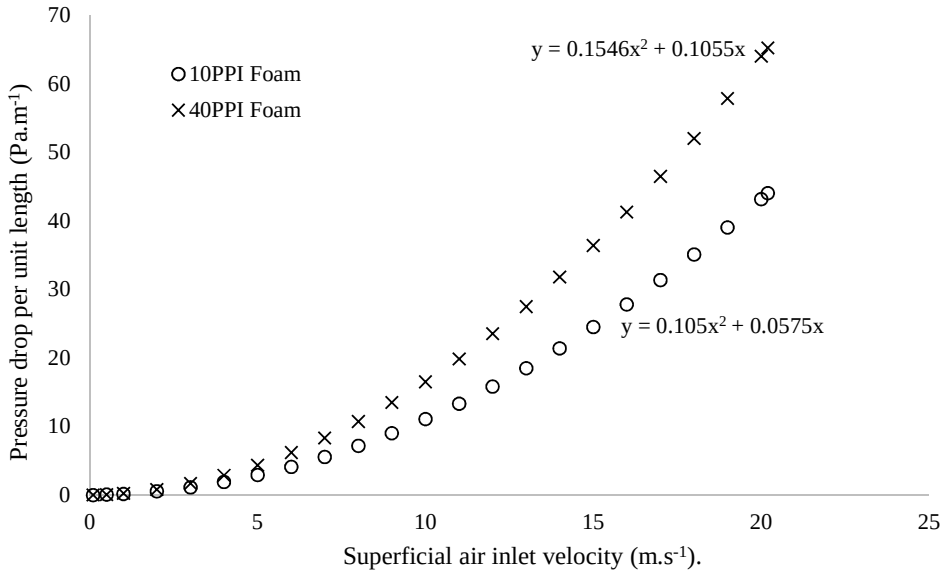


Fig 2.3. Plots of pressure drop per unit length (Pa.m^{-1}) across 10 and 40PPI porous metallic structures against superficial air inlet velocity (m.s^{-1}) [**adapted from Dukhan, 2013**].

The number of pores in one linear inch is termed as pores per inch abbreviated as PPI (UAF, 2014) and it can be obtained by counting the total number of pores in the direction of flow path using Scanning electron microscopy (SEM), optical images or X-Ray computed tomography images of similar structure (Dukhan and Minjeur, 2010). The PPI helps determine the mean pore size of porous structures and the region of interest needed to account for its permeability and inertial coefficients using porelevel approach. A typical example is comparing the pressure drop developed across the 10 and 40PPI metallic foam structures given in Fig 2.3. The 10PPI has larger pore sizes approximately 2.54mm per pore while that of the 30PPI has in approximation 0.64mm per pore. The 40PPI offers a higher resistance to airflow than the 10PPI and could be useful for high impact applications with little or no interest in flow across the porous material. For a given flow regime, the permeability and Form drag is constant but it varies over different velocities at a given PPI. Though, the selection of a given range of velocities would depend on the foam application and the limitation of the experiment.

2.3.5 Reynolds number for porous media flow

The term Reynolds number is defined as a dimensionless quantity which describes the fluid flow pattern and the regime of manifestation when fluid flows through open channels or porous medium. The idea was introduced and popularised by George Gabriele Stokes (1851), and Osborne Reynolds (1883) respectively.

Various authors have used Reynolds number to classify the regime of fluid flow. Lage et al., (2005), described the pore diameter sized Reynolds number (Re_D)

of viscous dominated flow in porous media at very low-velocities to be less than unity (Re_D < 1.0) and the behaviour of fluid flow in this regime strongly depends on the morphological features of the porous matrix (Dybbs and Edward, 1984). Nield and Bejan (1992) described the transition of fluid from Darcy to Forchheimer flow regime as smooth and takes place over a range of 1 < Re_D < 10. The flow in this regime is still laminar but non-linear as inertial forces become imperative and the Darcy-Dupuit-Forchheimer law (Eq 2.15) holds. The non-linearity deviation from the Darcy regime is caused by inertial effects and not turbulence as the flow is laminar. Turbulence arises at much higher velocities (Dukhan, 2013). Boomsma and Poulikakos (2002), found out that the departure from Darcy in an open-celled foam took place at 14 < Re_D < 27 (≥ 0.110m/s) while du Plessis and Wouldberg (2008) gave an expression for Reynolds number determination in this regime as a function of open porosity, ∅ (Eq 2.16). The Forchheimer or form drag dominated, post-Forchheimer unsteady laminar and completely turbulent flow regimes were described by Lage et al., 2005, to be within 10 < Re_D < 150, 150 < Re_D < 300 and Re_D > 300 respectively.

$$Re = \frac{50.8}{C_d} * \frac{(1-\emptyset)^{\frac{1}{3}}}{\left(1-(1-\emptyset)^{\frac{1}{3}}\right)} \qquad 2.16$$

where C_d = 1.90 and *Re* is the Reynolds number (0 ≤ *Re* ≤ 71 critical *Re* range) and ∅ is the porosity (0 ≤ ∅ ≤ 1.0).

The determination of Reynolds number in packed beds has been limited to the mean particle or cell diameter, D_p, (Muskat & Botset, 1931, Coulson, 1949 and Ergun, 1952) as a measure of its characteristic linear dimension (Eq 2.17) but may differ when used for metal foam structures.

From a sequence of experimental data on pressure drops and superficial velocity measured for an open-celled metal foam, Boomsma and Poulikakos (2002) and Edouard et al. (2008) proffered that the preferred characteristic linear dimension for determination of Reynolds number is its Darcian permeability, k_0, (Eq 2.19) as it considers all the macroscopic parameters which best described the geometrical behaviour of the porous matrix. However, the work of Bonnet, Topin and Tadrist, 2008 argued otherwise by using the cell or pore diameter as the preferred characteristic linear dimension for computing Reynolds number (Eq 2.17) of fluid flow through open-celled metal structures. Eq 2.19 and 2.20 show a Reynolds number description of the Forchheimer model in terms their permeability-based (Re_k) and pore diameter-based (Re_D) Reynolds numbers. Their corresponding Forchheimer coefficients are represented as C_{FK} & C_{FD} whilst ∇p, μ and v_s are the pressure drop per unit thickness, fluid viscosity and superficial fluid velocity respectively.

$$Re_D = \frac{\rho v_s}{\mu} D_p \qquad 2.17$$

$$\frac{\nabla p}{v_s} = \frac{\mu}{k_0} + Re_D . \frac{\mu}{D_p} . \frac{C_{FD}}{\sqrt{k_o}} \qquad 2.18$$

$$Re_K = \frac{\rho \sqrt{k_0}}{\mu} v_s \qquad 2.19$$

$$\frac{\nabla p}{v_s} = \frac{\mu}{k_0} + Re_k . C_{FK} . \frac{\mu}{k_0} \qquad 2.20$$

2.3.6 Boundary conditions

A boundary condition is a form of an equation or a stated restriction that limits the possible solutions to a differential equation (Mifflin, 2002). It is a condition

where a differential equation is solved. Setting out the right boundary condition when resolving the fluid models thereof, can help us to differentiate between right and wrong or solve our computation easily. Table 2.1 presents a summary of most commonly used boundary conditions for application involving fluid flows.

Table 2.1: Summary of common boundary conditions for fluid flow (Hesketh, 2008).

Boundary	**Boundary conditions**	**Equation**	**Use**
Wall	Sliding Wall	$v = v_w$	Used to specify the velocity of a moving wall.
	No-slip (default)	$v = 0$	Zero velocity at the wall.
Inlet	Velocity	$v = -nv_o$ or $v = v_o$	To specified constant velocity or a defined velocity by an equation as $v = a(1 - (\frac{r}{R})^2)$. Where n is a unit vector normal to the surface.
	Pressure, no viscous stress	$p = p_o$ and $\mu(\nabla v + (\nabla v)^T)n$	Use to describe fluid inlet perpendicular to the boundary.
Outlet	Velocity	$v = -nv_o$ or $v = v_o$	Be careful not to over-specify.
	Pressure, no viscous stress	$p = p_o$ and $\mu(\nabla v + (\nabla v)^T)n$	Used to describe fluid outlet perpendicular to the boundary.
Symmetry	Slip/symmetry condition	$v.n = 0$	Used to specify no velocity perpendicular to a surface or an area. For example, fluid flow in a 3D porous object, the inlet and outlet may be velocity or pressure flow while the other sides are treated as symmetry.
	Normal flow/pressure or 'straight – out' BC	$p = p_o \quad \& v.t = 0$	Used for fully developed flow perpendicular to the area.
	Outflow/Pressure BC	$p = p_o$	Used for known pressure.
Periodic	Velocity	$v_{(xo)} = v_{(x1)}$	This typically implements standard periodicity so that, the value of the solution is the same on the periodic boundaries. This isn't suitable for spherical or elliptical objects but a line, cube and rectangular are the most intuitive and common choice and thus can be applied to the side walls of the objects.
	Pressure	$p_{(xo)} = p_{(x1)}$	
Open **Closed**	Velocity and Pressure	$v_{(o)} = v_{(1)}$ $p_{(o)} = p_{(1)}$	Describing boundaries in contact with a large volume of fluid. For the open boundary, fluid can both enter

$v_{(o)} = 0$ $p_{(o)} = 0$	and leave the domain on boundaries whilst it can only access the entrance of the object in case of the closed boundary condition.

2.4 Sound and Acoustic

Sounds are part of our daily life experience even in the corridors of our comfort zone, marketplace, religious places, and city areas. Sources of this sound can be a vibrating speaker that sets the vibrating accord into motion, a running engine and that produced in tsunami wave. Sound can be transmitted through a medium as either longitudinal or transverse waves or both in some cases. The wave of alternating pressure deviation from the equilibrium pressure, resulting in rarefaction and compression through gases, plasma and liquids as medium is called a longitudinal wave, while transverse waves (in solid or sound absorbing material) are waves at a right angle to the direction of propagation at alternating shear stress (NPR, 2014).

Sundry definitions of sound exist depending on how it is perceived. Some define it as noise while some spotted that excessive level of sound must be attained before it can be regarded as noise (FTCS, 1969). The physics definition of sound is described as vibrations that propagate through a medium of air or water as a mechanical wave of pressure and displacement. The reception of such wave and perception by the brain is the physiology and psychology definition of sound (FTCS, 1969). Psychoacoustics is a field dedicated to this study. The science that deals with the studies of sound in a medium (solid materials, liquid or gas) is called acoustics. The person on the job in the field of acoustical engineering is called an Acoustical Engineer while a scientist in this field is called Acoustician (ANSI, 1994).

Sound exists because of interaction of the flow of fluid particles resulting in frictional contact and heat generation when they encounter a porous or solid

body. The concept of fluid flow cannot be left out when discussing acoustic absorption in porous media. As much as sciences deal with discovery, the acoustic engineer is saddled with the responsibility of either enhancing the sound or providing a solution for its reduction by sound absorbing materials and equipment. Typical examples of these sound absorbing materials are wool, hemp, kevlar, polyesters, wood and recently metal foams.

2.4.1 Helmholtz wave equation

The equations that described the propagation of sound in fluids are derived from the governing equations of fluid flow. They are the conservation of mass also known as the continuity equation, conservation of momentum also known as the Navier-Stokes equation, energy conservation equation, the model constitutive equations, and an equation of state to describe the relationship between thermodynamic variables. Neglecting viscous effects, lossless and adiabatic flow, and a linearized isentropic equation of state are assumptions made for the classical case of pressure acoustics, which describes most acoustic phenomena accurately. Under these assumptions, the acoustic pressure field is described by one variable (amplitude of pressure p) and is governed by the wave equation (Eq 2.26).

$$\frac{1}{\rho_o c^2}\frac{\partial^2 \rho}{\partial t^2} + \nabla.\left(-\frac{1}{\rho_o}(\nabla p - q)\right) = Q \qquad 2.26$$

The terms Q (N/m^3) and q ($1/s^2$) are the monopole and dipole source terms respectively. An unboxed and small boxed loudspeaker at low frequencies is a typical representation of a measure of dipole and simple source terms

respectively (Russell et al., 1998). It is often preferable to solve the wave equation in the frequency domain for one frequency at a time because acoustic problems often involve simple harmonic waves such as sinusoidal waves $(p(x,t) = p(x)\,sin(wt)\ \ or\ p(x,t) = p(x)\,exp(iwt))$. Thus, the propagation coefficient k is defined as:

$$\frac{1}{\rho_o c^2}\frac{\partial^2 \rho}{\partial t^2} = \frac{\nabla^2 p}{p} = -k^2 \qquad 2.27$$

Using this assumption for pressure field, the time-dependent wave equation reduces to the well-known Helmholtz equation:

$$\nabla.\left(-\frac{1}{\rho_o}(\nabla p - q)\right) - \frac{k^2}{\rho_o}p = Q \qquad 2.28$$

The wave number w is defined as:

$$w = kc = 2\pi f \qquad 2.29$$

Substituting equation 2.29 into 2.28 gives:

$$\nabla.\left(-\frac{1}{\rho_o}(\nabla p - q)\right) - \frac{w^2}{\rho_o c^2}p = Q \qquad 2.30$$

Neglecting the monopole and dipole source term result to the simplified well known Helmholtz equation:

$$w^2 p + c^2\nabla^2 p = 0 \quad \text{or } \nabla^2 p + k^2 p = 0 \qquad 2.31$$

2.4.2 Acoustic absorption

The acoustic properties of sound absorbing materials are often described by their absorption potential at varying degree of frequencies. The Absorption

coefficient represents how much of the sound is absorbed. Sun, et al., 2010 described the sound absorption coefficient of a porous material as the ratio of sound intensity absorbed (I_a, W/m^2) to incident sound intensity (I_i, W/m^2).

An extensive work by Attenborough and Umnova over the period of 1993 to 2003 pointed out the derivation of sound absorption coefficient as a function of specific acoustic surface impedance (Z) and characteristics impedance (Z_c) of the porous material. This model has been justified by many researchers in the field of acoustics with little deviation between the experimental and predicted values. Umnova, et al., 2003 reported that, when sound waves enter the pore of porous medium at an audible or high frequency, sound energy is created, and a phase is changed because of viscous drag and thermal exchange in pores of the porous structure. More so, if this layer of a sample is backed by a rigid impervious wall on its rear face, the analytical specific surface acoustic impedance in Wright (2005) was expressed as a function of sample thickness (L), sample porosity ($\emptyset$), fluid density (ρ_o), propagation coefficient (k), fluid characteristic impedance (Z_c) and speed of sound in fluid (c_o) as shown in Eq 2.32. The real (resistance) and imaginary (reactance) parts of this equation in Kino and Ueno (2008) are associated with energy loss and phase change of the acoustic field. Similarly, Wright (2005) relates the sound absorption coefficient of a porous material as a function of their surface acoustic impedance given in Eq 2.32 and that of fluid (Z_o) as shown by Eq 2.33.

$$Z = \frac{iZ_c \cot(kL)}{\emptyset \rho_o c_o} \qquad 2.32$$

$$A_C = 1 - \left(\frac{Z - Z_o}{Z + Z_o}\right)^2 \qquad 2.33$$

2.4.3 Techniques for enhancing acoustic absorption

Elimination of resonance (vibration) and reduction of acoustic energy to a significant extent are key factors considered in the choice of porous absorbing materials as soundproofing device. The performance of this acoustic material is dependent on the amount of sound energy absorbed and represents the sound absorption characteristics (Muhammad et al., 2013) over a range of frequency. Fig 2.4 represents the transmission of the high sound pressure wave through a porous absorber to low sound wave energy with the help of acoustical material (Bies and Hassan, 2009).

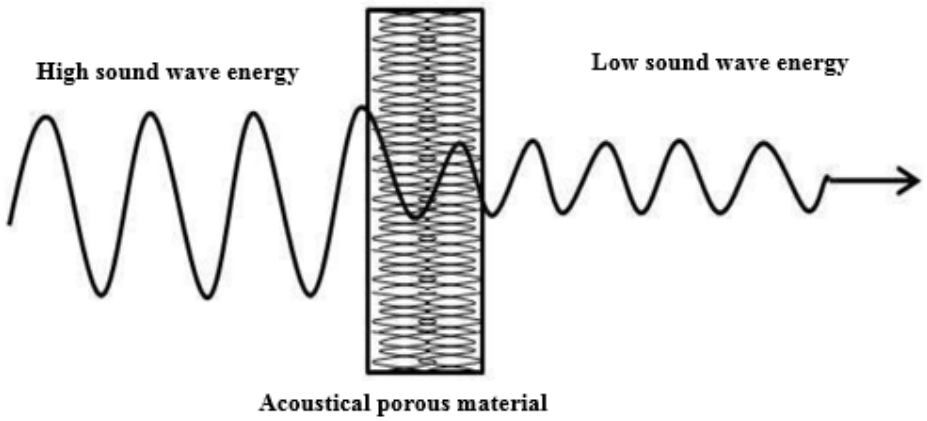


Fig 2.4. Reducing high sound wave with an acoustic material (**adapted from Bies and Hassan, 2009**).

The significance of metallic foam structure as an acoustic absorber is its ability to manipulate its microstructure whilst the conventionally used soundproofing fibrous materials do not possess the strength to withstand mechanical compression and drilling. The open-celled metallic structure allows propagated pressure wave to access its network of small interconnected pores (Han, et al., 2003) and is considered useful in many application areas such as heat exchanger, sound absorbers, catalyst (Lautensack and Kabel, 2009). Close-celled foam structures (Fig 1.2) are generally considered poor sound absorbers owning to

their insistence in a greater reflection of sound waves from the metallic surface but can be improved via rolling or cell fracturing (Lu, & He, 2000 and Wang, et al., 2011) to give way to air movement. Under this, some of the cells' faces break and become a passageway for the sound pressure wave to fully assess the interior of the microstructure or in-and-out movement of air particles.

Qiam and Li (2000) show that the sound absorption of porous materials is generally improved when the sound wave impacts the smaller pores first. The size of the pores and connectivity of metal foams is one of its characteristic features leading to the defining characteristic absorption potential of the material. The shape, size, and porosity of metallic foam structures that allow the passage of fluids are not only defined by the fillers size and shape but also in their packing density and arrangements (Langston and Kennedy, 2014). The interconnection of the fillers (touching spheres) determine the outcome of the microstructural arrangement (porosity, surface area, permeability, tortuosity, pore sizes, and openings). Other methods like increased porous layer thickness, the presence of a back cavity or air gap, hole drilling/rolling of metal foams, and the patterns in the arrangement of the space fillers (packing of spheres) are available (Ashby et al., 1999, Li et al., 2011, and Muhammed et al., 2013) for improving the sound absorption of porous metallic foam.

The sound absorption coefficient of porous materials increases with an increase in thickness at different frequencies. Study on the combined polyethylene filled with metallic hydroxides and cross-linkable polyethylene in Yeh et al. (1995) shows that the peak of absorption of this material can be obtained even at low frequencies due to the extension of the pore channels that result in significant fluid pressure drops and energy loss within the microstructure. This was

confirmed in the recent experimental and computational work conducted in Li et al. (2011), Li, et al. (2013), Liu and Chen (2014), Lu and He (2000), and Zielinski (2015) for a metallic structure with unique near-spherical pore diameter and apertures. An approximate relationship between the porous layer thickness, *L*, and selected frequency range, *f*, is numerically described in Liu & Chen, 2014 in Eq 2.34.

$$fL = \text{constant} \qquad 2.34$$

Experimental work on sound absorption measurement of polyurethane foams (Fig 2.5) by Muhammed et al. (2013), and porous aluminium foams (Fig 2.6) by Lu and He (2000) showed that, an improvement in the characteristic absorption curve of porous structure was observed with the insertion of a back cavity or airgap, resulting in a shift in the characteristic absorption curve to frequency minima than the hardbacked measurement. The air medium provides additional resistance to the unconverted (sound waves-heat) or unabsorbed transmitted wave from the material. Soundwave becomes weak due to friction with air particles, which convert sound energy into heat. The mechanism of this sound wave dissipating in the air medium was described in Norton and Karszub (2003), Crocker (2007), and Li, et al. (2011) as the Helmholtz resonance effect. Reducing the thickness of an acoustical material while maintaining its absorption potential can also be done by inserting airgap.

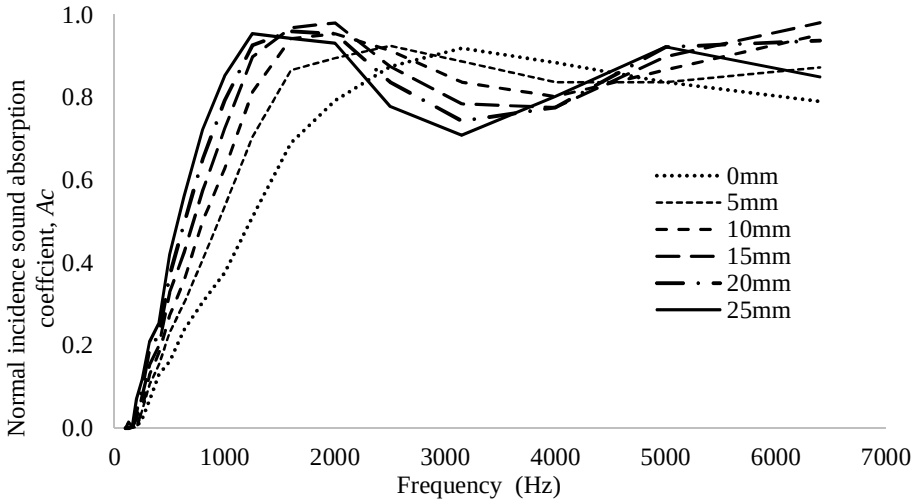


Fig 2.5. Plots of measured sound absorption coefficient of Polyurethane foam at airgap of 0, 5, 10, 15, 20 & 25mm adapted from [**adapted from Muhammed et al., 2013**].

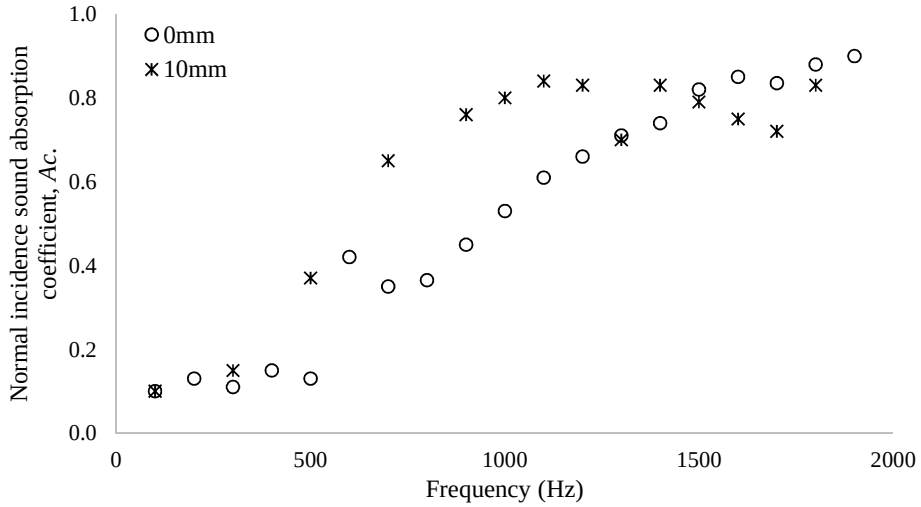


Fig 2.6. Plots of measured hardbacked and 10mm airgap sound absorption coefficient of "bottleneck-type" porous aluminium foam structure against Frequency (Hz) [**adapted from Lu and He, 2000**].

2.5 Poroacoustic parameters

The parameters used to describe the vibro-acoustic behaviour of porous materials are classified into two categories: the structural and the elastic parameters. The structural parameters are related to the interaction between the fluid and solid phases in the materials. The number of these parameters used in models to predict the fluid behaviour can vary from 1 to 8 depending on the

material of consideration and structural morphology. Fig 2.7 shows the growing complexity of motionless skeleton and appropriate models developed to mimic the acoustic behaviour of this microstructure.

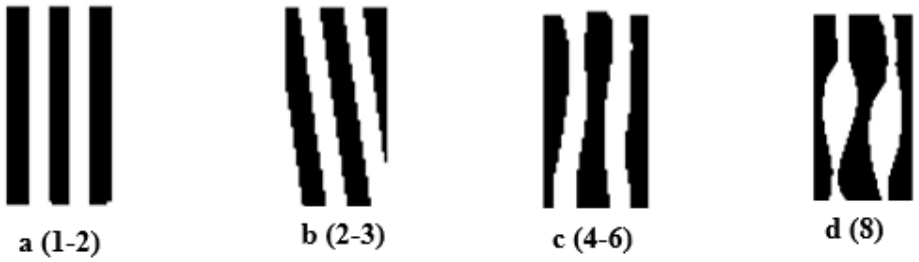


Fig 2.7. Schematic representation of the growing complexity of motionless skeleton of (a) straight cylindrical pores (b) slanted cylindrical pores (c) non uniform sections and (d) non-uniform sections with possible constrictions regarding the microstructure of the porous materials and the number of poroacoustic models needed to describe its sound absorption behaviour (**sourced from *http://apmr.matelys.com/index.html***).

These structural parameters of the porous medium are: open porosity ($\emptyset$), high-frequency limit of the dynamic tortuosity (τ) and the airflow resistivity, (σ), can be directly measured while viscous characteristic length, ($\wedge$), thermal characteristics length, ($\bar{\wedge}$), static thermal permeability (k_0'), static viscous (τ_0) and static thermal (τ_0') tortuosity are estimated from characterization techniques (Acoustic Porous Material Recipes, APMR). Though, the last three parameters are rarely in use as they still need further development to be characterized experimentally (Perrot et al., 2013).

The elastical parameters describe the visco-elastic behaviour of the solid phase of the material. Studies of acoustical porous media are usually limited to small deformation vibrations these parameters thus reduced to the ‘elastical and damping’ ones (Young’s moduli, Poisson’s ratio and structural damping coefficients).

2.5.1 Static airflow resistivity

The static airflow resistivity (σ) also term commonly reduced to resistivity and the porosity are the two most known parameters, used to describe the acoustical behaviour of porous materials. It is defined as the ratio of the static gas pressure between both sides of the material to the airflow speed. It reflects the air permeability through porous materials and is also defined as the resistance within a unit of thickness of material (Yeh et al., 1995). Mathematical expression of the relationship between the static airflow resistivity and permeability (k_o) or pressure drop in a unit length (∇p) is given by Eq 2.35.

$$\sigma = {}^{\mu}/_{k_o} \; or = \frac{\Delta P}{vL} \qquad 2.35$$

Some authors prefer to use static viscous permeability (k_o) which has the dimensions of a surface (m^2). Its unit is $N.s.m^{-4}$ and is mathematically represented above. The term μ is the dynamic viscosity of air ($\sim 1.80 \text{x} 10^{-5} \text{N. s. m}^{-2}$) at ambient temperature and pressure whilst *v* is the fluid velocity and *L* is the thickness of the porous body.

The major difference between k_o and σ is that the former does not depend on the fluid property while the latter is specific to a fluid (Hinze and Rosler, 2013). Eq 2.35 indicates that a high airflow resistivity is an indication of low permeability of the material. Such porous material will require high pressure for fluid to squeeze through (Oun and Kennedy, 2015). In other words, if a fluid passes through a porous structure easily, such material has high permeability, low airflow resistivity and requires low pressure to squeeze the fluid through. This airflow resistivity can also be measured using flowmeter and permeability of a material is often measured in m^2.

2.5.2 Open porosity

Unlike the permeability of porous structure defined as a measure of the flow resistance through the porous body, the open porosity ($\emptyset$) commonly reduced to porosity refers to the ratio of the fluid volume occupied by the continuous fluid phase to the total volume of porous body (Beranek, 1942). It is also defined as the ratio of interconnected pore fluid volume to the total bulk volume of the porous aggregate (Dullien, 2012, and Perrot et al., 2013).

$$\emptyset = {}^{v_f}/_{V_B} \tag{2.35}$$

Porosity and pore size of metallic foam structures can be controlled with variation in the size of salt beads (space holder) and packing densities used during the manufacturing process (Kennedy, 2012). The porosity of a metal foam can be enhanced by dipping it in NaOH or $Ca(OH)_2$ solution or blowing agents like the TiH_2 (Kim, et al., 2009). Dullien, 2012 shows that displacement method for the bulk volume and fluid saturation method for the pore volume can be used to measure the porosity of a porous material. Similarly, the porosity of a porous material can also be measured with the help of porosimeter. This method is called mercury intrusion porosimetry and it provides reliable information about the pore size, specific surface, pore volume, density and particle distribution of the microstructure (Abell et al., 1999, and Oun and Kennedy, 2014). High resolution tomography images of the “real” porous materials combined with image processing routes involving volume generation, thresholding and smoothing can also be used to determine its porosity (Petrasch et al., 2007, Bodla, et al., 2010, Peng, et al, 2012, and De Carvalho et al., 2017).

2.5.3 High-frequency limit of dynamic tortuosity

The High-frequency limit of dynamic tortuosity often reduced to tortuosity (Johnson et al., 1987) is a property of a curve being tortuous (twisted; having many turns). For porous structures, tortuosity is defined as interconnectedness or sinuosity of the pore space (Adler, 1992) or the ratio of the shortest route to boundary distance of porous structure. It can also be defined as a measure of how winding a path that a fluid element travels between two points within a medium (Perrot et al., 2013). The description of the acoustic behaviour of materials defines tortuosity as one of the acoustical parameters that depend on the interaction of the pore fluid and pore geometry. The Johnson et al version of poroacoustic models uses the high-frequency limit of the real part of dynamic tortuosity to account for the visco-inertial interaction of the fluid in pores with the skeleton. This interaction makes the effective fluid heavier than the pore fluid (Zielinski, 2013). This is the more reason the defined tortuosity is always greater than unity.

Sometimes crude approximations are generally used when tortuosity serves as the basis for predictions. For example, it is common practice to make tortuosity as the inverse of porosity in the case of molecular diffusion (Satterfield, 1970). For a straight path tortuosity is 1.0; for metal foam structure it is between1.00 – 3.00 and for a circle, it is infinite (Perrot et al., 2013). The equation describing the tortuosity of porous media flow can be traced back to Archie (1942) and, Winsauer et al. (1952). Archie inferred it equation for the tortuosity from experimental data as given in Eq 2.36 while Winsauer et al. (1952) measured tortuosity by an independent electrical method (Eq 2.37).

$$F_r = af^{-m} \quad 2.36$$

$$\tau^{1.67} = \emptyset F \tag{2.37}$$

where *a* is a constant value close to 1.0; F_r is the formation resistivity; $\emptyset$ is the fractional porosity and $1.4 < \mathrm{m} < 2.3$ exist for unconsolidated sands to indurated sandstone and 1.0 for straight pore.

In a separate study, tortuosity (Eq 2.38) was accounted for using theoretical studies on diffusivity transport in porous systems consisting of spontaneously overlaying monosized spheres (Weissberg, 1963, Ho and Streider, 1982, and Matyka et al., 2008). Johnson et al. (1987) proposed the high-frequency limit of dynamic tortuosity as a function of the material homogenization volume V, and fluid particle velocity at high frequencies (*v*) Eq 2.39.

$$\tau = 1 - 0.25 ln\emptyset \tag{2.38}$$

$$\tau = \frac{\frac{1}{V}\int_V v^2 dV}{\left(\frac{1}{V}\int_V \vec{v} dV\right)^2} \tag{2.39}$$

Du Plessis and Wouldberg (1994) gave a mathematical expression of the tortuosity of metallic foam structure as a function of open porosity (Eq 2.40) and was further reorganized in Du Plessis and Fourie, 2002 (Eq 2.41). Their expression was based on a geometrical modelling of the internal structure of the porous material. For a much smaller viscous boundary layer compared to the characteristic size of the pores of porous matrix.

$$\frac{1}{\tau} = \frac{3}{4\emptyset} + \frac{\sqrt{9-8\emptyset}}{2\emptyset}\cos\left\{\frac{4\pi}{3} + \frac{1}{3}\cos^{-1}\left[\frac{8\emptyset^2 - 36\emptyset + 27}{(9-8\emptyset)^{3/2}}\right]\right\} \tag{2.40}$$

$$\tau = 2 + 2\cos\left[\frac{4\pi}{3} + \frac{1}{3}\cos^{-1}(2\emptyset - 1)\right] \tag{2.42}$$

Bhattacharya et al. (2002) proposed the tortuosity of aluminium foam structures as a function geometrical function value, G (0.5831 & 1.00) for the porosity of 97% and 85% respectively and G interpolated with the given range of porosity (Eq 2.43). They also argued that their relation is valid for predicting pressure drop (Eq 2.44) over a wide range of porosities in porous metallic structures.

$$\frac{1}{\tau} = \frac{\pi}{4\emptyset}\left[1 - \left(\frac{1.18}{G}\sqrt{\frac{1-\emptyset}{3\pi}}\right)^2\right] \qquad 2.43$$

$$\frac{\Delta p}{LV} = \frac{\mu(1-\emptyset)^2}{\emptyset^3}.\frac{\tau^2\sigma}{\tau-1} + \frac{(1-\emptyset)}{\emptyset^3}.\frac{\tau^2\sigma}{6}.\rho V \qquad 2.44$$

2.5.4 Viscous and thermal characteristic lengths

One of the advantages of pore-level numerical simulation over macroscale simulation is the enhancement of pore geometry and localized view of the porous structure. This enables a good understanding of the internal structure (cell sizes, openings, surface area, and tortuosity) of the porous medium in relation to its hydrodynamic or pressure wave behaviour. This porous structure consists of a connected metal frame (skeletal phase) saturated with air (occupying the porous region). When sound pressure wave propagates the pores and openings of a porous structure at an audible frequency, high sound energy is created resulting in the formation of viscous and thermal layers. Thus, the dissipation of acoustical energy through a porous material involves the visco-inertial, thermal and structural dissipation effects (Perrot et al., 2013).

The dissipation resulting from the friction of air particles with the structural wall as sounds propagate through the porous material is termed the viscous-inertial dissipation effects. A thermal wave is created as a result of successive

compression and dilatations when sound waves propagate through the porous medium. The thermal dissipation effects exist when there is significant heat exchange between the air particles and structural wall. The heat exchanges between the particles of air and structural frame result in the build-up of the thermal boundary layer (Olny and Panneton, 2008). This definition justifies that both the viscous and thermal characteristics length are classified as structural parameters as it depends on the fluid and the localized pore geometry of the structure (frame).

The structural dissipation is dependent on the mechanical properties of the material. Though, the skeletal structure of metal foams depends on the processing route employed and can be changed by mechanical compression and rolling techniques as earlier stated. Fig 2.8 presents a diagrammatic representation of the viscous (window or pore diameter openings) and thermal (pore diameter size) characteristics length of porous material as proposed in Olny and Panneton (2008).

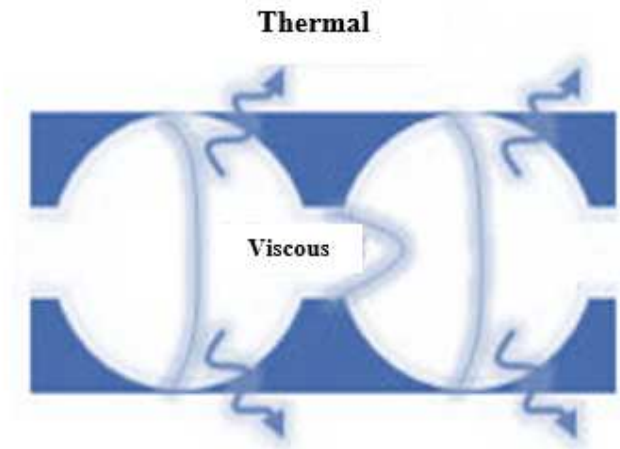


Fig 2.8. Schematic view of viscous and thermal characteristics lengths [**adapted from Olny and Panneton, 2008**].

The use of acoustic porous media models also known as poroacoustic models to predict the acoustical behaviour of porous materials requires characterization of the viscous and thermal characteristic lengths using scanning electron microscopy, optical imaging or X-Ray computerized tomography techniques. Johnson et al. (1987) expresses the viscous characteristics length (∧) to be twice the ratio of the weighted by the velocity in the volume and on the surface of an inviscid (low or no viscosity) fluid (Eq 2.45) whilst the thermal characteristics length ($\bar{\wedge}$) is a generalization of a hydraulic radius and is defined as equal to twice the interconnected pore volume to pore wet surface ratio (Eq 2.46). Where v is the superficial fluid local velocity, Ω_f is the interconnected pore fluid volume, Ω is the bulk volume of the porous aggregate (computational domain), $\partial\Omega$ is the pore wet surface ratio (or fluid-solid or domain boundary), *V* and *S* are classified as volume and surface area.

$$\wedge = 2\frac{\int_{\Omega} v^2 dV}{\int_{\partial\Omega} v^2 dS} \qquad 2.45$$

$$\bar{\wedge} = 2\frac{\int_{\Omega} dv}{\int_{\partial\Omega} dS} = 2\,{}^{\Omega_f}\!/_{\partial\Omega} \qquad 2.46$$

Reported in Johnson et al. (1987) and Olny and Panneton (2008), the average radius of the smaller pores (pore windows) is described to be the viscous characteristics length while that of the larger pores (pore sizes) to be thermal characteristic length. A mathematical relation of viscous characteristic length for most porous materials without noticeable pore roughness and that of slit-like pores were also proposed in Johnson et al. (1987) to be a function of low-frequency limit of dynamic tortuosity ($\tau = 1/\cos\hat{}\theta$), permeability ($k_o$) and porosity ($\emptyset$) of the structure as presented in Eq 2.47 and 2.48 respectively. They

also specified the range of viscous characteristics length for usual acoustical porous structure to be within 11-350um.

$$\Lambda = \sqrt{\frac{8\tau k_o}{\emptyset}} \qquad 2.47$$

$$\Lambda = \sqrt{\frac{12\tau k_o}{\emptyset}} \qquad 2.48$$

In conclusion, many authors have worked out different approaches for characterizing parameters in porous media: the acoustical and non-acoustical methods. The main non-acoustical approach is used for characterizing the airflow resistivity and the tortuosity (Johnson, et al., 1982). The acoustical method is subdivided into low and high-frequency methods. The low-frequency method is based on using impedance tube while the high-frequency method is based on ultrasound techniques (Leclaire, et al., 2012). For a complete characterization of the tortuosity, static thermal permeability, viscous and thermal characteristic lengths simultaneously, Zielinski (2013) suggested inverse identification methods using a standing wave tube as shown in Fig 2.9.

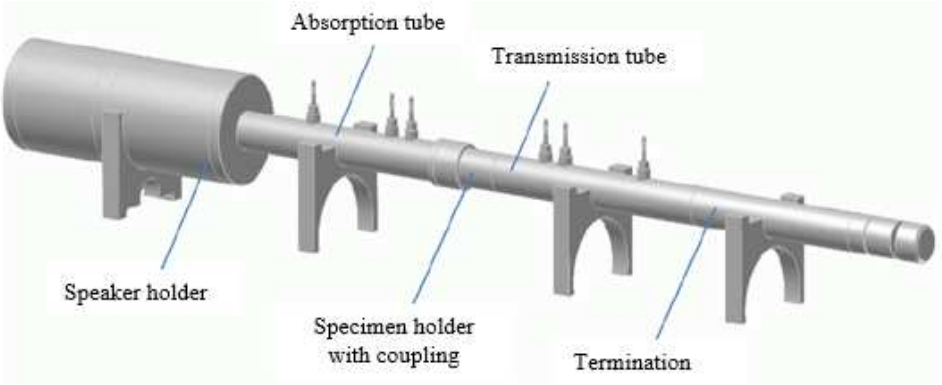


Fig 2.9. A 4-microphone, AFD 1200-AcoustiTube® - measuring setup with sample holding section (**adapted from AFD Analysis software 1201 user guide**) used to estimate the tortuosity, static thermal permeability, viscous and thermal characteristics length.

2.6 Acoustic porous media models

The propagation of sound wave in an isotropic homogeneous material is determined by complex quantities, the characteristic impedance, Z_c, and the propagation coefficient, k, (Delany and Bazley, 1970). The propagation coefficient is sometimes called the complex wave number, and is given in Eq 2.49,

$$Z_c = R + iX = \sqrt{\rho_{(w)} K_{(w)}} \quad \text{and} \quad k = A + i\beta = w\sqrt{\frac{\rho_{(w)}}{K_{(w)}}} \qquad 2.49$$

where $K_{(w)}$ is the bulk modulus, $\rho_{(w)}$ is the effective density, w is the angular or radial or circular frequency mathematically described as $2\mu f$, R is called the complex acoustic resistance, X is the complex acoustic acceptance, A is the attenuation constant (nepers/m; 1 neper is 8.68dB) and β is the phase constant (rad/m).

The propagation of sound pressure wave in porous media can be described by propagation models. These propagation models are classified as the “equivalent solid” (uniform pressure), “equivalent fluid” (motionless skeleton) and the Diphasic (Biot’s theory) models (Acoustic Porous Material Recipes, APMR). For certain frequency range and appropriate boundary conditions, the skeletal (equivalent fluid) or fluid (equivalent solid) is considered motionless and no pressure wave propagates in the solid (equivalent fluid) or fluid (equivalent solid) phase of the microstructure and when wave propagates in both phases, it is termed Diphasic and described by Biot’s theory. This theory (Biot) is most reliable in describing the vibro-acoustic of porous materials (Biot, 1956).

Several models have been developed considering the contributions of the skeletal and fluid phases over a frequency range. Typical examples are the Zwikker and Kosten (1949), Biot (1956), Attenborough (1983), Delany and Bazley (1970), Mikki (1990), Allard and Champoux (1992), Johnson et al. (1993), Wilson (1993) and William (2001) poroacoustic models.

2.6.1 Primeval models

An extensive research at the Technische Hogeschool in Delft city of Netherland by a group of physicists provides the cardinal and practical model describing the acoustic behaviour of porous materials with elastic frame published in Zwikker & Kosten (1949) book titled "Sound Absorption Materials". For many years after disclosure of their original work, there has been a success applauded for their uncomplicated and understandable structure and presently in use with numerous references in the last decade. The proposed Zwikker-Kosten models available in their book were said to provide the static air pressure (P_o) and force acting on the skeletal frame per unit cross section (P_m) as a function of the mean velocity of solid material (v_m) and that of air (v_o), density of skeletal (frame) material (ρ_m) and that of air (ρ_o), open porosity of the porous material ($\emptyset$), incompressibility modulus of air (K_o), specific frame thickness (L_m) and coupling coefficient (S) defined in termed of angular frequency in (Eq 2.50-2.54).

$$-\frac{\partial P_m}{\partial x} = \rho_m \frac{\partial v_o}{\partial t} + S(v_o - v_m) \quad 2.50$$

$$-\frac{\partial P_o}{\partial x} = \rho_o \frac{\partial v_m}{\partial t} + S(v_m - v_o) \quad 2.51$$

$$-\frac{\partial P_m}{\partial x} = L_m \frac{\partial v_o}{\partial x} - \frac{(1-\emptyset)}{\emptyset}\frac{\partial P_o}{\partial t} \quad 2.52$$

$$-\frac{\partial P_o}{\partial x} = \emptyset K_o \frac{\partial v_m}{\partial x} - (1-\emptyset)(K_o - P_o)\frac{\partial v_o}{\partial t} \quad 2.53$$

$$S = jw\rho_o(\tau - 1) + \emptyset^2 \quad 2.54$$

For many years, the stated differential equations have been used for the study of elastic porous materials but were further expatiated by Biot (1959) by improving the coupling coefficient for a better approximation of the structural frame and understanding of the fluid-structure interactions when pressure wave accesses the interior cellular structure of porous materials. Also, Keith Attenborough (1983) modified the Zwikker-Kosten equations to predict the acoustical characteristics of sands and rigid fibrous absorbent soil as a function of five structural parameters namely, open porosity (Ø), tortuosity (τ), steady shape factor (C_o), dynamic shape factor (C_D) and flow resistivity (σ). The model was developed to give accurate predictions of the characteristic absorption behaviour of the porous structure with a better fit to measured data.

From a large number of experimental data in fibrous materials with porosities close to unity, Delany and Bazley (1970) proposed empirical expressions for the characteristic acoustic impedance (Z_c) and complex wavenumber (k) using the +$j$wt (sinusoidal time variation) time convention (Eq 2.55 & 2.56). The validity of this expression is between 0.01 < $\frac{f}{\sigma}$ <1.00. That is, suitable for very low frequencies (<100Hz) and not also exact for very high frequencies (>10 kHz) of fibrous materials (Jones, 2010). Only one parameter (typically, the static airflow resistivity, σ) was needed to describe the acoustic behaviour of porous material using this model. The fit of experimental data used by Delany and Bazley (1970)

was later used by Allard and Champoux (1992) with the same boundaries and came up with the expression for Z_c (Eq 2.57) and k (Eq 2.58) with close agreement between the two models.

$$Z_c = \rho_o C_o \left[1 + 9.08\left(10^3 \frac{f}{\sigma}\right)^{-0.75} - j11.9\left(10^3 \frac{f}{\sigma}\right)^{-0.73}\right] \quad 2.55$$

$$k = \frac{w}{C_o}\left[1 + 10.8\left(10^3 \frac{f}{\sigma}\right)^{-0.70} - j10.3\left(10^3 \frac{f}{\sigma}\right)^{-0.50}\right] \quad 2.56$$

$$Z_c = \rho_o C_o \left[1 + 0.0571\left(\rho_o \frac{f}{\sigma}\right)^{-0.754} - j0.0870\left(\rho_o \frac{f}{\sigma}\right)^{-0.732}\right] \quad 2.57$$

$$k = \frac{w}{C_o}\left[1 + 0.0978\left(\rho_o \frac{f}{\sigma}\right)^{-0.700} - j0.1890\left(\rho_o \frac{f}{\sigma}\right)^{-0.50}\right] \quad 2.58$$

In the case of multiple layers, Mikki (1990) noticed that the real part of the surface impedance when computed with the Delany and Bazley (1970) model sometimes becomes negative at low frequencies. From the same experimental data carried out by Delany and Bazley (1970), 20yrs later, Mikki proposed modifications of expressions to correct the characteristic acoustic impedance (Z_c) and propagation coefficient (k) and was named the Delany-Bazely-Mikki models as shown in Eq 2.59 and Eq 2.60 respectively. Though, Mikki takes care not to extrapolate the boundaries ($0.01 < \frac{\mathrm{f}}{\sigma} < 1.00$) even when he had observed his revised expressions are well-behaved in a larger frequency range, in particular $\frac{f}{\sigma} < 0.01$, $0 < \emptyset < 1.0$ and 1,000< σ <50,000 Pa.s/m^2.

$$Z_c = \rho_o C_o \left[1 + 5.50\left(10^3 \frac{f}{\sigma}\right)^{-0.632} - j8.43\left(10^3 \frac{f}{\sigma}\right)^{-0.632}\right] \quad 2.59$$

$$k = \frac{w}{C_o}\left[1 + 7.81\left(10^3 \frac{f}{\sigma}\right)^{-0.618} - j11.43\left(10^3 \frac{f}{\sigma}\right)^{-0.618}\right] \quad 2.60$$

2.6.2 Visco-inertial and thermal effects using Johnson et al acoustic models

To accurately model acoustics in geometries with small dimensions, it is necessary to include thermal conduction effects and viscous losses explicitly in the governing equations. Having studied the acoustic behaviour of porous material with a motionless skeleton having arbitrary pore shape, Johnson et al. (1987) proposed a semi-phenomenological model to describe its complex density (Eq 2.61). Four parameters are involved in the calculation of the dynamic density, open porosity (∅), static airflow resistivity (σ), high-frequency limit of the tortuosity (τ), and the viscous characteristic length (∧).

$$\rho_{(w)} = \tau\frac{\rho_o}{\emptyset}\left\{1+\frac{\sigma\emptyset}{iw\rho_o\tau}\sqrt{1+i\frac{4\tau^2\mu\rho_o w}{\sigma^2{\wedge}^2\emptyset^2}}\right\} \qquad 2.61$$

Retaining this proposed model (Eq 2.61) for viscous the dissipation effect, Allard and Champoux (1992) proposed an expression for the dynamic bulk modulus for the same kind of porous material as a function of open porosity, thermal characteristics length, static atmospheric pressure (P_o), specific heat ratio (γ), angular frequency (w) and thermal conductivity (k_T) of porous materials and was titled the Johnson- Champoux-Allard (JCA) model (Eq 2.62).

$$K_{(w)} = \gamma\frac{{}^{P_o}/_{\emptyset}}{\gamma-(\gamma-1)\left\{1-i\frac{8k_T}{\bar{\wedge}^2C_p\rho_o w}\sqrt{1+i\frac{\bar{\wedge}^2C_p\rho_o w}{16k_T}}\right\}^{-1}} \qquad 2.62$$

The limitation for this model observed in Olny et al. (2004) was that the low frequency limit of the real part of the dynamic mass density $\rho_{(w)}$ expressions is not exact as ω tends to zero. Similarly, the expression for $K_{(w)}$ was not also correct and the thermal characteristic length ($\bar{\wedge}$) was used to represent the

medium at high frequency range of thermal effect. The expression of bulk modulus in Allard and Champoux (1992) (Eq 2.62) was further modified by Lafarge et al. (1997) with the introduction of a third non-acoustical microstructural parameter (static thermal permeability, k_0') to describe the low-frequency behaviour of thermal effects and was termed the JCAL model (Eq 2.63).

$$K_{(w)} = \gamma \frac{{}^{P_o}/_{\emptyset}}{\gamma-(\gamma-1)\left\{1-i\frac{\emptyset k_T}{k_0' C_p \rho_o w}\sqrt{1+i\frac{4{k_0'}^2 C_p \rho_o w}{k\emptyset^2}}\right\}^{-1}} \quad 2.63$$

Despite the inclusion of static thermal permeability to the Johnson-Champoux-Allard model, his expression was still not exact, at low frequencies. Prides et al. (1993) refined the JCA and JCAL expressions to describe the visco-inertial (five structural parameters) and thermal dissipative effects (four structural parameters) to obtain the complex density (Eq 2.64) and bulk modulus (Eq 2.65) of acoustic fluid for pore with motionless skeleton having arbitrary pore shapes. Also, theoretical determination of the static thermal permeability (k_0'), static viscous (τ_0) and static thermal (τ_0') tortuosity were accounted for using the dimensionless shape factors (M_1, M_1', N_1 and N_1') in Eq 2.66 (Perrot et al., 2013).

$$\rho_{(w)} = \tau\frac{\rho_o}{\emptyset}\left\{1+\frac{\mu\emptyset}{iw\rho_o k_o \tau}\left(1-\frac{2k_o\tau}{\emptyset\Lambda^2\left(\frac{\tau_o}{\tau}-1\right)}+\frac{2k_o\tau}{\emptyset\Lambda^2\left(\frac{\tau_o}{\tau}-1\right)}\sqrt{1+\frac{i\rho_o w\Lambda^2\left(\frac{\tau_o}{\tau}-1\right)^2}{\mu}}\right)\right\}$$

2.64

$$K_{(w)} = \frac{\frac{\gamma P_o}{\emptyset}}{\gamma-(\gamma-1)*\left[1+\frac{k\emptyset}{iw\rho_o C_p k_0'}*\left(1-\frac{2k_0'}{\emptyset\bar{\wedge}^2(\tau_0'-1)}+\frac{2k_0'}{\emptyset\bar{\wedge}^2(\tau_0'-1)}\sqrt{1+\frac{i\rho_o w C_p \bar{\wedge}^2(\tau_0'-1)^2}{k_T}}\right)\right]^{-1}} \quad 2.65$$

$$M_1 = \frac{8\tau}{\emptyset \Lambda^2} k_o \quad M_1' = \frac{8}{\emptyset \bar{\Lambda}^2} k_0' \quad N_1 = \frac{M_1}{4\left(\tau_0/\tau - 1\right)} \quad N_1' = \frac{M_1'}{4\left(\tau_0' - 1\right)} \tag{2.66}$$

In summary, a total of eight structural parameters were needed to describe the propagation of pressure wave through porous structures backed by rigid backing or back cavity using the JCAPL poroacoustic model.

2.6.3 Wilson model

Due to the important role played by pore morphology and shape factor in the vibro-acoustical behavioural prediction of the sound pressure wave across porous structures, Keith D. Wilson (1993) proposed a model to predict the complex density and bulk modulus of the structure with triangular and circular aperture and near-spherical pore sizes. The model focused on the relaxation-matched behaviour of the porous medium and was capable of predicting porous materials regardless of its specific pore structure and the usual definition of low and high frequencies as shown below.

$$V_c = \frac{1}{\rho_c} = \frac{\emptyset}{\rho_o \tau^2} + \left\{1 + \left(\frac{\tau^2}{\emptyset} - 1\right) S_x \left(D_p / \delta_{vor}\right)\right\} \tag{2.67}$$

$$\beta_{(w)} = \frac{1}{K_{(w)}} = \frac{\emptyset}{P\gamma}\left\{1 + (\gamma - 1)\, S_x \left(D_p / \delta_{ent}\right)\right\} \tag{2.68}$$

$$S_x = \frac{3}{(1-i)x}\left\{\coth(1-i)\, x - \frac{1}{(1-i)x}\right\},\ \delta_{vor} = \sqrt{\frac{2\mu}{w\rho_o}} \text{ and } \delta_{ent} = \sqrt{\frac{2k}{w\rho_o c_p}} \tag{2.69}$$

Though, more than one parameter (permeability, dynamic tortuosity, and porosity) is required to describe the acoustical behaviour of porous structures using Wilson's model but it provides simpler models with no Bessel and Kelvin functions (Wilson, 1993) and realistic for all frequencies. The simplified

Wilson's model for complex density (ρ_c) and bulk modulus ($K_{(w)}$) for circular and triangular pores are related to its complex specific volume (V_c) and complex compressibility ($\beta_{(w)}$) presented in Eq 2.67-2.69.

The term S_x in the proposed models (Eq 2.67-2.69) is termed the Bessel function which is dependent on the pore geometry; D_p is the pore diameter size; P is the ambient pressure; γ is the specific heat ratio; ρ_o is the fluid density $w = 2\pi f$ is the angular frequency; μ is the fluid viscosity; C_p is the specific heat capacity at constant pressure; k is the thermal conductivity of the material; N_{pr} is the air Prandtl number; δ_{vor} and δ_{ent} are the vorticity and entropy mode boundary layer thickness respectively.

In order to accurately model the acoustic absorption of porous structures with near-spherical openings using Wilson's model, it is necessary to specify the bulk modulus infinite frequency limit ($K_\infty = \frac{P\gamma}{\emptyset}$), the density infinite frequency limit ($\rho_\infty = \frac{P\tau^2}{\emptyset}$), the vorticity-mode relaxation time ($\tau_{vor} = \frac{2\rho_o\tau^2}{\emptyset\sigma}$) and the entropy-mode relaxation time ($\tau_{ent} = N_{pr}.\tau_{vor}$) in the physics modules acoustic software (COMSOL Multiphysics 5.2™ user guide).

Other poroacoustic models were developed to mimic the surface acoustic impedance and normal incidence absorption coefficient of porous structures with specific pore morphology. A typical example of this is the William EDFM model proposed in 2001. This model put forward the expression of effective density fluid model (EDFM) for acoustic propagation in sediment obtained from Biot's theory with a close agreement in their predicted values. Table 2.2 presents a tabular representation of the porous media acoustic model thereof, their

applicability, limitations and structural parameters needed to fully describe the acoustic behaviour of porous materials.

Table 2.2. Acoustic porous media models

Models	Limitation	Application	Structural parameter(s)
Zwikker & Kosten, 1949	All frequency	Straight cylindrical pores	$\emptyset, \tau$ & k_o
Biot, 1959	All frequency	Straight cylindrical pores	$\emptyset, \tau$ & k_o
Attenborough, 1983	All frequency	Sand and rigid fibrous	$\emptyset, \tau, k_o, C_o$ & C_D
Delany & Bazley, 1970	$0.01 < \frac{f}{\sigma} < 1.00$	Fibrous materials with straight cylindrical pores	k_o
Allard & Champoux, 1992	$0.01 < \frac{f}{\sigma} < 1.00$	Fibrous materials with straight cylindrical pores	k_o
Mikki, 1990	$0.01 < \frac{f}{\sigma} < 1.00$	Fibrous materials with slanted cylindrical pores	k_o
Johnson, Koplik & Dashen, 1987 and Champoux & Allard, 1992	All frequency	Non-uniform section	$\emptyset, \tau, k_o, \Lambda,$ & $\bar{\varkappa}$
Lafarge, Lemarinar & Allard, 1997	Not exact low frequency	Non-uniform section	$\emptyset, \tau, k_o, \Lambda, \bar{\varkappa},$ & k_0'
Prides, Morgan & Gangi, 1993	All frequency	Non-uniform section with possible constrictions	$\emptyset, \tau, k_o, \Lambda, \bar{\varkappa}, k_0', \tau_0$ & τ_0'
Wilson, 1993	All frequency	Suitable for structures with circular and triangular pores	$\emptyset, \tau, k_o, D_p$& D_w

2.7 Separating low and high frequencies regime in a porous absorber

The pressure drop experiment in porous media described by Henry Darcy's law is often used in the determination of the static viscous permeability as well as the airflow resistivity of the porous material. The description of acoustic properties of porous materials using the JCA five (5) parameters models gives an insight to account for the visco-inertial and thermal behaviour of acoustical materials. The resultant effect that arises from the creation of viscous and thermal boundary layers is due to the fact that the separating pore fluid leaves the structural phase behind as it propagates through it. When viscous forces dominate the inertial forces, it is termed the low-frequencies regime and when

inertial forces dominate the viscous forces, it is termed as high-frequencies regime. A more realistic way of showing this is the use of a characteristic angular frequency in Biot, 1956a & 1956b and presented in Fig 2.10 and Fig 2.11 below.

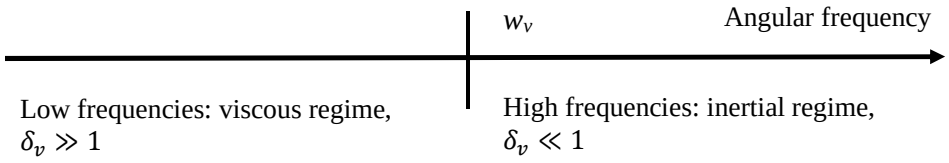


Fig 2.10. Frequency-dependent visco-inertia dissipation mechanism.

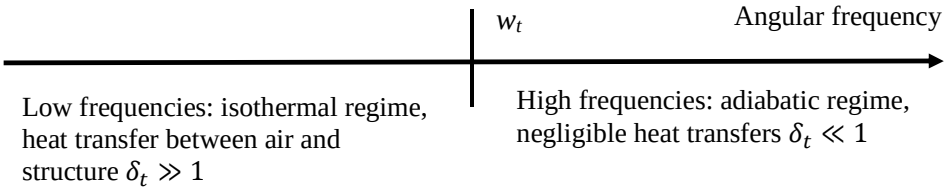


Fig 2.11. Frequency-dependent thermal dissipation mechanism.

For the existence of viscous boundary layer, when the pulsation is much smaller than the viscous characteristics angular frequency w_v and viscous boundary layer thickness much larger than unity ($\delta_v \gg 1$), the flow is purely viscous. Also, for pulsation much larger than the viscous characteristics angular frequency (w_v) and viscous boundary layer thickness much smaller than unity ($\delta_v \ll 1$), the inertial effects dominate the viscous effects. Same is repeated for the classification of the thermal boundary layer in the low and high frequency regimes (Johnson et al., 1987). Below the thermal characteristic angular frequency(w_t), the air compression and dilations are isothermal as heat transfer exists between the fluid and structure (Lafarge et al., 1997). Above the thermal characteristic angular frequency(w_t), it is classified as the adiabatic-regime with negligible heat transfers. This helps to distinguish between the low and high frequency regimes.

A good porous absorber should have interconnected pore network for the dissipation mechanism within the possible volume for significant visco-inertial and thermal dissipation as acoustic wave travels through it. Kirchhoff (1868 and 1974) gave mathematical relations for the numerical determination of viscous and thermal boundary layer thickness as a function of fluid properties and frequency and are presented in Eq 2.70 and 2.71 below. The frequency is represented as f while δ_v, δ_t, η, ρ_o, k, C_p are the viscous boundary layer thickness, thermal boundary layer thickness, fluid dynamic viscosity, fluid density respectively, thermal conductivity of the fluid and fluid specific heat capacity at constant pressure respectively.

$$\delta_v = \sqrt{\frac{\mu}{\rho_o 2\pi f}} \tag{2.70}$$

$$\delta_t = \sqrt{\frac{\mathrm{k}}{\rho_o C_p 2\pi f}} \tag{2.71}$$

The distinction between the viscous dominated (low frequencies) regimes and inertial dominated (high frequencies) and that of the low and high frequencies regime for the thermal effects is shown from a numerical computation for a frequency range between 100 and 4500Hz using Eq 2.70 and 2.71. Table 2.3 shows the calculated values of viscous and thermal boundary layer thickness for fluid properties obtained at standard atmospheric temperature and pressure.

Table 2.3. Estimation of viscous and thermal boundary layer thickness

$T = 20^oC$, $C_p = 1.0 * 10^3$(J/kg.K), k $= 2.6 * 10^{-2}$(W/m.K), $\eta = 1.8 * 10^{-5}\left(N.\frac{s}{m^2}\right)$ & $\rho = 1.204$kg/m^3.			
	$f = 100Hz$	$1.56 * 10^{-4}m$	$\delta_v \ll 1$ ~ High frequency inertial regime
δ_v	$f = 4{,}500Hz$	$2.33 * 10^{-5}m$	$\delta_v \ll 1$ ~ High frequency inertial regime
	$f = 100Hz$	$1.85 * 10^{-4}m$	$\delta_t \ll 1$ ~ High frequency thermal regime
δ_t	$f = 4{,}500Hz$	$2.77 * 10^{-5}m$	$\delta_t \ll 1$ ~ High frequency thermal regime

A simple analysis of visco-inertial and thermal dissipation effects for these audible frequencies range, shows that for a metal to be a good sound absorber the pore opening (pore connectivity) should be in the order of 100μm (Lu, 2000) or within the ranges of 10-1000μm (Perrot et al., 2013) and 11-350μm specified by Johnson et al. (1987). Closed pore structures are characterized by very low openings (Utsuno, 1989) and an observable sound absorption coefficient from experimental measurements of pressure wave across this structure in Lu and He, 2000 was considered poor.

2.8 Multiscale Asymptotic Modelling Approach

Much of the work in terms of modelling of fluid flow in the porous body has been limited to macroscopic or semi-empirical flow characteristics (Boomsma and Poulikakos, 2001) using volume-average equations. The behaviour of complex systems under extreme conditions can be analysed using multiscale or microscale modelling (Ortiz, 2012).

The precise preservation of more accurate local geometrical function (Bodla et al., 2010) through a representative elemental volume or control volume of the porous body makes pore-scale modelling imperative. This model is useful in the understanding of the behaviour of fluid in the porous body for a subset of the porosity range due to the approximate representation of the local geometry. This method can produce accurate results for fluid flow in complex porous media if an accurate representation of geometry is preserved.

Lee et al. (2009) described multiscale asymptotic modelling (MAM) approach as the asymptotic analysis of governing equation. This is a multiscale approach

or method employed in the determination of the macroscopic acoustic parameters at microscale level by deriving well-defined microscale equations from independent macroscopic variables equations via averaging over a unit cell. The ratio of microscopic-macroscopic length is (ε).

$$\varepsilon = {}^{d_1}/_{d} = \frac{\text{microscopic variation (unit cell length)}}{\text{macroscopic variation (frequency dependent length)}} \qquad 2.72$$

The adoption of Delany-Bazley-Mikki (DBM) model to mimic the acoustic behaviour of porous matrices implies that a single physics (Stokes or Creeping flow) equation is used to determine the pressure drop within the micro-length and eventually, the static viscous permeability from Darcy equation of fluid flow. Accounting for the visco-inertial and thermal dissipation (near walls viscosity and thermal conduction) effects due to the frictional force and heat exchange that exists between the fluid and structural frame when sound pressure wave propagates a porous medium leading to the Johnson et al version of poroacoustic model.

The MAM method expressed in Lee et al. (2009) can be used as a microscopic approach to account for the static viscous and static thermal permeabilities of porous materials subjected to the derivation of the microscopic equation from a set of coupled frequency-domain viscous-thermal equations and boundary conditions. The frequency dependent equations are the equation of state for perfect gas, Navier-Stokes (momentum) equation, the equation of continuity and the energy equations. The derived frequency-dependent energy equation in Lee et al. (2009) for the determination of the static thermal permeability (k'_o) solved with the appropriate boundary conditions (isothermal and periodic boundary

conditions on the wall and the relevant pair faces respectively) is presented in Eq 2.73-2.75.

$$\rho_o iw \frac{\Pr}{\eta} k'_o - \nabla.(\nabla.k'_o) = 1 \text{ (fluid domain } \Omega_f) \quad 2.73$$

$$\Pr = \mu \frac{C_p}{K} \quad 2.74$$

$$\rho_o iw \Pr \frac{K}{\eta}\left(\frac{k'_o}{K}\right) = 1 + K\Delta k'_o \left\{\frac{1}{K}\right\} \quad 2.75$$

where $\rho_o$is the fluid velocity; μ is the dynamic viscosity of the fluid; ρ_o, P_o & $T_o$are the fluid density, fluid pressure and temperature determine at STP respectively; ρ, P & T are the varying fluid density, pressure and temperature respectively; *R*, C_p and C_v are the gas constant, specific heat capacity at constant pressure and volume respectively; λ is the bulk viscosity and the thermal conductivity is represented as *K* as defined in the Fourier's law of heat transfer by conduction.

2.9 Summary

In this survey, diverse routes in the production of metallic foam structure have been made known with emphasis on the negative pressure infiltration processes (replication casting process) preferred in this work due to their economic advantage and important control of microstructural parameters during casting. Fundamental to this work, what is known about the flow of fluid through metallic structures as well as its acoustical behaviour when presented to sound pressure wave has been described. The review contained within the range of contents including continuity and momentum equation, pore-scale and fluid

models, flow regimes and permeability estimation, Helmholtz wave equation, acoustic absorption, poroacoustic models, structural parameters and multiscale asymptotic modelling. It is to this end that all the literature covered herein will assist in the experimental and numerical study of pressure drop and pressure wave across porous metallic structures. This would serve as a guide to the design of porous absorber with novel attributes that could assist to cut down vibration significantly and provide heat sink when used as a soundproofing device in high-end loudspeakers very early on. The next chapter of this work focused on preliminary understanding of the permeability of porous structures using sphere-packing models.

CHAPTER 3

THE PERMEABILITY OF VIRTUAL MACROPOROUS STRUCTURES GENERATED BY SPHEREPACKING MODELS: COMPARISON WITH ANALYTICAL MODELS

3.1 Summary

In this chapter, the results of the numerical simulation of fluid flow through "virtual" spherical packed beds of monosized structures are presented as an alternative approach to computing the permeability of realistic porous structures typical of those made by casting processes. Fluid dynamic simulation of the permeability of these structures agrees well with experimental measurements and similar modelling of structures derived from X-Ray tomographic images. By varying the model structures, the "bottleneck" flow concept proposed by analytical models in the literature was substantiated, confirming the high dependence of permeability on the size of the windows connecting the pores, but also highlighting the need for accurate determination of the connectivity of the pores for these models to be accurate.

NB: An article from this chapter has been published in Scripta Materialia in 2016. Click on the link *https://doi.org/10.1016/j.scriptamat.2016.06.037*

3.2 Introduction

Porous metals are commonly used as structures that interact with a fluid in processes such as heat exchange and storage, filtration and separation. Pivotal to the performance of these structures is the resistance to fluid flow that is provided by the porous body, usually described by the pressure drop per unit length developed across the structure as a function of the flow rate (or velocity) of the fluid through it. For laminar flow conditions in a given fluid, the permeability

of the porous structure, which is affected by the porosity, pore size, shape, and connectivity, relates flow rate and pressure gradient through Darcy's law.

In Goodall et al (2006 and 2007) and Despois et al (2007), porous metals made by the infiltration of liquid metal into a bed of sacrificial particles were said to have offered a more convenient fabrication method with the potential to vary the porosity and pore size independently, thereby giving a good level of control over the structure and hence the fluid flow behaviour. Fig 3.1 shows the typical structure of porous metals made by replication of packed beds of near-spherical NaCl beads by Langston and Kennedy (2014) and X-Ray CT image showing typical pore morphology. Important structural features to note include the size of the pores (dictated by the size of the porogens) the fraction of pores (dictated by the packing behaviour of the porogens – in this case affected by tapping in a mould) and the number and size of the windows connecting the pores (dictated by the ability of the infiltrating molten aluminium to penetrate the small spaces at the contact points between salt beads and the number of particle-particle contacts).

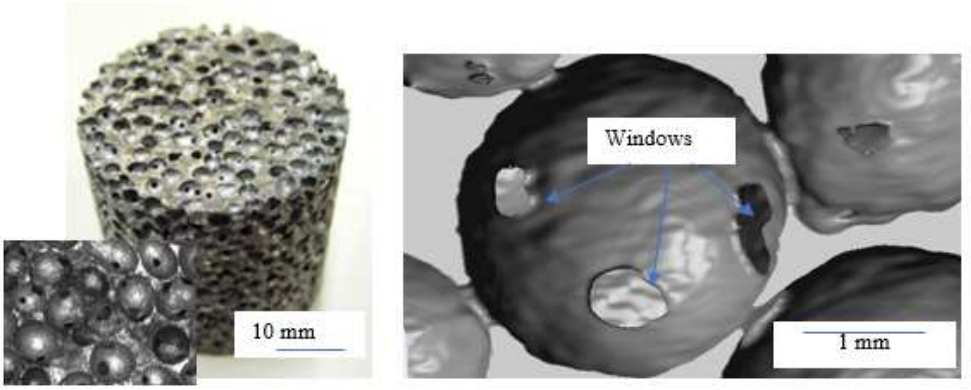


Fig 3.1. An optical micrograph left of a porous sample made by vacuum casting using near-spherical NaCl (**adapted from Langston and Kennedy, 2014**) and right, an X-Ray CT (μCT) image showing the typical pore connectivity.

The models to predict the coordination number (N_C) and permeability (k_0) of the porous structure available in the literature (Depois and Mortensen, 2005 and

Furman et al., 2013) and presented in chapter one are useful and could assist in the preliminary understanding of the flow behaviour of this structure when presented to flowing fluid. The coordination number (Eq 1.1) is defined as a function of packing fraction, Ø, and the window radius, r_w, (Eq 1.2) in terms of the infiltration pressure, Pi, and pore (particle in virtual structure) size, D_p. The model in (Depois & Mortensen, 2005) reduces to the same expression for permeability for the case of dense random particle packing if N_C = 6 but not a typical of this packing condition (Jinnapat and Kennedy, 2011 & 2012).

Reasonable correlation between experimental measurements of permeability and the models was observed in both cases, with deviations attributed, in part, to the non-spherical nature of some of the salt particles used. Thus a strong dependence upon the size of the windows connecting the pores and the permeability is apparent and controlling the window size, through varying the infiltration pressure (Furman et al., 2013) has the capacity (for a given pore size) to vary the permeability by more than a factor of 10 and would be more convenient way to vary the permeability rather than by altering the packing (porosity) through additional and potentially costly processing steps. This part of the study aims to further test the “bottleneck” flow assumption and the accuracy of these models by simulation of fluid flow through virtual 3D structures that are accurate reproductions of real porous metals made by the infiltration route, but in which the structural characteristics can be controlled precisely, as demanded by the analytical models. The novel approach to generating these virtual structures, which could be further exploited to predict the permeability of more complex porous structures, is detailed.

3.3 Image Processing and representative volume

A prior study by this group (Langston and Kennedy, 2014) demonstrated that the discrete element method (DEM) can be used to accurately model the packing of spherical NaCl particles (both monosized and in binary mixtures) and from this the structures of porous metals made by the infiltration thereof. Coupled with a simple mathematical processing of the spatial data for the packed spheres and development of the conditions for contacting of neighbouring beads, the number of windows linking neighbouring pores, and their size, was also accurately predicted, enabling useful insights into the connectivity of these structures.

This study has adopted this same DEM method and has created packed beds of monosized spheres, controlling the packing fraction by altering the coefficient of friction between the particles, giving packing conditions varying from loose to dense random packing (in the range of packing fraction from 0.59 to 0.64). Simple code written in MATLAB was used to process *x*, *y*, *z* particle coordinates and radius data from the DEM simulation, applying a criterion to determine whether particles are connected. This method is detailed in (Langston and Kennedy, 2014) but in brief, two particles are assumed to be connected if the gap separating them cannot be filled by the infiltrating liquid. This ability to fill the gap is controlled by the capillary radius, r_c, determined from the Laplace equation (Eq 1.2). For the Al-NaCl system (Jinnapat and Kennedy, 2011 and 2012) an infiltration pressure of 1 bar leads to a capillary radius of approximately 20μm and hence particles separated by 40μm are deemed “contacting” for this infiltration condition. An extension to this previous study is the graphical representa-

tion of this connection through calculation of the radius of the zone that is excluded from infiltration by the liquid (using a simple geometrical model also presented in (Langston and Kennedy, 2014) and adding the position of the centre of the contact and the radius to the data set. The Matlab code then draws a series of 2D sliced (binary) images of the particles (Fig 3.2) and contacts and exports them as tiff files (in this case at a resolution of 300 dpi).

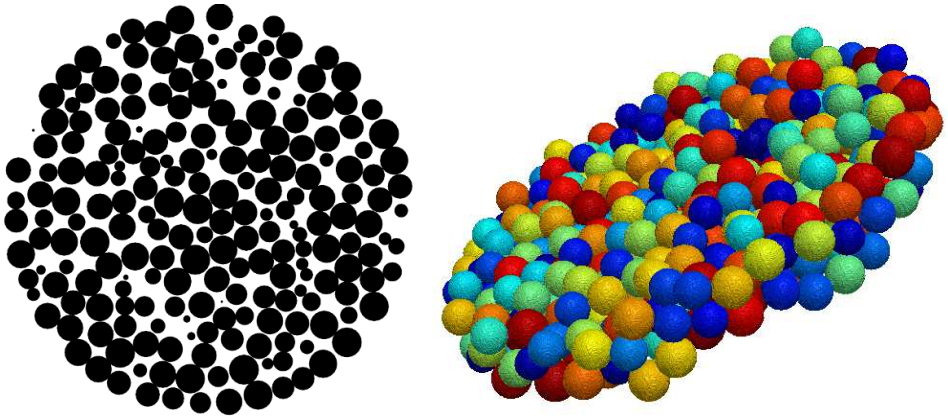


Fig 3.2. Two-dimensional (2D) and three-dimensional (3D) images of the virtual porous structure for pore sizes 2.0-2.5mm and 10μm capillary radius.

A representative model was created by converting the 2D slices into a 3D volume (Fig 3.2) within the ScanIP package of Simpleware™, a 3D image processing, analysis, and model generation software package. Thresholding of the images was carried out and then a smoothing function was applied on the three-dimensional volume to minimize facets created by the slicing process. A smart mask process (with 10 iterations) was preferred to a recursive Gaussian smoothing (RGS) operation as this more accurately preserved the imported geometry, in particular, the geometry of the windows (openings). A cubic representative volume element (RVE) that was 6 times the particle or pore radius was extracted from the center of the samples, the size of which was determined by shrinking a volume until the porosity differed by 2% from the initial (bulk) value (Fig 3.3).

This approach was compared to a more robust and highly computational approach to determine an RVE based on isotropic flow computations for a linear pressure variation (LPV), impermeable side wall (ISW) and solid side wall (SSW) boundary conditions with reasonable agreement to extract the RVE from the centre (>40% of the total volume) of the packed structures. Porosity and pore radius measurements were made within ScanIP module of Simpleware™ to ensure that the sphere dimensions and packing characteristics were a close representation of the DEM data.

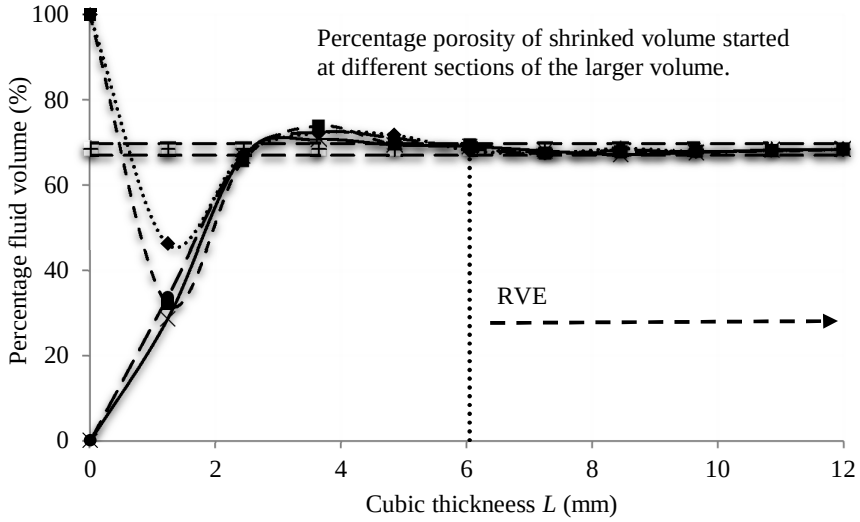


Fig 3.3. The plot of percentage fluid volume in metal foams (%) against cubic elemental thickness (mm) for determination of representative volume element.

Fig 3.4 presents the internal morphology of DEM structures of mean pore size, 2mm, and capillary radius, 10-80μm, between connecting particles (salt granules in realistic casting) created in ScanIP. The two-dimensional (2D) slice view in Fig 3.5 shows that an increase in coordination number (pore contacts) is attained by increasing the capillary radius in the sphere-packing (DEM) model (decreasing the infiltration pressure used during the "real" casting processes). At 10μm capillary radius, the DEM structure exhibits low contacts between the packed beads and increases progressively from 10 to 80μm. This is an indication that

the coordination number of contacting pores in a porous metal matrix is strongly dependent on the capillary interaction between connecting beads during its processing.

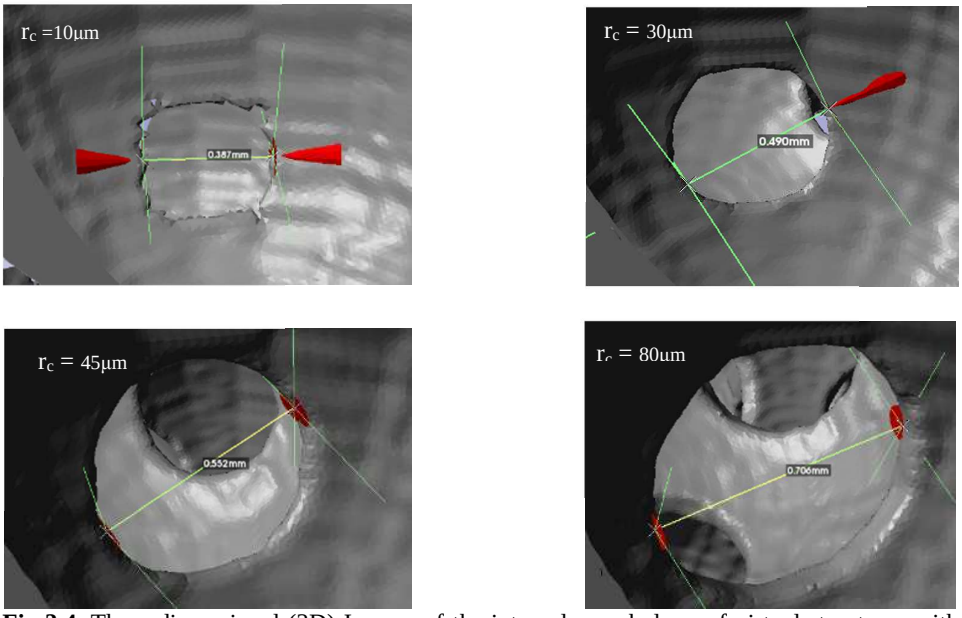


Fig 3.4. Three-dimensional (3D) Images of the internal morphology of virtual structures with 2mm mono-sized spherical for 10, 30, 45 and 80µm capillary radius.



Fig 3.5. Two-dimensional (2D) Images of the DEM virtual structures of uniform (2mm) pore sizes for a 10 and 80µm capillary radius.

Fig 3.6 presents images of the structures generated by DEM and that they closely replicate "real" structures as presented in the CT images in Fig 3.1. The key features are replicated viz. the typical number, size, and geometry of contacts. It is also clear from these images (taken from the same location) how increasing the capillary radius not only increases the size of the inter-particle contacts (window radius) but also the number of particle contacts (coordination number). It is

also apparent that for identical distributions (and packing fractions) of spheres, the porosity of the porous metal will increase (albeit slightly) with increasing capillary radius, owing to the reduced capacity for filling of the inter-sphere spaces.

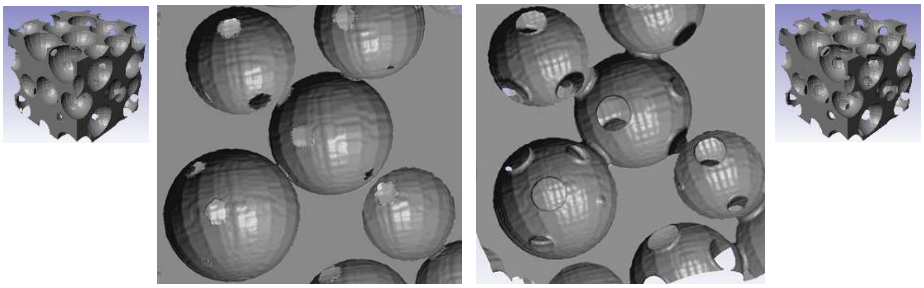


Fig 3.6. Images of DEM structure and RVE for different capillary radii (left) 10μm and (right) 80μm.

The importance of permeability in relation to the performance of porous structures cannot be overlooked. At a very low fluid velocity, the permeability of the porous material was reported in Dybbs and Edward, 1984 to strongly depend on the structural parameters and topology of the geometrical structure. Fig 3.7 presents the plot of dimensionless computed value of the permeability to the square of the pore size ratio (both for the isotropic and flow direction coordinates) against dimensionless RVE flow length to pore size ratio for a 2mm mean pore size DEM virtual spherical structures at a 10μm capillary radius. The plots of porosity and a specific surface (ratio structural surface area to bulk volume) against dimensionless RVE flow length to pore size ratio are presented in Fig 3.8.

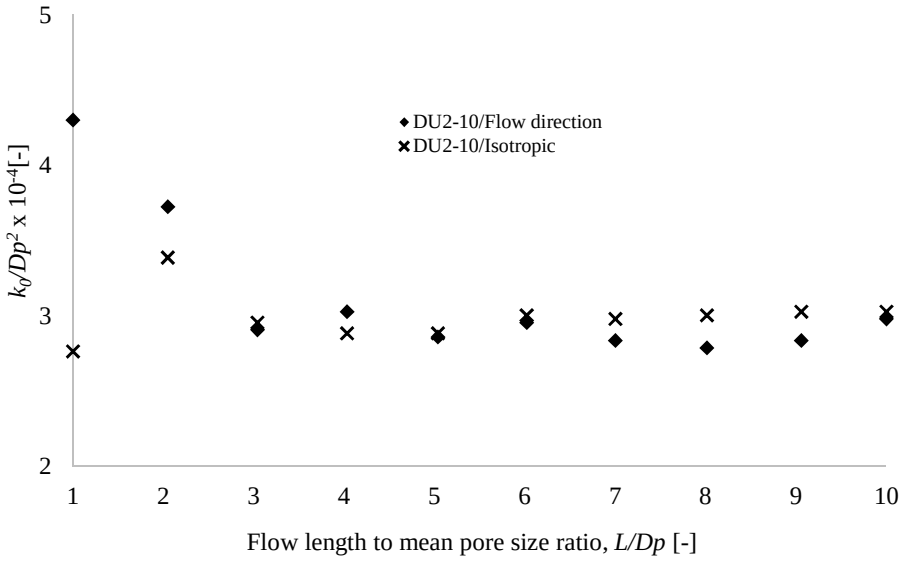


Fig 3.7. Plots of isotropic and flow directional representation of permeability to pore size ratio, k_0/Dp^2 [-] and against the dimensional flow length to pore size ratio (L/Dp) [-] for a virtual DEM spherically celled structure (pore size, 2mm, and capillary radius, 10μm).

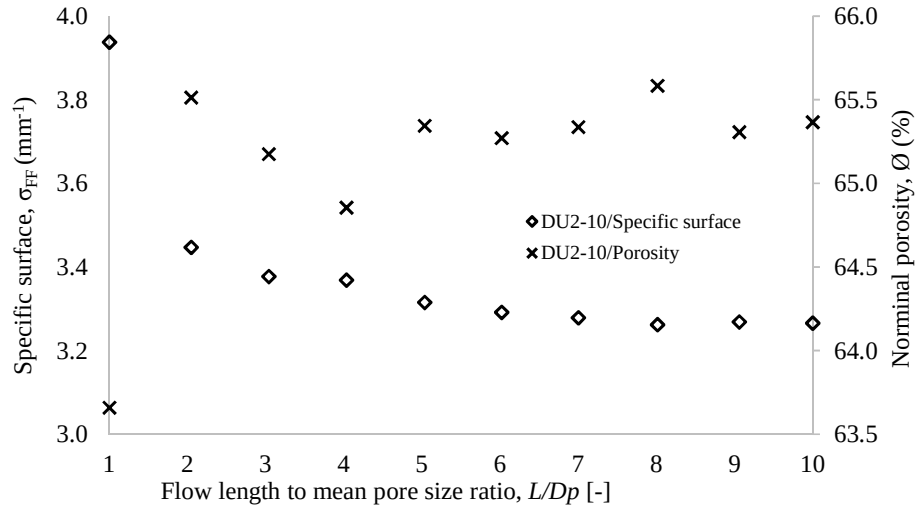


Fig 3.8. Plots of porosity (%) and a specific surface (mm^{-1}) against the dimensional flow length to pore size ratio (L/Dp) [-] for a virtual DEM spherically celled structure (pore size, 2mm, and capillary radius, 10μm).

For a chosen flow thickness 3x the mean pores sizes and beyond, reasonable and tolerable deviation of structural and flow parameters were observed when compared to large volume data typically 10x the mean pore sizes. In this range, the computed values of the mean openings, mean pore sizes, porosity, tortuosity,

specific surface (ratio of structural surface area to bulk or fluid volume, σ_{FB}) and permeability of the porosity matrix are 276±7μm, 2.04±0.02mm, 65.3±0.2%, 1.79±0.003, 3.3±0.05mm^{-1}, 1.21±0.05m^2. The significant variations in permeability for RVE flow length below 3x mean pore sizes is attributed to the changes in the structural parameters. This may be favourable computationally considering time and convergence but the lack of accurate capture of complete information necessary to represent the entire volume may deviate the modelling outcome from a realistic data. It is therefore important to choose a flow length 3x the mean pore sizes for characterizing the structural parameters needed for predicting flow behaviour of this material.

3.4 Simulation

Simulations were performed using the +Flow module in Simpleware™, using a built-in Stokes flow solver. The permeability in the flow direction was determined from the calculated pressure drops (the outlet pressure was set to zero) for a series of flow velocities (for water) in the laminar flow regime. Impermeable side wall boundary conditions were applied (the normal velocity component at the walls is constrained to zero) but for the RVE size chosen and for the reasonably symmetrical structures, a less than a 3% difference in the permeability was observed when either linear pressure variation or solid sidewall boundary conditions were applied (Fig 3.3).

Extensive scale-dependent and mesh-dependent studies were conducted to determine the optimum balance of mesh scale to convergence time and accuracy. A linear tetrahedral mesh (LTM) was used and to capture information in the

"bottleneck" areas the mesh growth rate was optimized leading to element counts of the order of 1.5-2.5million (Fig 3.9). Permeability values obtained in the same way using the CFD module in COMSOL Multiphysics 5.0^{TM} were within >95% agreement with the +Flow module.

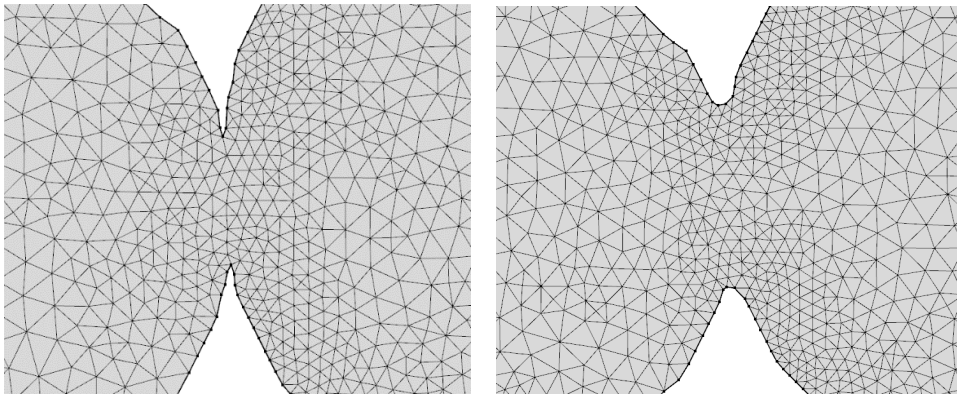


Fig 3.9. Two-dimensional images of meshed "bottleneck" zone of "virtual" porous structures for different capillary radii (left) 10μm and (right) 80μm.

Computational fluid dynamics (CFD) modelling was performed for structures constructed from monosized spheres that were 1, 2 and 3mm in diameter, for capillary radii between 10 and 80μm, leading to porosities between 60 and 68%, typical of structural characteristics that might be observed for porous metals made by salt bead replication using vacuum or low-pressure casting methods. Fig 3.10 shows the typical flow behaviour in these structures, for the same region but extremes of the capillary radius. Rate-controlling "bottleneck" flow is apparent through the windows between pores, highlighted by the regions of high velocity that correspond to the colour scale and which is also indicated by the velocity vectors. Streamlines that have been superimposed onto these plots show recirculation of fluid in "dead end" pores at the low capillary radius and that at high capillary radius the flow is less constricted as the interconnectivity of the pores increases.

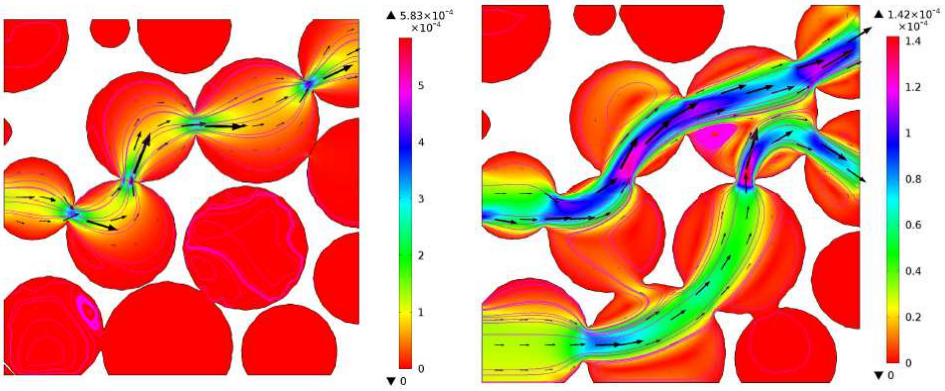


Fig 3.10. Representations of flow behaviour (surface fluid velocity scale and streamline for a 2μm.s^{-1} pore inlet velocity, v_p) on 2D DEM mono-sized slices for different capillary radii (left) 10μm and (right) 80μm [*Numerical scales unit for the legends measured in m.s^{-1}*].

3.5 Results and discussion

Fig 3.11 plots the ratio of the CFD permeabilities to those predicted by Eq 1.1, using data for porosity, coordination number, and window radius derived from the Matlab code, against the normalized capillary radius. It should be noted that for $r_c/r_p > 0.016$, the agreement between the two is good, with on average, CFD predictions being 3% higher. Below this ratio (for large pore sizes and small capillary radii), the CFD predictions for the permeability increase more rapidly than those for the model and this most likely indicates that these conditions stretch the capacity for accurate geometrical construction and smoothing (reflected by more jagged-edged pores in Fig 3.6). It is expected that at very much higher r_c/r_p ratios than those investigated in this study, realistic geometries might also be difficult to produce as neighbouring windows start to overlap.

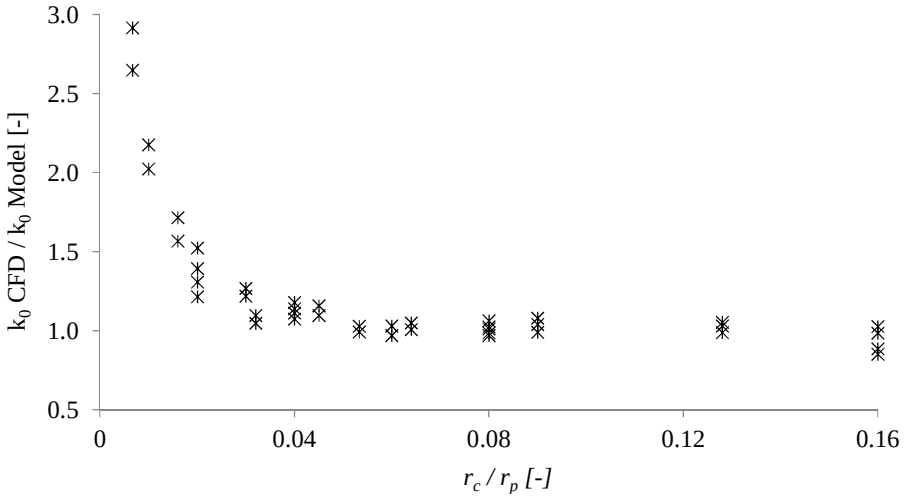


Fig 3.11. The influence of normalized capillary radius on the ratio of CFD to modelled permeability.

Fig 3.12 shows how significantly the virtual porous structure changes with capillary radius for 2mm diameter spheres with a nominal packing fraction (and thus porosity) of 60% (which increases to 61% for the highest capillary radius). It can be seen that the window radius more than doubles over the range of capillary radii investigated and that the coordination number increases much more significantly than for the very small change in packing fraction that would be predicted by the N_C expression in Eq 1.1 (although for constant capillary radius, changes in porosity lead to increases in coordination number that are consistent with those predicted by Eq 1.1. If N_c is determined from the porosity alone, using Eq 1.1, CFD predictions are still in reasonable agreement, overestimating the model by, on average, < 20%. The model in (Furman et al., 2013) was found to underestimate experimental and CFD data for the permeability of structures made at low pressure (high capillary radius) and it is likely that neglecting the strong effect of capillary radius on the coordination number contributes strongly to this discrepancy.

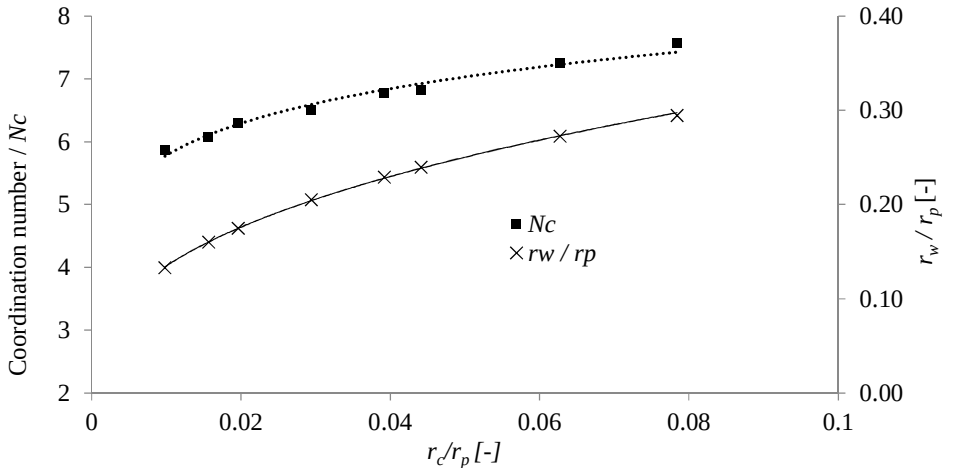


Fig 3.12. The influence of normalized capillary radius on the ratio of structural parameters.

For comparison, CFD simulation was performed on a 3D model constructed from a series of 2D CT slices taken of a porous metal made by infiltration of near-spherical beads, 2.0-2.5mm in diameter, at 0.9bar (reported in Langston and Kennedy, 2014). From the average window diameter in this structure (180μm in Langston and Kennedy, 2014), closest agreement with DEM-derived virtual structures is for those generated with capillary radius values between 10 and 20μm. The permeability of the CT structure was $1.14\times10^{-9}m^2$, for equivalent DEM-derived structures with capillary radius values of 10 and 20μm, they were 1.09 and $1.48\times10^{-9}m^2$, showing excellent agreement between flow simulation in "real" and "virtual" structures. Experimental measurement of the permeability in the laminar flow region for this same sample, using a variable head permeameter like that used in (Furman et al., 2013), yielded values of $1.28\pm0.09\times10^{-9}m^2$ (Njoku, 2014), confirming a good correlation between flow simulation and experimentation.

3.6 Extension to binary-sized structures

To vary widely packing density of the mono-sized structures for particle sizes between 2.0 and 2.5mm, spherical structures with particle sizes between 0.5 and 1.0mm were introduced into the larger sized structures to see what benefit therein. Images and CFD numerically simulated (using similar procedure thereof) values of pressure drop and permeability data of these binary-sized structures using the sphere-packing models are presented in this section.

For capillary radius, r_c, typically between 10 and 80μm, packing densities in the ranges of 63-64%, and 68-75% were achieved for both the monosized (L-L) and mixed-sized (L-S) packed structures respectively. Fig 3.13 shows the relationship between the average window radius, r_w, and capillary radius, r_c, for these structures representing contacts made by packed beds of L-L (2.0-2.5mm), and a 25vol% addition of smaller sized beads (0.5-1.0mm) in larger ones (L-S). For the DEM monosized (DU) and mixed-sized (DN 25%S) packing arrangements, their average window radius (r_w) representing the mean value of the windows formed by connecting pores shows a 2nd order polynomial relation against increased capillary radius shown in Fig 3.13. The increase in the permeability of the structures is attributed to the simultaneous widening in the "bottleneck" region of these structures coupled with increasing contacts between connecting pores (coordination number, N_C) as capillary radius increases for all packings. This represents the effects on reducing the applied liquid infiltration pressure during realistic casting of porous metallic structures.

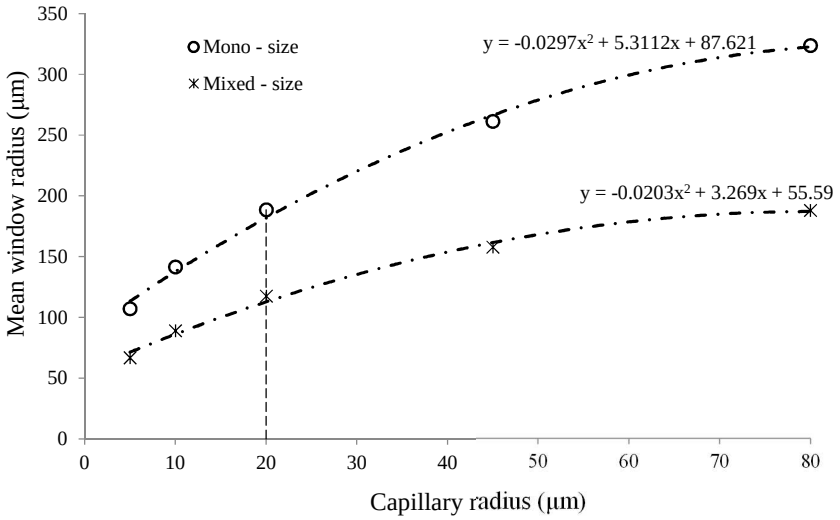


Fig 3.13. Plots of mean window radius, r_w, (µm) against capillary radius, r_c, (µm) for a mono-sized (2.0-2.5mm) and binary-sized (25vol%S) DEM packings.

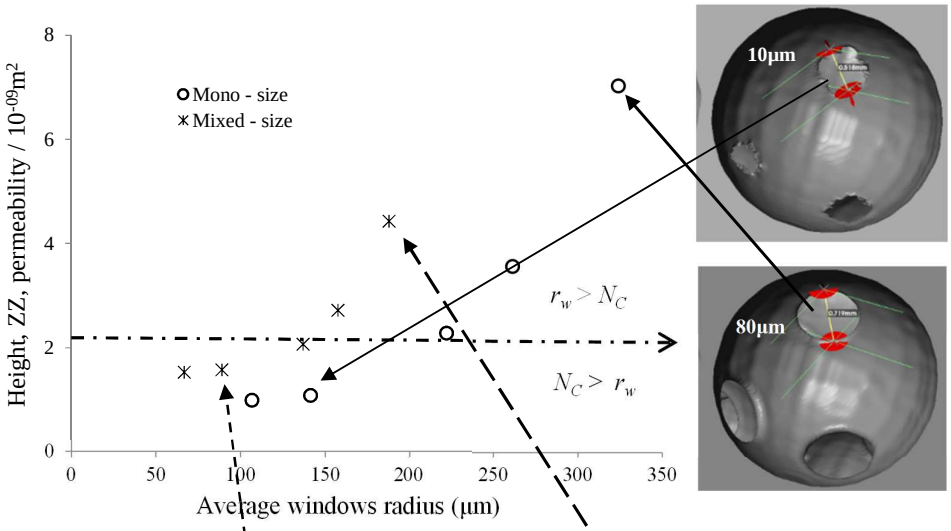
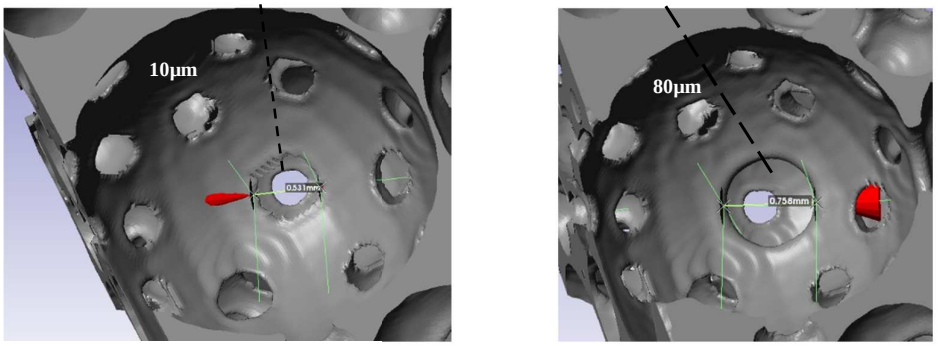


Fig 3.14: Plots of unidirectional permeability $k_0/10^{-09}m^2$ against mean window radius (µm) for mono-sized (DU) and 25vol%S mixed-sized (DN) structures and their images for a 10 and 80µm capillary radii.



In Fig 3.13 and Fig 3.14, within the specified ranges of the mean pore diameter openings (windows) obtained for both packings, it is precise to say that the increased particle contacts and packing density created by the mixed-sized (L-S) structures have significant effects on the flow behaviour of the "virtual" porous structure. For a similar value of capillary radius, the mean window radius of the monosized (L-L) structure is larger than the mixed-sized (DN 25%S) but the number of contacts created by the latter outweighs that of the former (monosized packings) and thereby contributes more to its flow and overall surface area. However, this statement is only valid for capillary radius less than 30μm (higher infiltration pressure in realistic casting process). For capillary radius greater than 30μm (low infiltration pressure in real casting), the large windows size exhibited by the L-L structure outweighs the excessive degree of contacts offered by the L-S in terms of its contribution and resistance to the flowing fluid.

The homogeneous addition and mixing of small and large sized beads DEM packing (DN25%S) causes significant changes structure-related and flow parameters of the porous medium as shown in Table 4.1. Fig 3.15 and 3.16 present three-dimensional images of the numerically simulated velocity ($m.s^{-1}$) and pressure (Pa) plots data of an incompressible fluid (water at density, $997.78kg.m^{-3}$, and dynamic viscosity, $9.772x10^{-4}$ Pa.s) for the "virtual" monosized and 25vol%S mixed-sized structure for a pore inlet velocity of $2.5mm.s^{-1}$. This indicates a lower pressure drop per unit length of $1150Pa.m^{-1}$ achieved for the mixed-sized structure due to the low resistance (ligament thickness) offered by this virtual structure when compared to the monosized structure (top) with a unit pressure drop of $1704Pa.m^{-1}$.

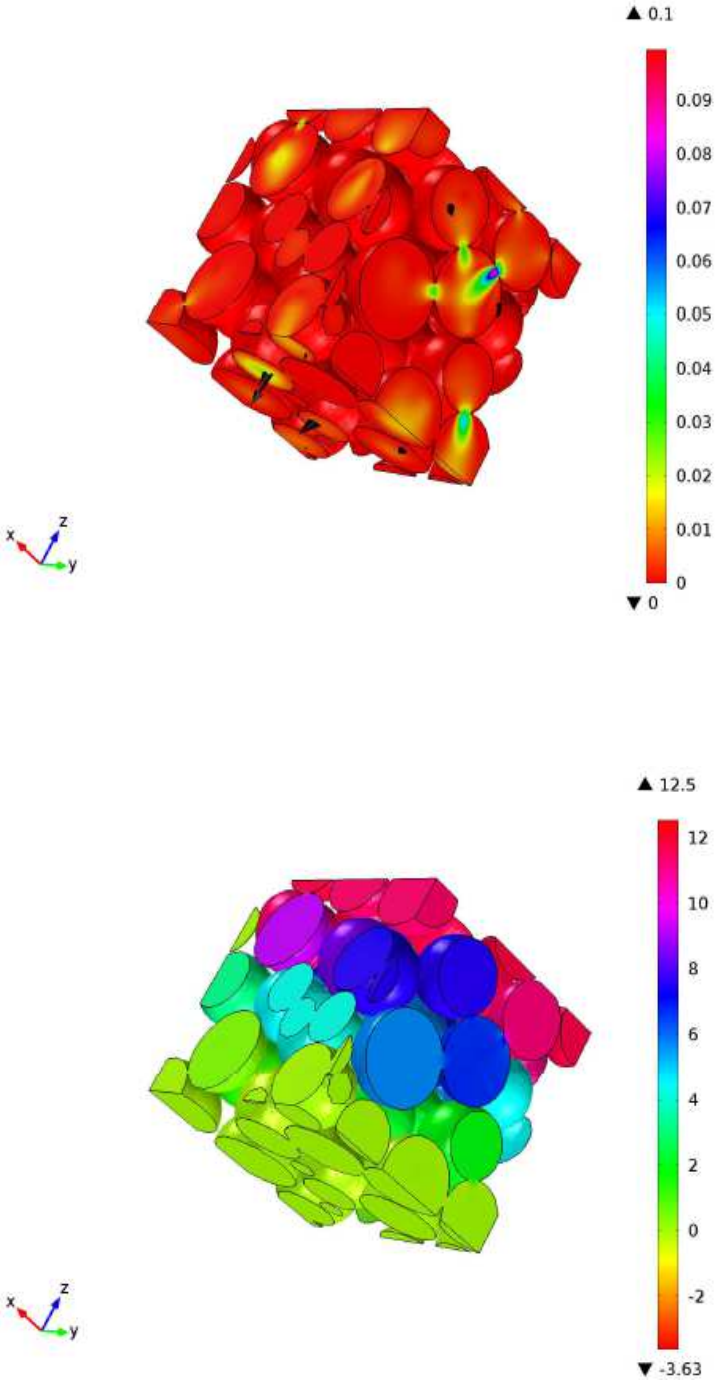


Fig 3.15. Three-dimensional (3D) numerically simulated velocity (top) and pressure (bottom) profile plots for water flow across the monosized (2.0-2.5mm) virtually-packed structures for a pore inlet velocity of 2.5mm.s^{-1} [*Numerical scales unit for the legends measured in m.s^{-1} and Pa both for the velocity and pressure plots respectively*].

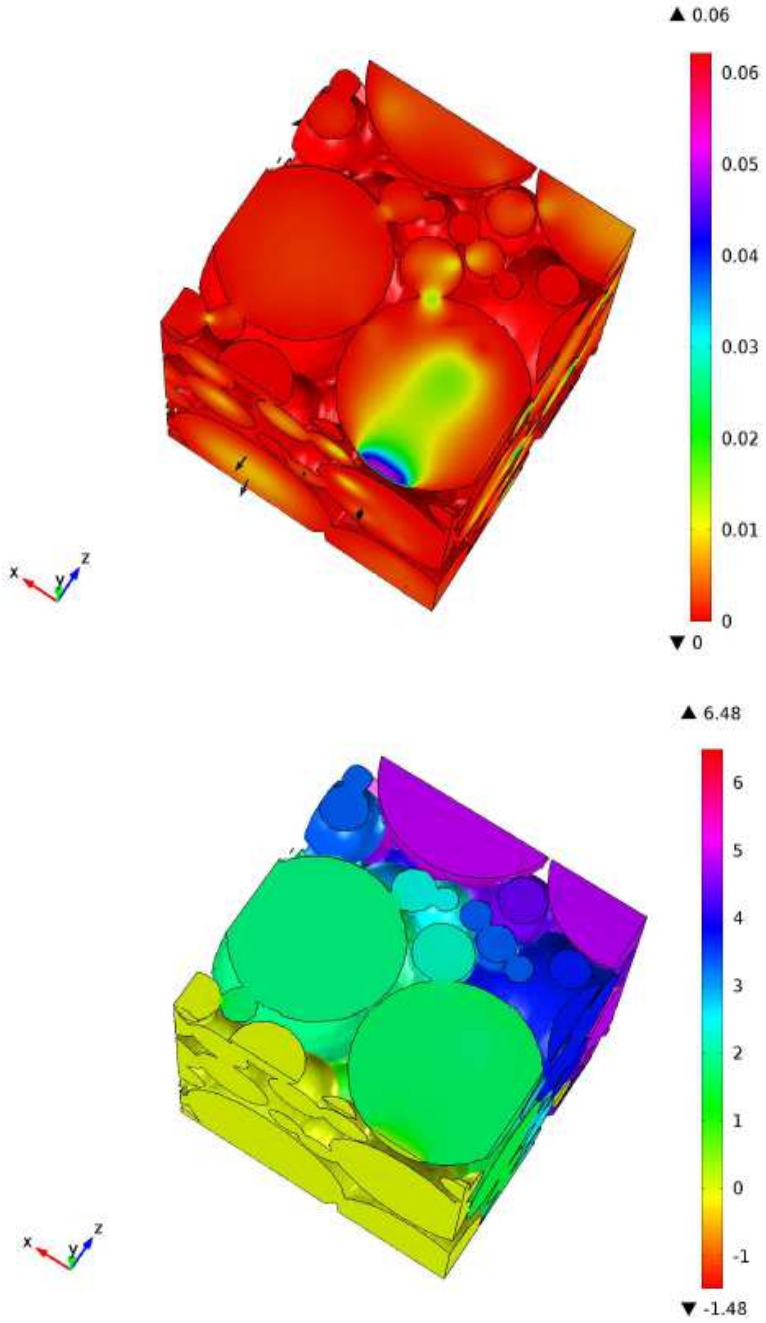


Fig 3.16. Three-dimensional (3D) numerically simulated velocity (top) and pressure (bottom) profile plots for water flow across the 25vol%S mixed-sized virtually-packed structures for a pore inlet velocity of 2.5mm.s^{-1} [*Numerical scales unit for the legends measured in m.s^{-1} and Pa both for the velocity and pressure plots respectively*].

Fig 3.17 and Fig 3.18 presents the unit pressure drop against superficial fluid (water) velocity for the monosized and mixed-sized packing arrangements at Darcy and Darcy-Forchheimer regimes respectively. At extremely low

velocities in Fig 3.17, typically below 0.5mm.s^{-1}, losses were mainly due to skin friction (Dybbs and Edward, 1984, and Boomsma and Poulikakos, 2002) and pressure drop across these structures was observed to be linearly dependent on the flow velocity. Beyond this velocity (Fig 3.18), the onset of inertia was observed (viscous forces are negligible while contraction and enlargement become imperative) and can be described by the Darcy-Dupuit-Forchheimer second order polynomial fitting of curves using Eq 2.15. Within this range of velocities, the results look promising as it follows the quadratic trend of relation achieved for experimental and X-ray CT computations of pressure drop per unit length of fluid flow through porous media available in the literature (Tadrist et al, 2004; Lacroix et al., 2007 and Dukhan et al., 2014). More so, the addition of smaller sized-sized structures help creates extra windows and increases flow across the structures. With this, structures made from mixed-sized packings are expected to be more complicated and the pattern of fluid flow through it would behave differently from that of monosized pores.

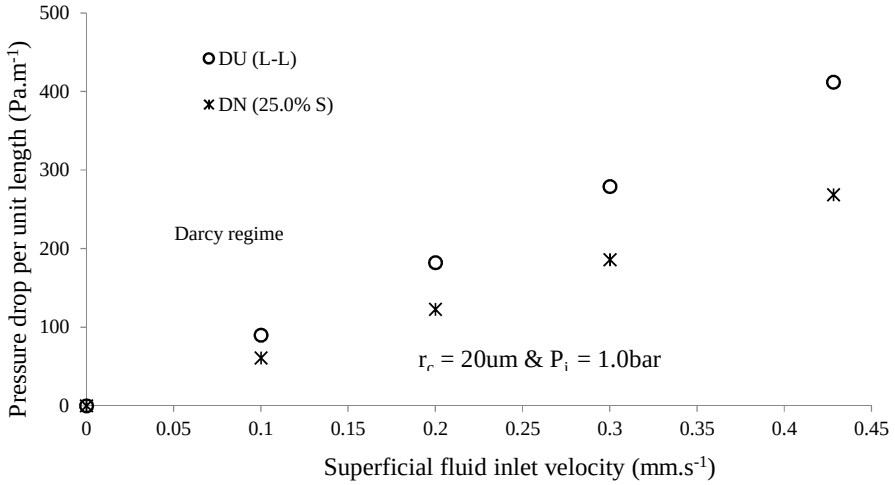


Fig 3.17. Plots of unit pressures pressure drop (Pa.m^{-1}) against superficial fluid (water) velocity (mm.s^{-1}) for the monosized and 25vol%S mixed-sized DEM structures at Darcy regime.

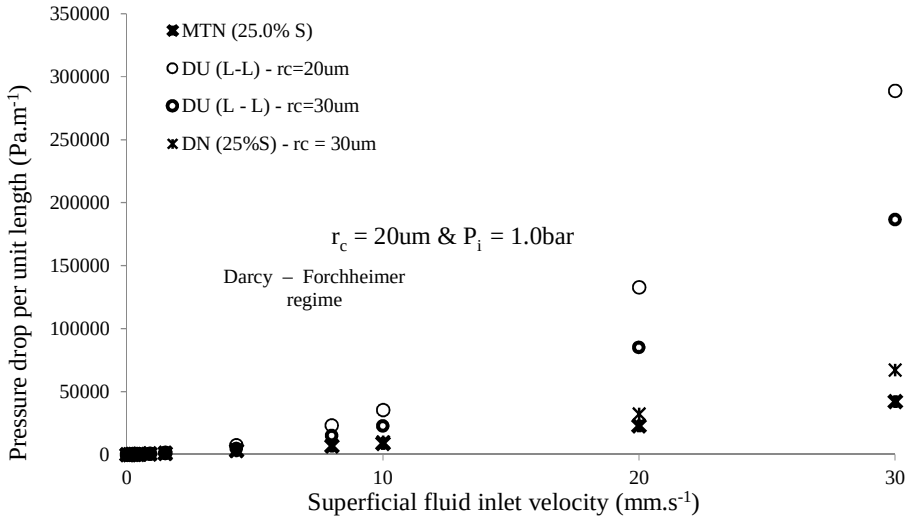


Fig 3.18. Plots of unit pressures pressure drop (Pa.m^{-1}) against superficial fluid (water) velocity (mm.s^{-1}) for the monosized and 25vol%S mixed-sized DEM structures at Darcy-Forchheimer regime.

A tabular representation of structural and flow data for these structures are presented in Table 3.1. This shows that increase in permeability of fluid flow is attained from low to high degree of capillary radius resulting in increased particle contacts and openings (dictating the flow) made by connecting pores within the porous matrix. High-pressure drops and low permeability were achieved for DEM packed structures at a capillary radius of 20μm which is a negative of what is achieved for the near-spherical packed structure at highest capillary radii of 80μm. This is mainly because small size windows which distort the permeation of fluid are created for smaller capillary radius and thereby causing significant resistance to the flow of fluid. The size of the windows and the degree of contacts between the structures eventually dictate the flowing fluid through it. The size of the windows created by the L-L structure outweighs that of the smaller sized (S-S) structure and this is the reason for its high permeability and low-pressure drop developed. High pressure drops over this near-spherical foam replicated structure is associated with high superficial velocity and that the

pressure drops across this structure decreases in the direction of fluid flow (Darcy, 1856).

Table 3.1. Structural and flow data for DEM and µCT mono-sized, L-L, and mixed-sized, L-S, structures.

Sample type		r_c (um)/*Pi*	*Dp* (mm)	r_w (um)	Porosity, Ø (%)	Darcian permeability $k_0/ 10^{-09}m^2$
(L – L)	DU(L-L)	10	2.290	141.585	63.462	1.034
	DU (L-L)	20	2.270	188.615	63.581	1.470
	DU (L -L)	30	2.290	222.285	63.505	1.952
	DU (L-L)	80	2.360	323.864	64.058	6.158
(L – S)	DN (6.25%S)	20	1.142	147.143	68.878	2.742
	DN (12.5%S)	20	0.866	131.390	71.884	3.175
	DN (18.25%S)	20	0.854	122.807	74.029	3.243
	DN (25.0%S)	20	0.831	117.540	73.933	1.866
	DN (25.0%S)	30	0.831	137.179	74.009	1.979
	DN (31.2%S)	20.0	0.807	113.597	75.974	3.027
	DN (37.5%S)	20.0	0.792	110.320	74.286	2.426
	DN (50.0%S)	20.0	0.779	106.049	75.404	3.176
(S – S)	DU (S - S)	20.0	0.753	97.519	66.079	0.388

To further substantiate the impact of structural variations on the flow performance of the binary-sized structures, numerical simulation of the permeability of these structures was studied by varying the capillary radius of the sphere-packing model, typically between 10 and 80µm, capable of replicating by the casting process. Also, the volume of the smaller-sized structures in larger ones was varied between 6.25-50 vol%. Fig 3.19-3.26 present a 2D streamline and arrow velocity profile plots for the mixed-sized packings (6.25 - 100vol %) for a 20 and 80µm capillary radii and superficial fluid inlet velocity, $2.5mm.s^{-1}$. Pressure drop across these structures was observed to decrease in the direction of the flow and high within the "bottleneck" zones of the structures as indicated by the intensity of the colour scales in the Figures below.

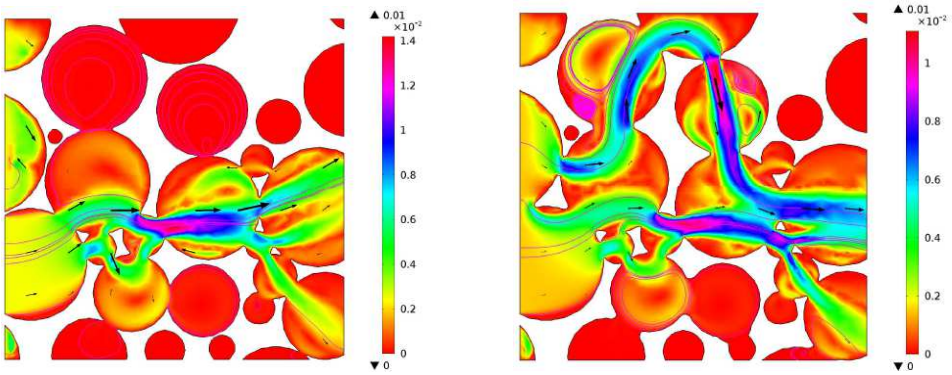


Fig 3.19. Representations of flow behaviour (surface fluid velocity scale and streamline for a 2.5mm.s^{-1} pore inlet velocity, v_p) on 2D DEM binary-sized (6.25 vol%S) slices for different capillary radii (left) 20µm and (right) 80µm [*Numerical scales unit for the legends measured in m.s^{-1}*].

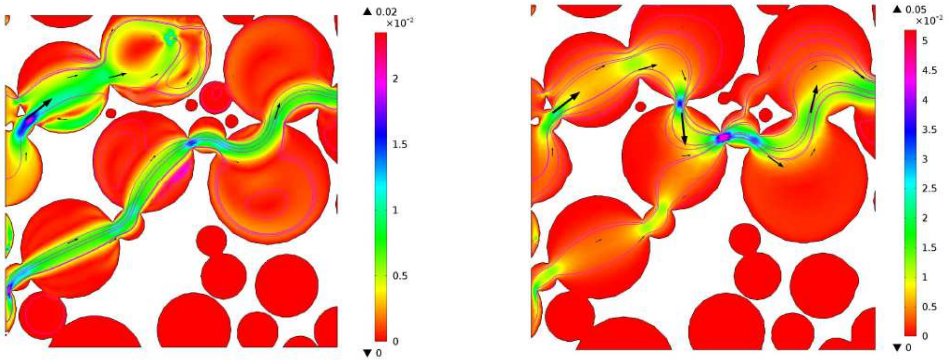


Fig 3.20. Representations of flow behaviour (surface fluid velocity scale and streamline for a 2.5mm.s^{-1} pore inlet velocity, v_p) on 2D DEM binary-sized (12.5 vol%S) slices for different capillary radii (left) 20µm and (right) 80µm [*Numerical scales unit for the legends measured in m.s^{-1}*].

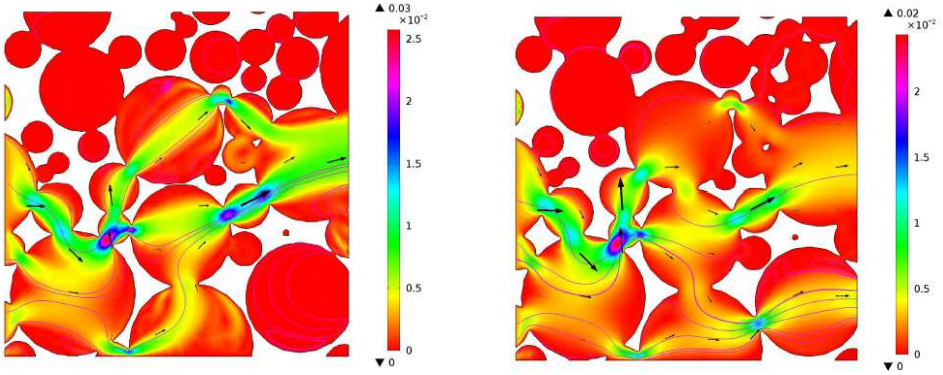


Fig 3.21. Representations of flow behaviour (surface fluid velocity scale and streamline for a 2.5mm.s^{-1} pore inlet velocity, v_p) on 2D DEM binary-sized (18.25 vol%S) slices for different capillary radii (left) 20µm and (right) 80µm [*Numerical scales unit for the legends measured in m.s^{-1}*].

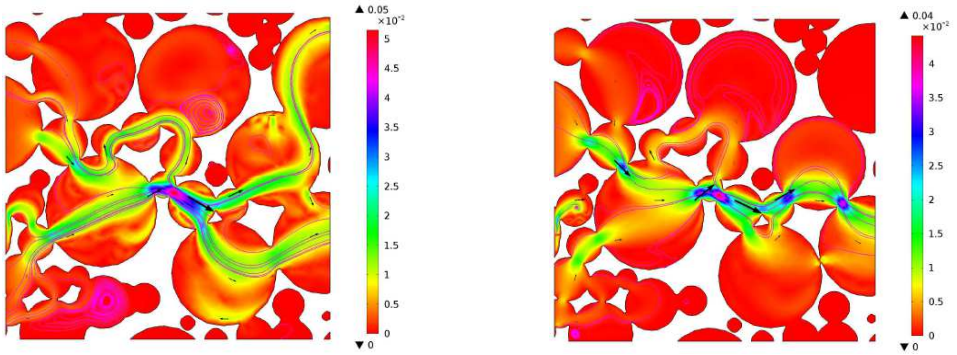


Fig 3.22. Representations of flow behaviour (surface fluid velocity scale and streamline for a 2.5mm.s^{-1} pore inlet velocity,v_p) on 2D DEM binary-sized (25.0 vol%S) slices for different capillary radii (left) 20µm and (right) 80µm [*Numerical scales unit for the legends measured in m.s^{-1}*].

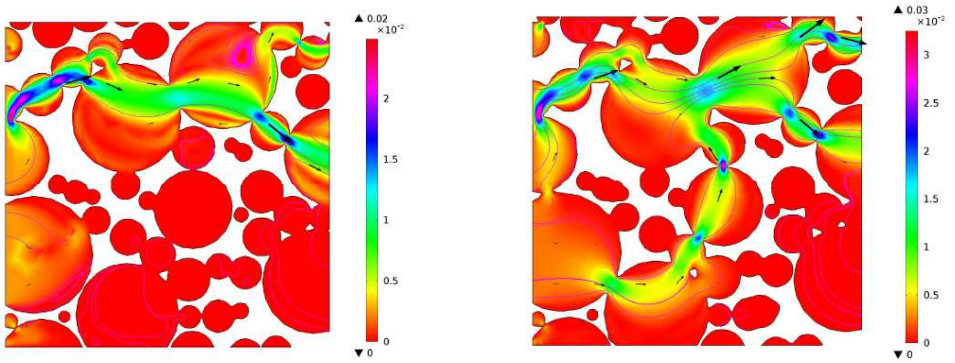


Fig 3.23. Representations of flow behaviour (surface fluid velocity scale and streamline for a 2.5mm.s^{-1} pore inlet velocity,v_p) on 2D DEM binary-sized (31.2 vol%S) slices for different capillary radii (left) 20µm and (right) 80µm [*Numerical scales unit for the legends measured in m.s^{-1}*].

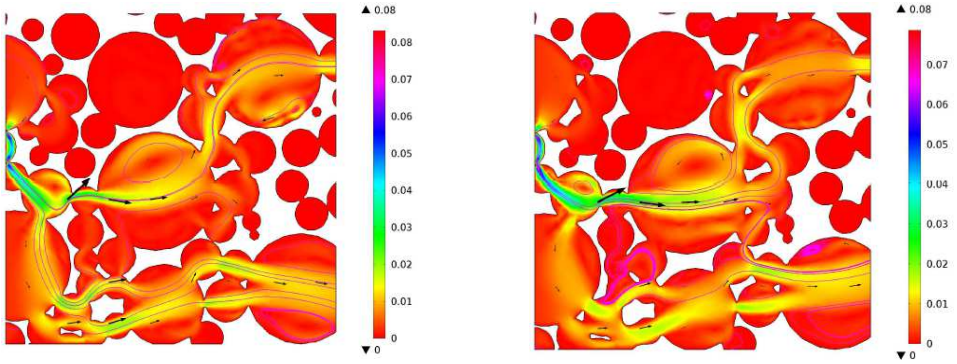


Fig 3.24. Representations of flow behaviour (surface fluid velocity scale and streamline for a 2.5mm.s^{-1} pore inlet velocity,v_p) on 2D DEM binary-sized (37.5 vol%S) slices for different capillary radii (left) 20µm and (right) 80µm [*Numerical scales unit for the legends measured in m.s^{-1}*].

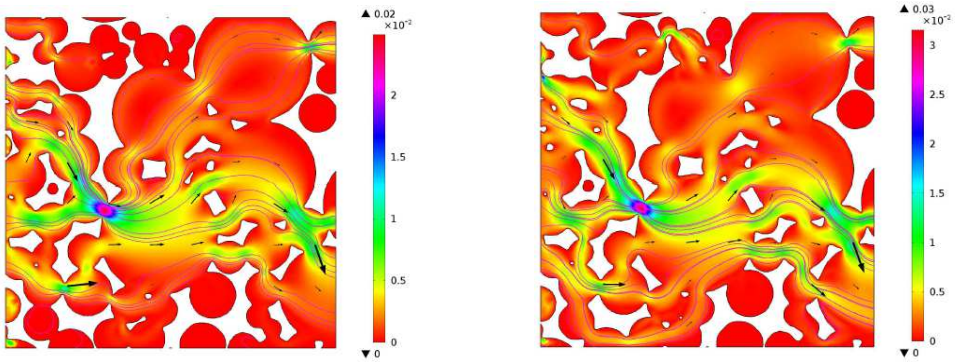


Fig 3.25. Representations of flow behaviour (surface fluid velocity scale and streamline for a 2.5mm.s^{-1} pore inlet velocity,v_p) on 2D DEM binary-sized (50 vol%S) slices for different capillary radii (left) 20µm and (right) 80µm [*Numerical scales unit for the legends measured in m.s^{-1}*].

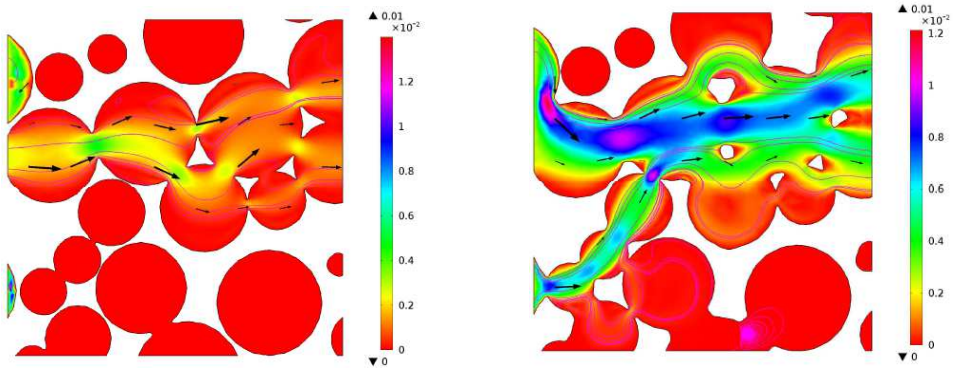


Fig 3.26. Representations of flow behaviour (surface fluid velocity scale and streamline for a 2.5mm.s^{-1} pore inlet velocity,v_p) on 2D DEM binary-sized (100 vol%S) slices for different capillary radii (left) 20µm and (right) 80µm [*Numerical scales unit for the legends measured in m.s^{-1}*].

Fig 3.27 and Fig 3.28 present the coordination numbers, N_C, (at 10µm capillary radius) and permeabilities, k_0, (Darcy regime) computed (capillary radii 10-80µm) for DEM spherical packed monosized (L-L & S-S) and binary-sized, L-S, structures.

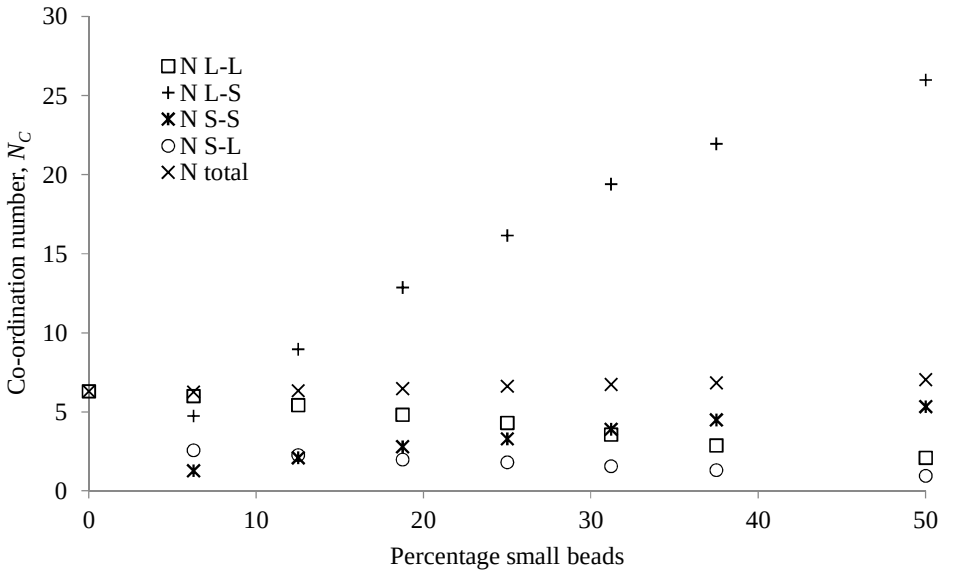


Fig 3.27. Plots of coordination number, N_C, against percentage various (0-50vol%) addition of binary-sized spherical packings for a 10µm capillary radius.

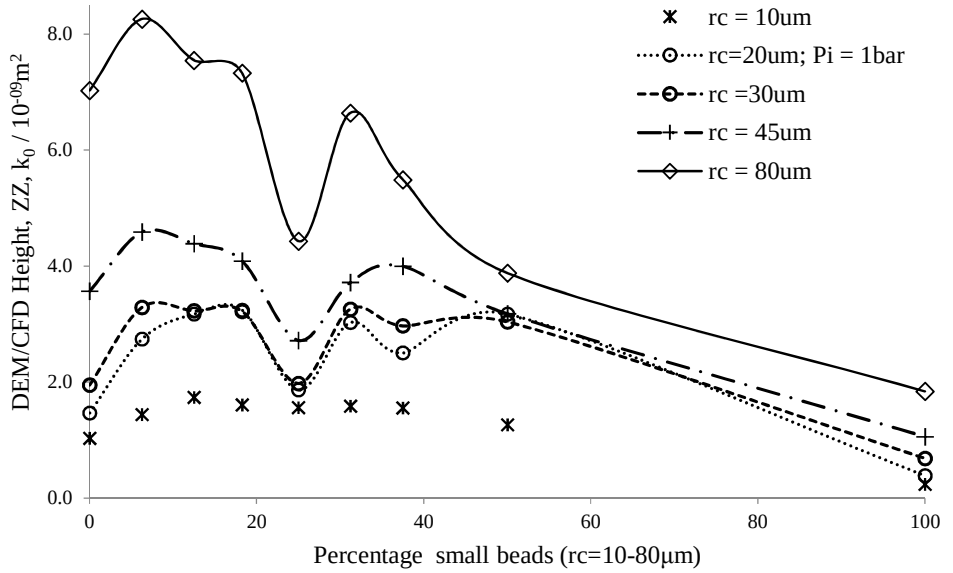


Fig 3.28. Plots of Darcian permeability, $k_0/10^{-09}m^2$, against percentage various (0-50vol%) addition of binary-sized spherical packings for capillary radius between 10-80µm.

The increased connectivity openings offered by the 100vol% monosized (L-L) structure enabled more fluid to permeate through it and resulting in the higher value of permeability than that of 100vol% small sized, S-S, structure. Continues addition of smaller sized beads into larger ones creates more openings, increases the coordination number and packing density (fluid volume) of L-S structure

and decreases the possible contacts made this structure (Fig 3.27). This reduces the mean openings but the improved contacts between connecting pores within the microstructural arrangement to an extent ($\leq$ 18.25 vol%S for capillary radii between 10 & 20μm), increases the permeability of the virtual porous matrix (Fig 3.28).

A typical example of this is to compare the structural variation of the L-L and L-S structures for the initial introduction of the 6.25vol% smaller sized spherical structures, DN (6.25%S), presented in Table 3.1. For a 10μm capillary radius, computed values of the mean openings, porosity, and Darcian permeability are 142μm and 111μm, 63.5% and 68.0%, and $1.04x10^{-09}m^2$ and $1.44x10^{-09}m^2$ for the L-L and 6.25vol% L-S structures respectively. Similarly, the porosity and permeability of the 12.5vol% L-S virtual structure increases to 70.6% and $1.75*10^{-09}m^2$ respectively. Above this 12.5%volume addition, a decline in permeability is observed due to smaller windows created by the more S-S contacts and a decrease in the contacts between the L-L structures. For this capillary radius of 10μm, a region of stability is recorded between 25-37.5% additions of smaller-sized beads due to the minimal differences in their average coordination number of the structure (Fig 3.27). The offset created by the increase in the coordination number of L-S is balanced by the decrease in that of S-S and L-L. Excessive increase in the percentage volume of S-S above this region ($\geq$ 37.5vol %) further decreases the permeability of the porous structure. Despite an increase in the coordination number of S-L, the reduction in the contacts made by L-L and S-S structures causes a decrease in their openings (increased ligament thickness) indicating a high foam surface area and low foam permeability (Fig 3.28). Lastly, the observable dip in the permeability curve at

25vol% packing addition is attributable to the combined low mean diameter openings and porosities of these structures for most of the packing arrangements as evidence in Table 3.1.

Any of the sphere-packing arrangements allows the manipulation of its capillary radius to achieve desired macroscopic parameters useful for specific engineering design of "bottleneck-type" structures for optimum performance. In realistic casting, a porous metallic structure produced at very low infiltration pressure, typically, ¼ bar (high capillary radii, 80μm for virtual packing), has the potential of having extremely large openings in its structural phase, offering minimal resistance to the passage of fluid. Such high-density structure may not support engineering applications where strength and structural rigidity are essential but is useful for low weight applications. However, the visually fascinating low-density porous structures has the potential of being used as an impact energy absorption (Cho et al., 2012) and excellent mixing (T'Joen et al., 2010) of fluid due to its low tortuous path with reduced resistance to flowing fluid.

In contrast, foam replicated structures produced at very high infiltration pressure ($\geq$ 0.9 bar) through the manipulation of DEM packing of smaller sized beds (S-S), or the larger sized (L-L), monosized structures offered high ligament widths with greater resistance to the flowing fluid. Such foam type isn't good for engineering application where continuous movement of fluid is imperative but useful for high-impact applications.

3.7 Conclusions

Experimental measurements and CFD modelling of CT images of real structures demonstrate that, the DEM/CFD approach is capable of creating realistic porous metal structures with monosized cells. The good correlation between the output from the DEM/CFD process and the analytical models substantiates the "bottleneck" flow concept developed in these models and the resulting high dependence of the permeability on the size of the windows connecting the pores. However, there are other contributing factors such as porosity, pore diameter sizes, and packing arrangements. This also highlights the importance of accurate representation of the coordination number, which is a complex function of several parameters and not easy to measure by microscopy or from CT images, if the analytical models are to be accurate.

It is in this light that a precision measurement and CFD modelling using tomography images and sphere-packing models to account for the pressure drop developed across the "real" porous metallic structures is recommended for study. This approach could prove useful in the design of porous absorbers in loudspeaker; to quantify the permeability of porous materials needed for sound absorption modelling.

CHAPTER 4

MEASUREMENT AND NOVEL SIMULATION OF AIRFLOW THROUGH POROUS ALUMINIUM FOAM STRUCTURES WITH SPHERICAL CELLS

4.1 Summary

In this chapter, experimental measurement and pore-scale numerical simulation of airflow across open-celled aluminium foam structures with near-spherical cells varying in pore sizes and interstices are presented. The aluminium foam structures were produced by infiltrating liquid aluminium metal into packed beds of near-spherical hydro-soft salt beads (produced in the University of Nottingham, United Kingdom) varying in particle sizes, packing densities and infiltration pressures.

Airflow through this structure was studied in an experimental set-up assembled to accurately measure air pressure-drops against a superficial inlet fluid velocity. High-resolution (26μm voxel size) X-ray computerized tomography (μCT) and discrete element simulation packing of near-spherical structures (DEM) were used to produce 2D images of the porous matrix adopting the pore-level technique. Image processing, watershed segmentation, and smoothing were carried out on a 3D representative fluid volume of the porous structure whilst the well-known Navier-Stokes equation was solved on an optimized linear tetrahedral mesh matrix for laminar flow of air. The viscous terms of these structures were observed to greatly depend on the connectivity of the connecting pores while the inertial terms depend on their porosity, strut thickness, surface roughness and fluid velocity. By varying the porosity and bottleneck of the "virtual" structures, a less than 10 percent tolerable deviation from the reality of

computed flow data was achieved whilst that obtained using tomography images lies in the purview of 0.2-0.8%. Thus, this highlights the non-homogeneity effects of the structure in which the X-ray CT images provide a more visceral assessment of the porous matrix but also providing a near-realistic description using the "virtual" structures to predict the flow behaviour of these "bottleneck-type" materials. Lastly, theoretical models to predict the viscous (permeability) and inertial (Form drag coefficient) terms as a function of structural parameters were developed through structural erosion of the CT structures to provide "semi-virtual" structures and this can be used to aid the design of porous material with novel attributes.

NB: A full article on the airflow measurement and CFD modelling using CT images has been published in Acta Materialia (Click on the link https://doi.org/10.1016/j.actamat.2018.02.051) and there are potential for more papers from this chapter.

4.2 Introduction

Engineers and scientists in the past have determined the permeabilities of many soils and sands varying in degree of particle sizes and interstices measured in Darcy (D) or milliDarcy (mD) to avoid the intricacy of prefixes like terms (10^{-09}, 10^{-10}, 10^{-11}, 10^{-12}). The numerical value of permeability, k_o, measured in the horizontal or vertical plane for a given packed beds of rocks depends on the degree of its particle sizes and interstices (Zimmerson, 2003) and the addition of correction factor, Kozeny constant, (Kozeny, 1927, Carman, 1937, Karimian and Straatman, 2008, Liu and Hwang, 2012 and Ozgumus et al., 2014) was proposed to bridge the gap between analytical model and reality due to the anisotropic and complicated tortuous flow paths of the porous medium.

While packed beds are often made from packing of naturally occurring rocks and sands, artificially-made porous structures made from metals and alloys such as metal foam (aluminium, nickel, titanium, copper, steel etc) are remarkably useful as structures that interact with a fluid in processes like sound absorption, filtration and catalysis, heat exchange and storage etc. An important feature of this structure is the resistance provided by its skeletal configuration when presented to flowing fluid across the pores and interstices of the porous matrix, often described by the unit pressure drop developed across the inlet and exit of the structure as a function of superficial fluid velocity and properties of the fluid. Measuring or estimating and controlling the unit pressure drop is imperative to the design of porous metallic structures with enhanced performance.

Flow through open-celled metallic foams (Fig 1.2) is more complicated by the opening of its windows or interconnection of its pores (Habisreuther et al., 2009). This interconnection in porous metal foam enabled its high porosity, permeability, large foam surface area per unit bulk volume (specific surface) and thermal conductivity (Ranut et al., 2013, and Dukhan et al., 2014) which has made it beneficial for use as pressure reduction and heat transfer devices (Ranut et al., 2013). Understanding the behaviour of fluid flow through this structure with open porosities between 80-95% has been proven experimentally by Innocentini et al. (1999), Tadrist et al. (2004), and Oun and Kennedy (2014). The unidirectional (horizontal) flow permeability and inertial coefficient were calculated by fitting the pressure-velocity data into the Hazen-Dupuit-Darcy (Darcy-Forchheimer) second order polynomial model (Eq 4.1) with $\nabla P, k_o, \rho \,\&\, C$ described as the pressure drop per unit foam thickness, L, Darcian permeability, fluid density and the Form drag coefficient respectively. The

pressure drop per unit foam thickness (∇P) in the Phillipe Forchheimer model can be expressed solitarily in the first term of the LHS of the equation only at very low velocities (Darcy regime) where losses are mainly due to skin friction whilst the second term predominates at high velocities (laminar-turbulent regime) where viscous forces are negligible while contraction and enlargement are significant (Harker et al., 2002, and Du Plessis and Wouldberg, 2008).

$$-\frac{\partial p}{\partial x_i} = \nabla p = \frac{\mu}{k_o} v_s + \rho \frac{C_F}{\sqrt{k_o}} v_s^2 \qquad 4.1$$

Experimental hole-drilling and mechanical compression techniques by Lu et al. (1999) are useful approaches to changing the structural topology of porous metallic foams which invariably affect the fluid flow performance of the materials. Other techniques like changes in the packing density, salt sizes and applied differential pressures by Kennnedy (2012), and Langston and Kennedy (2014) was observed to alter the structural arrangement of the porous matrix made by the replication process. As a result of this, both the viscous (permeability, k_0) and inertial (Form drag coefficient, C and/or Forchheimer coefficient, C_F) terms in the Forchheimer model are greatly affected. Adopting, reliable and more convenient modelling routes capable of replicating the structural and flow parameters of this structure is key, but in addition, these processes must enable some flexibility to mimic the geometrical features when presented to flowing fluid during computation and to accurately predicts the measured flow data of the structure.

Simplified and idealized geometrical models to echo the shape and morphology of porous metallic structures have been developed with the aim of capturing important characteristics of the foam matrix, typically the pore, shapes, and

openings. Cardinal examples are Lord Kelvin and Weaire-Phelan (W-P) unit cell representation of porous structures. Reported in Thomson, 1887, Kelvin proposed a "virtual" representation of foam topology to be a polygon with eight non-planar hexagons of no net curvature and six planar quadrilateral faces. Weaire and Phelan (1994), developed the W-P cell structure that reduces the surface energy of Kelvin's cells by 0.3% and consists of a tetrakaidecahedron with twelve pentagonal faces and two hexagonal faces and an irregular dodecahedron with pentagonal faces. Space-filling of cellular solids (cuboids or cubes) was proposed by Gibson and Ashby (2001), cylinder structures for heat transfer by Lu et al. (1998), and rectangular prism for high porosity flow in a porous metallic structure by Du Plessis et al. (1994). Efforts were made by Thomas Zileinski (2015), to develop porous structures with spherical cells with the purpose of predicting non-acoustical structural parameters of the microstructure for sound absorption. Though, permeability prediction of this structure was limited to flow in the Darcy regime.

Pore-level numerical simulation of flow through highly porous metallic structures (85-95%) using X-ray computed tomography images to capture the fluid and structural information have been used successfully in predicting the flow behaviour with a tolerable agreement (1-5% deviation) between the predicted and measured values of unit pressure drop across the porous structure (Degischer et al., 2013, Diani, et al., 2015, and De Carvalho et al., 2017). This has not been extended to laminar flow of fluid through porous structures with spherical cells or simple "bottleneck" type structures, proven in Lu and He (2000), Li et al. (2014), and Otaru and Kennedy (2016) to be of lower porosities. Though simple and combined analytical models developed in Despois and

Mortensen (2005), and Furman et al. (2013) were used to substantiate the permeability of the "bottleneck" structure at Darcy regime (Chapter 3) to greatly depend on the openings connecting the pores of these unique porous structures. For laminar flow of fluid conducted on microcellular "bottleneck" aluminium foam structures (pore volume fractions from 0.66-0.86 and nominal pore size between 108-425μm) made by replication-casting processes, Weber et al. (2017) extended the theoretical permeability predicting "bottleneck" model to flow beyond Darcy and to show that k_0 and C terms in the Darcy-Dupuit-Forchheimer model are greatly influenced by the openings (connectivity) than the pore diameter sizes.

The use of discrete element modelling (DEM) simulation packing of spherical beds to imitate the fluid-structural domain of porous matrix provides an alternative and economical way of characterization and computational study of fluid flow through open-celled foam structures. Modelling procedures employing pore-level numerical simulation involving image processing of a micro-geometrical representative volume generation, filtering/smoothing, watershed segmentation (mean pore size), centreline statistic (mean window size) characterization (porosity, volume, tortuosity, and surface area), mesh-scale dependent and flow study are well documented in chapter 3 of this work and has been published in Otaru and Kennedy (2016).

This chapter considers a realistic laminar air flow behaviour in open-celled aluminium foam structures (pore volume fraction, 70-80% and pore dimensions, 1.0-1.4mm, 2.0-2.5mm and 2.5-3.15mm) with near-spherical cells manufactured by the replication-casting process. The computational fluid dynamics approach considers the utilization of X-ray computerized tomography (μCT) images of

the “real” structures and “virtual” spherical structures (DEM) obtained from discrete element simulation packing of spherical beds for the reconstruction of the three-dimensional micro-geometrical representative porous matrix based on the required pore volume (porosity) for effective flow of fluid across the macroporous structure. Also, theoretical descriptions of permeability and form drag are presented as a function of the structural parameters of the porous matrix to supplement the available options to predict the flow behaviour of bottleneck structures for laminar flow of fluid.

4.3 Specimen manufacture and characterization

The manipulation of packed beds of porogens to create windows within the metal matrix is imperative for engineering design and application. Production of the porous aluminium (Al) foam structures used in this work was achieved using the procedure in (Jinnapat and Kennedy, 2010) and (Langston and Kennedy, 2014). In brief, a liquid metal consisting of 99.5% of aluminium (800^{o}C below the melting point of the salts used) was poured into a mould consisting of hollow packed beds of Nottingham University (NU) near-spherical salt (particle sizes, X~1.0-1.4mm, Y~2.0-2.5mm and Z~2.5-3.15mm) and solidify after mixing before compaction at the desired infiltration pressure between 0.25 and 0.9 bar. Preheating of the bulk of space holders or beads was employed for a temperature range 450-600^{o}C to avoid premature solidification of the melt. The foam with salt (occupying its pore space) was then machined in a super-precision Gamet bearing lathe machine to get the desired shape and sizes to fit into a hollow pipe assembled for pressure drop experiment. This was then sintered by dissolution in a warm (40^{o}C) water incubation bath for 72 hours to leave porosity. The

resulting NU metal matrix produced consists of a skeletal structure (solid) which gives the foam its structural rigidity, pores occupied by air and interconnected windows that allow the passage of fluid through it.

The pore volume fractions of the porous structures were measured based on their mass-scale ratio whilst optical images of the structures reveal in detail, the pore diameter sizes, and openings. X-ray computed tomography (μCT) was carried out on each of the different Y samples (made between a quarter of a bar to one bar) using Xradia-500 microscopes (Fig 4.1a) to produce two-dimensional (TIF files) CT slices with a voxel dimension of 26μm. On the other hand, MATLAB™ was used to generate 2D DEM slices of spherical structures based on the results of discrete element simulated packed structures detailed in chapter 3 and presented in Langston and Kennedy (2014).



Fig 4.1a. An Xradia-500 Microscope instrument used for capturing 2D CT slices of the porous metallic foam structures.

A three-dimensional representative volume element (RVE) of the porous structure was generated in ScanIP module within Simpleware™ using the 2D CT and DEM slices individually. A similar procedure for image processing involving segmentation and mask creation to follow the boundary walls reported in chapter 3 was employed to process the "virtual" and CT images. Unlike

binary images used for "virtual" spherical structures, accurate determination of threshold limit of the grayscale (gray level) of the CT images is important towards the preservation of pores, pore volume, and connectivity within the microstructural arrangement based on shades of gray from black to white. Fig 4.1b presents tomography 2D slices (no, optimised and full threshold) of foam structure characterized by nominal porosity of 72.84%, pores sizes between 1.0-1.4mm and applied differential pressure of 0.9bar.

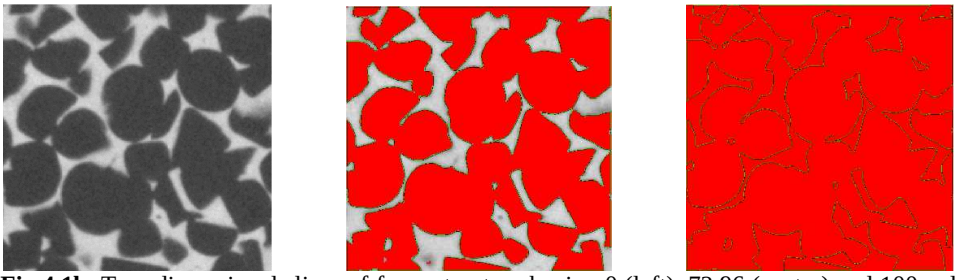


Fig 4.1b. Two-dimensional slices of foam structure having 0 (left), 72.96 (centre) and 100 vol percent threshold limit.

The extent of thresholding has resultant effects on the nature of the microstructure and its macroscopic parameters. Thresholding below the nominal porosity value (measured within ScanIP module of Simpleware^{TM}) of the foam structure separates the particles from each other thereby reducing its capillary interaction between connecting pores, connectivity, coordination number and bulk volume. This results in the low value of Darcian permeability (computed in FLOW module of Simpleware^{TM}) with an increased specific surface area of the microstructural arrangement. Thresholding above the nominal porosity increases the connectivity between pores and in turn, increases its bulk volume. Typically, for lower and upper threshold limits between 62 and 85% using Fig 4.1b, Darcian permeability increases exponentially ($k_0 = 0.0035e^{0.0992Ø}$) whilst the specific surface (foam surface area to bulk volume) linearly decreases ($\sigma_{FB} = 14.612-0.1399Ø$) with respect to the measured porosity of the material.

Care was taken at ensuring that the minimal deviation between the nominal porosity of processed image and that of the realistic foam structure is maintained to preserve accuracy. To determine the nominal porosity of this structure (density ~ 2.7g.cm^{-3}), the foam diameter, depth and weight were measured using a digital vernier calliper and smart weight digital scale. The fluid volume fractions of the processed representative volumes (RVE's) were measured and an average deviation of ±0.5% was achieved in comparison with the measured nominal porosity of the realistic foam structures.

The specific surface (σ_{FB}) was determined as a ratio of foam surface area to the bulk volume whilst its mean pore and window sizes of these structures were respectively determined by a watershed segmentation on the particles (particle separation) and computing a mean minimum area of circles across some centrelines adjoining two pores of a large volume of image data within the ScanIP. Values of the structural openings and pore sizes of the CT images are in agreement with that obtained with an optical image view of the "real" structure using Image J software.

4.4 Meshing and CFD simulation

Computational fluid dynamics (CFD) modelling of laminar air flow through these structures was possible by solving the well-known steady-state compressible Navier-Stokes equation (Eq 2.3) on a meshed-fluid domain representative matrix (RVE) using the Single-Phase flow module of COMSOL Multiphysics 5.0^{TM}. A foam thickness, typically between 8x and 10x its average pore radius were extracted below and above its center, was used as RVE and

corresponds to have a similar porosity to that of the large volume of the "real" foam structure. For the preservation of continuity, an inlet pore-velocity ($v_s = \emptyset v_p$) was applied. Also, a zero-outlet pressure ($P=0$), suppress backflow, no slip ($u = 0$) boundary conditions (BC) on the walls and symmetrical ($u.n = 0$) BC on the remaining facets of the porous structure was applied.

Accurate capturing of the gradients in flow velocity within the "bottleneck" regions of the porous structures was made possible through workable application of an elementary mesh-scale dependent study performed to determine an optimum mesh balance capable of converging faster and minimizing simulation error. A linear tetrahedral mesh (LTM) was applied to the fluid domain of the representative matrix carried out in the FE module of Simpleware™ using a growth rate of 1.3. For the purpose of accuracy and time convergence, the mesh dependent-study were conducted to grow the tetrahedral cells from the re-entrant edges leading to the large chunks of smaller-sized cells, typically ranging between 1.5-5.0x the image resolution within the "bottlenecks" zones whilst the maximum cell sizes occurring in the centre of the pores was set to be 6.75x the minimum edge length value (Fig 4.2).

Computed pressure drops obtained using the specified range of minimum edge length was compared to the highest density mesh structure (close to 6 Mcells) that could be solved computationally with the available PC specification. Efforts were made to improve the mesh structure (increased mesh density more than double) by maintaining the minimum edge length to 1.5x image resolution and reducing growth rate to 1.2. Fig 4.3 shows that the computed output values of pressure drop ratio against mesh density (Mcells) indicate a less than 0.2% increase, signalling a negligible benefit to reduce the smaller-sized mesh at the

"bottleneck" to below 2.7x voxel dimension (2-3 Mcells) used when compared with the consequence of computational time (using the commercial CFD software) which is more than 10x longer.

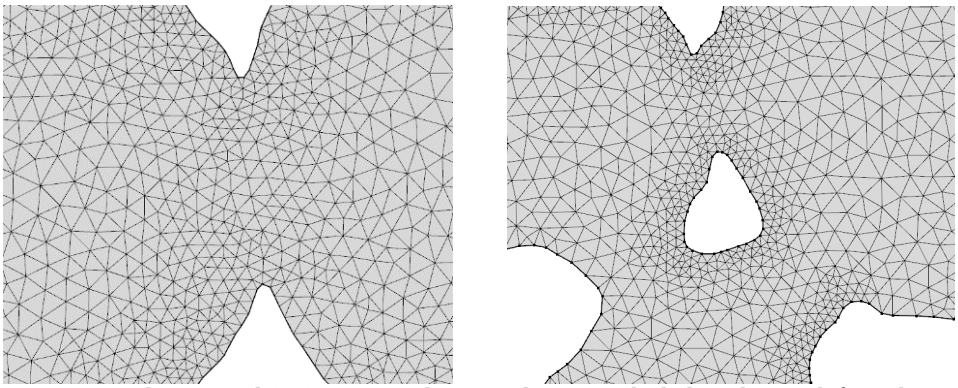


Fig 4.2. Two-dimensional (2D) images indicating a linear tetrahedral mesh growth from the re-entrant edge and the bottleneck regions of structures with the highest (left) and lowest (right) pressure differential.

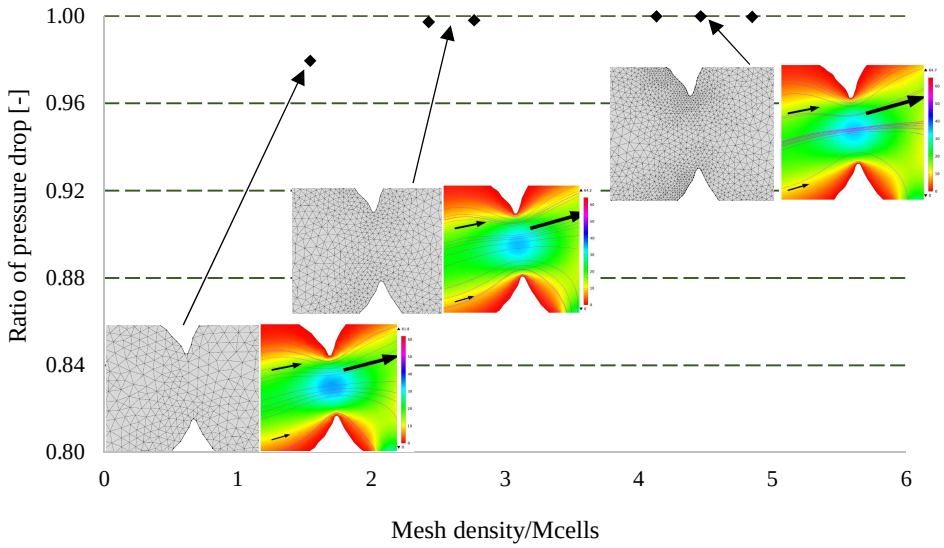


Fig 4.3. Plots of pressure drop ratio [-] against mesh density/Mcells showing the effect of mesh structure to capture flow information on the "bottleneck" and pore region of Al porous structure with spherical cells [*Numerical scales unit for the legends measured in* $m.s^{-1}$].

Lastly, computed values of permeability attained for all the Y structures, by solving Stoke's equation (Darcy regime) on highly dense (in the order of 26-30Mcells) hexahedral/quadratic tetrahedral meshes (HQTM), only indicates a less than 0.3% decrease when compared to the optimized LTM mesh structures. The HQTM is formed by creating a conformal alteration to the unrefined part of

a mesh by splitting the neighbouring elements to get rid of hanging nodes (Schneider, Schindler & Weiler, 1996b). Though, this type of mesh structure is quite expensive to resolve in commercial CFD software due to its high degree of freedom requiring high memory usage and computational time. Most commercial CFD software uses the Taylor-Hood P_2-P_1 elements (quadratic elements for the velocity and linear element for pressure) for its computation. By default, the use of stabilized P_1-P_1 elements (linear for both the velocity and pressure computations), which obviously reduces the number of unknowns and makes computation faster with less memory utilization in the +FLOW solver of Simpleware™ (Chen, 2014 and Simpleware Reference Guide, 2014).

4.5 Experimental measurement of pressure drop

The experimental setup in Fig 4.4 was designed to accurately measure pressure drops across an open-celled aluminium foam structure at a defined flow rate of air movement. The experimental setup and measurement methods were designed similar to those reported in (Oun and Kennedy, 2014 and 2015). In detail, it consists of compressed air supply unit, a Norgren F74G 40um G 1/2" automatic pneumatic filter (working pressure 0/10bar), a nickel-plated brass hydraulic needle valve series (FT 1251/2 & connection thread BSP 3/8"), standard (stable, easy-to-read, ±3% of full scale) precision-machined acrylic Flo-Rite™ air flow meters (0-140LPM) a flow straightener, a mid-flange assembly of foam sample holder with a GEMS sensors pressure transducer (0-2.5/25bar) and a data-log PC installed with 2016 NI LabVIEW signal for data acquisition.

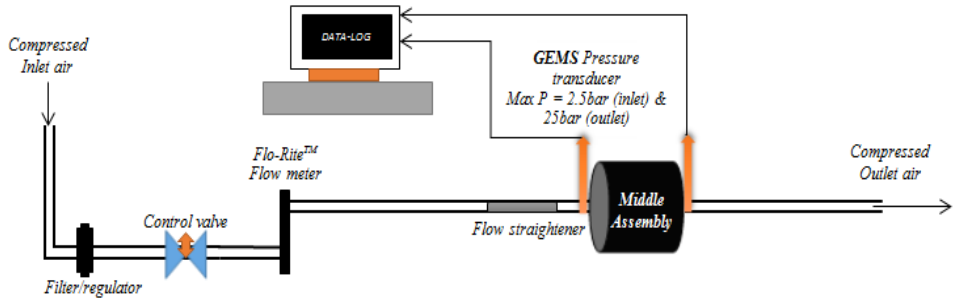


Fig 4.4. Schematic representation of air flow measurement.

A precisely machined foam sample of diameter, 25±0.2mm, and foam thickness 34.5±0.3mm (conferred to be the maximum length of the sample holder in the mid-assembly without the need of a spacer) was wrapped with a PTFE (polytetrafluoroethylene) tape to prevent air-bypass by ensuring total control of air passage only through the pores and windows of the foam structure and as well maintain a tighter fit and greater coefficient of friction with the wall of the mid-flange of 21.183mm internal diameter (flow diameter). The filter regulator made up of element material sintered polypropylene was used to remove water vapour and impurities (filtration size, 40μm) from the air supply. Two pressure transducers were connected to both the inlet (0-2.5bars) and outlet (0-25bars) of the mid-assembly. Pressure-transducer voltage calibration was done using a digital pressure indicator (DPI 601) for the inlet transducer (0-2.5bars) whilst the outlet pressure was conferred to be atmospheric.

An unmitigated power supply was ensured by using 3 x 9Volts non-rechargeable batteries supplying 8-30volts GEM transducers. This was done to minimize noise effects and as well minimizes the gap in error band. The needle valve with a minimum and maximum operating temperature of -20 to +100^{o}C and 210 bars maximum operating pressure was used to control the outflow of air into the flow meter from the filter regulator operating at 2.5bars. This nickel-plated brass

hydraulic needle valve consists of a double-acting valve for controlling and shutting off the flow and a single-action valve for flow control with free counter current.

A plot of pressure and voltage difference measured across the foam structure shows a perfectly fitted (P-ΔV) linear correlation (Fig 4.5) of mean standard deviation 1.63 and 0.77% determined for the inlet and exit transducers respectively. A minimum steady time of 2 minutes was allowed before taking the average sum of 2,000-3,000 voltage data recorded in a space of 2-3 minutes by the data acquisition PC device translating to upstream and downstream gauge pressures.

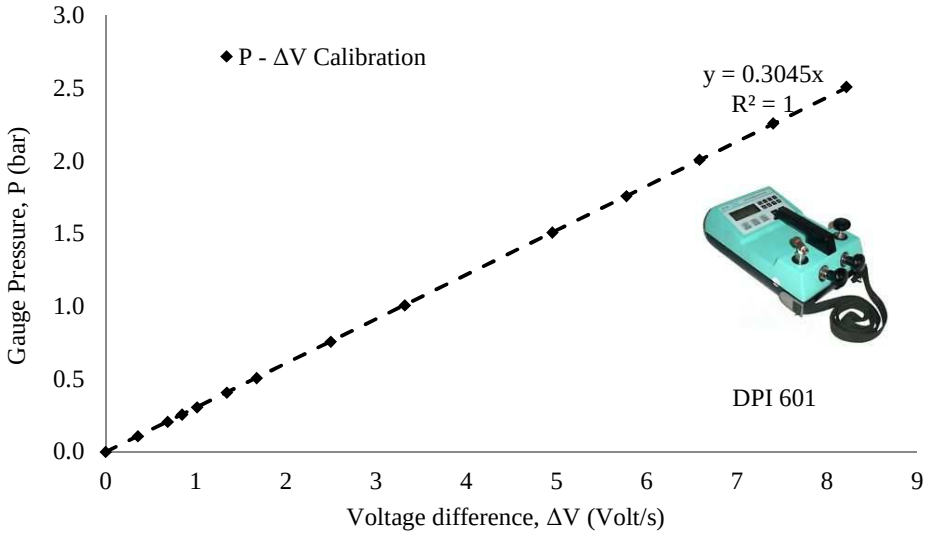


Fig 4.5. Inlet pressure-voltage calibration a digital pressure indicator (DPI 601).

The flowmeter available in metric scales was used to determine the air flow rate (0-140LPM) before it flows through the mid-flange (sample holder) via the flow straightener. Upstream and downstream air pressures drop across the foam sample were taken with the help of the GEMS pressure transducers and data-log for the given range of flow rates. The measured upstream and downstream gauge pressures were converted to absolute pressures by simply adding the measured

gauge pressures with atmospheric pressure (Khayargoli et al., 2004, Mostafid, 2007, Dukhan, 2013, and Oun and Kennedy, 2014). Due to the fractional change in the air as opposed to liquid, care was taken to account for compressibility effects to avoid significant underestimation of the static pressure variation caused by an alteration in the density of the flowing fluid (air) across the foam cross section (Bonnet et al., 2008, Dukhan, 2013, Edouard et al., 2008, and Oun and Kennedy, 2014). Eq 4.2 was applied to determine the "real" pressure drop (ΔP) across the structure as a function of the inlet (P_i) and outlet (P_0) absolute pressures while P_R was taken as reference or atmospheric pressure.

$$\Delta P = \frac{P_i^2 - P_o^2}{2P_R} \qquad \text{Eq 4.2}$$

4.6 Results and discussion

The results and discussion section of this work are grouped into structural characterization and flow parameters obtained for flowing air across the different porous Al structures for both measured and modelled derived values presented in graphs, tables, and figures. Images are obtained from optical microscope, scanning electron microscope (SEM), X-ray tomography images and sphere-packing models.

4.6.1 Structural characterization

Table 4.1 presents the structural parameters for the different porous metallic structures produced using hydrosoft-based salts for particle sizes in the range of 1.0-1.4mm, 2.0-2.5mm and 2.5-3.15mm represented by the following symbols in the table. X1 (1.0-1.4mm) and Z1 (2.5-3.15mm) structures were produced using a liquid metal infiltration pressure of 0.9 bar whilst the Y (2.0-2.5mm) structures were produced at 0.90 (Y1), 0.50 (Y2), 0.33 (Y3) and 0.25 (Y4) bars.

X-ray CT images of the Y structures were taken to determine their structural parameters. Key parameters like porosity, mean pore size, and mean openings or connectivity measured from the 3D CT volumes (CFD) and presented in Table 4.1 agrees closely with the measured structural data of the "real" foam structures.

As expected, structural measurements of pore sizes lie closely to within the mean average salt particle sizes used for the casting process. The mean openings between connecting pores decrease with increased casting pressure differentials and the pore volume fraction (porosity) predominantly controlled by the packing density of the beads. Though, this is also affected by the variation in liquid infiltration pressure with lower pressure differential leading to less complete filling of the interstices of the packed beds and the higher level of porosity as shown in Y4 structure.

Table 4.1. Measured and X-ray CT structural parameters of the porous Al structure.

Sample	Infiltration pressure difference, Pi (bar)	Porosity, Ø (%)	Mean pore size, Dp (mm)	Mean connec-tivity, Dw (μm)
EXPT-Y1	0.90	70.55	2.21 ± 0.15	643 ± 17
μCT-Y1		70.53	2.23 ± 0.17	651 ± 24
EXPT-Y2	0.60	72.55	2.23 ± 0.12	728 ± 24
μCT-Y2		72.56	2.22 ± 0.17	720 ± 20
EXPT-Y3	0.45	75.09	2.22 ± 0.16	727 ± 15
μCT-Y3		75.21	2.27 ± 0.15	741 ± 21
EXPT-Y4	0.25	78.22	2.25 ± 0.24	920 ± 25
μCT-Y4		78.40	2.23 ± 0.25	899 ± 19
EXPT-X1	0.90	72.03	1.21 ± 0.18	275 ± 10
EXPT-Z1	0.90	75.08	2.75 ± 0.21	710 ± 23

Fig 4.6 presents typical optical microscope images of X1 (left) and Z1 (left) porous Al structures and scanning electron microscope images of salt used, both cast at an infiltration pressure of 0.9 bar. Similar images of the Y1 (left) and Y4 (right) structures are presented in Fig 4.7 in addition with the watershed

segmented particles obtained from the processed 3D CT representative volume with a measured roundness (mean particle circularity) to within 0.8-0.85 for the four Y's structures.



Fig 4.6. An optical microscope images of foam structures cast with salts with particle sizes (left) X1/1.0 – 1.4mm and (right) Z1/2.0-3.15mm structures both produced at 0.9 bar.

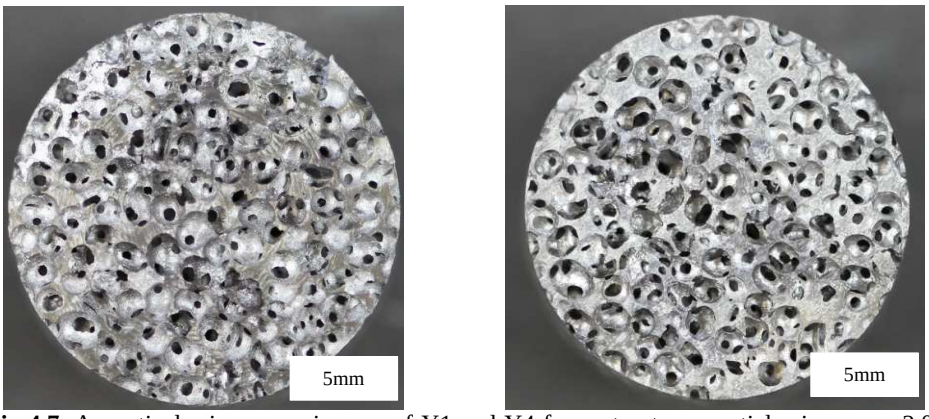


Fig 4.7: An optical microscope images of Y1 and Y4 foam structures particle size range 2.0-2.5mm.

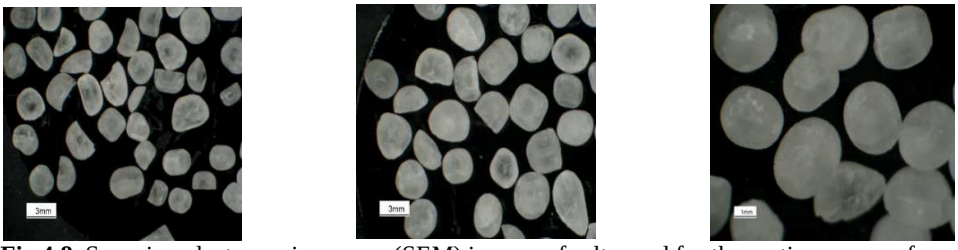


Fig 4.8. Scanning electron microscope (SEM) images of salts used for the casting process for particle sizes 1.0-1.4mm (left), 2.0-2.5mm (middle) and 2.5-3.15mm (right).

These figures confirm the shapes and sizes of the salt beads to dictate the morphology and pore sizes of the structures respectively. These also show

smaller and multiple rounded windows or connectivity between near-spherical connecting pores and the size of these windows increases with increased pore/particle sizes and infiltration pressure differential used (Table 4.1). Visual assessment of the two-dimensional (2D) model contours (Fig 4.9) and (3D) volumes of the CT processed images reveal that not only the window sizes of the structures are affected with variation in pressure differentials but also the number of contacts (coordination number) between connecting pores is also affected. Previous work by Langston and Kennedy (2014), and Otaru and Kennedy (2016) have shown that coordination number per cell is dependent on that obtained for packing of salt beads affected by variation in packing density and particle shapes and sizes. For monosized "virtual" near-spherical monosized structures of roundness close to unity, typical values between 6 and 7 are attained and higher for distorted near-spherical shaped salt beads (Fig 4.7 & 4.8) used in this study (Fig 4.9).

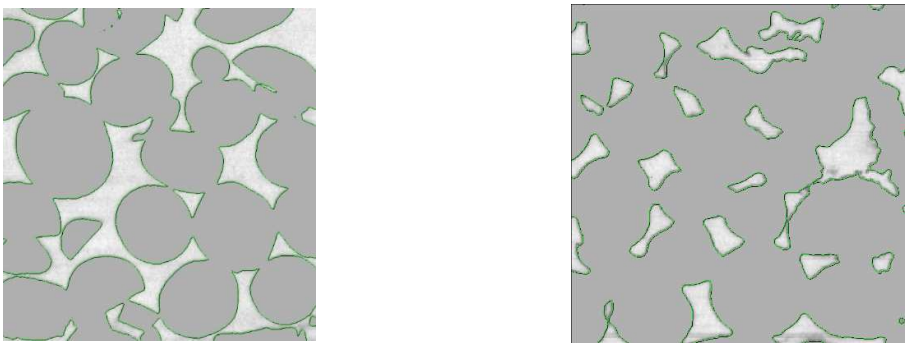


Fig 4.9. A two-dimensional model contour of porous Al structure taken from CT images for the highest Y1 (left) and lowest Y4 (right) pressure differentials.

Fig 4.10 presents three-dimensional images of the structural phase of the X-ray CT and DEM-based cubical representation of the Y1 structures. A tabular representation of Y1 and Y4 structural data obtained for the two pore-level approaches are presented in Table 4.2. The proximity between structural

morphology and the window diameter openings of the CT and "virtual" images measured from 3D volumes in ScanIP indicates somewhat benefit in the use of the "virtual" structures to mimic flow through these macroporous structures.

Despite applying similar image processing procedure and smoothing/filtering, the lack of observable difference in the ratio of the structural phase surface area to the bulk volume (termed as specific surface) is attributable to the high surface roughness of the "real" structure represented by the CT images and could affect the flow behaviours of these structures. The mean pore sizes of the two modelling approaches differed by 4 and 7% for the Y1 and Y4 structures respectively and this is mainly due to dilation effects imposed on the fluid domain of the "virtual" representative structures to create a structure capable of replicating the window sizes and porosity of the CT or "real" structures. This is still within tolerable value for differential pore sizes and flow behaviour through these structures has been proven to greatly depend on the "bottleneck" between connecting pores (Furman et. al, 2013, Otaru and Kennedy, 2016, and Weber et al., 2017).

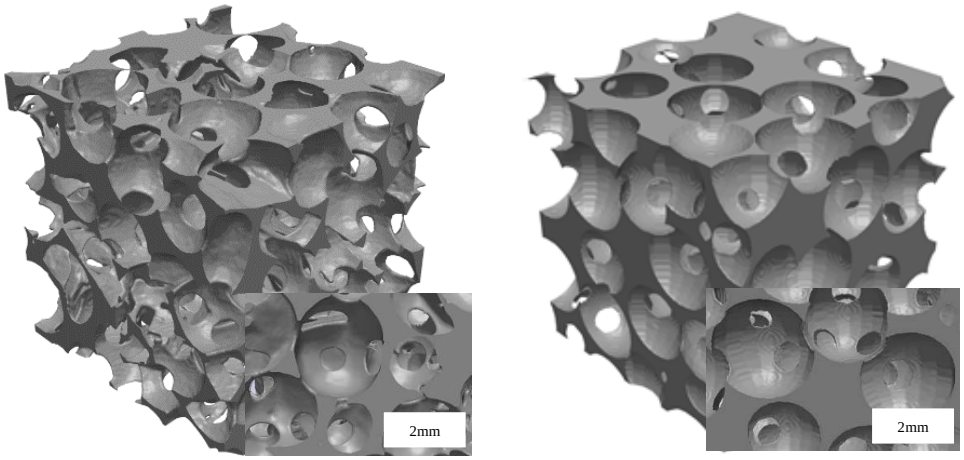


Fig 4.10. Three-dimensional X-ray CT (left) and DEM (right) images of structural domains representative Y1 structures.

Table 4.2. X-ray CT and DEM based structural parameters of Y1 and Y4 structures.

Sample	Porosity, Ø (%)	Mean pore size, Dp (mm)	Mean connectivity, Dw (μm)	Specific surface, σ_{FB} (mm^{-1})
μCT-Y1	70.53	2.23 ± 0.17	651 ± 24	2.54
DEM-Y1	71.75	2.33 ± 0.08	617 ± 10	2.48
μCT-Y4	78.40	2.23 ± 0.25	899 ± 19	2.05
DEM-Y4	78.25	2.41 ± 0.15	892 ± 12	1.92

4.6.2 Experimental measurement of airflow through Al structure.

4.6.2.1 Test on documented foam samples and repeatability analysis

To ensure accuracy of the experimental setup in Fig 4.4 is preserved and the right data were obtained, care was taken to the first test for leak detection and an airflow measurement on a 20mm thick Inconel 450μm (metal alloy) foam sample (Fig 4.11) of density and pore volume fraction, 828kg/m^3 and 84% respectively was carried out and compared to existing data available in the literature (Oun and Kennedy, 2015). A plot of pressure drops per unit length (Pa.m^{-1}) against superficial air inlet velocity (m.s^{-1}) for the Inconel foam structure followed a second order Forchheimer relation and a reasonable agreement of 99.7% was attained in comparison with the literature data reported by Oun and Kennedy (2015).

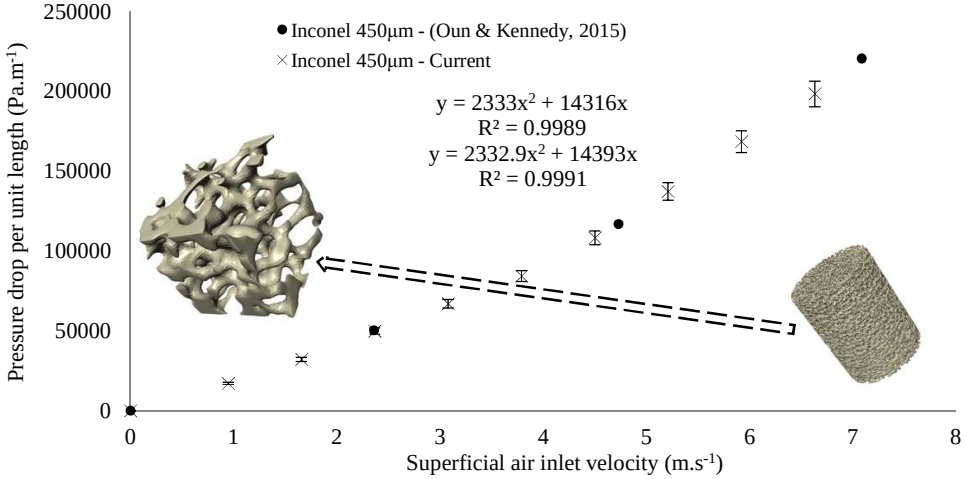


Fig 4.11. X-ray CT images of Inconel 450μm foam structure and a plot of pressure drops per unit length (Pa.m^{-1}) against superficial air inlet velocity (m.s^{-1}) for the structure.

Also, airflow measurement through a 12mm thick Recemat RCM-NCX 1723 sample shows reasonable agreement with numerically simulated (using X-ray CT images of the "real" structure) and measured values of unit pressure drop across the foam sample (De Carvalho et al., 2017). Computationally, flow length was reported to have a considerable influence on the flow performance due to the inhomogeneous topology (combination of irregular dodecahedron and tetrakaidecahedron cell with pentagonal faces described as the Weaire-Phelan, 1994 model) of the sample geometry. This resulted in a non-uniform connectivity and variable length; thereby necessitating a more developed flow field computationally (increased computational time) to fully describe the entire flow field in a large sample especially at higher flow velocities. Flow behaviour through the "bottleneck-type" structures presented herein may differ from the Inconel 450μm and Recemat RCM-NCX 1723 samples but the observable agreements between our measured and literature data confirm the precise experimental setup and the sureness of any measured data of unit pressure drop across structures of any morphology and sizes.

Experimental (Coulson, 1949, Bear, 1972, Mostafid, 2007, and Dukhan, 2013), analytical (Ergun, 1952, Du Plessis & Wouldberg, 2008) and computational models (Peng, et al., 2012, Petrasch, Wyss and Steinfield, 2007, De Carvalho et al., 2014, and Otaru & Kennedy, 2016) available in the literature have shown that the pressure drop developed across a porous body when presented to a flowing fluid is a function of its thickness and the superficial inlet fluid velocity. The unidirectional, steady-state and fully developed pressure drop of airflow across Z1 (2.5-3.15mm) aluminium foam structure was measured repeatedly (reassembling the experimental setup and flipping both sides of the foam

structure) at different air superficial velocity ranging from 0.6-6.63m.s^{-1} (14–140LPM) and was divided by its porous body thickness (L=34.5mm) to determine the pressure drop per unit length ($\Delta P/L$) presented in Fig 4.12. Also, a reduced pressure drop ($\Delta P/LV$) was determined by dividing the pressure drop per unit length against superficial air inlet velocity presented in Fig 4.13.

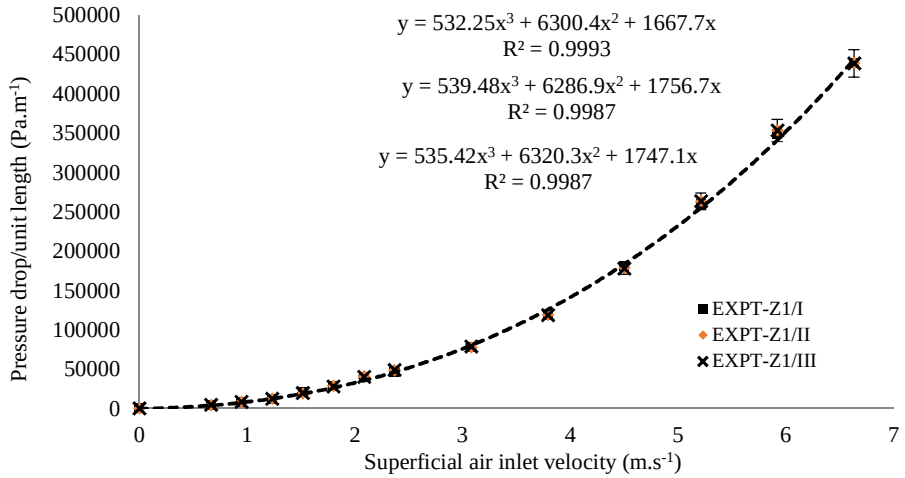


Fig 4.12. Experimental pressure drop per unit length (Pa.m^{-1}) against air superficial inlet velocity (m.s^{-1}) for a repetitive test on aluminium foam sample Z1 (2.5-3.15mm).

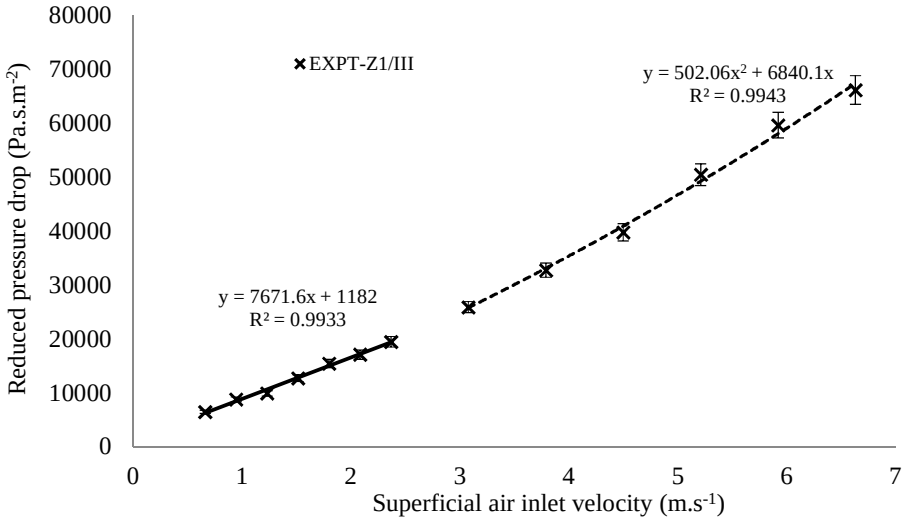


Fig 4.13. Experimentally reduced pressure drop (Pa.s.m^{-2}) against air superficial inlet velocity (m.s^{-1}) for a repetitive test on aluminium foam sample Z1 (2.5-3.15mm).

The pressure-velocity relationship in Fig 4.12 for the given range of velocity (0.6-6.63m.s^{-1}) studied shows a parabolic trend of pressure drops with velocity

and can be described by a quadratic polynomial (3rd order Forchheimer relation). Fig 4.13 shows a clear distinction between the range of fluid velocity which clearly follows 2nd and 3rd order Forchheimer relation. This shows that fluid velocity ranging between 0.6 and 2.36 $m.s^{-1}$ (14-50LPM) obeys the 2nd order Forchheimer relation with a correlation of 99.33%. Hence, the viscous (Permeability) and inertial (Form drag) terms of this fluid flow behaviour can easily be determined using the 2nd order quadratic model of Hazen-Dupuit-Darcy (Eq 2.15) fit of a pressure gradient to superficial velocity. Above this velocity range, a third order Forchheimer relation is observed for a correlation of 99.43%. A detailed understanding of the flow behaviour and the regime of occurrence is done using Darcy-Weisbach approach.

4.6.2.2 Reynolds number and Friction factor relation

In practically all cases, the term Darcy's law for flow through porous structures is valid providing its mean pore/particle diameter-based Reynolds number (Re_D) does not exceed some value between 1 and 10 (Bear, 1972). Lage et al. (2002), specified this regime to be a transition from Darcy to Forchheimer whilst complete Darcy regime was reported to exist at $0 \leq Re_D \leq 1.0$. Complete laminar, laminar-turbulent transition and fully developed turbulent regimes were reported for Reynolds number between 10-150, 150-300 and > 300 respectively.

A more simplified approach to understanding the pattern of flow and regime of manifestation is the use of Darcy-Weisbach approach usually done by plotting a dimensionless Fanning friction factor (f_F) against mean pore diameter-based Reynolds number (Bear, 1972, and Oun and Kennedy, 2014) as shown in Fig

4.14 for Z1 structure, typified having the largest cell sizes and 0.9 bar differential pressure. Optical images of this structure revealed a mean pore size of 2.77mm measured and was taken as the characteristics linear dimension (D_P) of the "bottleneck-type" structure as used in Boomsma and Poulikakos (2002). Mathematical representations of the Fanning friction factor (f_F) and pore-diameter based Reynolds number (Re_D) are presented in Eq 4.3 and Eq 4.4 as a function of pressure drop (ΔP), superficial velocity (V), mean pore diameter or characteristic linear dimension (Dp), fluid density (ρ) and fluid dynamic viscosity (μ).

$$f_F = \frac{\Delta P}{\left(\rho V^2/_2\right)} \qquad \text{Eq 4.3}$$

$$Re_D = \frac{\rho V D_P}{\mu} \qquad \text{Eq 4.4}$$

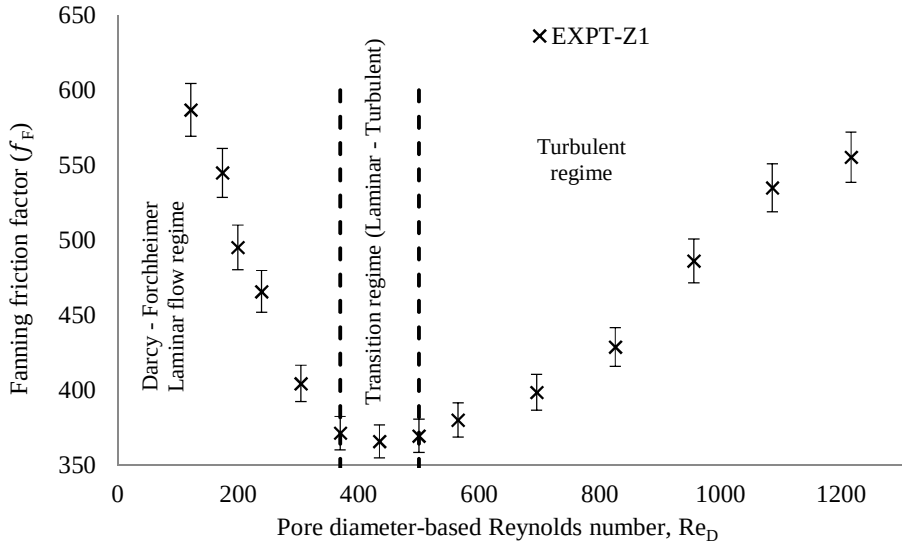


Fig 4.14. Plots of dimensionless Fanning friction factor (*f*) against pore diameter-based Reynolds number (Re_D) for airflow through the lowest window-sized (Z1) porous Al foam structure.

Notable observations from the plot are the range of values estimated for the Reynolds number, typically to within 122-1221 for the specified velocity range (0.6-6.6 $m.s^{-1}$) and the regimes of manifestation with increased fluid velocity in the porous structure. Below 435 value of Reynolds number ($v_s \leq 2.36$m/s), there

exists a power law relationship between the Fanning friction factor and Reynolds number. Viscous forces predominate inertial forces at the lower end of this laminar flow regime whilst inertial forces predominate viscous forces at the upper end of this regime. This regime is termed as the non-linear laminar flow regime and can be simply be described by the 2nd order Forchheimer relation (Eq 2.15). The permeability (k_0), Form drag (C) and Forchheimer coefficient (C_F) determined in this regime are $18.98 \times 10^{-09} m^2$, $6474.63 m^{-1}$ and 0.89 respectively.

A significant contribution of wall function (increased Form drag) deviates its behaviour away from power law and this regime is termed as Transition regime. In this case, the transition from laminar to turbulent flow exists for velocity and Reynolds number range of $2.36 \leq v_s \leq 2.72$m/s and $435 \leq Re_D \leq 494$ respectively. As Re_D increases beyond 494, the turbulent flow is observed (Darcy's law not valid) and inertial forces completely dominate the fluid flow across the porous aluminium foam structure. This is an indication that high flow velocity of the fluid through a porous media is a major contributory factor in attaining turbulence (Lage et al., 2002) while the non-linearity deviation from Darcy is caused by inertial effects (Dukhan, 2013) and not turbulence even though the flow is laminar for $Re_D \leq 435$.

Other foam structures conformed to having a similar trend of the Darcy-Weisbach approach, but their Reynolds number and friction factor differ from each other due to the variation in the structural parameters resulting from the use porogens (salts) of different sizes and the important applied differential pressure used during the casting process. A typical example of this is the flow behaviour through foam structure X1 made with packed porogens with the least particle

sizes in the range of 1.0-1.4mm and at 0.9 bar liquid foam infiltration pressure. Darcy-Forchheimer, transition regime and turbulent regime for flow through this structure were attained for pore diameter-based Reynolds number, typically in the range of $48 \leq Re_D \leq 152$, $152 \leq Re_D \leq 173$ and $173 \leq Re_D \leq 485$ respectively (Fig 4.15). Similarly, the ranges of Reynolds numbers attained for these regimes for flow through the Y4 structure with the largest openings are $97 \leq Re_D \leq 453$, $453 \leq Re_D \leq 663$ and $663 \leq Re_D \leq 977$ presented in Fig 4.16.

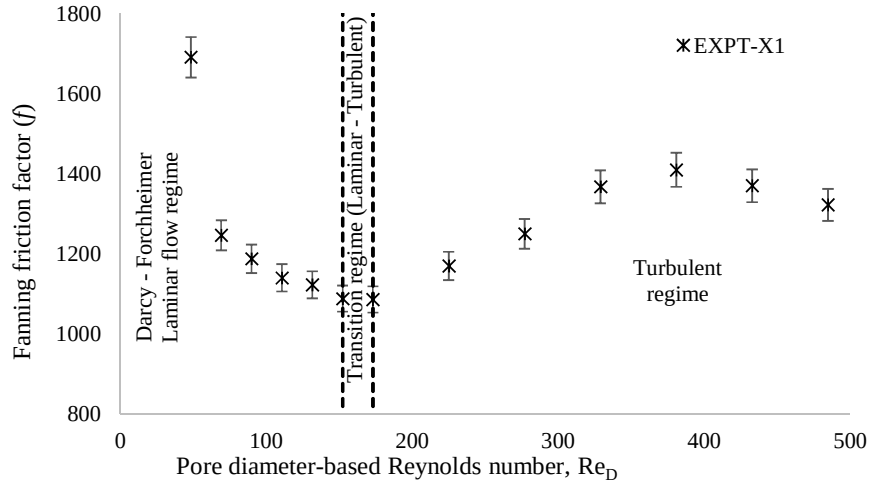


Fig 4.15. Plots of dimensionless Fanning friction factor (f_F) against pore diameter-based Reynolds number (Re_D) for airflow through the lowest window-sized (X1) porous Al foam structure.

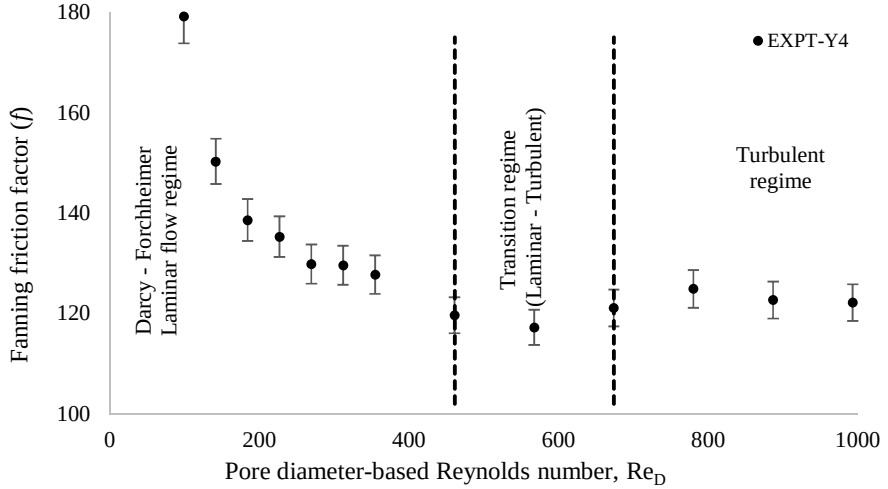


Fig 4.16. Plots of dimensionless Fanning friction factor (f_F) against pore diameter-based Reynolds number (Re_D) for airflow through the largest window-sized (Y4) porous Al foam structure.

Understanding this flow pattern is necessary towards the determination of viscous (permeability) and inertial (Form drag and Forchheimer coefficients) of fluid flow through porous structures of any topology and cell sizes. Though, the square root of permeability ($\sqrt{k_0}$) has been reported (Dybbs and Edwards, 1984, Kececioglu and Jang, 1994, and Kouidri et al., 2015) to be useful in defining the true characteristic linear dimension of these structures due to the fact that the permeability and not cell size represents more the inherent morphology of the porous structure. A plot of the Fanning friction factor against the permeability-based Reynolds number may indicate low values of Reynolds number but the behavioural trends from Laminar to Turbulent regime remain the same irrespective of the choice of characteristic linear dimension chosen.

4.6.2.3 Experimental measurement of air pressure drop

A plot of the unit pressure drop ($Pa.m^{-1}$) measured for the six foam structures for the different range of pore sizes and differential pressures against the superficial air inlet velocity ($m.s^{-1}$) is presented in Fig 4.17. These polynomial trends can be fully described by the 2nd order Darcy-Dupuit-Forchheimer model with flow regime particularly to be within Laminar using Fig 4.14-4.16. Dividing the pressure drop per unit structural thickness measured for all the six foam samples by the superficial velocity (reduced pressure drop) and plotting against the superficial air inlet velocity as reported in (Dukhan, 2013, and Oun and Kennedy, 2015), the laminar flow unit pressure drop (Fig 4.17) can be further substantiated and to ensure the accurate choice of physics used in numerical simulation approach is selected. Such a plot is presented in Fig 4.18 for all the structures with a linear dependence fit (R^2 > 99%) indicating the

measured pressure drops to be within the Forchheimer regime except for the X1 structure with the lowest cell sizes.

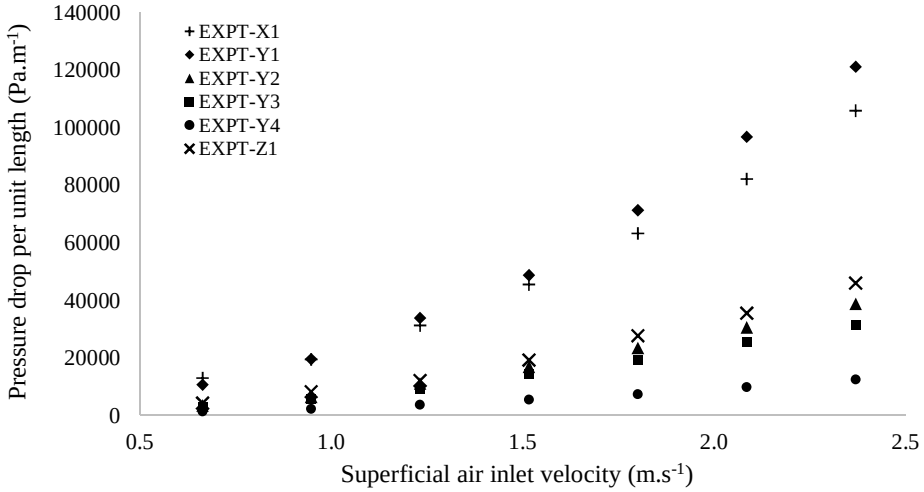


Fig 4.17. Plots of measured pressure drop per unit length ($Pa.m^{-1}$) against superficial air inlet velocity ($m.s^{-1}$) six foam structures.

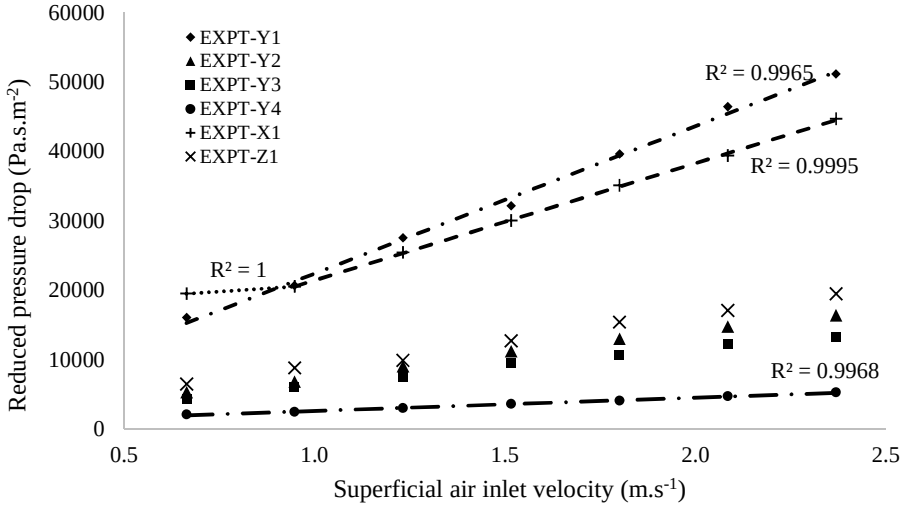


Fig 4.18. Plots of reduced pressure drop per unit length ($Pa.m^{-1}$) against superficial air inlet velocity ($m.s^{-1}$) six foam structures.

Flow through this X1 structure (Fig 4.18) indicates the presence of Darcy regime for the first two velocities with little or no substantial difference between their reduced pressure drops and Forchheimer regime exist for flow between 0.9-2.36$m.s^{-1}$ with a linear dependence of very close fit. The difference and order of

magnitude in the measured unit pressure drop for all the foam structures can be classified into low, mid and high-pressure drop. Higher values of pressure drops are observed for samples with the lowest porosities (X1 and Y1) whilst the lowest pressure drop is attained for the sample (Y4) with largest openings and conferred to have the highest porosity value (Table 4.1). The similarity in the intermediate pressure drop attained for the Y2, Y3, and Z1 structure is greatly influenced by the little difference in the changes associated with porosity and openings between the connecting cell sizes within the microstructures.

The size of the pores within the porous structure influences the tortuous path (tortuosity) and interstices available as pore volume for the flow of fluid (air). Larger pore sizes (opposed to smaller pore sizes) yielded a low tortuous path (tortuosity), low specific surface and large fluid volume which invariably resulted in low-pressure drops and high permeability of fluid measured across the foam structures. This flow trend is observed for foam X1, Y1 and Z1 structures (produced using similar liquid pressure differential of 0.9 bar) at very low velocity were the flow behaviour of the structure are largely dependent on the openings of the structures (Dybbs and Edward, 1984). At high velocity greater than $1 m.s^{-1}$, the high pressure drops attained for Y1 structure when compared to the X1 structure are largely due to the increased “strut” thickness resulting in lower porosity value of the Y1 structure; thereby providing more resistance to the flowing fluid across the structure. Optical imaging of these structures (Fig 4.6-4.7) revealed a near-spherical structure for the Y1 structure whilst the X1 structure consists of highly irregular-shaped, inhomogeneous cells and large window to pore ratio (resulting from more half sized spherical salts

used during casting) thereby providing lesser resistance to flowing fluid at high velocities.

The behaviour of airflow through this structure is also affected by the number of windows (coordination number) existing with the porous matrix, typically, flow through Y structures made for different liquid differential pressures. At high infiltration pressures, liquid foams (aluminium) are forced into spaces created by packed beds of porogens thereby reducing the connectivity sizes and the number of windows available for permeation of fluid. Fig 6.19 plots the window to pore size ratio against the liquid pressure differential used for the different Y samples indicating a power inverse relation between these parameters. It is evident from this Figure that at low differential pressure, the connectivity (openings) between connecting pores within the porous structure is larger than that produced at high infiltration pressure provided the similar pore sizes are maintained. The lowest specific surface (structural surface area to bulk volume ratio, σ_{FB}), the lowest pressure drops per unit foam thickness and the largest window sizes is associated with lowest infiltrated pressure Y1 sample (high capillary interaction between connecting pores) whilst a reverse order of macroscopic and flow data were obtained for the highest liquid infiltrated pressure Y1 structure (low capillary interaction between connecting pores). Tabular representation detailing values of the specific surface and other structural parameters of the Y porous structures is presented in Table 6.5A of the appendices.

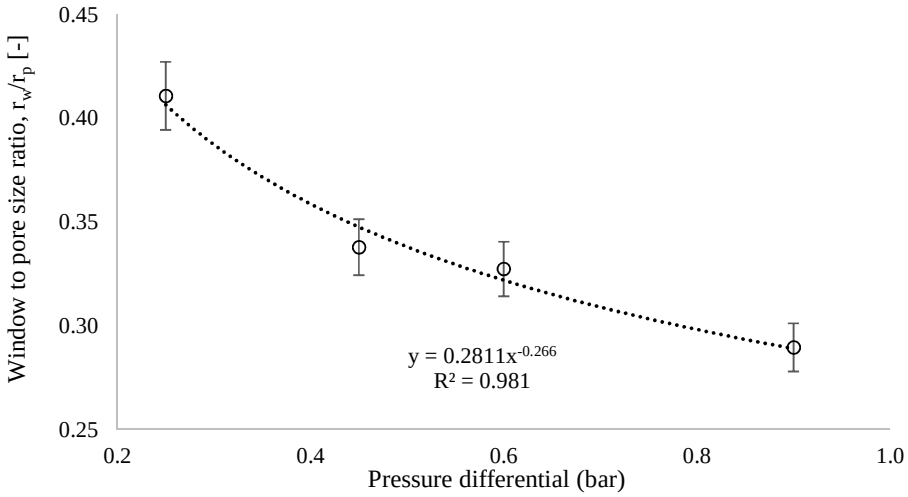


Fig 4.19. The relationship between pressure differential (bar) and the ratio of window to pore sizes [-] for the cast samples.

4.6.3 CFD simulation of airflow through Al structures using X-ray CT images of the "real" structure.

Pore-level computational modelling approach adopted in this study generally requires structure-derived representative volume element (RVE) smaller in volume and flow length than the "real" sample. There is the possibility that disagreement between this modelling approach and experimental measurements may result from the choice of RVE size which is based on the skeletal structure rather than the flow geometry (Petrasch et al., 2007, Bodla et al., 2010, and De Carvalho et al., 2017).

Related experimental and modelling works available in the literature (Dukhan and Patel, 2008, De Carvalho et al., 2017, and Oun and Kennedy, 2015) generally considered structure-derived RVE's flow path smaller in length than the length independent "critical" thickness for developing flow through this complex structure. For more open, highly porous metallic structures, some 20-50 pore diameter sizes were considered to be an appropriate critical thickness and pressure drop increases for flow through structures below the critical thickness (Mostafid, 2007, and De Carvalho, et al., 2017). Though, the related articles on the critical thickness were carried out on flow through irregular-shaped highly porous metallic structures with a topology similar to Lord Kelvin and Weaire-Phelan (W-P) unit cells like the Recemat, Alantum and Inconel foams which are different from structures presented herein.

A sensible analysis on the required thickness of our low-density near-spherically celled porous structures needed to aid in the choice of RVE size capable of predicting accurately the measured flow data considering the limited available computational resource was made perfectly clear by realistically measuring flow

through 10mm thick samples. At the extremes of porosity levels (Y1 and Y4 samples), the 10mm thick samples were made by sectioning from the center of a long sample after testing and pressure drop was measured for these shorter samples.

Fig 4.20 plots the normalized pressure drop (ratio of unit pressure drop measured on the smaller to the long thick sample length) against the superficial air inlet velocity. Discrepancies between the measured pressure drop observed for smaller Y1 structure (10 mm thick) are no more than 4% higher than the longer sample, highest at the highest velocity and for the smaller Y4 structure, they are all roughly 5% below the longer sample (34.5mm thick). The close proximity between the experimental values of the longer and shorter structures is attributed greatly to slight differences in their density (porosity) which is slightly lower for the shorter Y1 structure (70.21%) and slighter higher (78.90%) for the shorter for the Y4 structure.

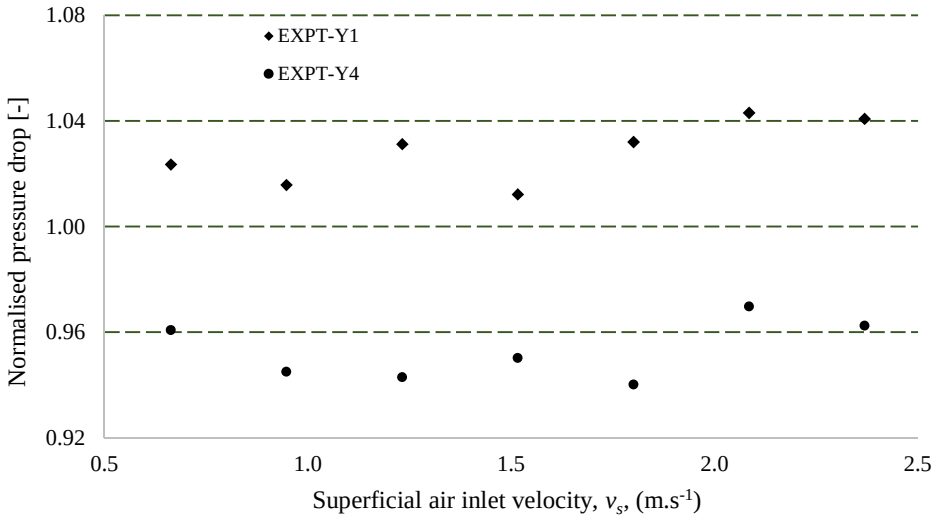


Fig 4.20. Normalised pressure drop [-] for 10 mm thick samples, plotted against superficial flow velocity.

The no clear or considerable length effects on flow through the shorter and longer samples is, however, of great benefits considering the numerical computation of flow through this structure. Though, fluid flow through this low-density and much restricted "bottleneck-like" structures speedily promotes the evolution of flow in open channels (pipes) to flow in contorted structures when compared to flow through the more open Weaire-Phelan and Kelvin-like unit cell structures (Dukhan, 2013, Dukhan and Patel, 2008, De Carvalho et al., 2017, and Oun and Kennedy, 2015). Hence, the choice of relatively small samples, typically, 8-10x the mean pore radii, during simulation of fluid flow through these "bottleneck-type" structures to enable more prudent computing, is unlikely to lead to a significant deviation from the measured data made on a longer sample. Also, a time-demanding and computationally intensive simulation performed on an RVE size that more than doubles the original length only resulted in a 2% decrease in the unit pressure drop, within the expected scatter owing to the non-homogeneous nature of the "real" structures resulting from the presence of halving-sized salts used during casting.

The velocity profile plots of CFD simulation of laminar airflow performed on a two-dimensional images taken from different sections of the three-dimensional CT volume of the lowest (Y1, top) and highest (Y4, bottom) porosity structures computed at superficial air inlet velocity of $1 m.s^{-1}$ are presented in Fig 4.21 to clearly understand the flow behaviour that exists within this "bottleneck-like" structures. Flow from left to right (indicated by arrows) is observed for connected pores and the intensity of the colour scale (values presented in the legends) is largely dependent on the window sizes and contacts made by connecting pores (Langston and Kennedy, 2014, and Otaru & Kennedy, 2016).

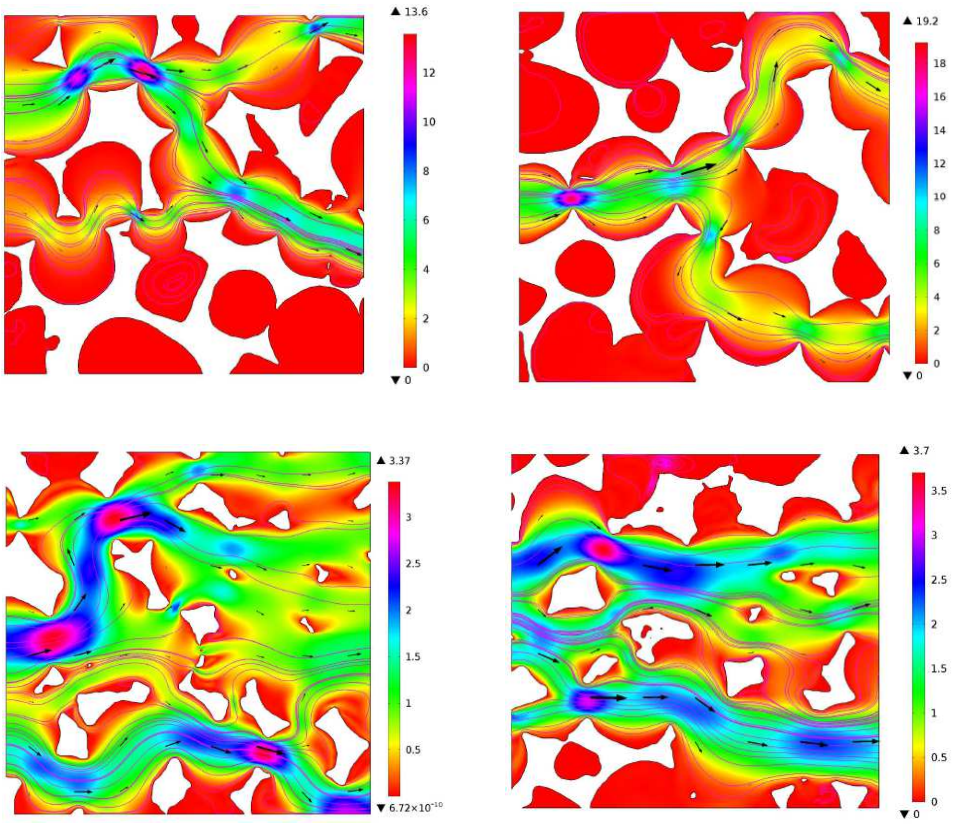


Fig 4.21. Two-dimensional (2D) velocity profile plots for flow (left to right) through "virtually-created" porous samples Y1 (top) and Y4 (bottom) for an inlet pore velocity of 1m s^{-1} [*Numerical scales unit for the legends measured in* $m.s^{-1}$].

For Y1 structure, the tendency of constrictive response is higher than the highly porous Y4 structure due to their important smaller window sizes and fewer number of connected pores thereby providing a greater restriction to flowing fluid. Pressure drop developed across this structure (Y1) is expected to be higher with increased velocity and would be much higher for structures produce with similar technological routes and process parameters but at much higher differential pressure (Otaru and Kennedy, 2016). Conversely, the porosity, window sizes and the number of connecting pores increase for Y4 structure made at the lowest differential pressure, less distorted flow is observed from the incoming airflow to the exit region. Flow through this type of less constricted structure is similar to the one presented in De Carvalho et al. (2017), and Weber

et al. (2017) whilst that of the highly distorted structure is similar to the one presented in Langston and Kenned (2014), and Otaru and Kennedy (2016) discussed in previous chapters. More images of similar velocity profile plots of Y1 structures at different mesh scale resolution is presented in Fig 4.1A-4.8A of the appendix page.

To compare the measured and X-ray CT based numerically simulated study, a plot of the unit pressure drop developed across the thickness of the structure against superficial air inlet velocity for the laminar flow of fluid is presented in Fig 4.22. Also, computed values of permeability, Form drag coefficient (C) and Forchheimer coefficients (C_F) done by fitting the pressure-velocity data into the Darcy-Dupuit-Forchheimer model (Eq 2.15) for both the measured and CT model is presented in Table 4.3. The exclusive contribution of the viscous and inertial terms in the Forchheimer equation to the pressure drop is observed and the contribution from the Form drag or Forchheimer coefficient increases with increase superficial air inlet velocity, typically within 64-99% for these samples.

Table 4.3. Measured and X-ray CT structural parameters of the porous Al structure.

Sample	Permeability, k_0 /10^{-09} (m^2)	Form drag coefficient, C, (m^{-1})	Forchheimer coefficient, C_F [-]
EXPT-Y1	13.37	17583.26	2.03
μCT-Y1	13.51	17465.76	2.03
EXPT-Y2	17.00	5416.74	0.71
μCT-Y2	17.08	5801.76	0.76
EXPT-Y3	19.26	4491.40	0.62
μCT-Y3	18.01	3985.55	0.53
EXPT-Y4	31.24	1635.75	0.29
μCT-Y4	33.45	1700.52	0.31
EXPT-X1	4.16	14249.65	0.92
EXPT-Z1	18.98	6474.63	0.89

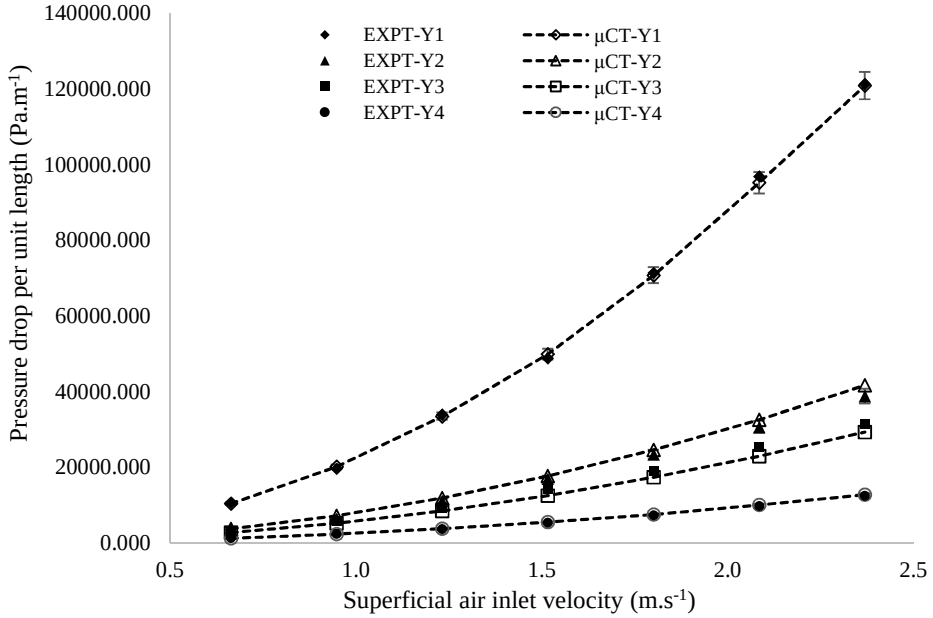


Fig 4.22. Graph of measured and modelled (using X-ray CT images) pressure drops per unit thickness ($Pa.m^{-1}$) against superficial air inlet velocity ($m.s^{-1}$).

Agreement between the experimentally measured and X-ray CT CFD computed values of unit pressure drops for all samples (Y1-Y4) is good with an average mean square root (R^2) fit to the measured data of 99, 105, 95 and 102%, as porosity increases respectively. Despite the lack of observable changes in porosity level, pore morphology and shape popularized by packing errors and the presence of splintered-half-sized spherical salts used during casting of these structures, a ±2% discrepancy in the computed values of unit pressure drop measured for RVE's taken at different Z position within the porous matrices was observed. These deviations are within the expected and established limits for the precise prediction of flow behaviour in more open porous structure as specified in (Diani et al., 2015).

4.6.4 Comparison with CFD simulation of airflow through "virtually-derived" macroporous spherical structures.

Fluid flow through "computer-generated" spherical structures mirroring the skeletal and air phases of the "real" metallic structures were carried adopting image processing steps, RVE generation, characterization and numerical simulation similar to the CT-derived structures. Structural characterization of this "virtual" structures shows very little or no clear deviation from the CT images as presented in Table 4.2.

Fig 4.23 presents velocity profile plots carried out on resolving flow through equally spaced three-dimensional RVE sizes ($8x8x8mm^3$) of the X-ray CT (top) and DEM-derived (bottom) structures at an extremely low ($3.35mm.s^{-1}$) and high ($1.25m.s^{-1}$) pore inlet velocities to serve as a basis for comparison. Within the laminar air flow through these structures, there exist little or insignificant deviations between the velocity scales recorded in the legends which can be attributed to the tolerable agreement between the structural parameters of the porous structures, most importantly, their window sizes and porosities. With this, there is the confidence that flow computed through the "virtual" structures within the specified range of laminar flow would not deviate largely from the experimentally measured values of pressure drops and CT computed flow data.

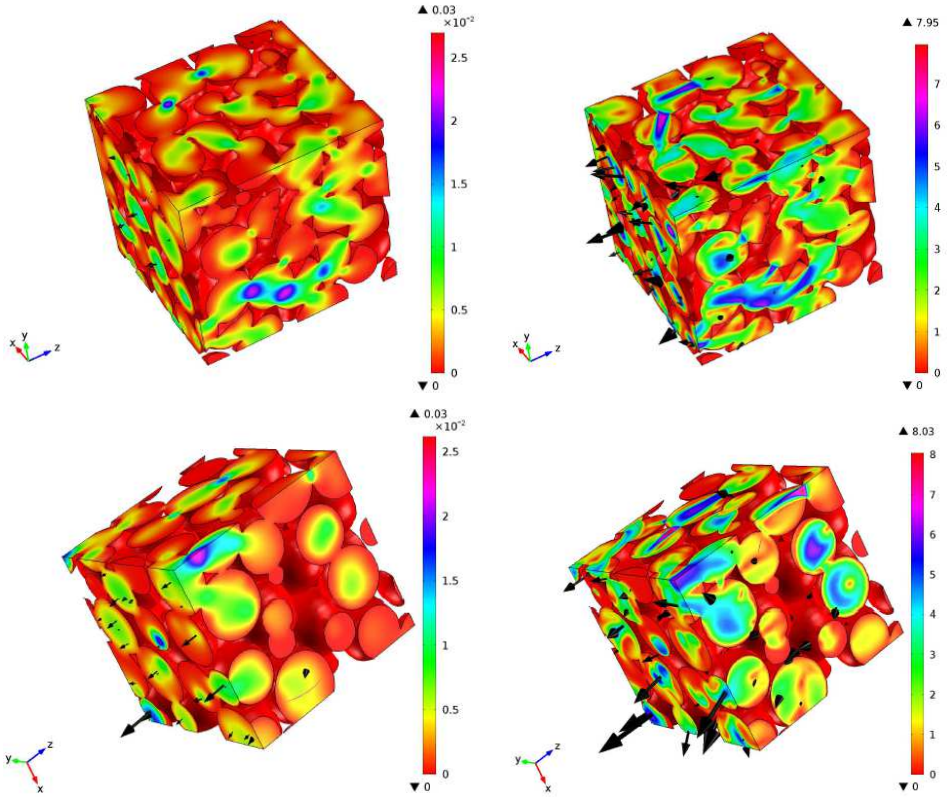


Fig 4.23. Three-dimensional (3D) velocity magnitude profile plots computed using X-ray CT images of the "real" structure (top, Ø=75.2%, D_w=741µm & D_p=2.0-2.5mm) and DEM "virtual" macroporous spherical structures (bottom, Ø=74.7%, D_w=731µm & D_p =2.0-2.5mm) of similar RVE three dimensional spaces (8x8x8 mm^3) for a pore inlet velocity of 3.35mm.s^{-1} (left) and 1.25m.s^{-1} (right) [*Numerical scales unit for the legends measured in m.s^{-1}*].

Fig 4.24 presents the unit pressure drops (Pa.m^{-1}) developed across the "virtual" (DEM) and "real" structures against superficial air inlet velocity (m.s^{-1}). At the extremes of porosity levels, the agreement between the DEM and CT models is good with pressure drop at the highest for the lowest-porosity structure and lowest for the highest porosity structure. At the mid-porosity value for the "virtual" structure, the agreement is good when compared to the experimentally measured and CT data for flow through the mid-porosities "real" structures, precisely, Y2 and Y3 (Fig 4.24). At the extreme porosity levels, per usual, Y1 and Y4 structures, the percentage deviation of computed unit pressure drop developed across the CT-derived structure are respectively 0.14% (lower) and 0.95% (higher) when compared to the experimentally measured data of unit

pressure drop developed across the "real" structures. Similarly, for the DEM-derived structures, the percentage deviations from reality are 3.49% (lower) and 8.48% (lower) respectively for the lowest and highest porosity structures and are presented in Fig 4.25. A tabular representation of the computed permeability (both at Darcy and Forchheimer regimes), Form drag and Forchheimer coefficients for both the CT and "virtually" DEM-derived macroporous structures are presented in Table 4.4. The Darcy values of permeabilities were computed by resolving pressure drops across the CT and DEM structures using Stokes equation available in the Fluid module of COMSOL Multiphysics 5.0™ at very low superficial air inlet velocities, typical below 5mm.s^{-1} (i.e. $Re_D < 1.0$), and neglecting the inertial term in Eq 2.15 to compute permeability values.

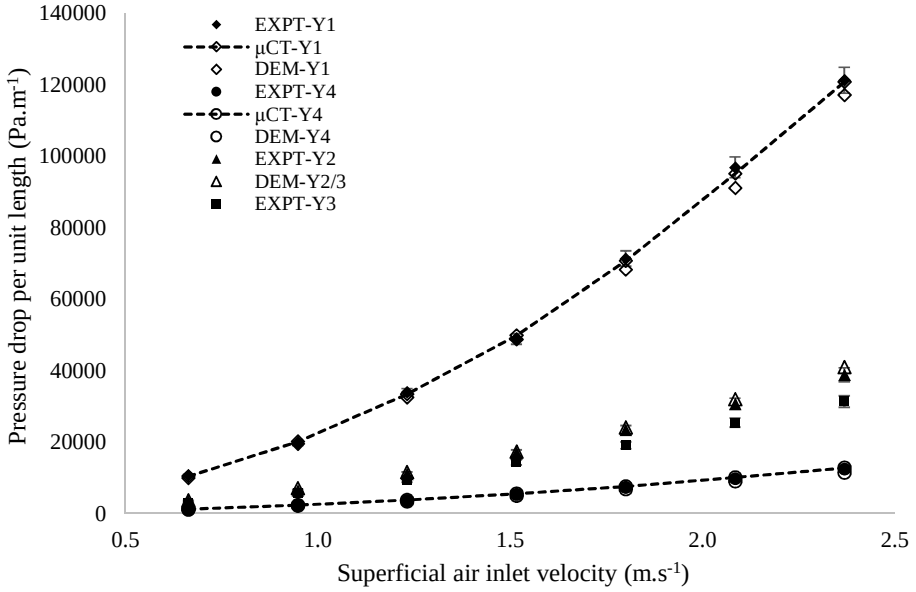


Fig 4.24. Graph of measured and modelled (using X-ray CT and DEM images) pressure drops per unit thickness (Pa.m^{-1}) against superficial air inlet velocity (m.s^{-1}) for Y1-Y4 structures.

Table 4.4. X-ray CT and DEM based flow parameters of Y1 and Y4 structures.

Sample	Permeability k_0 /10^{-09}m^2 (Darcy)	Permeability, k_0 /10^{-09}m^2 (Forch-heimer)	Form drag coefficient, C, (m^{-1})	Forchheimer coefficient, C_F, [-]
µCT-Y1	10.50	13.50	17465.76	2.03
DEM-Y1	10.10	12.31	16798.37	1.86
µCT-Y4	28.33	33.45	1700.52	0.31
DEM-Y4	29.50	34.51	1515.66	0.28

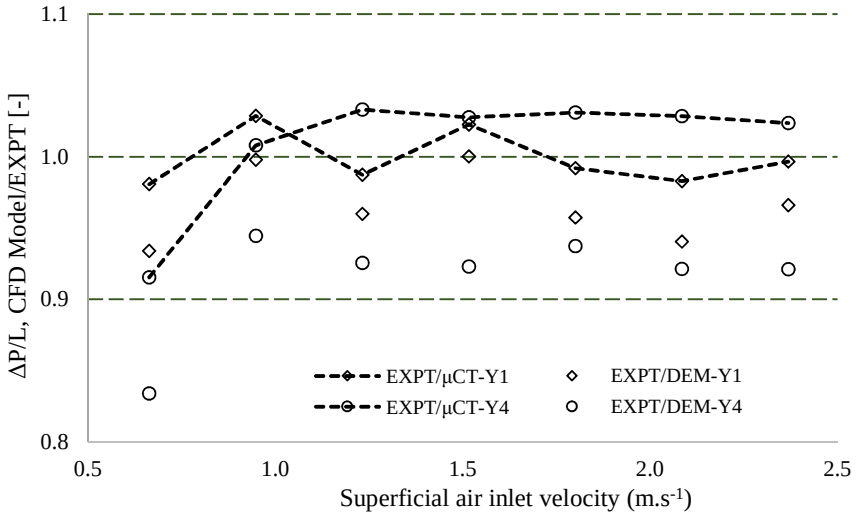


Fig 4.25. Plots of the ratio of measured to CFD modelled (X-ray CT and DEM) unit pressure drop [-] against superficial air inlet velocity ($m.s^{-1}$) for Y1 and Y4 structures.

The X-ray CT approach to modelling the unit pressure drop developed across the "real" structure appeared to be more literal in defining the flow behaviour of these structures both at the low and high velocities when compared to the outcome of the flow through the "virtually-replicated" structures. This is attributed, in part, to the non-spherical nature of the "real" salt samples used during casting and has the capacity to vary the size of the "bottleneck" and contacts made by connecting pores within the microstructure (Otaru and Kennedy, 2016). Structural inhomogeneity of the "real" samples resulting from the presence of half-sized salts reduces the mean circularity of the CT samples to within 0.80-0.85 whilst the DEM-derived structure is homogeneous all through with mean circularity close to unity, typically, between 0.99-1.0 (Fig 4.26). There is the hope that deviation between the "real" and "virtual" structures can be minimized to a greater extent if the salt used during casting can be made more spherical with little or no unwanted half-sized cells appearing in the "real" structures (Fig 4.6-4.10). This would help reduce dependency on the CT images

as an outlet and supplement the available options for understanding and predicting flow behaviour across "bottleneck" structures at reduced operational cost. Other benefits like variation in the structural morphology, pore and window sizes, easy to process binary images and reduced computationally time and memory are associated with the DEM-derived structures. Due to the homogeneous nature of the DEM structures, it is easier to compute flow on a nearly isotropic and lesser-sized RVE structure (typically for flow length 6x the mean pore radii giving equal porosity as computed for the larger volume) when compared to the non-homogenous near-spherical CT structures presented herein.

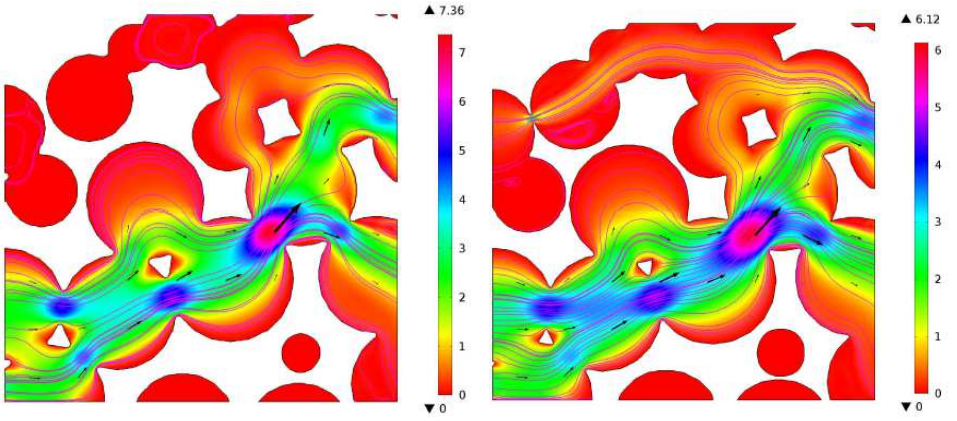


Fig 4.26. Two-dimensional (2D) velocity profile plots for flow (left to right) through porous samples Y1 (left) and Y4 (right) for an inlet pore velocity of 1m s^{-1} [*Numerical scales unit for the legends measured in* $m.s^{-1}$].

4.6.5 Modelling challenges associated with X-ray CT computation.

Computational modelling of flow through the structure-derived RVE CT representation of the whole test sample is uncommonly feasible owing to the computational power needed to resolve such exceedingly high-density cells occupying the fluid domain matrix of the porous structure. Though, morphology and local variations in porosity may occur between the "real" sample and RVE controlled volume used in the CT modelling, but precise predictions of the experimentally measured data are greatly dependent on the accurate

representation of the model structure using high-resolution CT images, image processing complexities and the choice of boundary conditions applied to the geometrical RVE CT volume. Image rendering and thresholding of the greyscale CT images can be a herculean task but the need to ensuring the windows and pores geometry is accurately preserved is underpinning to the actualization of unequivocal model values in this study.

The contributory effects of developed flow during modelling cannot be unnoticed especially for the lowest density structure, Y1. Whilst changes in the RVE flow direction from 6-15mm yielded very little or no clear discrepancies in the computed unit pressure drop developed across the 3D CT volume of Y2, Y3 and Y4 structures, the initial agreement between the experimentally measured and computed values of unit pressure drop developed across an 8mm thick (and below) RVE length is weakest (R^2~92) for the Y1 structure. This is the structure where the representation of the "real" structure at both the CT and image processing thresholding are most challenging. This was also observed for near-spherical "bottleneck" structures of this type, typically with large pores and small windows presented in (Otaru and Kennedy, 2014). Erosion and dilation of the skeletal phase of this microstructure would respectively lead to a far-reaching over-estimation of the "real" values. It became apparently clear (Fig 4.22) that extending the RVE CT flow length to 10mm thick and above for this low-density structure (Y1) significantly improved our prediction from 92 to 99% of the "real" value but at the price of extremely high computational time and power.

In the "real" measurement on 10mm shorter samples of this structure, overall agreement is 97% closer to flow measured on the longer 34.5mm sample. Hence,

capturing detailed and efficient information on the windows sizes, contacts and pores within this inhomogeneous low-density structure through developed flow resulted in accurate predictive values of unit pressure drops across the structure. A 2D (YZ section) visualization of the actual 3D CT computed velocity (left) and pressure (right) profile plots for a superficial air inlet velocity of 1m.s^{-1} are presented in Fig 4.27 with air flowing from top to bottom of the structures. The lowest density structure Y1 is presented on top with x, y and z dimensions of 8x8x10mm^3 whilst the highest density structure (Y4) is presented at the bottom with x, y and z dimensions of 8x8x8mm^3. Similarly, Y2 and Y3 structures have the same dimensions as Y4.

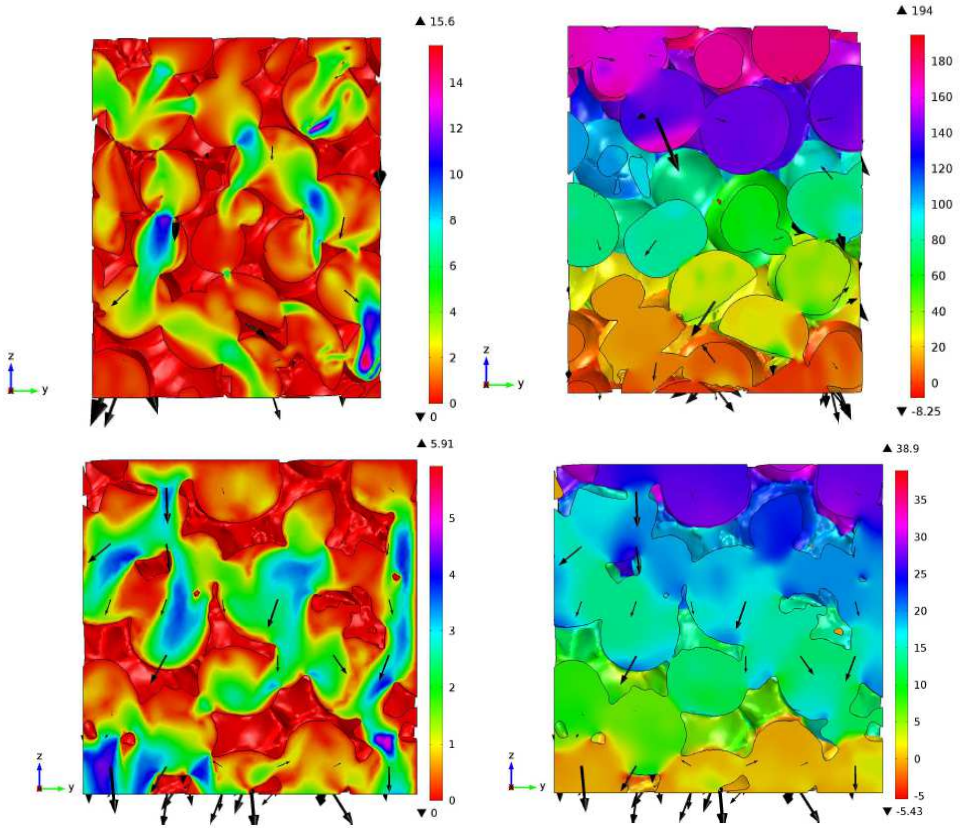


Fig 4.27. Two-dimensional (2D) visualization of the actual three-dimensional (3D) CT volume of the velocity (left) and pressure drop (right) distribution for flow through porous samples Y1 (top) and Y4 (bottom) for air superficial inlet velocity of 1m s^{-1} [*Numerical scales unit for the legends measured in m.s^{-1} and Pa for the velocity and pressure plots respectively*].

4.6.6 Extension to "semi-virtual" CT structures

While "virtual" representation of widely used highly porous metallic structures like the Inconel and Recemat samples have been presented in the literature using Lord Kelvin and Weaire-Phelan unit cell approaches, the DEM packing of near-spherical structures presented herein has shown the possibility to predict the structural and flow parameters of "real" metallic structures made by replication casting of near-spherical salts without having necessarily to produce the "real" samples. The enormous benefits in the flexibility of microstructural variation of the "virtually" created structures undoubtedly gave the DEM structures greater advantages over the CT representation of the "real" structures. Also, computational power, time and cost could be cut short through the theoretical and analytical relations that exist between the flow and structural parameters of the porous matrices.

Understanding of the microstructural effects on the changes in the pressure drop behaviour (in the absence of producing the "real" samples) can be done through sensibly creating "semi-virtual" three-dimensional RVE CT volumes from the "real" RVE CT structures. Erosion (subtracting pixels) of the RVE CT skeletal phase or dilation (adding pixels) of the RVE CT fluid phase within the ScanIP module of Simpleware^{TM} is like the application of lower differential pressure, typically below 1bar, during casting of the "real" samples (1 pixel = 26μm). In contrast, dilating the skeletal phase or eroding the fluid phase of the RVE CT structure is like the application of higher differential pressure, typically above 1bar, during casting. The Navier-Stokes equation was resolved for the RVE CT and adapted CT structure for velocities between 0.6 and 2.36m.s^{-1}. Also, CFD pressure drop was attained for very low velocities, typical for pore diameter

Reynolds number less than 1 to assist in predicting the permeability of these structures in the Darcy regime of fluid flow. Fig 4.28 presents two-dimensional fluid domain model contour view (top) and three-dimensional (bottom) skeletal phase of the "real" RVE CT structure Y3 and structural eroded structures with 1- (center, Y31) and 2- (right, Y32) removed.

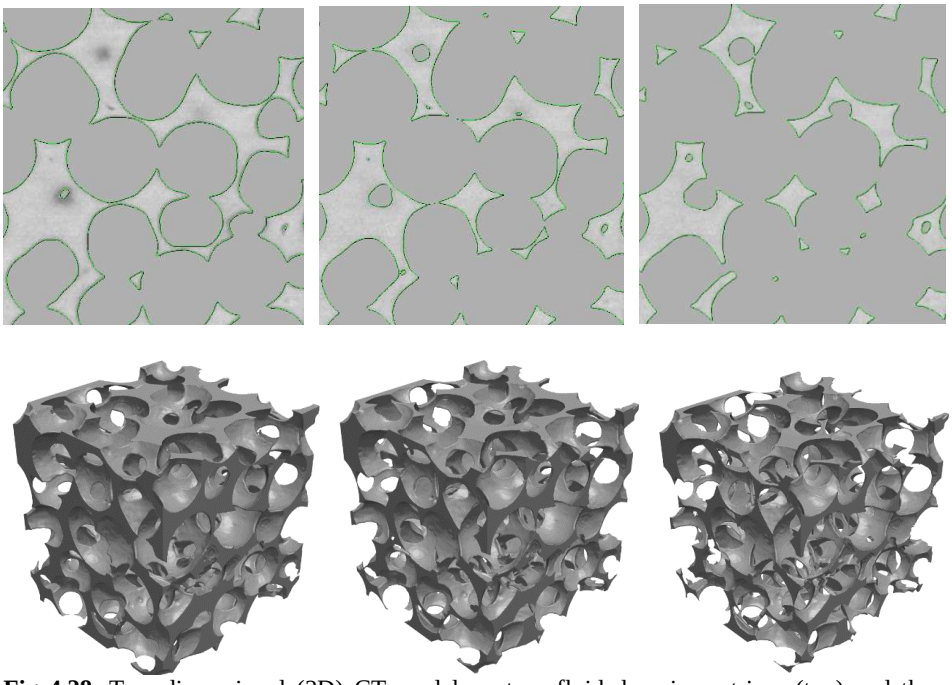


Fig 4.28. Two-dimensional (2D) CT model contour fluid domain matrices (top) and three-dimensional (3D) CT RVE skeletal phases (bottom) for lowest porosity structure, Y3 (left) and after structural erosion of 1- (center, Y31) and 2- (right, Y32) pixels removed from the skeletal phase for 8.5mm flow thickness.

Fig 4.29 presents CFD computed data obtained for the unit pressure drops developed across the "real" CT structures, Y3 and Y4 and the "semi-virtual" structures, Y11-Y15, with 1-5 pixels removed from the skeletal phase of the lowest porosity real CT structure, Y1. Similarly, tabular representation of the structural and flow parameters for the "real" and "semi-virtual" structures are presented in Table 4.5. Evidently, porosity, pore contacts, pore openings, pore sizes and structural specific surface (defined as the ratio of the surface area of the 3D RVE CT structure to its volume, σ_{FF}, whilst the ratio of the structural

surface area to the bulk volume is represented by σ_{FB}) consistently increase for the adapted "semi-virtual" CT structures from the "real" 3D CT RVE volume (Fig 4.28 and Table 4.5).

Fig 4.29 shows that the pressure drops developed across the "semi-virtual" structures (flow thickness, 8.5mm) consistently decrease with the removal of pixel elements from the skeletal phases. A 2D representation of the actual 3D (YZ-axis) of velocity and pressure profile plots presented in Fig 4.30 shows the highest velocity of 8.45m.s^{-1} and highest pressure of 81.5Pa recorded on the legends (scale bar) for the "real" CT structure with mean openings, 741μm. The velocity and pressure drop consistently decrease with 1-pixel (mean openings, 921μm) and 2-pixels (mean openings, 1163μm) removed from the skeletal phase of the Y3 structure, typically, 5.97 to 4.42m.s^{-1} and 53.6 to 24.4Pa respectively. Also, a significant increase in permeability, k_0, and decrease in Form drag coefficients, C, were consistent with those affected by microstructural changes because of reduction in applied differential pressure in the "real" sample. Typical examples are the close agreements between the structural parameters and unit pressure drop developed for the "real" Y3 RVE CT sample and the 1-pixel structural eroded "semi-virtual" sample Y11.

Table 4.5. Structural and flow data for the real, Y3 & Y4 and eroded (Y1i) CT structures.

Sample	Ø (%)	Dp (mm)	Dw (mm)	$k_0/10^{-09}m^2$ (Forchheimer)	C (m^{-1})	σ_{FF} (m^{-1})	σ_{FB} (m^{-1})
μCT-Y1	70.8	2.23	0.69	13.90	17583.26	6413.09	2649.08
μCT-Y11	76.8	2.29	0.84	21.28	4152.82	7351.45	2214.70
μCT-Y12	82.1	2.36	1.02	40.32	1399.60	8031.83	1853.30
μCT-Y13	86.6	2.43	1.15	50.73	826.96	8581.19	1564.39
μCT-Y14	90.2	2.48	1.35	117.04	509.96	9776.44	1062.27
μCT-Y15	93.0	2.55	1.57	223.95	286.76	10567.74	791.27
μCT-Y3	75.2	2.27	0.74	18.007	3985.55	7312.92	2410.80
μCT-Y4	78.2	2.23	0.89	33.45	1700.52	7455.44	2054.44

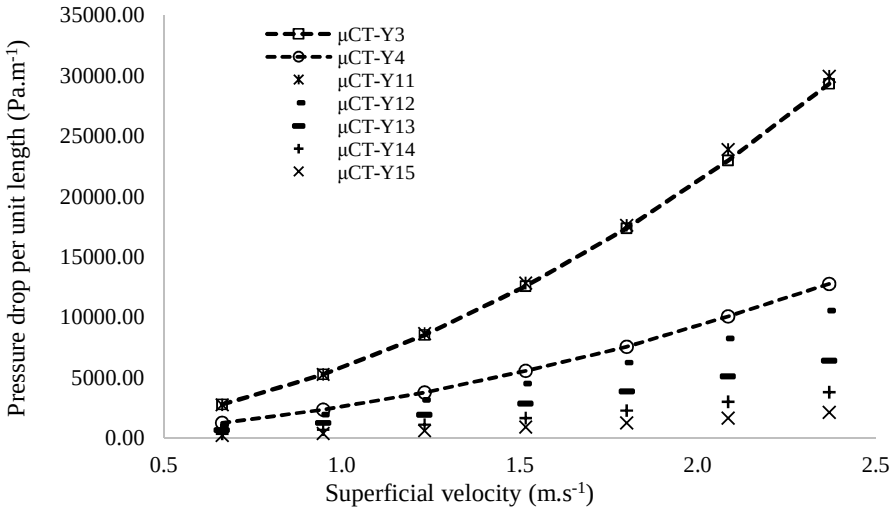


Fig 4.29. Plots of simulated pressure drop per unit length ($Pa.m^{-1}$) against superficial air inlet velocity ($m.s^{-1}$) for semi-virtual structures (structural domain erosion, 1-5 pixel removed) using CT images compared with simulations for near-equivalent "real" samples.

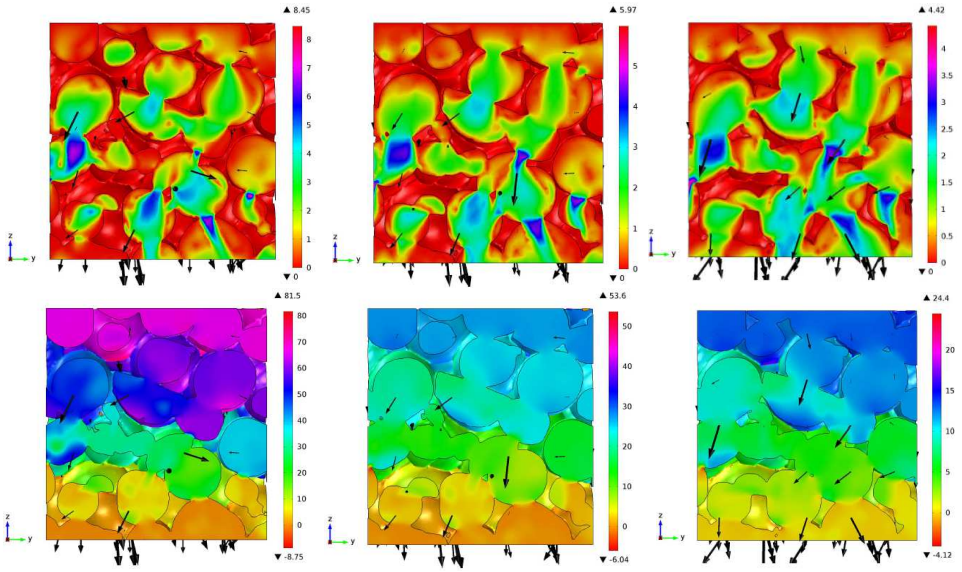


Fig 4.30. Two-dimensional (2D) visualization of the actual three-dimensional (3D) CT volume of the velocity (top) and pressure drop (bottom) distribution for flow through porous samples Y3 (left) and after structural erosion of 1- (centre, Y31) and 2- (right, Y32) pixels removed from the skeletal phase of the microstructure for superficial air inlet velocity of 1m s^{-1} [*Numerical scales unit for the legends measured in* $m.s^{-1}$ *and Pa for the velocity and pressure plots respectively*].

In addition, the unit pressure drop developed across the "real" Y4 RVE CT sample is slightly higher than the 2-pixels structural eroded (Y12) structure due to the important smaller window sizes, mean pore sizes and porosity of the "real" Y4 RVE CT structure, typically 892µm, 2.23mm and 78.2% respectively whilst

for the lower pressure drop Y12 structure, the structural parameters recorded are 1017μm, 2.36mm and 82.1%. The mean openings and computed value of permeability consistently increase with continued structural erosion, but care was taken not to over erode the structures in order to avoid isolated and lost skeletons (ligaments) within the porous structures. Tabular representation of structural and flow data computed for all the "real" and "semi-virtual" structures are presented in Table 4.5A of the appendix pages.

Analytical relationship between the structural parameters and permeability of the "bottleneck-type" porous structures were made possible through the application of dimensionless analysis. Fig 4.31 plots a reduced permeability against the reduced window to pore diameter size ratio using data obtained for the combined "real CT" and "semi-virtual" RVE CT samples with a linear ($R^2 \geq 0.95$) permeability dependent on the structural parameters of the porous medium. For Darcy and Forchheimer flow of fluid, the empirical constants W_1^* in Eq 4.5 below are observed to be 0.0121 and 0.0157 respectively; thereby given slightly higher permeability values at the Forchheimer than Darcy. Similarly, a plot of the high velocity dependent Form drag and Forchheimer coefficients against the computed values of Forchheimer permeability in Fig 4.32 shows a near-power inverse relation between the viscous and inertial terms of the porous matrices.

$$k_0 = W_1^* \frac{\emptyset}{(1-\emptyset)} r_p r_w \qquad \text{Eq 4.5}$$

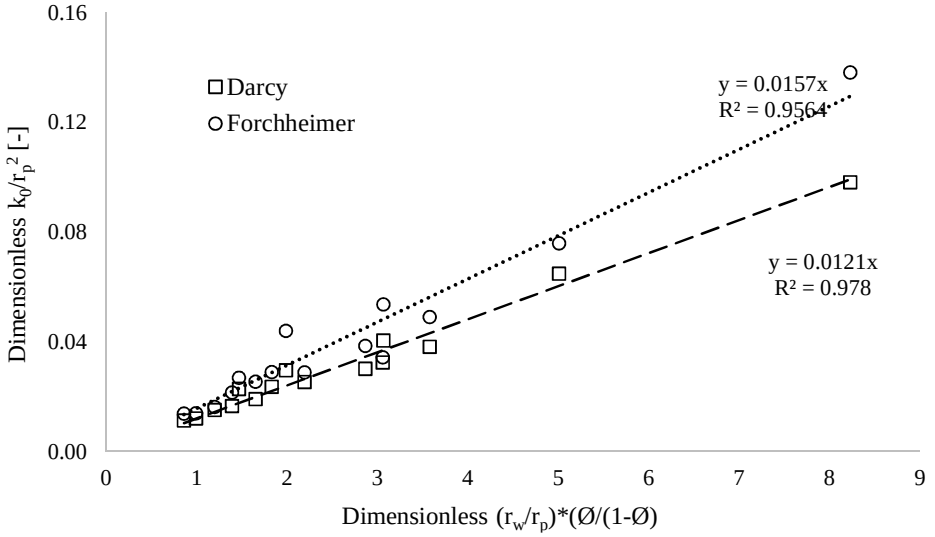


Fig 4.31. Dimensionless plots of permeability-structural parameters of the porous structures using CT images of Y's and fluid domain dilated structures.

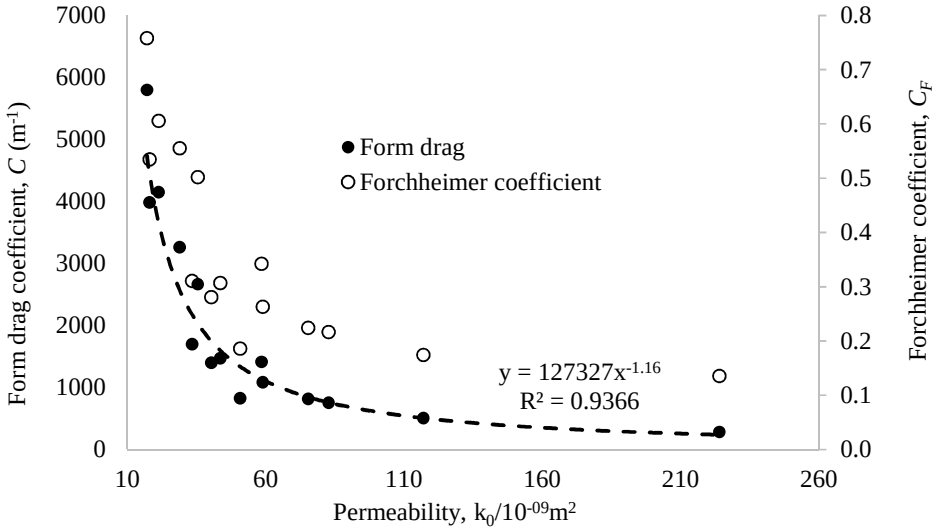


Fig 4.32. Graph of the viscous and inertial terms of the porous structure using the CT images of the Y's and fluid domain dilated structures.

Extensive work by Tadrist et al., 2004 points out that the well-known Ergun relation used for predicting flow through porous structures contains relatable practical relation between the viscous and inertial terms and the porosity of the materials. Whilst, the Ergun relation was said to accurately predict the pressure drop developed for flowing fluid across packed beds (Ergun, 1952, Richardson & Backhurst, 2002, Karimian & Straatman, 2008 and Liu & Hwang, 2012), the

direct application of similar model does not accurately predict the pressure drops developed across porous metallic structures (Dukhan, 2013). A reciprocal relation for the viscous and inertial terms was proposed in Dukhan and Patel, 2008 to be dependent on the frame (structure) surface area per unit structural volume (σ_{FF}), and structural surface area per unit bulk volume (σ_{FB}) respectively (Eq 4.6). A linear inverse dependence of the permeability against the reduced computed specific surface (within ScanIP) was observed in Fig 4.33 with empirical constants W_2^* obtained as 7.73 and 6.42 for flow in Darcy and Forchheimer regime respectively. A linear relation between the Form drag and reduced specific surface (σ_{FB}) in their natural log form was observed (Fig 4.34) and Eq 4.7 was attained to theoretically predict the value of Form drag in the Forchheimer regime of fluid flow.

$$1/k_0 = W_2^* \frac{(1-\emptyset)^2}{\emptyset^3 (1/\sigma_{FF})^2} \;\&\; C = W_3^* \frac{(1-\emptyset)}{\emptyset^3 (1/\sigma_{FB})} \qquad \text{Eq 4.6}$$

$$C = 1.059 \exp\left\{0.912\, ln\left(\frac{(1-\emptyset)\sigma_{FB}}{\emptyset^3}\right) + 1.647\right\} \qquad \text{Eq 4.7}$$

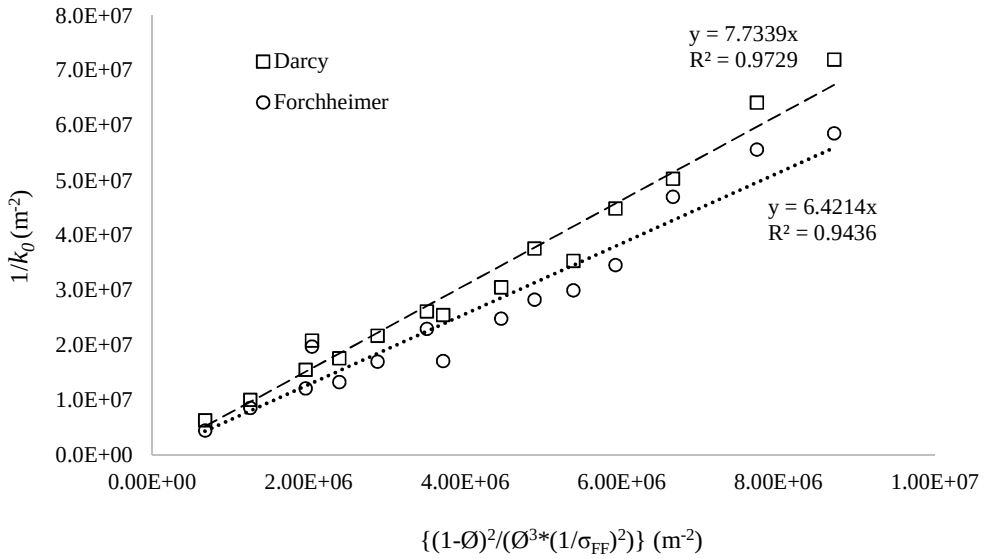


Fig 4.33. Plots of permeability inverse (m^{-2}) against structural parameters (m^{-2}) of the porous structure using the CT images of the Y's and fluid domain dilated structures.

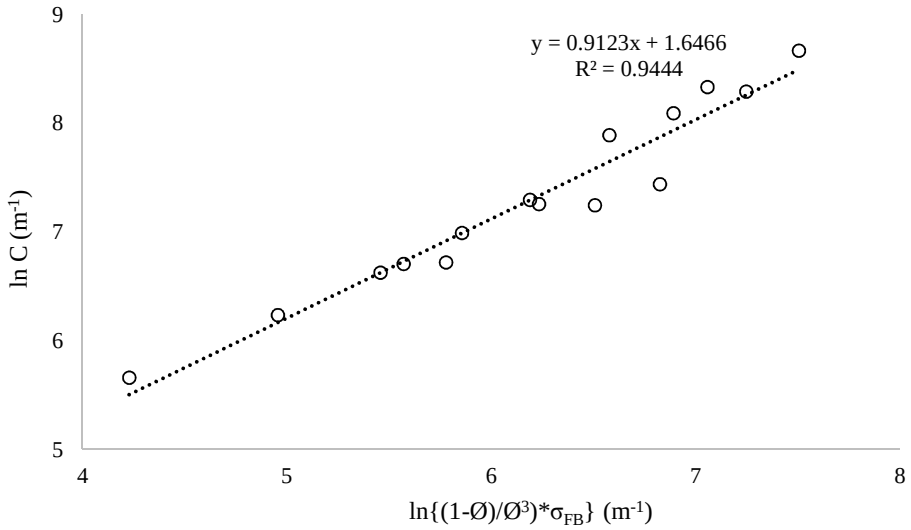


Fig 4.34. The plot of the natural log of Form drag coefficient (m^{-1}) against natural log of structural parameters (m^{-1}) of the porous structure using the CT images of the Y's and fluid domain dilated structures.

The work put together on this reciprocal relation by Antohe et al. (1997), Boomsma and Poulikakos (2002), Hwang et al. (2002), and Dukhan and Patel (2008) for the experimental measurement of pressure drop developed across 10-40PPI Duocel foams (topology similar to the Lord Kelvin and Weaire-Phelan unit cell representation) indicated a direct near-power law relation with 88 and 95% correlation coefficient respectively attained for the permeability and Form drag plots and empirical constants, smaller than the one predicted herein, for their range of sample sizes and topology. This shows that the empirical constants may vary for foams with different pore morphology and shape factor.

Comparative analysis of the measured values of k_0 and C for the "bottleneck-type" structures presented herein shows 5% less in the predicted values of these terms using our proposed models. For commercially-used high-density, Inconel 450μm and Recemat RCM-NCX 1723 samples structures, having different topologies from the one presented herein (84 and 91% porosities respectively), CFD values of permeability obtained in the Darcy regime are $1.41\pm0.12\text{x}10^{-09}m^2$

and $1.62\pm0.26\text{x}10^{-08}\text{m}^2$. The predictive values of permeability using Eq 4.5 are $1.65\text{x}10^{-09}$ and $1.63\text{x}10^{-08}\text{m}^2$ respectively. Similarly, these values are respectively $1.45\text{x}10^{-09}$ and $1.48\text{x}10^{-08}\text{m}^2$ using Eq 4.6.

The proximity between the measured and predicted values indicate the reliability of the proposed models to predict accurately the viscous and inertial terms of the porous metallic structures in the Darcy and Forchheimer regime despite their geometrical variations and shapes. With the empirical constants known, the viscous and inertial coefficients of porous metallic structures could be determined without the need to go through the costly experimental and computational modelling routes. Hence, the design of this novel material capable of withstanding any engineering applications could be aided through knowing values of k_0 and *C* at the least possible time. For flow at extremely high velocities (Turbulent flow regime), *C* is more important, conversely, *C* is neglected at the very low (Darcy flow regime) velocities and both are important for the laminar flow of fluid thereof. Tabular representation of the proposed models is presented in Table 4.6.

Table 4.6. A tabular representation of proposed models and their applications

Model name	Equations	Applications
Darcy	$k_0 = 0.0121\frac{\emptyset}{(1-\emptyset)}r_p r_w$	Suitable to predict permeability of porous metallic structures typified by porosity within 70 and 95% in the Darcy regime.
	$1/k_0 = 7.73\frac{(1-\emptyset)^2}{\emptyset^3(1/\sigma_{FF})^2}$	
Forchheimer	$k_0 = 0.0157\frac{\emptyset}{(1-\emptyset)}r_p r_w$	Suitable to predict permeability of porous metallic structures typified by porosity within 70 and 95% in the Forchheimer regime.
	$1/k_0 = 6.42\frac{(1-\emptyset)^2}{\emptyset^3(1/\sigma_{FF})^2}$	

	$C = 1.059 \exp\left\{0.912\, ln\left(\frac{(1-\emptyset)\sigma_{FB}}{\emptyset^3}\right) + 1.647\right\}$	Suitable to predict Form drag of porous metallic structures typified by porosity within 70 and 95% in the Forchheimer regime.

4.7 Conclusions

Structural characterization, flow measurement and pore-level numerical simulation of infiltration-processed "bottleneck-type" structures have been presented using tomography images of the "real" structures and sphere-packing model thereof. The permeability of the structures is said to greatly depend on the sizes of the "bottleneck" between connecting pores, typically higher for larger apertures and lower for smaller apertures. The inertial term increases for low-density structures and decreases for high-density structures with a reduced structural surface area to bulk volume.

Agreements between the experimental and modelled values of pressure drop developed across the "real" and "virtual" porous structures are good and within expected scatter. The simplicity in terms of structural re-arrangement of the virtual structure based on the known value of foam nominal porosity and high computational cost imposed by the CT approach makes the DEM approach an equitable alternative.

The extension to "semi-virtual" CT structures adapted from the "real" CT representative structures through structural erosion within ScanIP enables us to understand clearly the response of pressure drops in relation to changes in the structural parameters of the microstructures.

Analytical models capable of predicting the viscous and inertial terms of flow metallic structures were proposed to reduce the dependency on the costly experimental setup and CFD.

Knowledge acquired so far on structural and flow information of porous metallic structure could prove useful to the design of self-supporting and high impact porous absorber in loudspeaker application. Hence, there is the need to explore other structural parameters influencing the sound absorption behaviour of this material.

CHAPTER 5

NUMERICAL SIMULATION OF PRESSURE WAVE ACROSS "BOTTLENECK-TYPE" POROUS STRUCTURES

5.1 Summary

In this chapter, numerical simulation of sound pressure wave across "bottleneck-type" monosized porous structures using structural parameters obtained from X-ray CT images of "real" structures, sphere-packing model and the possible ranges of pore sizes needed for the realistic casting of "bottleneck" structures for soundproofing purposes are presented. Reasonable agreements between predicted and measured data available in the literature were substantiated for this structure and extended to model commercially available sound absorbing structures with nearly transversely isotropic cells to structures with non-uniform sections and possible constrictions. By varying the pore sizes, capillary radius and connectivity of the "bottleneck-type" structures, the characteristic absorption curve confirms the high dependence of acoustic absorption properties of the material on the permeability, porosity and window to pore size ratio; typically, within 0.4-1.5x$10^{-09}$$m^2$, 60-80% and 0.1-0.3 respectively, for efficient soundproofing.

NB: An article from this chapter has been published in Scripta Materialia (Click on the link: https://doi.org/10.1016/j.scriptamat.2018.03.022)

5.2 Introduction

Till present, noise and vibrational control in public places (industrial plants, football stadium, cricket grounds, and railway tunnels) and buildings (sport centres, musical rooms, religious rooms, pubs, clubs, and auditoria) are often done with the support of natural (glass wool, cotton, asbestos, fur felt, hemp, and

flax) and synthetic fibers (polyester, polypropylene, and kevlar) materials. These materials are known to be very good absorbers and inexpensive (Jorges and Malcom, 2010) but there low heat resistance, high-moisture content and decrease in absorption potential over time (Deng et al., 2008) has limited their applications across the wide spectrum of engineering soundproofing devices.

Artificially made lightweight, low moisture, high heat resistance, high specific surface, structural controlled and self-supporting non-flammable open-celled metallic structures for sound absorption are already commercially available (Xiaolin, et al., 2009) and has seen them used in a variety of locations. This distinctive combination of multi-practicable performance lends porous metallic structures to be useful in a wide range of noise and vibrational control thereby replacing the complex fibrous structures.

Studies have shown that enhancing the acoustic absorption performance of porous metallic structures are done by insertion of airgap during installation (Lu, and He, 2000, Bo and Tianning, 2009, and Muhammed et al., 2013) which predominantly becomes Helmholtz resonant absorption (Han, et al., 2003), increasing the porous body layer thickness (Yeh et al., 1995, and Liu and Chen, 2014), back cavity (Liu and Chen, 2014), hole-drilling or rolling and prearrangement of space fillers during production (Lu et al., 1999) as in the case of replication-casting process adopted in previous chapters.

Much difficulties are attached in controlling process variables during the processing of metal foams, therefore structural topology and properties (porosity, tortuosity, permeability, surface area, pore openings and pore sizes) can vary significantly with revealing the effect on the acoustic absorption

behaviour of the structure. For instance, a high porosity (90-95%) and open morphology corresponds to metal foams of large pore sizes, typically, between 2.5-5.0mm, low airflow resistance (Liu and Hwang, 2012, Otaru et al., 2018, Oun and Kennedy, 2014, and Han, et al., 2003) and performs extremely poorly when presented to absorbed pressure waves at low and high frequencies. This is confirmed in Lautensack and Kabel, 2009 for the sound absorption response of commercially used Recemat RCM-NCX 2733 structure.

The pores in open-celled structures are connected together with touching cells which evidently allows pressure wave to explore the internal architecture of the structure from the face presented to sound source to the exit. Experimental study on the sound absorption coefficient of Alporas foam structure in Lu et al. (1999) pointed out that, the sound absorption coefficient of this structure increases with a decrease in the relative density (R.D) of the sample. The relative density was observed to be small (~ 0.1) for effective sound absorption and under compression, sample porosity decreases (becoming closed-cells) and a shift in absorption curve to the frequency minimum and reduced peak of absorption were observed when compared to an uncompressed foam of similar thickness.

Sound absorption measurement of semi open-celled (2.0-4.0mm) foams in Lu et al. (1999) provides a peak absorption coefficient of 0.8 for frequency in the purview of 800-2000Hz. A comparative analysis of the absorption behaviour of metallic aluminium foams of different pore openings in Han, et al. (2003), favoured open-celled structure when compared to the closed ones. They show that the aluminium (Al) foam samples with a small nominal pore size, typically below 500μm, exhibit the best absorption peak when there is no airgap and predominantly Helmholtz resonant absorption in the presence of airgap.

Li et al. (2011) concluded that the sound absorption behaviour of "bottleneck" structures made by the replication-casting processes of packed beds of spherical salt (porogens) increases with increased number of smaller sized apertures, typically of mean connectivity size between 300-400μm and porosities to within 60-70%. An approximate window sizes (pore openings) value of 100μm was specified in Wang and Lu (1999), to be optimum with greater sound absorption and noise reduction coefficients. Lu and He (2000) measured the static air flow resistivity and sound absorption coefficient for cellular metals with semi-open cells having different packing densities, pore sizes and pore openings. The influence of pore sizes, porosity and foam layer thickness on the acoustic performance of porous Al foam structures were further substantiated in Lu et al. (2009), and Zielinski (2015) put forward the important of microstructural parameters on the acoustic performance of porous absorber using randomly generated spheres.

The structural thickness dependent normal incidence absorption coefficient also termed as the ratio of sound intensity absorbed to incident sound intensity, (Sun et al., 2001) at varying degree of frequencies for several commercially known porous absorbers available in the literature are presented in Fig 5.1 whilst images of the structures are presented in Fig 5.2. Typical comparison from an acoustic perspective in Fig 5.1 indicates that the "bottleneck-type" (AL foam) porous metal structures (as in the case of Li et al., 2014 samples) performs poorly over the essential mid-frequency range (2000-4500 Hz) when compared to the performance of the fibrous materials (glass wool fibre, GWF, and melamine foam, MF) and porous sintered fibre metals (SFM) as shown in Fig 5.1 and 5.2.

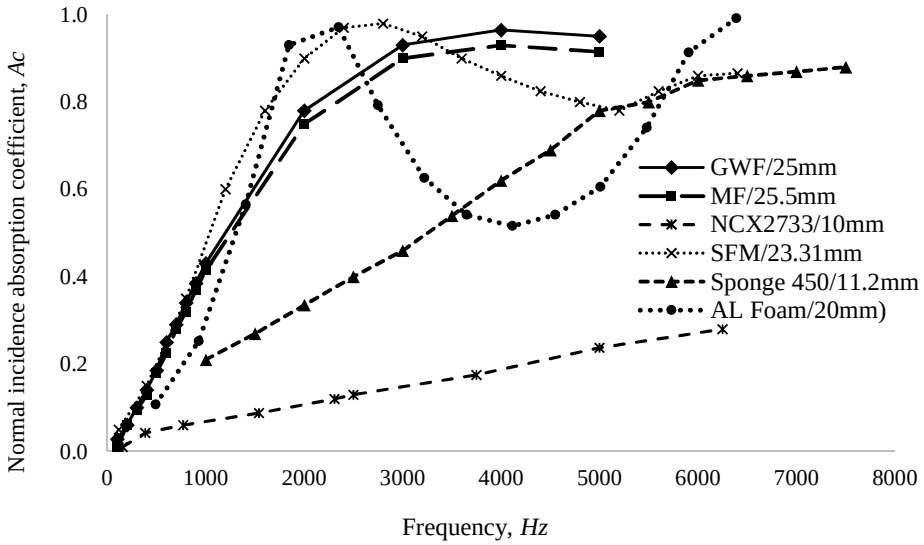


Fig 5.1. Plots of normal incidence absorption coefficient against frequency for a 25mm hard-backed glass wool fiber material (GWF, 98.7% porosity) by Kino and Ueno, 2008; 25.5mm hard-backed melamine foam (MF, 99.3% porosity) by Kino and Ueno, 2008; 10mm hard-backed nickel-chrome extra strong (NCX2733, 89.93% porosity) by Lautensack and Kabel, 2009; 23.31mm hardbacked porous sintered fiber metal (SFM, 90.94% porosity) by Bo and Tianning, 2009; 11.2mm hard-backed porous metal sponge 450 by Hinze and Rosler, 2014 and 20mm hard-backed open-celled aluminium foam structures with spherical cells presented by Li et al. 2014, (AL Foam, 60% porosity).

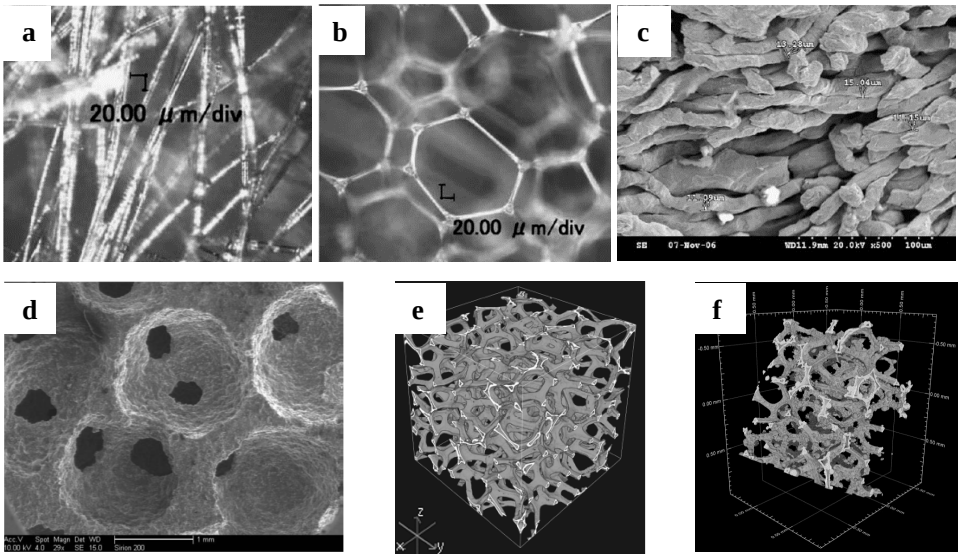


Fig 5.2. Digital microscope photograph of (a) Glass wool fiber material (GWF) by Kino and Ueno 2008 (b) Melamine foam (MF) by Kino and Ueno 2008 (c) Photographic cross-section of Porous sintered fiber metal structures (SFM) by Bo and Tianning, 2009 (d) Typical pore morphology of aluminium foam structure with spherical cells by Li et al., 2014 (e) 3D reconstructed X-ray CT image of nickel-chrome (NCX2733) extra strong structure by Lautensack and Kabel, 2009 and (f) 3D reconstructed X-ray CT image of porous metal sponge 450 by Hinze and Rosler, 2014.

This low-density (porosity~66%) semi open-celled structure (Fig 5.2d) is closely guided with connecting near-spherical pores to enable controlling of pressure waves to gainfully access the interior circular apertures and pores of the structure. When the number of cells in the structure is greater than one, succeeding cell naturally becomes cavity to a preceding cell exposed to incoming waves (Li et al., 2011).

Despite the improvement for this structure with its novel attributes (as in the case of Li et al., 2014) to perform well above pre-existing porous metallic structures particularly with those of geometry likened to Lord Kelvin and Weaire-Phelan (W-P) unit cell representations type (Fig 5.2e), their absorption potential is not envisioned to compare positively with commercially known soundproofing fibrous materials. An understanding of the changes of the foam properties (porosity, pores, and windows) resulting from microstructural alteration is essential for the optimization of this “bottleneck-type” structures toward increasing their absorption potential and is best performed by simulation. This part of the study is aimed at assessing the ability to numerically simulate the normal incidence absorption coefficient of the “bottleneck-type” porous metallic structures with the possibility to enhance their geometry, using only structural information and established models.

5.3 Structural characterization

The structural characterization and flow behaviour of “bottleneck-type” porous metallic structures using CT images of the “real” samples and “virtual” packed spherical structures to determine their structural parameters which relate the interaction between the fluids-solid phases in the materials have been carried out

using a representative volume element (RVE) reconstructed (in ScanIP) from 2D slices of images. These are well detailed in previous chapters and a few have been published in Otaru and Kennedy (2016), and Otaru et al. (2018). Also, the different poroacoustic models available in the literature which have been applied to model the characteristic acoustic impedance and sound absorption coefficient of porous absorbers for different structural morphology ranging from transversely isotropic pores to non-uniform sections with possible constrictions (Fig 2.9) are detailed in chapter 2 of this work.

Presently, the number of interdependent and indispensable structural parameters used in empirical models to describe the acoustical behaviour of porous materials varies between 1 and 8 depending on the complexity of the pore structure (Johnson et al., 1987). Typically, the airflow resistivity (σ), open porosity ($\emptyset$), dynamic tortuosity (τ), viscous characteristic length ($\wedge$), thermal characteristic length ($\bar{\wedge}$), static thermal permeability (k_0'), static viscous tortuosity (τ_0) and static thermal tortuosity (τ_0').

The airflow resistivity of these materials was determined to be a ratio of the fluid dynamic viscosity to the permeability of the porous structure (Yeh et al., 1995). Permeabilities (k_o) were determined by the numerical simulation of unit pressure drops per unit length (∇P) developed across a representative sample of porous body against superficial laminar fluid velocity (V) fitted to Darcy model (Eq 2.9). Important permeability data for most soundproofing devices are likely to be reported in the literature, but for "bottleneck-type" structures, model such as those in Despois and Mortenson (2005), and Furman et al. (2013) have shown to aptly predict permeability in the Darcy regime. More so, work by Otaru and Kennedy (2016) showed these models to accurately predict CFD simulations of

fluid flow through virtually-derived "bottleneck" monosized structures in the Darcy regime, better for those of higher capillary radius $r_c/r_p > 0.03$ (Fig 3.11).

As part of this work, the coordination numbers made by contacting spheres of particle sizes 1-3mm (used in chapter 3) were measured. For a range of pore openings, sizes, and porosities, the proposed "bottleneck" model was re-applied with an empirical fit to the measured coordination number (N_c) and fitted to the CFD permeability data with the following expression (with R^2~0.99) for window to pore ratio (r_w/r_p) between 0.17-0.40 (See Eq 5.1). Nominal porosities were measured to be the volume fraction of the representative volume element (RVE) fluid domain to the total volume of the macroporous structure and void spaces.

$$k_0 = \frac{1.03\, N_c\, \emptyset\, r_w^3}{6\pi\, r_p} \qquad \text{where} \quad N_c = 17\, \emptyset \left(\frac{r_w}{r_p}\right)^{0.27} \qquad \text{Eq 5.1}$$

At a very low inlet velocity, typically below 1mms^{-1}, the viscous characteristics length (^) was determined to be twice the ratio of weighted by the velocity in the RVE volume (Eq 2.45) and that of its RVE surface whilst the thermal characteristics length ($\bar{\pi}$) was determined to be twice the ratio of the wet pore RVE volume to the interconnected pore RVE surface (Eq 2.46) as reported by Perrot et al., 2013. As this information is commonly missing, Johnson, et al. (1987) showed that approximate values from the pore geometry can be used, typically half its window and pore sizes respectively (See Fig 2.8 reported in Olny and Panneton, 2008).

The absence of complete measured data for all the structural parameters thereof brings about an impediment to a more complete and comprehensive modelling

and is an iterating issue for many papers relating the sound absorption of porous metallic structures available in the literature. With knowledge of structural information like porosity, pore sizes, connectivity, and permeability, it becomes imperative to formulate reliable relationships with other parameters needed for modelling. Reported in Dukhan (2013), for porous metal structures, the dynamic tortuosity can be completely described as a function of the porous body of the material and is mathematically described by Du Plessis and Fourier (2012) (See Eq 2.42).

To establish confidence in the application of this tortuosity model, a reliability test was carried out using the porosities (packing fractions) of the virtual monosized structures (1-3mm) used in Otaru and Kennedy (2016). For an isotropic porous material with a random distribution of solid particles and voids, Dias et al. (2006) proposed an exponential model ($\tau = C_o \emptyset^{-n}$) of dynamic tortuosity (τ) dependent on porosity ($\emptyset$), shape factor, C_o and tortuosity factor (n ~ 0.4-0.6). A plot of natural log of the dynamic tortuosity against the natural log of packing density computed for "virtually-derived" porous structures for pore sizes ranging between 1 and 3mm, porosities between 0.67 and 0.69, and capillary radius to between 10 and 80μm reported in Otaru and Kennedy (2016), shows a linear inverse relationship with a strong fit of data (R^2~99.9%) and tortuosity factor, n is 0.55 (Fig 5.3) was attained. This theoretical model yielded explicit expressions indicating some reliable predicted values of dynamic tortuosity which lies within the lower and upper bound tortuosity factor of 0.4 and 0.6 respectively for most porous materials reported in Guo, 2015. Model output using this model is said to be in good agreement with experimental data (Dias et al., 2006) and are well documented in Guo, 2015.

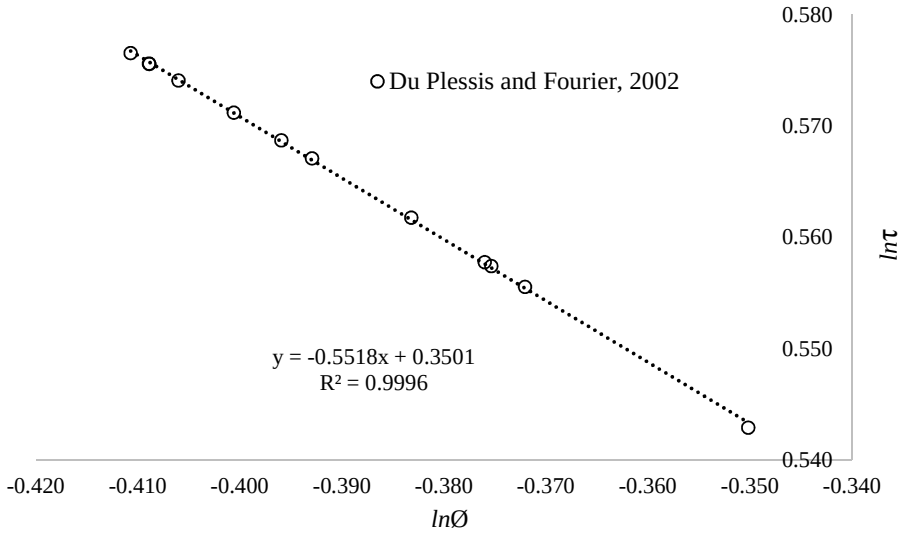


Fig 5.3. Graphical representation of natural log of dynamic tortuosity ($ln\tau$) against natural log of packing density (porosity, $\emptyset$) using analytically predicted values reported by Du Plessis and Fourier, 2002 (Tortuosity factor, n is 0.552, shape factor, $C_o$is 0.35 with a very good fit $R^2 =$ 0.999).

With known values of pore sizes, connectivity, permeability, porosity and dynamic tortuosity, modelling of the characteristic acoustic impedance and sound absorption coefficient of porous metallic structures using well-known poroacoustic models like Delany-Bazley-Mikki (DBM), Johnson-Champoux-Allard (JCA), and Wilson models is possible. The application of the Johnson-Champoux-Allard-Lafarge (JCAL) and Johnson-Champoux-Allard-Prides-Lafarge (JCAPL) models require determination of the remaining three parameters, typically static thermal permeability (k_0'), static viscous tortuosity (τ_0) and static thermal tortuosity (τ_0'), using dimensionless shape factors defined in Dukhan (2013) (See Eq 2.66). Considerable work in Lafarge et al. (1997) pointed out that the dimensionless shape factor in Eq 2.66, M_1', equals unity for structures with identical circular pores (like the one presented herein), 0.66 for slit, 0.3 for foam and 0.03 for glass wool. Using measured structural parameters of Al structures reported in Li, et al. 2014, computed values of this shape factor (M_1') were close to unity and in a similar trend, other dimensionless shape factors

(M_1, N_1 & N_1') are also equal to unity, but may differ from M_1' depending on the pore morphology. An example of the structural parameters of Al structure used Li, et al., 2014 is presented in Table 5.1.

Table 5.1. Structural parameters of Al structures with spherical cells in Li, Zhendong & Han 2014.

Property	**Determined by?**	**Value**	**Units**	**Model**
Porosity ($\emptyset$)	Measuring	0.6	-	JCA, JCAL, JCAPL, Wilson
Pore diameter (Dp)	Measuring	$1.60x10^{-3}$	m	
Window diameter (D_w)	Measuring	$0.31x10^{-3}$	m	
Permeability (k_0)	Measuring	$0.81x10^{-09}$	m^2	JCA, JCAL, JCAPL, Wilson
Dynamic tortuosity (τ)	Theoretical model	1.867	-	JCA, JCAL, JCAPL, Wilson
Thermal length	Half the pore diameter	$0.80x10^{-3}$	m	JCA, JCAL, JCAPL
Viscous length	Half the window diameter	$0.155x10^{-3}$	m	JCA, JCAL, JCAPL
Static thermal permeability (k_0')	Calculated, $M'_1 = 1$	$4.80x10^{-08}$	m^2	JCA, JCAL, JCAPL
Static viscous tortuosity (τ_0)	Calculated, $N_1 = 1$	2.334	-	JCAPL,
Static thermal tortuosity (τ_0')	Calculated, $N'_1 = M'_1 = 1$	1.25	-	JCAPL,

5.4 Simulation procedure

The simulation procedure of pressure wave propagation across porous structures was carried out with the following steps, namely; definition of structural and geometry parameters and variables, geometry creation, material selection, choice of physics and appropriate boundary conditions, meshing and solving within the pressure acoustic frequency domain module of COMSOL Multiphysics 5.2^{TM}. A two-dimensional (2D) tube geometry was created to mimic realistic standing wave tube measurement with inbuilt air (STP) as the material occupying the fluid domain in the tube geometry as shown in Fig 5.4. The geometry consists of a 20mm thick hardbacked porous structure (PS),

40mm thick fluid domain zone (FD) and 20mm thick perfectly matched layer (PML).

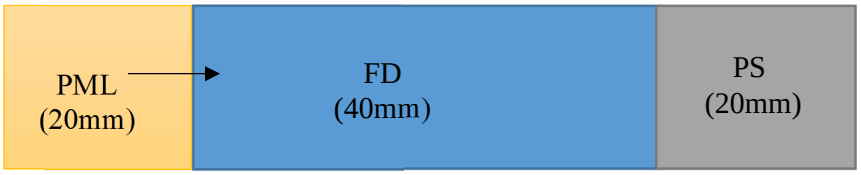


Fig 5.4. A two-dimensional geometry of a hardbacked porous structure in an impedance tube.

A triangular mesh of 21μm minimum elemental size, maximum elemental size half the minimum wavelength, a maximum element growth rate of 1.3, curvature factor of 0.3 and 1.0 resolution in the narrow region were applied to the FD and PS domains while the PML domain was confined to mapped mesh. A Helmholtz or linear acoustic pressure acoustic frequency domain ($20\mu Pa$ reference pressure) physics interface (Eq 2.31) which features total acoustic pressure (p), fluid density (ρ_o), propagation coefficient (k), monopole (Q) and dipole (q) source terms was solved on the PML and FD domains. The structural domain (PS) features an interchange between poroacoustic models (Attenborough, DBM, JCA, JCAL, JCAPL and Wilson) to account for their real specific surface acoustic impedance, Z, (Eq 2.32) and normal incidence absorption coefficient, Ac, (Eq 2.33) of the materials.

A background pressure field was applied on FD domain, perfectly matched layer on the PML domain whilst a periodic Floquent boundary condition was applied on the side faces. The inlet of PML and outlet of the PS were conditioned to sound hard boundary wall before solving. The computational time needed to resolve a solution is dependent on the number and range of frequencies considered, typically, an approximation of 65 frequencies were resolved in 2minutes for our specification.

A test on the influence of FD (air domain) variation shows insignificant effects on the simulation results. Also, a 2D/3D correlation factor is provided to compare the study of a 2D study (Fig 5.5, left) on resolving the structural macroscopic parameters using the Johnson-Champoux-Allard (JCA) poroacoustic model into a comparative estimation of an actual 3D half-tube model (Fig 5.5, middle & right) and a correlation coefficient of 99.2% was attained (Fig 5.6). The arithmetic mean of the sound absorption coefficient at the ⅓ octave frequencies (250, 500, 1000 and 2000Hz) also known as the Noise reduction coefficient (*NRC*), the average of the absorption coefficients for the twelve one-third octave (200-2500Hz) band also known the sound absorption average (*SAA*), the quarter wave resonance peak in absorption or the peak absorption coefficient (*Ap*) (Bell, 1982) along with the macroscopic parameters of the sound absorption curve (Han, et al., 2003 and Li, et al., 2014) enable the assessment of their relative acoustic performance.

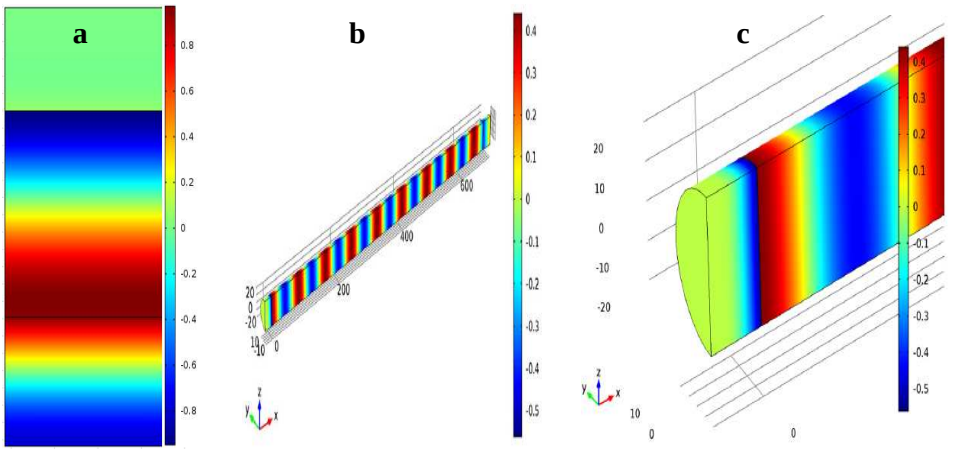


Fig 5.5. A 2D (a) and 3D half-tube (b & c) model representations of total acoustic pressure (Pa) computed for 25mm hardbacked glass wool fiber computed using Johnson-Champoux-Allard model [*Numerical scales unit for the legends measured in Pa]*.

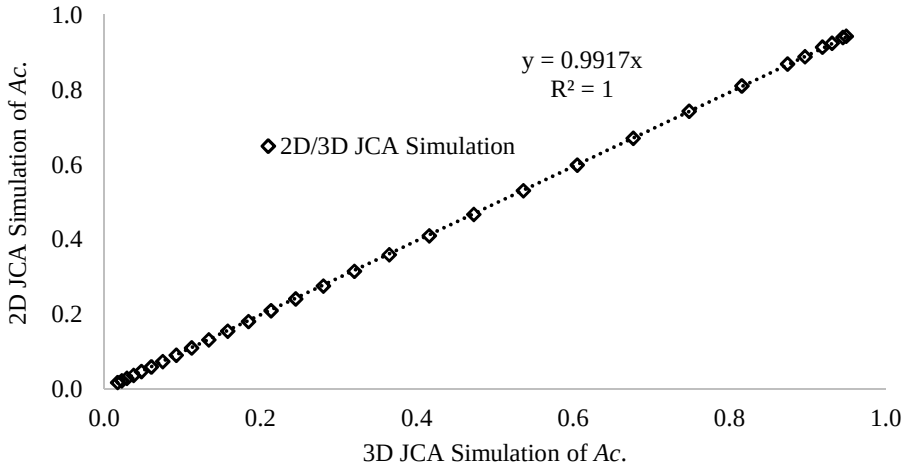


Fig 5.6. Vertical-axis, is a 2D and horizontal, is a 3D value of computed normal incidence absorption coefficient for a 25mm hardbacked glass wool fiber material using Johnson-Champoux-Allard model for the frequency of 100-6500Hz.

5.5 Model validation

To ensure accuracy is preserved and the right simulation data are obtained, care was taken to first put the acoustic porous media models and the set impedance tube representation into test by comparing simulation data to an existing measured data available in the literature. For non-spherical cell structures, measured (literature) and numerically simulated (current) data of normal incidence absorption coefficient of a 25mm hardbacked glass wool fiber (Kino and Ueno, 2008), 25.5mm hardbacked porous melamine foam structure (Kino and Ueno, 2008) and 23.31mm hardbacked, 20mm air-gap and 40mm air-gap porous sintered fiber metal (Bo and Tianning, 2009) are presented in Fig 5.7.

Structural data for the determination of absorption coefficient of these non-spherical celled structures along with their calculated values of the absorption peak (Ap), noise reduction coefficient (*NRC*) and sound absorption average (*SAA*) are presented in Table 5.2. Also, measured (literature) and simulated (current) values of the sound absorption coefficient of open-celled aluminium foam structures with spherical cells (bottleneck-type structures) are also

presented herein and would form an integral part of this work in relation to the consideration of predictive absorption coefficients using structure-related parameters of the "virtual" and "casted" Al structures with near-spherical cells.

Table 5.2. Structural (literature) and acoustic (current) data for non-spherical cell structures.

Literature	Material type	Ø (%)	∧ (μm)	$\bar{\kappa}$ (μm)	$k_0/10^{-9}$ (m^2)	τ	Ap/f_{max} (kHz)	*NRC*	*SAA*
Kino and Ueno, 2008	Glass wool fiber	98.70	132	237	1.084	1.009	0.965/4.00	0.369	0.347
Bo and Tianning, 2009	Porous sintered fiber metal	90.94	113	194	0.959	1.513	0.980/2.80	0.445	0.598
Kino and Ueno, 2008	Melamine foam	99.30	199	445	1.390	1.005	0.930/4.00	0.356	0.332

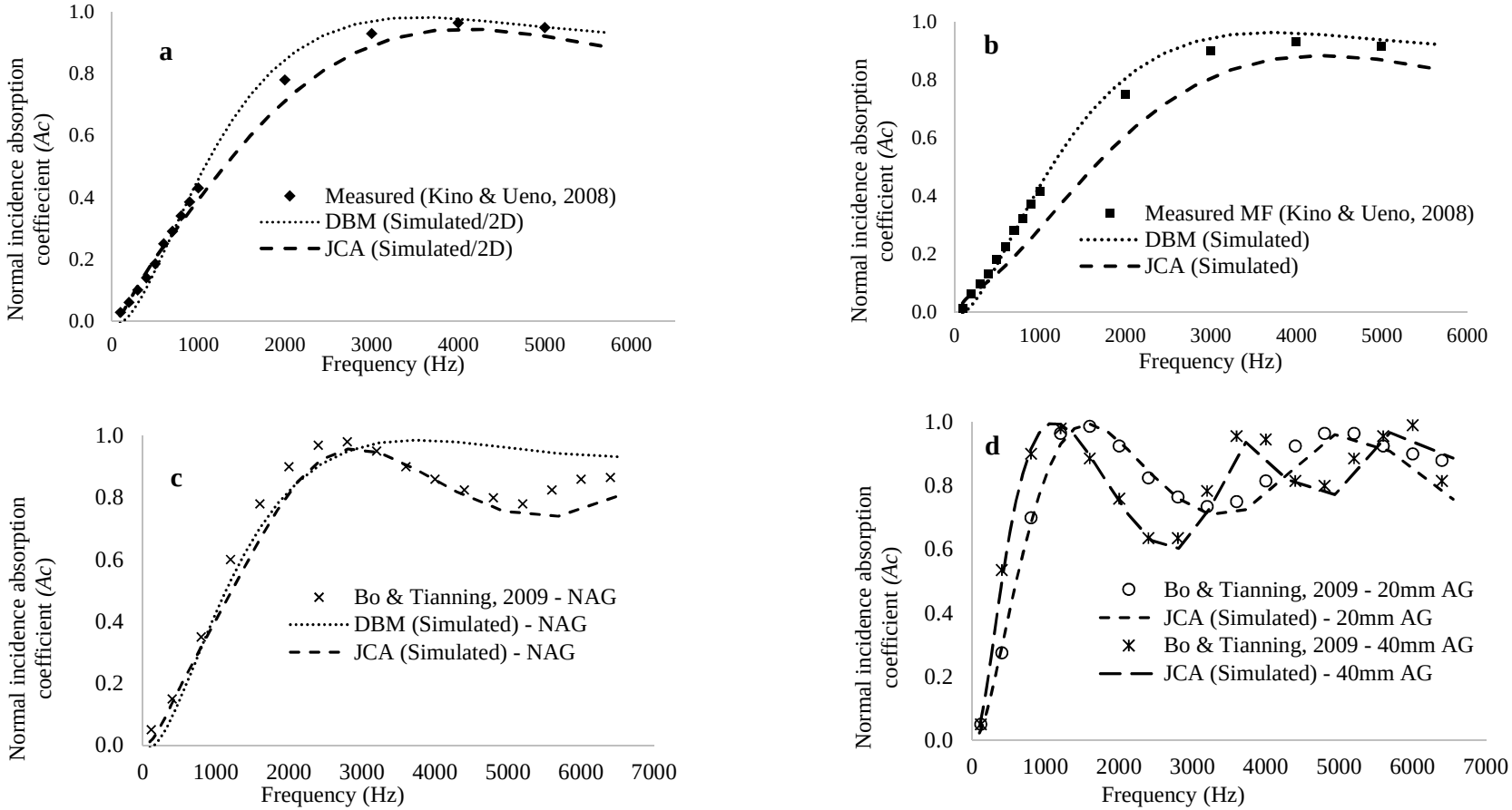


Fig 5.7. Plots of measured (literature) and simulated (current) normal incidence absorption coefficient against frequency (Hz) for (a) hardbacked glass wool fiber (b) hardbacked melamine foam (c) hardbacked porous sintered fiber metal and (d) airgap or cavity behind the porous sintered fiber metal.

The predictive absorption curve indicated reasonable fits to the experimental data observed for both the glass wool fiber and melamine foam structures for both models, and an overall better fit to the DBM model. A more likely cause of the better agreement is that the DBM empirical model (Fig 5.2a and 5.2b) was developed from the acoustic behaviour of fibrous materials in an impedance tube. The transversely isotropic nature of many glass fiber materials makes there microstructures simple. The hollow struts of these materials are interconnected and characterized by obvious open pores with important porosities close to unity (Table 5.2). Their characteristic absorption spectra are reported in (Hinze and Rosler, 2014, and Kino and Ueno, 2008) to majorly depend on the pore morphology and porosity of the materials.

At very low frequencies, typically below 200Hz, predictions using the DBM model are poor and this is said to be due to their negative values of their real specific surface acoustic impedance at these low frequencies (Mikki, 1990) and tends to overestimate prediction for frequencies above their air flow resistance. Within the frequency range under consideration, it is observed that the JCA-5 parameters model gives a better fit to the experimental data recorded for porous sintered fiber metal in Bo and Tianning (2009). In this case, the DBM model was not able to accurately predict the behaviour characterized by a dip in the absorption curve for frequencies beyond 3kHz but the JCA model aptly predict the behaviour of this structure for both cases of hardbacked and introduced back cavity (Helmholtz resonance absorption) simulation as presented in Fig 5.7c and Fig 5.7d. This shows that the growing complexity from a transversely isotropic structures (as in the case of glass wool fiber and melamine foam) to a more complicated structure (porous sintered fiber metal) with increased “struts”

thicknesses, reduced porosity, larger surface area and offering more resistance to the incoming pressure wave would require more than a permeability to accurately described their acoustic behaviour.

It is important to note that the structural morphology of melamine foam is likened to that of highly porous commercial metallic foam structures, typically Recemat RCM-NCX, Porvair, and Alantum. It would, therefore, presumably to say that the predictive outcome of the characteristic sound absorption curve using the Delany-Bazley-Mikki (DBM) model would provide a better fit to their measured values. This is simply shown in Fig 5.8 recorded for the sound absorption coefficient against frequency (500-7500Hz) for extremely porous metallic sponge 450 and 800 studied for various structural thicknesses reported in Hinze and Rosler, 2014.

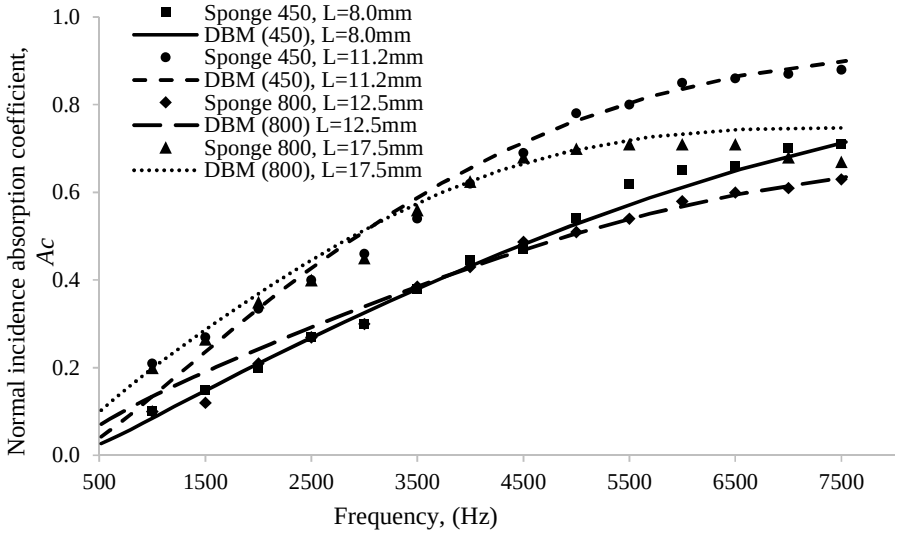


Fig 5.8. Plots of measured (Hinze & Rosler, 2014) and simulated (current) normal incidence absorption coefficient of hard-backed porous metal sponge 450 and 800 against frequency (500-7500Hz) at different structural thicknesses.

Predicting the measured normal incidence absorption coefficient of "bottleneck-type" structures available in the literature based on permeability alone would be convenient and timely. Sadly, predictions using the DBM model were poor for

the given range of frequency reported in Li et al. (2014) (Fig 5.9) and in the absence of values for the porosity, tortuosity, viscous and thermal lengths, the JCA model cannot be applied. Using measured and theoretically predicted values of structural data in Table 5.1, The JCA, JCAL, JCAPL and Attenborough models failed to reliably describe the measured characteristic absorption curves over a large portion of the frequency range.

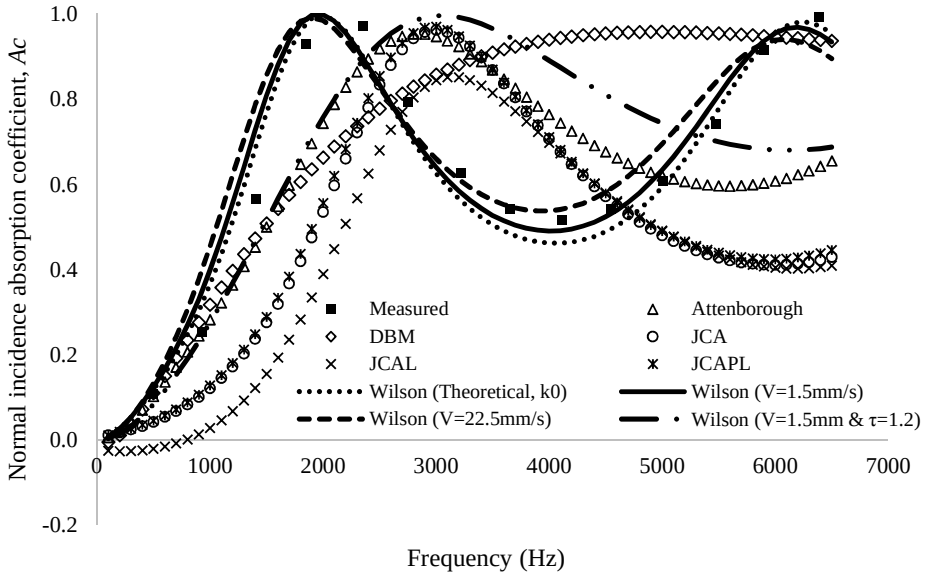


Fig 5.9. Plots of measured (Li et al., 2014, structure B) and modelled (current) normal incidence absorption coefficient (*Ac*) against Frequency (100-6500Hz) for a hard-backed 20mm thick aluminium foam structure (Tortuosity, $\tau = 1.867$) with spherical cells.

Similarly, despite requiring five-eight structural parameters to predict the sound absorption coefficient of this material, it is evident that the outcome in the application of JCAPL model in Fig 5.9 quadrate completely with that of JCA model whilst the JCAL matches the JCA and JCAPL results at higher frequencies, typically, beyond 3.8 kHz. Observably, the Johnson et al. models are not suitable for this "bottleneck-type" structure with circular apertures (pore openings) and spherical cavities (pores) but have been proven to be suitable for structures with non-uniform sections with possible constrictions as shown in Fig 5.7c and 5.7d. Hence, with known values of structural porosity, tortuosity and

permeability (both for measured values at 1.5 and 22.5mm.s^{-1} and predictive value using Eq 5.1), the Wilson model is evidently a good fit to the measured characteristic absorption curve in Fig 5.9.

The Wilson model was further extended to model measured and predicted sound absorption coefficient of other "bottleneck-type" structures in literature for varying structural parameters. For a hardbacked simulation, the modelled data show reasonable agreement with the measured data in Li et al., 2011 for the following frequencies in Table 5.3. Reasonable agreements between modelled (current) and measured sound absorption coefficient in Lu and He (2000) for frequencies; 500, 1000 and 1600Hz were also achieved for both hardbacked and airgap studies (Table 5.1A of the appendix page). Beyond the experimental maximum frequency of 1900Hz studied in Lu and He (2000), the agreement between their predicted and currently simulated values of noise reduction coefficients (*NRC*) and maximum peak of absorption (*Ap*) were within reason (Table 5.2a of the appendix page).

Table 5.3. Measured (Li et al., 2011) and predicted (current) sound absorption coefficient of aluminium foam structure with spherical cells (Ø~65%) at 500, 1000 and 2000Hz.

Measured				Measured, Ac			Predicted, Ac		
Samples	D_w (μm)	D_p (μm)	L (mm)	500Hz	1000Hz	2000Hz	500Hz	1000Hz	2000Hz
U1	300	1300	20	0.099	0.270	0.998	0.094	0.266	0.963
U2	300	1600	20	0.104	0.299	0.970	0.101	0.304	0.989
U3	300	1900	20	0.124	0.299	0.970	0.107	0.339	0.998
U4	320	1300	10	0.034	0.084	0.211	0.035	0.067	0.164
U5	320	1300	15	0.060	0.129	0.451	0.058	0.130	0.484
U6	320	1300	20	0.096	0.231	0.886	0.088	0.238	0.932

Accurate measurement or predicted value of porosity, tortuosity, and permeability of the "bottleneck" is key to the achieving reasonable prediction of the sound absorption curve using Wilson model. The wrong tortuosity value of 1.2 in Fig 5.9, failed to reliably predict the right vorticity-mode relation time, entropy-mode relation time and the density infinite frequency needed to

compute the surface acoustic impedance and the normal incidence absorption coefficient of the material. Similarly, theoretical predictions of the permeability of the low-density "bottleneck-type" porous structures at 1.5mm.s^{-1} reported in Li et al. (2014) using Eq 5.1 was not far from reality with predicted coordination ranging between 6 and 7 (Table 5.4). It is good to note that the flow behaviour of these "bottleneck" structures is largely controlled by their openings (Otaru and Kennedy, 2016) which is integral to predicting the acoustic performance of this structure.

Table 5.4. Measured (Li et al., 2014) and predicted structural of Al structures with spherical cells.

	Measured				Predicted		
Samples	Ø (%)	Dw (μm)	Dp (μm)	$k_0/10^{-09}m^2$	$k_0/10^{-09}m^2$	N_c	τ
A	57	260	1600	0.49	0.49	5.93	1.907
B	60	310	1600	0.81	0.97	6.55	1.867
C	63	360	1600	1.43	1.73	7.16	1.826

5.6 Discussion of results

The reasonable correlations between measured (literature) and predicted (current simulation) characteristic absorption curves in Fig 5.9 suggests that the sensible application of the Wilson model would provide a useful guide to the design and optimization of enhanced "bottleneck-type" porous structures for soundproofing purposes.

For a guide, a 20mm thick hardbacked (backed by a rigid wall) numerical simulation was performed using structural parameters of the "virtually-created" monosized packed spheres in Otaru and Kennedy, 2016, with pore diameter, pore openings, capillary radius and porosities ranging between, 1-3mm, 175-797μm, 10-80μm and 66-69% respectively (presented in Table 5.5). In addition, the computed normal incidence absorption coefficient (*Ac*) of the "virtual"

monosized structures against frequency (100-6500Hz) are presented in Fig 5.10-5.12 whilst values obtained for the maximum peak of absorption (*Ap*), noise reduction coefficient (*NRC*) and sound absorption average (*SAA*) are also presented in Table 5.5.

Fig 5.10 plots the normal incidence absorption coefficient against frequency (Hz) using structural parameters of the theoretically predicted (TH) and "virtually-created" (DU) monosized structures having a similar capillary radius (80μm) but different pore sizes (1, 2 and 3mm). Fig 5.11 shows similar plots but in this case, variation in capillary radius of the "virtual" structures with unchanging pore sizes was studied and the importance of pore openings is presented in Fig 5.12 by singling out structures with different pore sizes and capillary radius but similar openings.

Table 5.5. Structural parameters and acoustic properties of DEM monosized (1, 2 & 3mm) spherical structures.

DEM structures-capillary radii (μm)	D_w (mm)	Dp (mm)	Ø (%)	τ	k_0 m^2	*Ap*	*NRC*	*SAA*
DU1-10	0.175	1.02	66.994	1.770	4.61E-10	0.968	0.396	0.605
DU1-30	0.270	1.02	67.508	1.763	1.41E-09	0.974	0.338	0.514
DU1-45	0.313	1.02	68.169	1.754	2.28E-09	0.912	0.296	0.449
DU1-80	0.375	1.02	70.458	1.721	4.29E-09	0.792	0.233	0.359
DU2-10	0.274	2.04	66.319	1.780	1.21E-09	0.988	0.349	0.531
DU2-30	0.421	2.04	66.439	1.778	2.44E-09	0.908	0.291	0.440
DU2-45	0.492	2.04	66.631	1.776	4.23E-09	0.809	0.240	0.365
DU2-80	0.605	2.04	67.306	1.766	7.86E-09	0.678	0.184	0.286
DU3-10	0.370	3.06	66.440	1.778	5.23E-09	0.768	0.220	0.337
DU3-30	0.557	3.06	68.662	1.747	6.87E-09	0.702	0.194	0.300
DU3-45	0.645	3.06	68.707	1.746	9.36E-09	0.638	0.168	0.264
DU3-80	0.797	3.06	68.934	1.743	1.54E-08	0.537	0.133	0.212

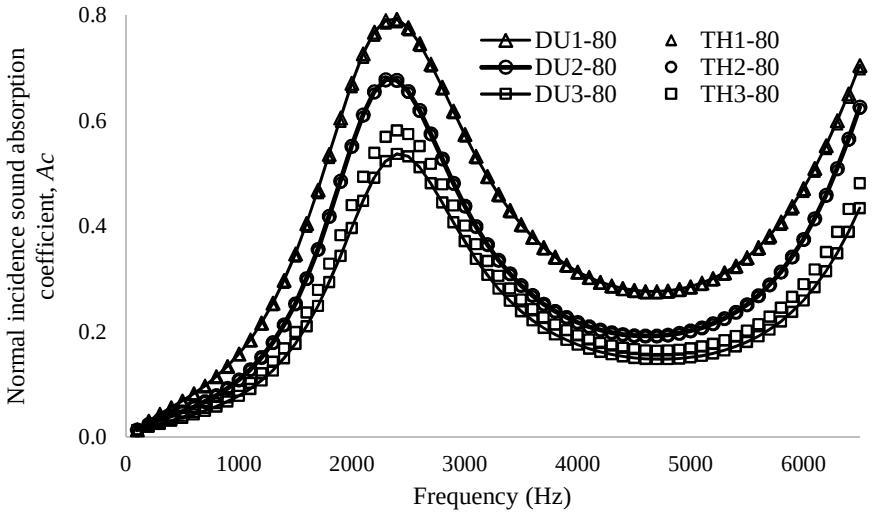


Fig 5.10. Plots of 20mm thick hardbacked numerically simulated normal incidence absorption coefficient (*Ac*) against frequency (Hz) using structural parameters of the theoretically predicted (TH) and "virtually-created" monosized "bottleneck" structures having a similar capillary radius of 80μm and different pore sizes, 1, 2 and 3mm.

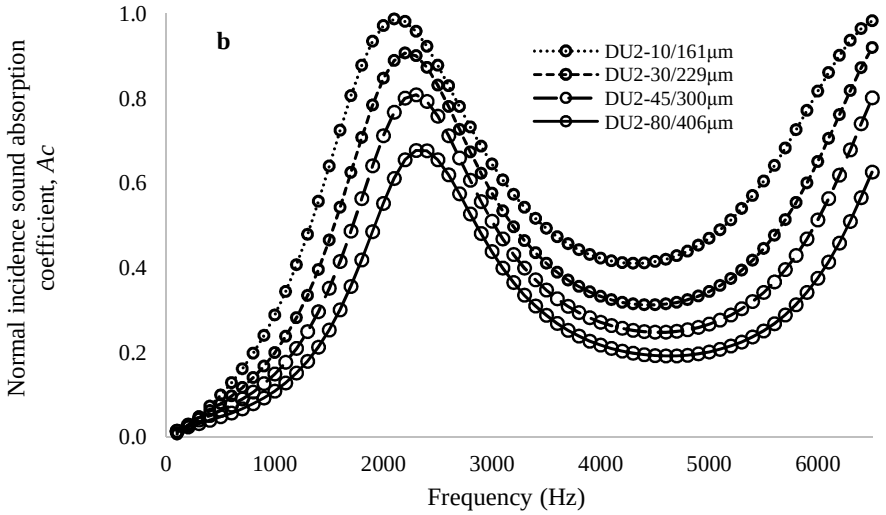


Fig 5.11. Plots of 20mm thick hardbacked numerically simulated normal incidence absorption coefficient (*Ac*) against frequency (Hz) using structural parameters of the "virtually-created" monosized "bottleneck" structures having similar pore sizes of 2mm and different capillary radius of 10, 30, 45 & 80μm.

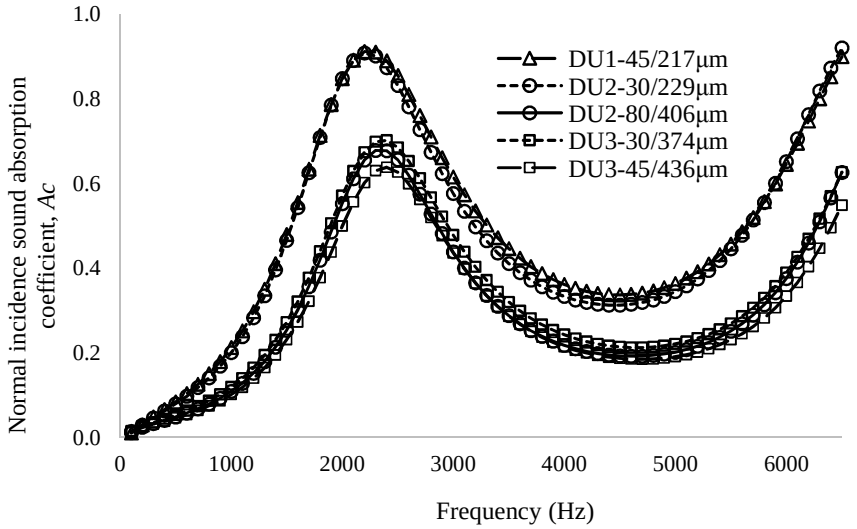


Fig 5.12. Plots of 20mm thick hardbacked numerically simulated normal incidence absorption coefficient (*Ac*) against frequency, Hz using structural parameters of selected "virtually-created" monosized "bottleneck" structures having different pore sizes and capillary radius but similar pore openings.

As expected, the absorption coefficient of these materials was noticed to greatly depend on their resistance (airflow resistivity or permeability) and packing density as pressure wave propagates through the pores and windows of the porous matrix (Zhang and Zhao, 2007). The contacts between the vibrating particles and the pore wall of the microstructure dissipate a significant amount of heat energy and diffusivity favoured by shortening wavelength (Smith, 1970) at audible frequency whilst interparticle collision at low frequency (< 1000Hz) is described as elastic with insignificant amount of lost energy confined to large particle wavelength (Johnson et al., 1987, and Champoux and Allard, 1992). The vibration increase caused by an increase in particle interaction at audible or high-frequency increases the characteristic absorption spectra to a peak. Oscillation tends to occur because the porous material is losing energy to the surrounding air resistance and the maximum peak of final equilibrium is achieved when the rate of lost energy equal to that of the incoming energy into the porous structure.

For the structural thickness independent study in Fig 5.10-5.12, the variations in the characteristic absorption spectra are an indication of the microstructural changes of the "bottleneck" structures used. These important parameters are the pore sizes (affected by the size of salt beads used in realistic metal foam casting), porosity (affected by packing density) and pore openings (affected by infiltration pressure in real casting and capillary interaction for the virtual structure). However, these parameters are interrelated as indicated in Table 5.5. Smaller sized structures, typically, 1mm pore diameter sizes corresponds to having smaller sized apertures and higher flow resistivity, as opposed to the larger pore sized structures, 2 and 3mm.

For pore sizes 1, 2 and 3mm and constant capillary radius in Fig 5.10, structures DU1-80, DU2-80, and DU3-80 are observed to have porosities between 67-70% and pore diameter openings of 375, 605 and 797μm respectively. The obvious differences in the acoustic response of these virtual structures can, therefore, be credited to the effect of pore diameter sizes. A high peak of absorption (0.792), noise reduction coefficient (0.233) and sound absorption average (0.359) were achieved for the 1mm pore diameter sized structure (DU1-80) whilst the corresponding acoustic response of the 2mm (DU2-80) and 3mm (DU3-80) sized structures shifts the absorption curves to frequency maxima with lower absorption peak and noise reduction coefficients (Table 7.5).

In Fig 5.11, the mean pore diameter sizes of the structure are limited to 1mm with possible variation in the capillary radius (r_c) of the microstructural arrangements between 10 and 80μm. The structure with the lowest pore openings of 175μm (DU1-10) was observed to have the broadest and strongest absorption peak with greater *NRC* and *SAA* than other microstructural

arrangements of wider pore diameter openings and capillary radius ranging between 30 and 80μm. This indicates the strong dependence of absorption coefficient on the pore diameter openings.

Evidently, for different pore sizes in Fig 5.10, the greatest absorption, noise reduction coefficient and sound absorption average correspond to the structure with the lowest pore diameter opening (DU1-80μm). Depending on the capillary radius (r_c) of the modelled structures used, the pore diameter openings can be made similar irrespective of their pore diameter sizes using the sphere-packing model in Eq 1.1. In Fig 5.12, the characteristic absorption curve of structure having pore diameter sizes of 1mm and capillary radius of 45μm (DU1-45) and that of 2mm pore diameter sized structure at capillary radius of 30μm (DU2-30) overlaps completely with each other (R^2~99%), due the inconsequential difference in their important pore diameter openings. Similarly, the acoustic absorptive response of the 2mm structure at 80μm capillary radius (DU2-80μm) lies midmost the response of 3mm structures at 30μm (DU3-30) and 45μm (DU3-45) capillary radius thereby underlining the conspicuousness of the pore diameter openings of the virtual structures to the rationalization of the characteristic absorption curve.

To further substantiate the importance of pore diameter openings and sizes on the acoustic performance of realistic porous structures with spherical cells; the preceding chapter of this work published in Otaru et al. (2018) has highlighted the airflow behaviour of these structures adopting CFD simulation using X-ray CT images of the real structures and sphere-packing (DEM) models to predict the pressure drop measured across porous matrices made at different pore sizes and liquid differential pressures. In brief, for a differential pressure of 0.9 bar,

the ranges of pore sizes are 1.0-1.4mm (X1), 2.0-2.5mm (Y1) and 2.5-3.15mm (Z1) were studied. To fully understand the importance of window sizes (openings) in response to their acoustic behaviour, the differential pressure used to drive liquid metal into the 2.0-2.5mm packed spherical salts were varied, typically, 0.9, 0.60, 0.45 and 0.25 bars thereby producing structures of similar pore sizes, but different pore diameter openings termed as Y1, Y2, Y3, and Y4 respectively (Table 5.6).

Table 5.6. Structural and acoustic parameters of porous structures with spherical cells (X, Y, and Z) characterized using CT images and DEM.

Samples	Ø	D_w (mm)	Dp (mm)	r_w/r_p	k_0 m^2	*Ap*	*NRC*	*SAA*
µCT-Y1	70.526	0.650	2.225	0.292	1.35E-08	0.555	0.140	0.222
µCT-Y2	72.563	0.720	2.215	0.325	1.71E-08	0.504	0.123	0.196
µCT-Y3	75.205	0.741	2.273	0.326	1.80E-08	0.486	0.118	0.187
µCT-Y4	78.397	0.899	2.226	0.404	3.34E-08	0.371	0.085	0.135
DEM-Y1	71.752	0.617	2.327	0.265	1.23E-08	0.571	0.145	0.229
DEM-Y2/3	74.736	0.731	2.373	0.308	1.91E-08	0.476	0.115	0.183
DEM-Y4	78.246	0.892	2.406	0.371	3.45E-08	0.366	0.084	0.133
µCT-X1	72.053	0.275	1.213	0.227	4.31E-09	0.787	0.231	0.357
µCT-Z1	75.243	0.732	2.774	0.264	2.20E-08	0.449	0.107	0.170

Fig 5.13 presents the computed normal incidence absorption coefficient of these structures characterized using X-ray CT images of the real sample against frequency. X1 structure with the lowest mean pore sizes, 1.213mm, and openings, 0.275mm yielded the highest absorption peak whilst the lowest absorption peak is associated with the Y4 structure with the widest openings and confer to have the highest permeability of $3.45x10^{-08}m^2$; dictated majorly by the size of the windows, 0.899mm (Otaru et al., 2018). The Z1 structure has the largest mean pore size, typically, 2.774mm but behaves better than the Y4 structure with a mean pore size of 2.226mm. This is majorly due to the important smaller window sizes of the Z1 structure (0.732mm) when compared to the Y4 structure and likened to the acoustic response provided by the Y2 and Y3

structures recorded to have mean window sizes of 0.720 and 0.741mm respectively.

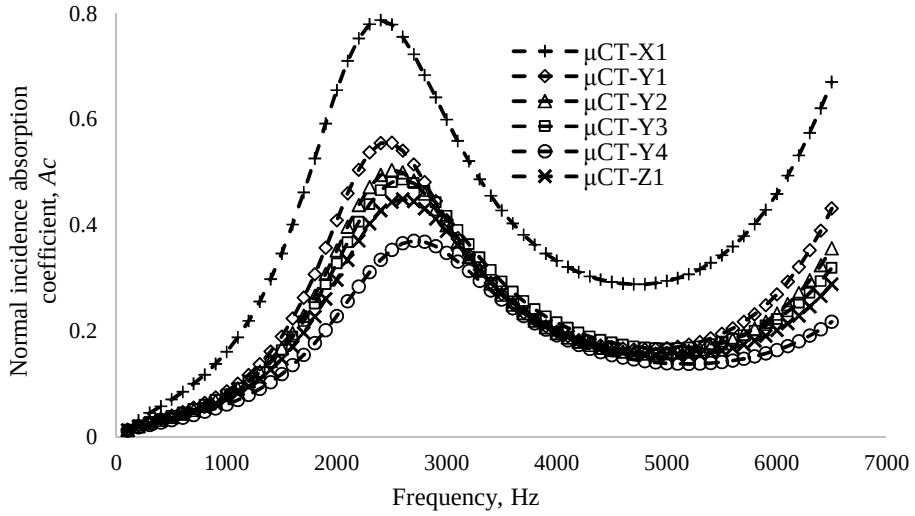


Fig 5.13. Plots of 20mm thick hardbacked numerically computed normal incidence sound absorption coefficient against frequency (Hz) using structural parameters of X, Y and Z samples obtained from X-ray CT images of the real sample.

Comparatively, the characteristic absorption spectra provided using structural parameters obtained from the CT samples of the real structure agree closely with that of the sphere-packing models presented in Fig 5.14. For similar porosity, pore diameter sizes and openings of the spherically celled Y structures, close agreement was observed in their computed values of permeabilities, *Ap*, *NRC* and *SAA* as provided in Table 5.6. The predictive acoustic response of these real samples is quite low when compared to commercially used soundproofing materials like those in Kino and Ueno (2008), and Bo and Tianning (2009). Additionally, the reasonable agreements between the characteristic absorption curves in Fig 5.10 and Fig 5.13 highlight the benefits in the use of sphere model (DU) and theoretically (TH) predictive value of permeability needed for predicting acoustic performance of the structure and a guide toward the enhancement of the material for efficient performance.

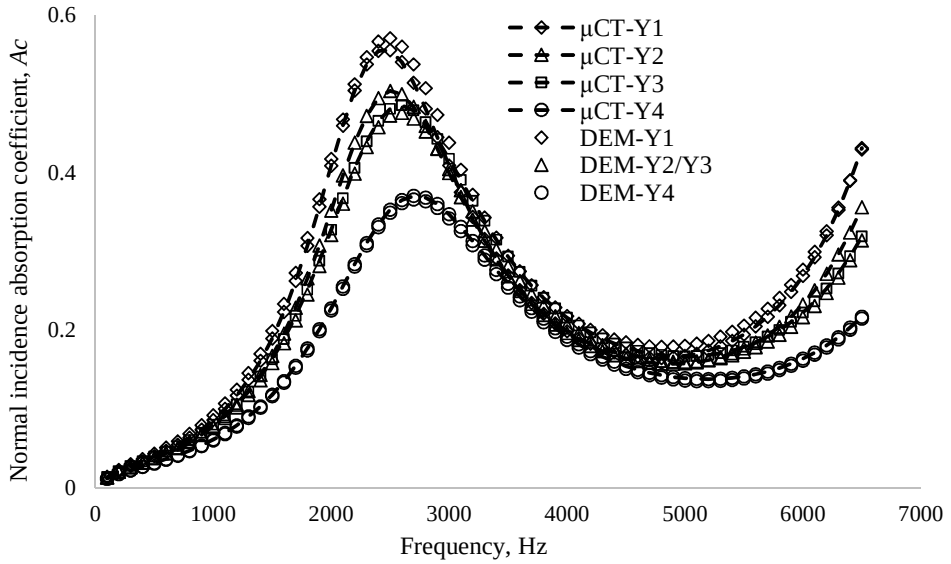


Fig 5.14. Plots of 20mm thick hardbacked numerically computed normal incidence sound absorption coefficient against frequency (Hz) using structural parameters of the Y samples (2.0-2.5mm) obtained from X-ray CT images of the "real" sample and "virtually-created" sphere-packing models.

5.7 Optimization and sensible application of "bottleneck" structures

So far, measurements and predictions of the characteristic sound absorption coefficient of "bottleneck-type" structures have shown that porosity and permeability are key structural parameters needed for minimizing resonance effects when exposed to the sound pressure wave. Detailed understanding of the contributions and optimization of these individual and interdependent parameters was done using theoretical models in Eq 1.2 and Eq 5.1 to account for permeability and pore openings and to explore much lower pore sizes, typically below 500μm, to figure out what benefit therein.

Table 5.7 shows possible ranges in values that are reasonable for the process. For a window to pore size ratio of 0.15 and 68% packing density, 200μm diameter particles give 30μm window diameter openings and permeability of $8.69 \times 10^{-12} m^2$. Similarly, 1400 and 1800μm mid ranges of pore diameter sizes yielded pore diameter openings of 210 and 270μm respectively; the largest pore

diameter sizes structure (3000µm) gives 450µm pore diameter openings and $1.95x10^{-12}m^2$ in permeability. Extending the packing density to 56 and 80%, structural permeability decreases by more than half and increases twice in approximation respectively. Increasing, the window to pore size ratio to 0.3 and 0.45 further widened the pore connectivity and reduces the surface area of the structure with observable increase in permeability.

Table 5.7. Structural and acoustic properties of "bottleneck-type" porous structures for window to pore ratio for 0.15, 0.30 and 0.45 and porosities, 56, 68 and 80%.

Samples	Ø (%)	r_w/r_p [-]	*Dp* (µm)	k_0 (m^2)	*Ap*	*f*peak (Hz)	*NRC*	*SAA*
A1	56	0.15	200	5.89E-12	0.288	6500	0.1071	0.1309
A2	56	0.15	1400	2.89E-10	0.873	1800	0.3694	0.5608
A3	56	0.15	3000	1.33E-09	0.992	2000	0.3349	0.4973
B1	80	0.15	200	1.20E-11	0.437	6500	0.1756	0.2120
B2	80	0.15	1400	5.89E-10	0.997	2200	0.3983	0.6102
B3	80	0.15	3000	2.70E-09	0.853	2500	0.2683	0.4115
C1	68	0.15	200	8.69E-12	0.365	6500	0.1406	0.1709
C2	68	0.15	1400	4.26E-10	0.961	2000	0.3994	0.6090
C3	68	0.15	3000	1.95E-09	0.936	2200	0.3102	0.4708
D1	56	0.45	200	2.14E-10	0.809	1700	0.3673	0.5457
D2	56	0.45	1400	1.05E-08	0.851	6500	0.1819	0.2611
D3	56	0.45	3000	4.81E-08	0.533	6500	0.0922	0.1367
E1	80	0.45	200	4.37E-10	0.979	2200	0.4140	0.6278
E2	80	0.45	1400	2.14E-08	0.438	2800	0.1054	0.1647
E3	80	0.45	3000	9.83E-08	0.228	2800	0.0492	0.0778
F1	68	0.45	200	3.16E-10	0.918	1900	0.4046	0.6086
F2	68	0.45	1400	1.55E-08	0.540	2400	0.1340	0.2126
F3	68	0.45	3000	7.10E-08	0.292	2500	0.0635	0.1045
G1	56	0.30	200	5.68E-11	0.613	6500	0.2936	0.3770
G2	56	0.30	1400	2.78E-09	0.995	6400	0.2869	0.4133
G3	56	0.30	3000	1.28E-08	0.813	6500	0.1676	0.2413
H1	80	0.30	200	1.16E-10	0.824	6500	0.4058	0.5403
H2	80	0.30	1400	5.68E-09	0.702	2600	0.1978	0.3046
H3	80	0.30	3000	2.61E-08	0.405	2800	0.0955	0.1496
I1	68	0.30	200	8.38E-11	0.724	6500	0.3557	0.4655
I2	68	0.30	1400	4.11E-09	0.810	2300	0.2404	0.3678
I3	68	0.30	3000	1.89E-08	0.502	2400	0.1219	0.1945

Practically, this permeability and window to pore ratio increase can be achieved by lowering the differential or infiltration pressure used in realistic casting processes (Otaru, et al., 2018); and in the sphere-packing model, it is achieved by increasing the capillary radius of connecting particles or erosion of the

structural phase of the "virtual" structure during three dimensional image processing in ScanIP (Otaru and Kennedy, 2018). A tabular representation of the structural and acoustic properties (to be discussed later) of the "bottleneck-type" porous structures are presented in Table 5.7 for the window to pore ratio of 0.15, 0.30 and 0.45 and porosities, 56, 68 and 80%. A detailed tabular representation to include more mid ranges of pore sizes needed for the effective study of the acoustic behaviour of "bottleneck" structures are presented in Table 5.6A of the appendices.

Fig 5.15 plots the numerically simulated normal incidence characteristic absorption coefficient against frequency for "bottleneck-type" porous structures for a constant window to pore ratio of 0.15, different pore sizes and porosities. Fig 5.16 presents the plots of computed values of the acoustic properties (*NRC*, *SAA*, and *Ap*) against predicted permeability of the structures. Near linear frequency dependent absorption responses were observed for structures with the lowest permeability values (A1, B1, and C1), typically, within $0.6\text{-}1.2\text{x}10^{-11}\text{m}^2$. This shows the attribute of low-density closed-cell "bottleneck" structures (Utsuno, et al., 1989, Lu, et al., 1999, and Lu and He, 2000) owing to their extremely low pore diameter openings thereby providing greater resistance to pressure wave at the surface of the material. An observable increase in the peak absorption and broadest absorption were attained for structures with the highest packing densities, else, for structures with the lowest packing density.

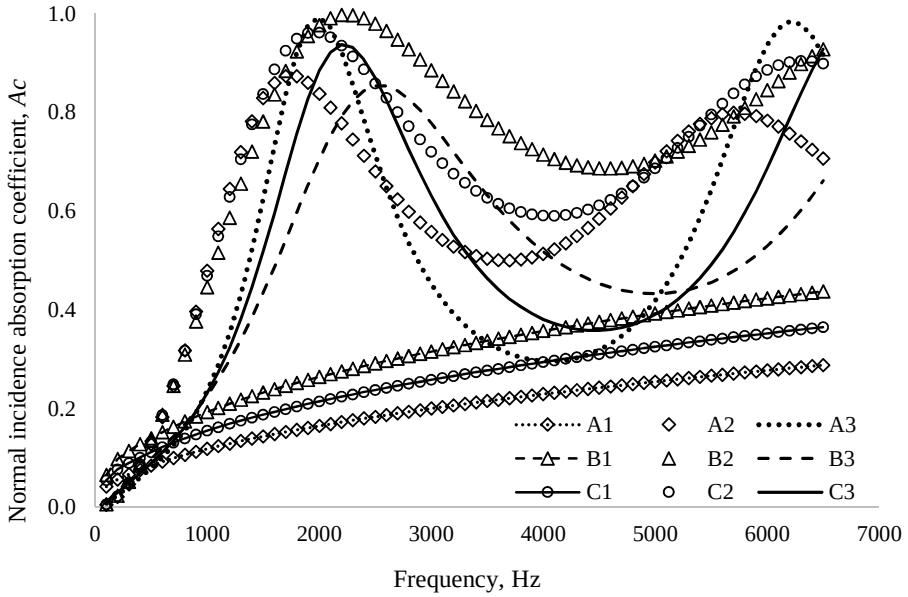


Fig 5.15. Plots of 20mm thick hardbacked normal incidence absorption coefficient against frequency (Hz) for structures with constant window to pore size ratio (r_w/r_p-0.15), for different pore sizes (*Dp*=200, 1400 and 3000μm) and different porosities, 56, 68 & 80% in Table 5.7..

Fig 5.16 shows that the absorption potential of this structure is relatively poor for highly open and highly closed structures with *NRC, SAA* and *Ap*, typically, below 0.3, 0.5 and 0.8 respectively and better for the mid permeability, ranging between 0.4-1.5x10^{-09}m^2. The consideration on which of the acoustic properties be given much priority would depend on the frequency range of application. For instance, at the low-frequency absorption (below 2500Hz), *NRC* and *SAA* should be given priority as it accounts for material behaviour at the one-third octave frequencies whilst the maximum absorption peak could either exist within and outside the frequency range depending on the permeability of the structure as shown in Table 5.7 and Fig 5.10-5.17.

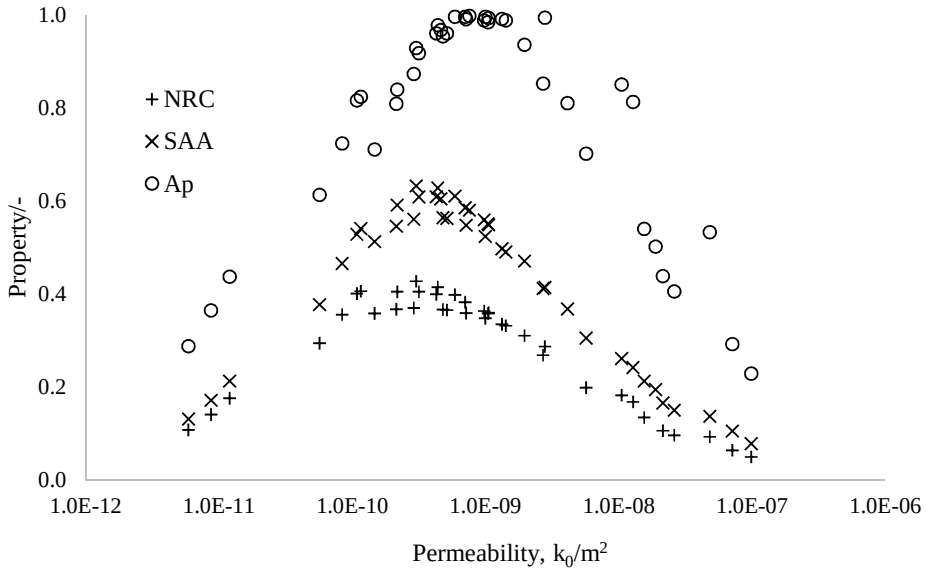


Fig 5.16. Graphical representations of acoustic properties of numerically simulated "bottleneck-type" structures against permeability for pore sizes between 200 and 3000µm.

The packing of spheres (salt beds) to achieve the desired structural porosity and window sizes of this novel "bottleneck-type" structure can be controlled experimentally. Lu and He (2000), and Langston and Kennedy (2014) have shown that high-density structures can be achieved through loose packing, with a large volume of void spaces created by touching spheres to be filled with infiltrated liquid metal at an extremely high temperature (600-800^{o}C). Similarly, highly porous structures can be achieved realistically through a dense packing of the salt beds whilst the pore diameter openings are largely controlled by simply varying the differential pressure as shown in the preceding chapter of this work. The sphere-packing model in Langston and Kennedy (2014), and Otaru and Kennedy (2016) adopted herein has shown that the 68% packing density is achievable for randomly packed monosized structures in Table 5.5. For a window to pore ratio of 0.15 and pore diameter sizes of 1400µm, the acoustic response of this structure (C2) nearly completely overlap with the "virtually-

generated" structure, DU1-10, with important pore diameter ratio of 0.17 and porosity of 67% as shown in Fig 5.17 and Table 5.8.

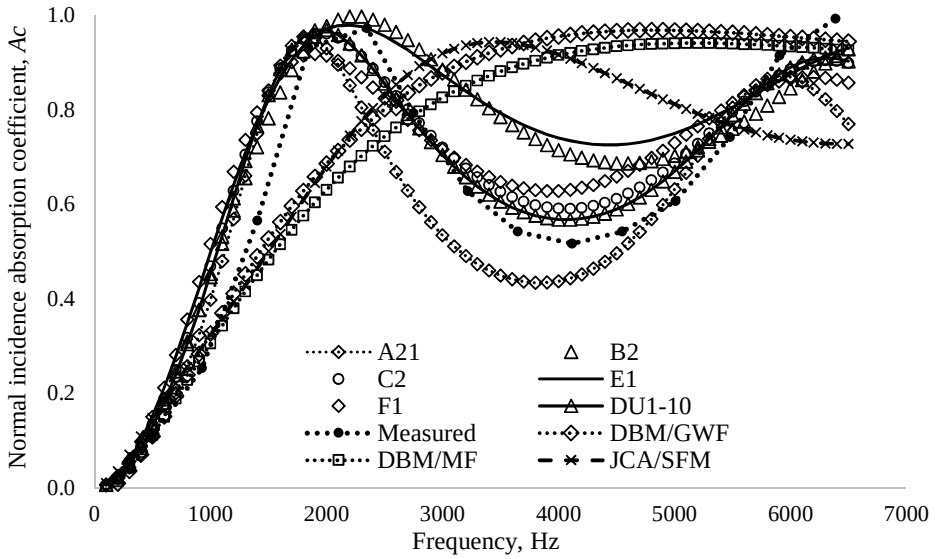


Fig 5.17. Plots of 20mm thick hardbacked numerically simulated and measured (Li et al., 2014) normal incidence absorption coefficient against frequency (Hz) for optimised "bottleneck-type" monosized structures and commercially used soundproofing glass wool fiber (Kino and Ueno, 2008), melamine foam (Kino and Ueno, 2008) and porous sintered fiber metal (Bo and Tianning, 2009).

Table 5.8. Structural and acoustic properties of numerically simulated and measured "bottleneck-type" porous structures and commercially used non-spherical porous soundproofing materials.

Samples	Ø (%)	r_w/r_p [-]	*Dp* (μm)	k_0 (m^2)	*Ap*	*f*peak (Hz)	*NRC*	*SAA*
A21	56.00	0.15	1800	4.77E-10	0.954	1800	0.366	0.564
B2	80.00	0.15	1400	5.89E-10	0.997	2200	0.398	0.610
C2	68.00	0.15	1400	4.26E-10	0.961	2000	0.399	0.609
E1	80.00	0.45	200	4.37E-10	0.979	2200	0.414	0.628
F1	68.00	0.45	200	3.16E-10	0.918	1900	0.405	0.609
DU1-10	66.99	0.17	1000	4.61E-10	0.968	2000	0.396	0.605
Measured	60.00	0.19	1600	8.10E-10	0.972	2350	0.337	0.415
DBM/GWF	98.70	0.56	474	1.08E-09	0.968	4800	0.291	0.441
DBM/MF	99.30	0.45	890	1.39E-09	0.943	5200	0.314	0.445
JCA/SFM	90.94	0.58	388	9.59E-10	0.941	3300	0.275	0.409

For a 20mm hardbacked numerical simulation in Fig 5.17, much improved acoustic properties were achieved for these structures better than that in Li et al. (2014) for porosity, 60% and window to pore ratio, 0.19, and those of non-spherical celled soundproofing materials in Kino and Ueno (2008), and Bo and

Tianning (2009). Also, the complexity in getting rid of salts completely from smaller pore diameter sized "bottleneck" structures (below 500µm), could provide a hindrance in its application; and if properly removed, they could prove useful in greatly minimizing resonance effects by lowering the differential pressure used during casting process (Table 5.8). Predictive performance of these small-sized and highly porous "bottleneck-type" structures (B2 and E1) in Fig 5.17 behaves well over the essential low (200-2000Hz) and mid-frequencies (2000-45600Hz) better than those "bottleneck-type" structures in Li et al. (2011), and Li, et al. (2014) and commercially used sound absorbing structures as well.

Structural length effects and airgap insertion were numerically considered for sensible application of the optimized C2 structure capable of reproducing realistically. For thicknesses ranging between 3 and 40mm, hardbacked numerically simulated values of the characteristic absorption curve is plotted against frequency in Fig 5.18. To fully understand the contributory effects of back cavity insertion to the rationalization of the characteristic absorption curve of these "bottleneck-type" structures, Fig 5.19 plots the noise reduction coefficients against structural thickness for hardbacked and airgap (cavities, 10, 25 and 50mm) behind (BHD) and between (BTW) two equally thick porous structures of similar topology. For thicknesses below 10mm, the absorption coefficient of this material is very poor and a shift in the absorption curve to the lower frequency with greater absorption peak was observed for improved structural thicknesses, 10 and 20mm. This shifts further to the lower frequency for thicknesses beyond the 20mm but the absorption peak drops to 91 and 84%

of the maximum absorption value at the 30 and 40mm thick structures respectively.

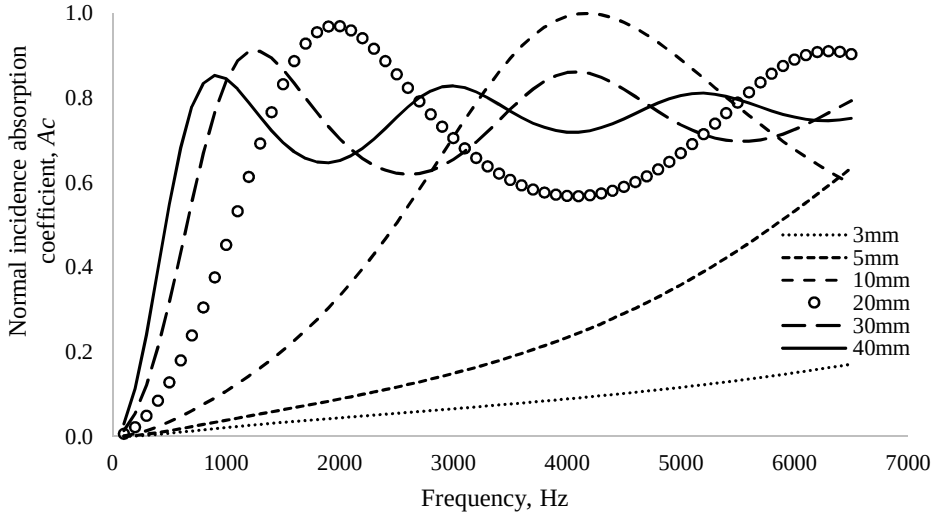


Fig 5.18. Plots of hardbacked numerically simulated normal incidence absorption coefficient against frequency (Hz) for optimized C2 structure for thicknesses between 5 and 40mm.

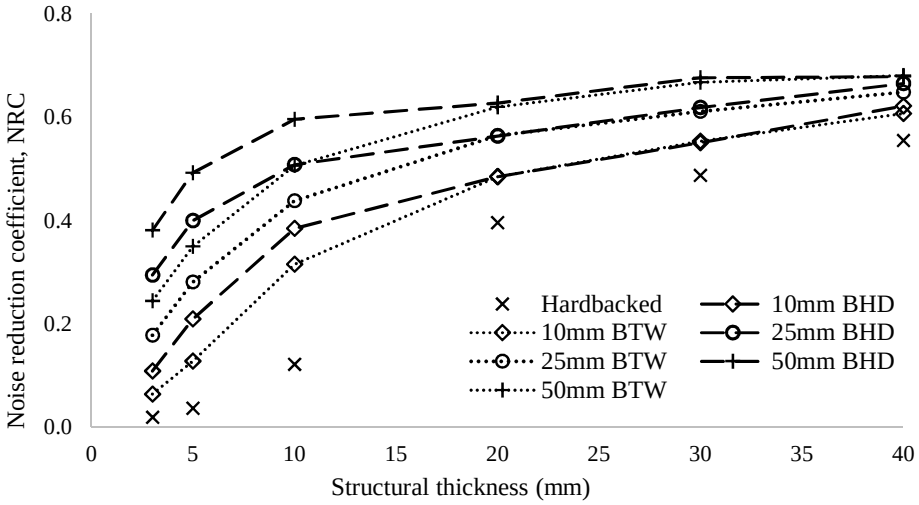


Fig 5.19. Plots of noise reduction coefficient (*NRC*) against structural thickness (mm) for 20mm thick hardbacked, 10, 25 and 50mm airgap behind (BHD) and between (BTW) two 10mm optimized C2 structures.

An observable shift in the predicted normal incidence absorption coefficient to the lower frequency was noticed with the insertion of airgap both behind and in between the structures. A higher absorption peak at the low frequencies (f < 2000Hz) favoured airgap between two equally thick samples whilst higher

absorption peak and curve favoured airgap insertion behind the structures at higher frequencies (f > 2000Hz). Structural vibration at the low frequencies is quite low (Johnson et al., 1987) and exited pressure wave from the preceding sample into the succeeding sample is further re-energised, striking the surface of the second sample and thereby giving a higher absorption peak at the low frequencies whilst continuing travelling of sound wave within a longer length structure, shifts the absorption curve to the lower frequencies with reduced energy associated with structural vibration. In Fig 5.19, for structures below the 20mm thickness, higher *NRC* favoured airgap insertion behind the structures and above this thickness. There are not any significant differences in the insertion of airgaps behind or between equally thick samples. Thus, the choice of structural thickness and cavity insertion would depend on the frequency range of applications.

5.8 Erosion and dilation effects using the sphere-packing model

In the sphere-packing model, erosion and dilation of the skeletal phase of the "virtual" porous matrix could be of assistance toward the design of material with novel attributes. Erosion of the skeletal phase of closed celled structures further widened the windows and, else, it is termed dilation of much opened "bottleneck" structures as shown in Fig 5.1A-Fig 5.12A of the appendices. A tabular representation of structural parameters of eroded and dilated structures along with their numerically computed values of acoustic properties is presented in Table 5.7A of the appendices.

Changes in the inherent properties of the 1mm pore diameter sized structure having the least pore diameter openings (DU1-10) were observed with porosity

and pore sizes increasing by 6-7% and 2-4% respectively and windows nearly double upon erosion (pixels removed). Also, the dilation of the structural phases of structures with the widest openings having 1mm pore sizes (DU1-80), reduces their porosity, pore diameter sizes and windows in similar percentages observed as in case of erosion. The absorption potentials (*Ap*, *NRC*, and *SAA*) of DU1-10 (no erosion) and DU1-E1 (1 pixel removed) structures look good due to their important window to pore ratio of 0.172 and 0.270 and a permeability of $4.6x10^{-10}$ and $1.47x10^{-09}m^2$ was attained respectively for both structures. This is within the range of permeabilities observed in Fig 5.16 attributable to having the optimum values of acoustic properties.

A further increment in the openings of this structure by removing 2-pixels element, greatly increases their permeability and window to pore ratio but reduces the absorptive performance of the structure to less than 90% peak absorption and may not be good to cast our spherically celled porous metallic structure with such operating parameters for efficient soundproofing. Also, the peak absorption, noise reduction coefficient and sound absorption average of dilated DU1-80 structure increases between 0.792-0.911, 0.233-0.292 and 0.359-0.435 respectively. This is due to the important reduction in the mean openings and window to pore size ratio of the original structure (DU1-80) from 364-309μm and 0.364-0.309 respectively. Continued dilation of the structural phase seems unfavourable for the 1mm sized structure at 10μm capillary radius but looks better when applied on a much-opened structure with large pore sizes (2-3mm pore sizes) at the 10μm capillary radius.

In summary, accurate determination of pore sizes and pore openings are key to the rationalization of predictive sound spectra and properties of this “bottleneck-

type" porous metallic structure with the permeabilities of excellent absorbers typically ranging between 0.4-1.5x$10^{-09}$$m^2$ for any packing density between 60-80%. To achieve this permeability, it is advisable to maintain the window to pore size ratio to within 0.1-0.3. Below and above these specified ranges, the structure would either be too close or too open for the effective absorption of the sound pressure wave and poor vibrational control.

5.9 Conclusions

Pore-level CFD determination of permeability using X-Ray tomography images of "real" structure and analytical "bottleneck" approach available in the literature, make clear that the "virtual" macroporous structure is efficient in replicating porous metal foams made by sintering dissolution process of packed beds of spherical salts and the precise determination of other macroscopic parameters needed for sound absorption modelling.

The variations in absorption peak, absorption band and shifts of absorption curve to either the frequency minima or maxima at varying degree of the capillary radius and pore sizes indicate a strong dependence of the normal incidence absorption coefficient on the important permeability and porosity of the structure.

Alteration to the "bottleneck" structures to model more intricate monosized structures for pore sizes below 500μm and to explore the opportunity to which the larger pore size structures could be useful, was done, to achieve the optimum structural parameters needed for casting processes. The extent to which this structure thrust back pressure wave to access its interior cellular structure was

achieved for pore diameter openings below 75μm and becomes poor absorber for window diameter opening beyond 350μm. The potential for the "bottleneck" structures to respond well to the absorption of sound pressure wave was achieved for permeabilities, porosities and window to pore ratio between 0.4-1.5x$10^{-09}$$m^2$, 60-80% and 0.1-0.3 respectively.

Furthermore, structural erosion and dilation of more closed and more opened structures carried out within ScanIP only provide a useful tool for stretching the important of microstructural effects on the acoustic performance of realistic porous structure in the virtual sense and can be replicated by simply varying the differential pressure used in the real casting of the metallic structures using Eq 1.2.

Lastly, the absorption potential of this structure was further improved at the ⅓ octave frequencies through increased porous layer thickness and an appropriate airgap insertion, computed numerically.

CHAPTER 6

CONCLUSIONS AND FUTURE WORK

The research presented in preceding chapters has enclosed a spectrum of unanswered questions regarding the flow and acoustic behaviour of porous aluminium foams with major emphasis on “bottleneck-type” structures. The work has encompassed studies on the manufacture, flow behaviour and acoustic absorption in these structures leading to the design and optimization of materials capable of replacing conventionally used porous absorber in high-end speakers. The key conclusions drawn out from this work are reiterated below.

- Determination of the structural and flow information of mono-sized “bottleneck-type” structures is possible using sphere-packing models.
- Structural and flow information of these structures can be varied widely for mixed-sized (bimodal) packing arrangements.
- Air CFD simulation across these structures using tomography images and sphere packing model were within experimental scatter and proposed theoretical models can be used to quantify flow behaviour at low and high velocities. These represent a novel finding.
- Appropriate ranges of optimized non-acoustical macroscopic parameters needed to the design of enhanced “bottleneck-type” structures were achieved for hardbacked and airgap pressure wave simulations.
- These parameters could prove useful in the design of porous metallic structures for efficient sound absorption in loudspeakers

Statement of Originality

Chapter 3 onwards is original work. Characterization, flow simulation and acoustic absorption through porous structures using discrete element simulation (DEM) packing of near-spherical structures has not been studied and this represents a significant breakthrough to pore-scale technique. The application of this technique is presented in Chapter 3 to Chapter 5 of this work. Three papers from these chapters have been published in highly esteemed Elsevier journals of high impact factor ratings and there are provisions for more potential papers. Lastly, proposed theoretical models to predict the viscous and inertial terms of these unique structures using “structural-adapted” X-ray CT images of the real structures is new and has been published by this group in Acta Materialia, Elsevier Journal, February 2018.

REFERENCES

ABELL, A. B., WILLIS, K.L. and LANGE, D. A. (1999), Mercury Intrusion Porosimetry and Image Analysis of Cement-Based Materials, *Journal of Colloid and Interface Science*, Vol 211, Pp. 39-44.

Acoustic of Porous Material Recipes 2014, http://apmr.matelys.com/index.html.

ADLER, P. M. (1992), Porous Media: Geometry and Transport, Boston, Butterwort-Heinemann.

ALLARD, J. F. and CHAMPOUX, Y. (1992), New Empirical Equations for Sound Propagation in Rigid Frame Fibrous Materials, *J. Acoust. Soc. Am*. 91(6). Pp 3346-3353.

ANSI, (1994), America National Standard: Acoustic Terminology, Sec 303 en.wikipedia.org/wiki/sound06-01-05.

ANTOHE, B., LAGE, J. L., PRICE, D. C. and WEBER, R. M. (1997), Experimental Determination of the Permeability and Inertial Coefficients of Mechanically Compressed Aluminium Metal Layers. *ASME J. Fluids Eng.,* Vol 11, Pp 404-412.

ARCHIE, G. E. (1942), The Electrical Resistivity Log as an Aid in Retaining Some Reservoir Characteristics, *Trans AIME*, 116, Pp 54-62.

ASHBY, M. F., EVANS, A. and KENNEDY, A. R. (2006), The Role of Oxidation during Compaction on the Expansion and Stability of Al Foams made via a PM Route, *Advanced Engineering Materials*, Vol 8, Pp 568-570.

ASHBY, M. F. and TIANJIN, L. U. (2003), Metal Foams: A Survey, Science in China Series (b), Vol. 46, No. 6, Pp 521-530.

ASHOLT, P. (1999), Metal Foams and Porous Metal Structures, ed Banhart, J. Ashby, M. F. and Fleck, N. A. (Bremen, Germany: MIT-Verlag, p.133.

ASMAR, B. N., LANGSTON, P. A. and MATCHETT, A. J. (2002). A Generalized Mixing Index in Discrete Element Method Simulation of Vibrated Particulate Beds. *Granular matter* 4(3): 129-138.

ATTENBOROUGH, K. (1983), Acoustical Characteristics of Rigid Fibrous Absorbents & Granular Materials, *J. Acoust. Soc. Am*. Vol 73, Pp 785-799.

ATTENBOROUGH, K. (1993), Models for the Acoustical Characteristics of Air Filled Granular Materials, *Acta Acoustica* 1, Pp 213-226.

BALLAGH, K.O. (1996), Acoustical Properties of Wool, *Applied Acoustics*, Vol. 48, No 2, Pp 101 – 120.

BANHART, J. (2001), Manufacture, Characterization, and Application of Cellular Metals & Metal Foams, *Progress in Materials Science*, Vol 46, Pp 559-632.

BANHART, J. (2006). Metal Foams: Production and Stability, *Advanced Engineering Materials*, Vol 8. Pp 781-794.

BANHART, J. AND BAUMEISTER, J. (1998), Deformation Characteristics of Metal Foams, *Materials Science*, Vol 33, 1431-1440.

BASAK, P. and RAJAGOPALAN, S. P. (1982), Effect of Non-Darcy Flow on Computing Seawater Intrusion Length, *Journal of Hydrogeology*, Vol 58, Issue 1-2. Pp 83-87.

BAUMGARTNER, F., DUARTE, I. and BANHART, J. (2000). Industrialization of Powder Compact Foaming Process. Advanced Engineering Materials, Vol 2, Pp 168-174.

BEAR, J. (1972), Dynamics of Fluids in Porous Media, *Dover Publications*, Pp 124-130.

BEJAN, A. (1984), Convection Heat Transfer, John Wiley & Sons.

BELL, L. H. (1982), Industrial Noise Control. Marcel Dekker, New York, P 199.

BERANEK, L. L. (1942), Acoustic Impedance of Porous Materials. *J. Acoustic. Soc. Am.* 13, Pp 248-260.

BHATTACHARYA, A., CALMIDI, V. V. and MAHAJAN, R. L. (2002), Thermo-Physical Properties of High Porosity Metal Foams, *Int. J. Heat & Mass Transfer*, 45, 1017.

BIES, D. A. and HANSEN, C. H. (2009), Engineering Noise Control, Spon Press, New York.

BIOT, M. A. (1956b), Theory of Propagation of Elastic Waves in a Fluid-Saturated Porous Solid II: Higher Frequencies Range, *J. Acoust. Soc. Am*, 28 (2), Pp 168-178.

BO, Z. and TIANNING, C. (2009), Calculation of Sound Characteristics of Porous Sintered Fiber Metal. *Applied Acoustics* 70, Pp 337-346.

BODLA, K. K., MURTHY, J. Y. and GARIMELLA, S. V. (2010), Microtomography-Based Simulation of Transport through Open-Cell Metal Foams, *CTRC Research Publication*, Purdue University e-Pubs. Pp 527-544.

BONNET, J. P. TOPIN, F. and TADRIST, L. (2008), Flow Laws in Metal Foams: Compressibility and Pore Size Effects. *Trans. Porous Med.* Vol 73. Pp 149-163.

BOOMSMA, K. and POULIKAKOS, D. (2001), On the Effective Thermal Conductivity of a Three-Dimensionally Structured Fluid-Saturated Metal Foam, *Int. J. Heat and Mass Transfer*, Vol. 44, Pp 827-836.

BOOMSMA, K. and POULIKAKOS, D. (2002), The Effect of Comparison and Pore Size Variations on the Liquid Flow Characteristics in Metal Foams, *ASME J. Fluids Eng.*, Vol. 124, Pp 263-273.

BRAM, M., STILLER, C. BUCHKREMER, H.P., STOVER, D. AND BAUER, H. (2000), High-porosity titanium, stainless steel and superalloy parts, *Advanced Engineering Materials*, 2:196.

CARMAN, P.C. (1937), Fluid Flow through Granular Beads, Chemical Engineering Research & Design: Transactions of the Institution of Chemical Engineers Part A, Vol 15, Pp 415-421.

CHANG-YOUNG, L. and MICHAEL, J. L. (2009), Acoustic Absorption Calculation in Irreducible Porous Media: A Unified Computational Approach, Georgia Institute of Technology, Atlanta, Georgia, Pp 1862-1870.

CHEN, L. (2014), A Simple Construction of a Fortin-Operator for the Two-Dimensional Taylor-Hood Element. Department of Mathematics, University of California, USA.

CHO, J. HONG, S. LEE, S., AND CHO, C. (2012), Impact fracture behaviour at the Material of Aluminium Foam. *Materials Science and Engineering*: A, 539, Pp 250-258.

CMI, (2014), Clay Mathematic Institute, Millennium Prize Problem.

CROCKER, M. J. (2007), Handbook of Noise and Vibration Control, John Wiley & Sons Inc, New Jersey.

COMSOL, (2015), Introduction to the Acoustic Module, US Patent, 7, 519, 518; 7, 596, 474 & 7, 623, 991. www.comsol.com/product/tutorial.

COULSON, J. M. (1949), The Flow of Fluids Through Granular Beds: Effects of Particle Shape and Voids in Streamline Flow. *Trans.Inst.Chem.Eng*, Vol 27, Pp 237-257.

DARCY, H. (1856), Les Fotaines Publiques de la Ville de Dijon, Dalmont, Paris.

DE CARVALHO, T. P., MORVAN, H. P. and HARGREAVES, D. (2014), Pore-Level Numerical Simulation of Open-cell Metal Foams with Application to Aero Engine Separators, *Turbine Technical Conference and Exhibition*, Dusseldorf, Germany.

DE CARVALHO, T. P., MORVAN, H. P., HARGREAVES, D., OUN., H. and KENNEDY, A. (2017), Pore-Scale Numerical Investigation of Pressure Drop Behaviour Across Open-Cell Metal Foams, *Tran Porous Med*, 117(2), Pp 311-336.

DEGISCHER, H. P., FOROUGHI, B. and KOTTAR, A. (2013). Tomography Based Material Model and Simulation of Deformation, DESTECH Publication, Inc. Technology & Engineering, USA.

DELANY, M. E. and BAZLEY, E. N. (1970), Acoustical Properties of Fibrous Absorbent Materials, *Applied Acoustics*, 3(2), Pp 105-116.

DENG, X. Z., LIU, H. S. and HUANG, X. Y. (2008), Numerical Simulation of Effect of CO_2 Content on Cell Nucleation in Microcellular Plastics Extrusion Processing for Supercritical CO2/PS, *Plastics Sci. Tech.* 36(8), Pp 30-32.

DESPOIS, J. F., and MORTENSEN, A. (2005), Permeability of Open-pore Microcellular Materials, *Acta Materialia* 53, Pp 1381-1388.

DESPOIS, J. F., MARMOTTANT, A., SALVO, L. and MORTENSEN, A. (2007), Influence of the Infiltration Pressure on the Structure and Properties of Replicated Aluminium Foams. *Material Science and Engineering A*, Vol 462, Pp 68-75.

DIANI A, BODLA K. K, ROSSETTO, L. and GARIMELLA S, V. (2015), Numerical Investigation of Pressure Drop and Heat Transfer through Reconstructed Metal Foams and Comparison against Experiments, *International Journal of Heat and Mass Transfer*, Vol 88, Pp 508-515.

DIAS, R., TEIXEIRA, J. A., MOTA, M. and YELSHIN, A. (2006), Tortuosity Variation in a Low-Density Binary Particulate Beds, *Sep. Purif. Technol*. Vol 51(2), Pp 180–184.

DU PLESSIS, J. P. (1994), Analytical Qualification of Coefficients in the Ergun Equation for Fluid Friction in a Packed Bed, *Transport in Porous Media*, Vol 16, Pp, 189-207.

DU PLESSIS, J. P. and FOURIE, J. G. (2002), Pressure Drop Modelling in Cellular Metallic Foams, *Chem. Eng. Sci.* Vol 57, Pp 2781-2789.

DU PLESSIS, P., MONTILLET, A. AND COMITI, J. (1994), Pressure-drop Prediction for Flow through High Porosity Metallic Foams, *Chemical Engineering Science*. Vol 49, Pp 3545-3553.

DU PLESSIS, J. P. and WOULDBERG, S. (2008), Porescale Derivation of Ergun Equation to Enhance its Adaptability and Generalization, *Chemical Engineering Science*, Vol 63, Pp 2576-2586.

DUKHAN, N. (2013), Metal Foams: Fundamental and Applications. DESTECH Publication, Inc. Technology & Engineering, USA, Pp 1-310.

DUKHAN, N., BAGCI, O. AND OZDEMIR, M. (2014), Experimental Flow in various Porous Media and Reconciliation of Forchheimer and Ergun Relation. *Experimental Thermal and Fluid Science*, Vol. 57, Pp 425-433.

DUKHAN, N. and MINJEUR, C. A. (2010), A Two-Permeability Approach for Assessing Flow Properties in Cellular Metals, *Journal of Porous Materials*, Vol. 18(2), Pp 417-424.

DUKHAN, N. and PATEL, P. (2008), Equivalent Particle Diameter and Length Scale for Pressure Drop in Porous Metals, *Experimental Thermal and Fluid Science* Vol 32, Pp 1059-1067.

DULLIEN, F. A. L. (2012), Porous Media: Fluid Transport and Pore Structure, Academic Press, 2nd Edition, Pp 6-110.

DYBBS, A. and EDWARDS, R. V. (1984), A New Look at Porous Media Fluid Mechanics-Darcy to Turbulent. *inJ*. Bear, M.Y. *Nato ASI series* E.

EDOUARD, D., LACROIX, M., HUU, C. P. and LUCK, F. (2008), Pressure Drop Modelling on Solid Foam: State-of-the-Art Correlation. *Chemical Engineering Journal*, Vol.144, Pp 299-311.

EDOUARD, D., IVANOVA, S., LACROIX, M., VANHAECKE, E., PHAM, C. and PHAM–HUU, C. (2009), Pressure Drop Measurements and Hydrodynamic Model Description of SiC Foam Composite Decorated with SiC Nanofiber Catalyst. *Today*, Vol 14, Pp 403-408.

ERGUN, S. (1952), Fluid Flow through Packed Column, *Chemical Engineering*, 48, Pp 89-94.

FTCS, (1969), Fundamental of Telephone Communication Systems. Western Electric Company. P2.1. en.wikipedia.org/wiki/sound06-01-2015.

FULARIA, D., LEE, P. D. and BERNARD, D. (2007), Determining the Fluid Flow and Deformation Behaviour of both Simulated and Measured Columnar-Dendritic Structures in Al-Cu Alloys, *5th Decennial Int. Conf. on Solidification Processing*, Sheffield, United Kingdom.

FURMAN, E. L. FINKELSTEIN, A .B. and CHERNY, M. L. (2013), The Permeability of Aluminium Foams Produced by Replicated-Casting. *Metals*. Vol 3, Pp 49-57.

GERGELY, V. and CLYNE, B. (2000). The FORMGRIP Process: Foaming of Reinforced Metals by gas Release in Precursors, *Advance Engineering Materials*, Vol 2, Pp 175-178.

GIBSON, L. J., ASHBY, M. F. (2001), Cellular Solids, *Structure and Properties,* Vol 2. Cambridge, Cambridge University Press.

GOODALL, R., MARMOTTANT, A., SALVO, L. and MORTENSEN, A. (2007), Spherical Pore Replicated Microcellular Aluminium: Processing and Influence on Properties, *Material Science and Engineering A,* Vol 465, Pp124-135.

GOODALL, R., DESPOIS, J. F., MARMOTTANT, A. and MORTENSEN, A. (2006), The Effect of Preform Processing on Replicated Aluminium Foam Structure and Mechanical Properties, *Scripta Materialia,* Vol 54, Pp 2069-2073.

GUO, P. (2015), Lower and Upper Bounds for Hydraulic Tortuosity of Porous Materials, *Transp. Porous Med,* Vol 109, Pp 659-671.

HABISREUTHER, P., DJORDJEVIC, N. and ZARZALIS, N. (2009), Statistical Distribution of Residence Time and Tortuosity of Flow through Open-celled Foams. *J.ces*. 07.033.

HAN, F., SEIFFERT, G., ZHAO, Y. and GIBBS, B. (2003), Acoustic absorption Behaviour of an Open-celled Aluminium Foam. *J. Phys. D,* 36, Pp 294 – 302.

HARKER, J. H., RICHARDSON, J. F. and BACKHURST, J. R. (2002), *Chemical Engineering*, Vol 2, Pp 193-233.

HESKETH, R. P. (2008), Flow Between Parallel Plates-Modified from the COMSOL ChE Library Module, Department of Chemical Engineering, Rowan University, Pp 3-4.

HETU, J. -F., ILINCA, F., MARCOTTE, J. -P, BARIL, E., LEFERBVRE, L. P. and INNOCENTINI, M. D. M. (2013). Numerical Simulation of the Flow through Metallic Foams: Multi-scale Modelling and Experimental Validation. DESTECH Publication, Inc. Technology & Engineering, USA.

HINZE, B. and ROSLER, J. (2014), Measuring & Simulating Acoustic Absorption of Open-Celled Metals. *Advanced Engineering Materials*, 16. No 3.

HO, F. G. and STRIEDER, W. (1982), A Mean Free Path Theory of Sound Diffusion in a Porous Medium with Surface Diffusion. II. Numerical Evaluation of The Effective Diffusivity For Arbitrary Knudsen Number, *The Journal of Chemical Physics* Vol 76, Page 673.

HWANG, J. J., HWANG, G. J., YEH. R. H. AND CHAO, C. H. (2002), Measurement of Interstitial Convective Heat Transfer and Frictional Drag for flow across Metal Foam, *Journal of Heat Transfer*, Vol 124, Pp 120-129.

INNOCENTINI, D. M. M., SALVINI, V. R., MACEBO, A. and PANDOLFELLI, V. C. (1999), Prediction of Ceramic Foams Permeability using Ergun Equation, *Mater. Res. 2*. P283.

JINNAPAT, A. and KENNEDY, A. R. (2010). The Manufacture Spherical Salt Beads and their use as Dissolvable Templates for the Production of Cellular Solids via a Powder Metallurgy Route. *Journal of Alloys and Compound*. Vol. 499, Pp 43-47.

JINNAPAT, A. and KENNEDY, A. R. (2011), The Manufacture and Characterization of Aluminium Foams Made by Investment Casting Using Dissolvable Spherical Sodium Chloride Bead Preforms. *Metal 1*(1), Pp 49-64.

JINNAPAT, A. AND KENNEDY, A. R. (2012), Characterization and Mechanical Testing of Open Cell Al Foams Manufactured by Molten Metal Infiltration of Porous Salt Bead Preforms: Effect of Bead Size. *Metals* 2(2), Pp 122-134.

JOHNSON, D. L., KOPLIK, J. and DASHEN, R. (1987), Theory of Dynamic Permeability & Tortuosity in Fluid-Saturated Porous Media, *J. Fluid Mech.*, Vol 176, Pp 176-402.

JOHNSON, D. L., PLANA, T. J., SCALA, C., PASIERB, F. and KOJIMA, H. (1982), Tortuosity & Acoustic Slow Waves, *Phys. Rev. Lett.* Vol 49, Pp 1840-1844.

JOHNSON, E. A. C. and YOUNG, P. G. (2005), On the use of a Patient-Specific Rapid-Prototyped Model to Simulate the Response of the Human Head to Impact & Comparison with Analytical Finite Element Models, *J. Biomech*, Vol. 38, Pp 39-45.

JONES, P. W. (2010), Measuring and Simulation of Acoustic Performance of Polyurethane Foam Filled Muffler: A Case Study, University of New South Wales, Sydney, Australia.

JORGES, P. A. and MALCOM, J. C. (2010), Recent-Trends in Porous Sound-Absorbing Materials, *Sound and Vibration*, Vol 44, Pp 12-17.

KARIMIAN, S. A. M. and STRAATMAN, A. G. (2008), CFD Study of the Hydraulic and Thermal Behaviour of Spherical-Void-Phase Porous Materials, *International Journal of Heat and Fluid Flow*, Vol 29, Pp 292-305.

KECECIOGLU, I. and JIANG, Y. (1994), Flow through Porous Media of Packed Spheres Saturated with Water. *ASME J. Fluids Eng*., Vol 116, Pp 164-170.

KENNEDY, A. R. (2012), Porous Metals and Metal Foams made from Powders. Powder Metallurgy. Manufacturing Division, University of Nottingham, Nottingham, UK.

KENNY, L. D. (1996), Mechanical Properties of Particles Stabilized Aluminium Foam. Materials Science Forum, Vol. 217-222, Pp 1883-1890.

KHAYARGOLI, P., LOYA, V., LEFEBVRE, L. P. and MEDRAJ, M. (2004), The Impact of Microstructure on the Permeability of Metal Foams, *CSME 2004 Forum*, Pp 220-228.

KIM, S. Y., NAKAJIMA, H. and HUR, B. Y. (2009), Fabrication of Lotus-Type Porous Nickel through Thermal Decomposition Method of Compounds by Mold Casting Techniques, *Metals and Metallic Foams*. Korean Journal of Materials Research, 19(5), 270-275.

KINO, N. and UENO, T. (2008), Comparison between Characteristic Lengths and Fiber Equivalent Diameter in Glass Fiber and Melamine Foam Materials of Similar Flow Resistivity, *J. App. Acoustics*, Vol 69, P. 325.

KIRCHOFF, G. (1974), On the influence of Heat Conduction in a Gas on Sound Propagation, R.B. Lindsay (Ed). Stroudsburg PA: Dowden, Hutchinson & Ross.

KOZENY, J. (1927), Ueber Kapillare Leitung des Wasser im Boden, Sitzungsber Akad. Wiss. Wien, 136(2), Pp 271-300.

KOUIDRI, A., MADANI, B., and ROUBI, B. (2015), Experimental Investigation of Flow Boiling in a Narrow Channel, *International Journal of Thermal Sciences*, Vol 98, Pp 90-98.

LACROIX, M., NGUYEH, P., SCHWEICH, D., PHAM-HUU, C. and SAVIN-PONCET, S. (2007), The Pressure Drop Measurement and Modelling on SiC Foams. *Chemical Engineering Science*, Vol 62, Pp 3259-3267.

LAGE, J. L., KRUEGER, P. S. and NARASIMHAM, A. (2005), Protocol for Measuring Permeability and Form Coefficient of Porous Media, *Physics of Fluids*, 17-088101.

LAFARGE, D., LEMARINAR, P. and ALLARD, J. F. (1997), Dynamic Compressibility of Air in Porous Structure at Audible Frequencies, *Acoustic Society of America*, Pp 1-12.

LAFARGE, D., LEMARINAR, P., ALLARD, J. F. and TARNOW, V. (1997), Dynamic Compressibility of Air in porous Structures at Audible Frequencies, *J. Acoust. Soc. Am.* 102:1995.

LANGSTON, P. and KENNEDY, A. R. (2014). Discrete Element Modelling of the Packing of Spheres and its Application to the Structure of Porous Metals made by Infiltration of Packed Beds of NaCl Beads. *Powder Technology*, 268, Pp 210-218.

LAUTENSACK, C. and KABEL, M. (2009), Modelling and Simulation of Acoustic Absorption of Open Cell Metal Foams, Cellular Metals for Structural and Fundamental Applications. Fraunhofer IFAM, Dresden. Pp 271-276.

LAWSON, C. L. and HANSON, R. J. (1974), Solving Least-Squares Problems, *Englewood Cliffs*, NJ: Prentice-Hall.

LE BARS, M. and WORSTER, M. G. (2006), Interfacial Conditions between a Pure and a Porous Medium: Implications for Binary Alloy Solidification, *J. of Fluid Mechanics*, Vol. 550, Pp 151-170.

LECLAIRE, P., KELDER, L., LAURIKS, M., MELON, M., BROWN, N. and CATAGENDE, B. (2012), Determination of the Viscous and Thermal Characteristic Length of Plastic Foam by Ultrasonic Measurement in Helium and Air, *J. Appl. Phy*. 80.

LEE, C. Y., LEAMY, M. J. and NADLER, J. H. (2009), Acoustic Absorption Calculation in Irreducible Ductile Porous Media: A Unified Computational Approach, *J. Acosut.Soc.Am*. 126(4):1862.

LI, Y., WANG, X., WANG, X., REN, Y., HAN, F., and WEN C., (2011), Sound Absorption Characteristics of Aluminium Foam with Spherical Cells, *Journal of Applied Physics* 110, 113525.

LI, Y., ZHENDONG, L. and HAN, F. (2014). Airflow Resistance and Sound Absorption Behaviour of Open-celled Aluminium Foams with Spherical Cells. *Procedia Materials Science* Vol 4, Pp 187-190.

LIU, J. F., WU, W. T., Chiu, W. C. and HEISH, W. H. (2006), Measurement and Correlation of Friction Characteristics of Flow through Foam Matrix. Exp. *Therm. Fluid Sci*. 30 P329.

LIU, H. L. and HWANG, H. R. (2012), Permeability Prediction of Fibrous Porous Media with Complex 3D Architectures, *Composite Part A*, Vol 43, Pp 2030-2038.

LIU, P. S. and CHEN, G. F. (2014), Porous Materials Processing and Applications, Tsinghua University Press Limited, Elsevier Inc. Pp 120-150.

LU, J. J., HESS, A. and ASHBY, M. F. (1999), Sound Absorption of Metallic Foams, *America Institute of Physics,* 99, 07511- 9.

LU, M., HOPKINS, C., ZHAO, Y and SEIFFERT, G. (2009), Sound Absorption Characteristics of Porous Steel Manufactured by Lost Carbonate Sintering, *Mater.Res. Soc. Symp.* Proc. Vol 1188-LL07-04.

LU. T. J. F and HE, D. (2000), Sound Absorption of Cellular Metals with Semi-Open Cells, *J. Acoust. Soc. Am.* 108 (4), Pp 1697-1708.

LU, T. J., STONE, H. A. and ASHBY, M. F. (1998), Heat Transfer in Open-cell Metal Foams. *Acta Materialia,* Vol 46, Pp 3619-3635.

MA, L. and SONG, Z. (1998), Cellular Structure of Aluminium Foams during Foaming Process of Aluminium Melt, Scripta Materialia, Vol 39 (11), p. 1523.

MATYKA, M., KHALILI, A. and KOZA, Z. (2008), Tortuosity-Porosity Relation in Porous Media Flow, Physical Review E 78, 026306.

MICHAEL, E. (2006), The Dawn of Fluid Dynamics: A Discipline Between Science and Technology. Wiley. P. ix. ISBN 3-527-40513-5.

MIFFLIN, H. (2014), The American Heritage ®, Science Dictionary.

MIKKI, Y. (1990), Acoustical Properties of Porous Materials-Modifications of Delany Bazley Model, J. *Acoust. Soc., Jpn* (E). 11(1), Pp 19-24.

MUHAMMED, M. M., SA'AT, N. A., NAIM, H., ISA, M. C., YUSSOF, N. H. N. and YATI, M. S. D. (2013), The Effect of Air Gap Thickness on Sound Absorption Coefficient of Polyurethane Foam, Marine Material Research group, Science and Technology Research, Institute of Defence, Ministry of Defence, Malaysia.

MONTMING, M. D., TANNENBAUM, A. R. and MACOSKO, C. W. (2004), The 3D Structure of Real Polymer Foam, *Journal of Colloid & Interface Science*, 280, Pp 202-423.

MOSTAFID, A. M. (2007), Entrance and Exit Effect of Flow through Metallic Foams. Department of Mechanical and Industrial Engineering, Concordia University, Quebec, Canada.

MUSKAT, M. and BOTSET, H. G. (1931), Flow of Gas through Porous Materials. *Physic 1*, Pp 27-47.

NARSILIO, G. A., BUZZI, O., FITYUS, S., YUN, T. S. and SMITH, D. W. (2009), Upscaling of Navier-Stokes Equation in Porous Media: Theoretical, Numerical and Experimental Approach. *Computers & Geotechnics*, 36: Pp 1200-1206.

NIELD, D. A. and BEJAN, A. (1992), Convection in Porous Media, Springer, 2nd ed. New York, Pp 8-91.

NJOKU, R. Unpublished research, University of Nottingham, 2014.

NORTON, M. P. and KARSZUB, D. G. (2003), Fundamental of Noise and Vibration Analysis for Engineers, Cambridge University Press, United Kingdom.

NPR, (2014), What Does Sound Look Like? enwikipedia.org/wiki/sound.

OLNY, W, ATALLA, N. and CASTEL, F. (2004), On the use of Perforations to Improve the Sound Absorption of Porous Materials: Innovative Applications of Materials for Acoustics Purposes, *Applied Acoustics*, Vol. 66, Pp 625-651.

OLNY, X. and PANNETON, R. (2008), Acoustic Determination of the Parameters Governing Thermal Dissipation in Porous Media, *J. Acoust. Soc. Am* Vol 123, Pp 814-824.

OLNY, X., PANNETON, R. and TRAN VAN, J. (2003), Experimental Determination of Acoustical Parameters of Rigid and Limp Materials Using Direct Measurements and Analytical Solutions, G.A.U.S Department of Mechanical Engineering, Universite de Sherbrooke, Canada, Pp 1-6.

OTARU, A. J. and KENNEDY, A. R. (2016), The Permeability of Virtual Macroporous Structures Generated by Sphere-Packing Models: Comparison with Analytical Models. *Scripta Materialia,* Vol 124, Pp 30-33.

OTARU, A.J., MORVAN, H. P. and KENNEDY, A. R. (2018), Measurement and Simulation of Pressure Drop across Replicated Microcellular Aluminium in the Darcy-Forchheimer Regime, *Acta Materialia,* Vol 149, Pp 265-275.

ORTIZ, M. (2012), Multiscale Modelling of Materials: Linking Microstructure & Macroscopic Behaviour, *DOE CSGF Conference*, Krell Institute.

OU, Y.X. (1997), Flame Retardant-Manufacturing, Properties and Applications, Weapon industry Press, Beijing.

OUN, H. and KENNEDY, A. R. (2014), Experimental Investigation of Pressure Drop Characterization across Multilayer Porous Metal Structure, *J.Porous Mater*. 21: 1133-1141.

OUN, H. and KENNEDY, A. R. (2015), Tailoring the Pressure Drop in Multi-layered Open-cell Porous Inconel Structures. *J Porous Mater.* 2: 1627-1633.

OZGUMUS, T., MOBEDI, M. and OZKOL, U. (2014), Determination of Kozeny-Constant Based on Porosity & Throat Size Ratio in Porous Medium

with Rectangular Rods, *Engineering Application of Computational Fluid Dynamics*, Vol. 8, No. 2.

PENG, S. HU, Q., DULTZ, S. and ZHANG, M. (2012), Using X-ray Computed Tomography Pore Structure Characterization for Berea Sandstone: Resolution Effect, *Journal of Hydrology*, Volumes, 472-473, Pp 254-261.

PERROT, C., CHEVILLOTTE, F., JAOUEN, L. and HOANG, M. T. (2013). Acoustic Properties and Applications. DESTECH Publication, Inc. Technology & Engineering, USA.

PETRASCH, J., WYSS, P. and STEINFELD, A. (2007), Tomography-Based Monte Carlo Determination of Radiative Properties of Reticulated Porous Ceramics. *Journal of Quantitative Spectroscopy & Radiative Transfer*, 105, Pp 180-197.

PETRASCH, J. WYSS, P. STAMPILI, R. and STEINFELD, A. (2008). Tomography-Based Multiscale Analysis of the 3D Geometrical Morphology of Reticulated Porous Ceramics. *J.Am. Ceram. Soc*., Vol 91(8), Pp 2659-2665.

PRAKASH O., SANG, H. and EMBURY, J.D. (1995), Structure and Properties of AlSiC Foam, Materials Science and Engineering: A, Vol 199 (2), Pp 195-203.

PRIDES S. R., MORGAN F. D. and GANGI A. F. (1993), Drag Forces of Porous-Medium Acoustics, *Phys. Rev. B* Vol 47, Pp 4964-4978.

QIAM, J. M. and Li, X. X. (2000), Preparation of Newly Sound-Absorbing PVC Matrix Foam, *Plastic Sci. Tech.*, 47(4), Pp 5-8.

RANUT, P., NOBILE, E. and MANCINI, L. (2013), High-Resolution Microtomography-Based CFD Simulation of Flow and Heat Transfer in Aluminium Metal Foams. *J.applthermaleng*, 11.056.

RAO, M. A. (2007), Rheology of Fluid and Semisolid Foods: Principles and Applications (2nd ed.). Springer. p. 8. ISBN 978-0-387-70929-1.

REHDER, J. E. (1983), Manufacturing of Cast Iron with Pre-Reduced Iron Ore Pellets, United State Patent 44011469.

REYNOLDS, O. (1883), An Experimental Investigation of the Circumstances which Determine Whether the Motion if Water shall be Direct or Sinuous, and of the Law of Resistance in parallel Channels, Philosophical Transaction of Royal Society, 174, Pp 935-982.

RHODES, M. B. (1980), Cellular and Non-cellular Polyurethanes, *International Conference*, Strasbourg, France, Pp 803-819.

RICHARDSON, M. and NANDRA, D. (1986), Cell, *Polym*. 5(6), 423.

RUSSELL, A. D., TITLOW, J. P. and BEMMEN, Y. (1998), Acoustic Monopoles, Dipoles and Quadrupoles: An Experiment Revisited, American Association of Physics Teachers, Department of Science & Mathematics, Kettering University, Flint, Malaysia.

SATTERFIELD, C. N. (1970), Mass Transfer in Heterogeneous Catalysis, Cambridge, MIT Press.

SHAPOVALOV, V. (1998). Porous and Cellular Materials for Structural Applications, Vol 521, ed. D.S. Schwartz et al. (Warrendale, PA: MRS), p 281.

SIMONE, A. E. and GIBSON, L. J. (1998). Aluminium Foams Produced by Liquid-State Processes. *Acta Materialia*, Vol. 46, Pp 3109-3123.

Simpleware Ltd Reference Guide, (2014), Converting 3D Images into Models, Version 7.0.

SMITH, B. H., SZYNISZEWSKI, S. and HAJJAR, J. F. (2012). Steel Foam for Structures: A Review of Applications, Manufacturing and Material Properties, *Journal of Construction Steel*, Vol 71, Pp 1-10.

SMITH, J. M. (1970), Chemical Engineering Kinetics. 2nd Edition, McGraw-Hill, Inc. United State.

SUN, F., CHEN, H., WU, J. and FENG, K. (2001), Sound Absorbing Characteristics of Fibrous Metal Materials at High Temperature, *Applied Acoustic*, Pp 221-235.

STOKES, G. G. (1851), On the Effect of the Internal Friction of Fluids on the Motion of Pendulums, Transaction of the Cambridge Philosophical Society, 9, Pp 8-106.

T'JOEN, C., DE JAEGAR, P., HUISSENE, H., VAN HERZEELE, S., VORST, N. and DE PAEPE, M. (2010). Thermo-Hydraulic Study of a Single Row Heat Exchanger Consisting of Metal Foam Covered Round Tubes. *International Journal of Heat and Mass Transfer*, Vol. 53, Pp 3262 – 3274.

TADRIST, L., MISCEVIS, M., RAHLI, O. and TOPIN, F. (2004), About the use of Fibrous Materials in Compact Heat Exchangers, *Experimental Thermal & Fluid Science* Vol 28, Pp 193-199.

THOMSON, W. (1887), On the Division of Space with Minimum Partitional Area. *Philosofical Magazine*, Vol. 5, Pp 503-514.

UAF, (2014), Universal Air Filter, www.uaf.com/frequently_asked _questions

UMNOVA, O., ATTENBOROUGH, K., STANLEY, E. and CUMMINGS, A. (2003), Behaviour of Rigid-Porous Layers at High Levels of Continuous Acoustic Excitation: Theory and Experiment, *Journal of Acoustical Society of America* Vol 114, Pp 1346-1356.

UTSUNO, H., TANAKA, T. and FUJIKAWA, T. (1989), Transfer Function Method for Measuring Characteristic Impedance and Propagation Constant of Porous Materials, *J. Acoust. Soc. Am.* Vol. 86. Pp 637-640.

VERSTEEG, H. K. and MALASEKARA, W. (2007), An Introduction to Computational Fluid Dynamics-The Finite Volume Method, 2nd Edition, Pearson Education Limited.

WANG, X., and LU, T. J. (1999), Optimized Acoustic Properties of Cellular Solids, *The Journal of the Acoustical Society of America*, Vol, 106, Pp 756-763.

WANG, Q. Z., LU, D. M., CUI, C. X. and LIANG, L.M. (2011), Material Science and Engineering, *J. Mater. Process Technol*, 211, 363.

WANG, B. C., ZHENG, W. and YUAN, X. M. (2009), Research Situation of Foam Plastic, *Eng. Plast. Applied*, 37(10), Pp 77-80.

WATSON, I. G., LEE, P. D., DASHWOOD, R. J. and YOUNG, P. (2006), Simulation of the Mechanical Properties of an Aluminium Matrix Composite Using X-ray Micro-tomography, *Metal Mater. Trans*., Vol 37A, Pp 551-558.

WEAIRE, D. and PHELAN, R. (1994), A Counter-Example to Kelvin's Conjecture on Minimal Surfaces, *Philosofical Magazines Letters*, Vol. 69, Pp 107-110.

WEBER, L., INGRAM, D., GUARDIA, S, ATHANASIOU-IOANNOU, A. and MORTENSEN, A. (2017), Fluid Flow through Replicated Microcellular Materials in the Darcy-Forchheimer Regime, *Acta Materialia*, Vol 126, Pp 280-293.

WEISSBERG, H. L. (1963), Effective Diffusion Coefficient in Porous Media, *Journal of Applied Physics* Vol 34, Page 2636.

WHITAKER, S. (1986), Flow in Porous Media I: A Theoretical Derivation of Darcy's law, *Transport in Porous Media*. 1: 3–25.

WILLIAM, K. L. (2001), An Effective Density Fluid Model for Acoustic Propagation in Sediments Derived from Biot's Theory, *J. Acoust Soc Am*. Pp 2276-2281.

WILSON, K. (1993). Relaxation-Matched Modelling of Propagation through Porous Media, Including Fractal Pore Structure, *J. Acoust. Soc. Am.* 94(2), Pp. 1136-1145.

WINSAUR, W. O., SHEARIN, H. M. Jr. and MASSON, P. H. (1952), Resistivity of Brine-Saturated Sand in Related to Pore Geometry, *Am. Assoc.Pet.Geol.Bull*, Vol 36, Pp 203-211.

WRIGHT, M. C. M. (2005), Lecture Notes on the Mathematics of Acoustics, University of Southampton, Imperial College Press (ICP), Pp 157-161.

XIAOLIN, W., FENG, P. and BAOJUN, C. (2009), Sound Absorption of Porous Metals at High Sound Pressure Levels, *Journal of Acoustic Society of America*, 126 (2).

YEH, J. T., YANG, H. M. and HUANG, S. S. (1995), Combination of Polyethylene Filled with Metallic Hydroxides and Cross-linkable Polyethylene, *Poly Deg Stab*, 50 (2), Pp 229-234.

ZHAO, Y. (2013), Porous Metallic Materials Produced by P/M Methods, *J. Powder Metal*, Vol 2, Page 3.

ZHAO, Y. Y. and SUN, D. A. (2001), A Novel Sintering Dissolution Process for Manufacturing Al Foams, *Script Materialia*, Vol 44, Pp 106-110.

ZHANG, L. P. and ZHAO, Y. Y. (2007), Fabrication of High-Melting-Point Porous Metals by Lost Carbonate Sintering, *Proceedings of the Institution of Mechanical Engineers Part B Journal of Engineering Manufacture,* Vol 222(2), Pp 267-271.

ZIELINSKI, T. G. (2013), Inverse Identification and Microscopic Estimation of Parameters for Models of Sound Absorption in Porous Ceramics: In-Proceeding of International Conference on Noise and Vibration Engineering, *International Conference on Uncertainty in Structural Dynamics*, Pp 95-109.

ZIELINSKI, T. G. (2015), On the Representativeness of the Representative Cells for the Microstructural-Based Predictions of Sound Absorption in Fibrous and Porous Media. *European Acoustics Association*. EuroNoise 2015.

ZIELINSKI, T. G. (2015). Generation of Random Microstructures and Prediction of Sound Velocity and Absorption for Open Foams with Spherical Pores, *Journal of Acoustical Society of America,* Vol. 137, No. 4, Pp 1790-1801.

ZIMMERSON, R. W. (2003), Equation for Fluid Flow in Porous Rocks. Department of Earth Science and Engineering, Imperial College, London, UK.

ZHOU, J. (2006), Porous Metallic Materials, *Advanced Structural Materials*, ed. e. Winston O. Soboyejo, CRC Press, Taylor & Francis Group, USA, 22.

ZULKIFLI, R., MOHD NOR, M. J. and TAHIR, M. F. M. (2008), Acoustic Properties of Multilayer Coir Fibers Sound Absorption Panel, *Journal of Applied Sciences*, Vol. 8, No 20, Pp 3709-3718.

ZWIKKER, C. and KOSTEN, C. W. (1949), Sound Absorbing Materials, Elsevier, New York.

APPENDICES

APPENDIX I: FLOW AND IMAGE DATA FOR AIRFLOW THROUGH POROUS METALLIC STRUCTURES.

Table 4.1A. Experimental data of pressure drop per unit length (Pa/m) over foam structures X, Y, and Z.

Vs (m/s)	EXPT-X1	EXPT-Y1	EXPT-Y2	EXPT-Y3	EXPT-Y4	EXPT-Z1
0	0	0	0	0	0	0
0.663	12924.38	10623.68	3487.82	2849.34	1372.68	4273.77
0.948	19446.77	19600.53	6454.21	5753.56	2343.01	8315.873
1.232	31311.32	33892.02	11087.54	9222.94	3655.17	12176.80
1.516	45530.85	48754.39	16957.84	14307.99	5412.68	19249.18
1.800	63220.58	71304.71	23428.26	19077.06	7325.47	27723.40
2.085	82156.42	96801.22	30690.37	25423.44	9802.23	35557.92
2.369	105886.2	121198.12	38835.50	31322.74	12476.18	46052.48

Table 4.2A. X-ray CT (μCT) and DEM computed values of pressure drops per unit length (Pa/m) for X, Y, and Z foam structures.

Vs (m/s)	μCT-Y1	μCT-Y2	μCT-Y3	μCT-Y4	DEM-Y1	DEM-Y2/3	DEM-Y4
0	0	0	0	0	0	0	0
0.663	10418.41	3761.31	2782.11	1256.45	9920.65	3712.11	1144.63
0.948	20160.77	7244.97	5267.27	2361.38	19559.42	7118.70	2212.82
1.232	33458.16	11913.49	8528.01	3775.75	32532.19	11634.98	3382.87
1.516	49854.20	17708.19	12564.93	5561.81	48761.91	17324.62	4995.02
1.800	70732.97	24609.50	17376.47	7552.69	68263.40	24103.70	6865.61
2.085	95131.82	32605.65	22963.83	10081.31	91035.19	31997.54	9031.18
2.369	120790.89	41684.84	29328.22	12769.38	117078.77	41006.13	11491.84

Table 4.3A. X-ray CT (μCT) computed pressure drops per unit length for Y1 and Y1i dilated structures (RVE cubic flow length ~ 8.8mm).

Vs (m/s)	Y1 (Pa/m)	Y11 (Pa/m)	Y12 (Pa/m)	Y13 (Pa/m)	Y14 (Pa/m)	Y15 (Pa/m)
0	0	0	0	0	0	0
0.663	9228.13	2746.10	1029.09	644.78	370.40	210.29
0.948	18270.60	5283.15	1954.20	1255.34	694.72	389.94
1.232	30362.76	8661.30	3174.43	1935.34	1122.83	624.88
1.516	45505.52	12827.26	4524.08	2843.36	1653.68	917.39
1.800	63737.49	17627.54	6250.59	3873.97	2274.82	1258.41
2.085	85060.96	23886.65	8252.73	5112.27	2994.69	1668.68
2.369	109459.18	29950.34	10559.59	6412.83	3813.07	2136.66

NB: Y1 means no structural dilation whilst Y1i represent structural dilation with i representing the number of pixels added to the fluid domain or removed from the skeletal matrix.

Table 4.4A. X-ray CT (μCT) computed pressure drops per unit length for Y2, Y3, Y4 and Y2i, Y3i and Y4i dilated structures (RVE cubic flow length ~ 8.5mm).

Vs (m/s)	Y2 (Pa/m)	Y21 (Pa/m)	Y22 (Pa/m)	Y23 (Pa/m)	Y3 (Pa/m)	Y31 (Pa/m)	Y32 (Pa/m)	Y4 (Pa/m)	Y41 (Pa/m)	Y42 (Pa/m)
0	0	0	0	0	0	0	0	0	0	0
0.663	3761.31	2139.39	1043.79	551.19	2782.11	1749.58	782.33	1256.45	973.03	604.16
0.948	7244.97	4115.57	1973.40	1022.98	5267.27	3365.69	1467.80	2361.38	1826.88	1112.73
1.232	11913.49	6740.15	3203.76	1648.61	8528.01	5512.05	2360.72	3775.75	2972.26	1791.21
1.516	17708.19	9989.86	4706.94	2415.11	12564.93	8169.65	3474.58	5561.81	4379.44	2619.24
1.800	24609.50	13896.68	6529.03	3338.46	17376.47	11364.63	4793.24	7552.69	6090.08	3625.27
2.085	32605.65	18395.56	8572.55	4403.36	22963.83	15043.78	6325.86	10081.31	8062.65	4780.82
2.369	41684.84	23540.89	10919.54	5616.63	29328.22	19251.61	8068.81	12769.38	10315.22	6098.58

Table 4.5A. Structural and flow data for Y1, Y2, Y3 and Y4 and Y1i, Y2i, Y3i and Y4i dilated structures.

Sample	Ø (%)	Dp (mm)	Dw (mm)	$k_0 / 10^{-09} m^2$ (Darcy)	$k_0 / 10^{-09} m^2$ (Forchheimer)	C (m^{-1})	C_F [-]	σ_{FF} (m^{-1})	σ_{FB} (m^{-1})
µCT-Y1	70.8	2.23	0.69	10.50	13.90	17583.26	2.07	6413.09	2649.08
µCT-Y11	76.8	2.29	0.84	19.91	21.28	4152.82	0.61	7351.45	2214.70
µCT-Y12	82.1	2.36	1.02	32.80	40.32	1399.60	0.28	8031.83	1853.30
µCT-Y13	86.6	2.43	1.15	48.02	50.73	826.96	0.19	8581.19	1564.39
µCT-Y14	90.2	2.48	1.35	99.89	117.04	509.96	0.17	9776.44	1062.27
µCT-Y15	93.0	2.55	1.57	159.11	223.95	286.76	0.14	10567.74	791.27
µCT-Y2	72.6	2.22	0.72	13.90	17.08	5801.76	0.76	6648.08	2528.00
µCT-Y21	78.2	2.32	0.90	22.32	28.94	3263.05	0.56	7694.02	2149.81
µCT-Y22	83.4	2.46	1.07	38.27	43.59	1470.99	0.31	8619.52	1709.54
µCT-Y23	87.9	2.60	1.28	64.40	82.75	753.43	0.22	9503.05	1311.02
µCT-Y3	75.2	2.27	0.74	15.60	18.007	3985.549	0.53	7312.92	2410.80
µCT-Y31	80.9	2.36	0.92	26.63	35.39	2667.88	0.50	8401.05	1986.14
µCT-Y32	85.9	2.48	1.16	46.08	58.93	1085.17	0.26	9581.37	1570.86
µCT-Y4	78.2	2.23	0.89	28.33	33.45	1700.52	0.31	7455.44	2054.44
µCT-Y41	83.3	2.31	0.92	39.32	58.43	1415.87	0.34	8768.61	1759.44
µCT-Y42	87.7	2.37	1.01	56.81	75.30	816.86	0.22	10371.12	1447.64

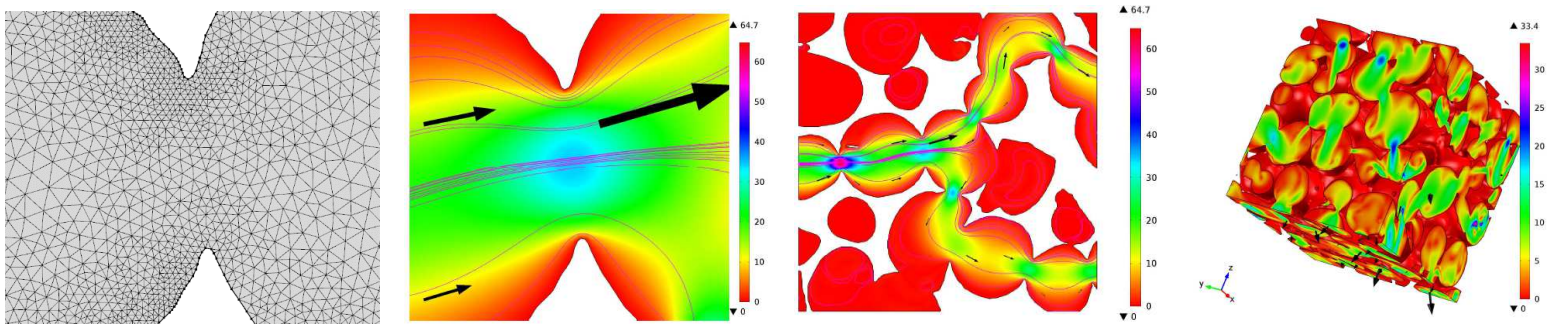


Fig 4.1A. Mesh structure and streamline velocity plots for Y1 structure at 1.5x res/6.75Lmin and 1.3 Growth rate for a superficial inlet velocity of 2.369 m.s^{-1} [*Numerical scales unit for the legends measured in m.s^{-1}].*

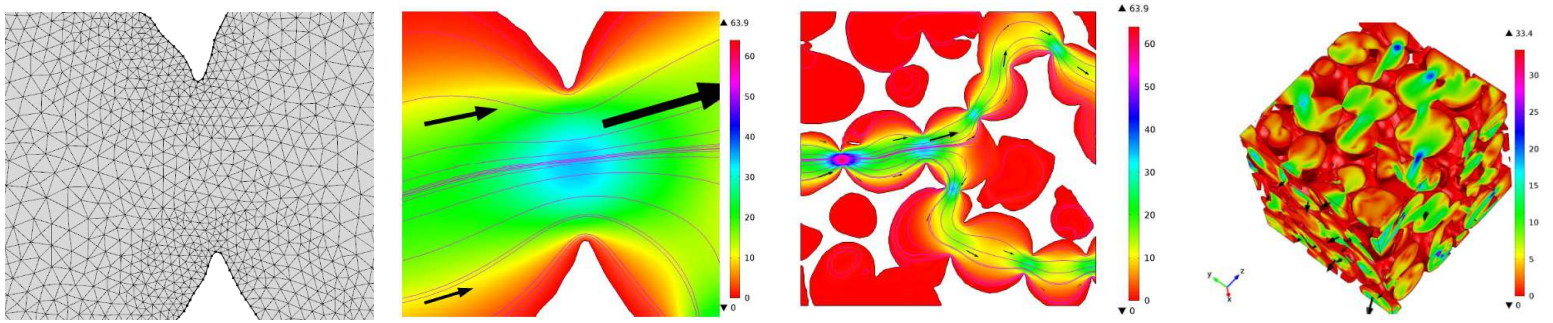


Fig 4.2A. Mesh structure and streamline velocity plots for Y1 structure at 2.1x res/6.75Lmin and 1.3 Growth rate for a superficial inlet velocity of 2.369 m.s^{-1} [*Numerical scales unit for the legends measured in m.s^{-1}].*

.

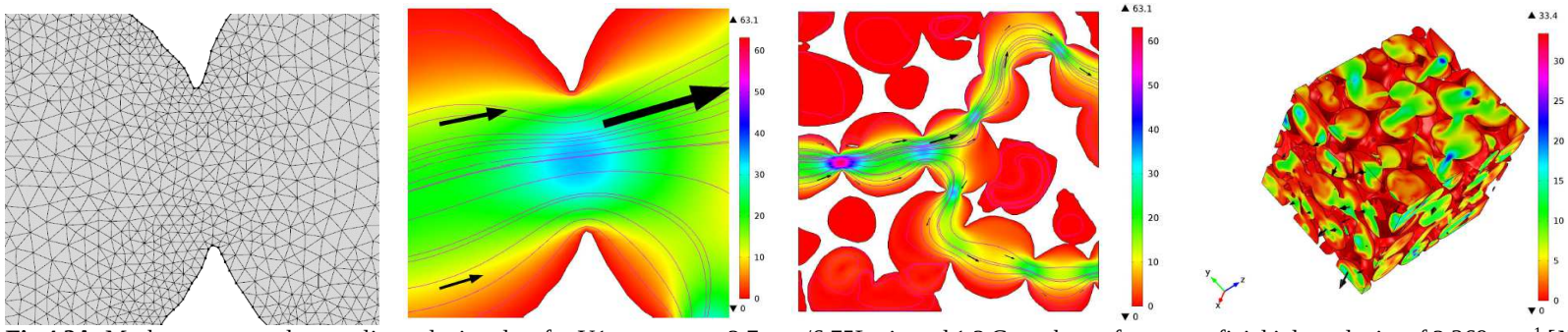


Fig 4.3A. Mesh structure and streamline velocity plots for Y1 structure at 2.7x res/6.75Lmin and 1.2 Growth rate for a superficial inlet velocity of 2.369 m.s^{-1} [*Numerical scales unit for the legends measured in m.s^{-1}].*

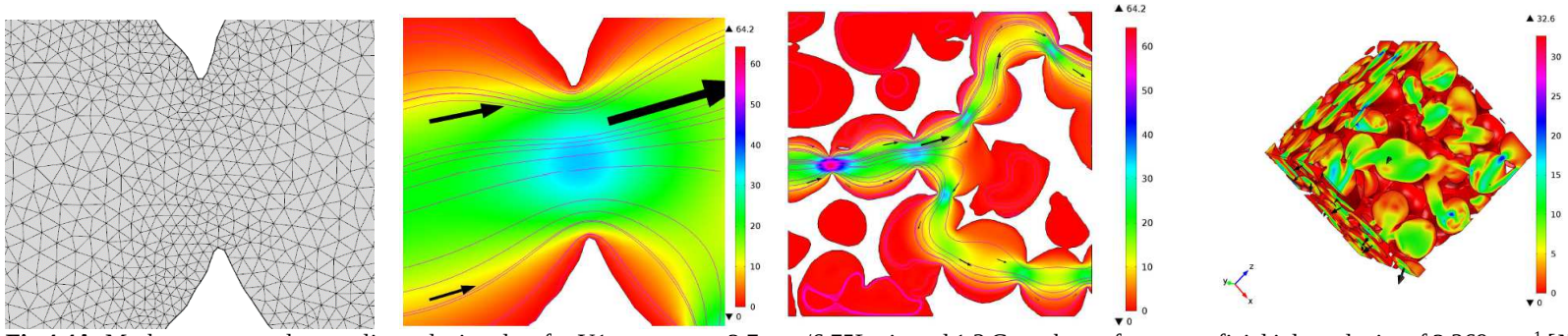


Fig 4.4A. Mesh structure and streamline velocity plots for Y1 structure at 2.7x res/6.75Lmin and 1.3 Growth rate for a superficial inlet velocity of 2.369 m.s^{-1} [*Numerical scales unit for the legends measured in m.s^{-1}].*

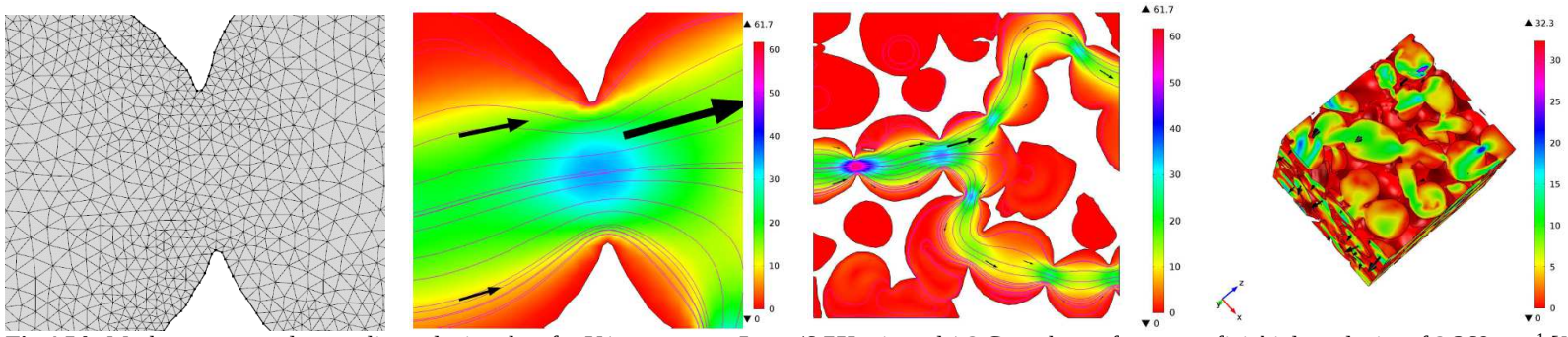


Fig 4.5A. Mesh structure and streamline velocity plots for Y1 structure at 5x res/6.75Lmin and 1.2 Growth rate for a superficial inlet velocity of 2.369 m.s^{-1} [*Numerical scales unit for the legends measured in m.s^{-1}].*

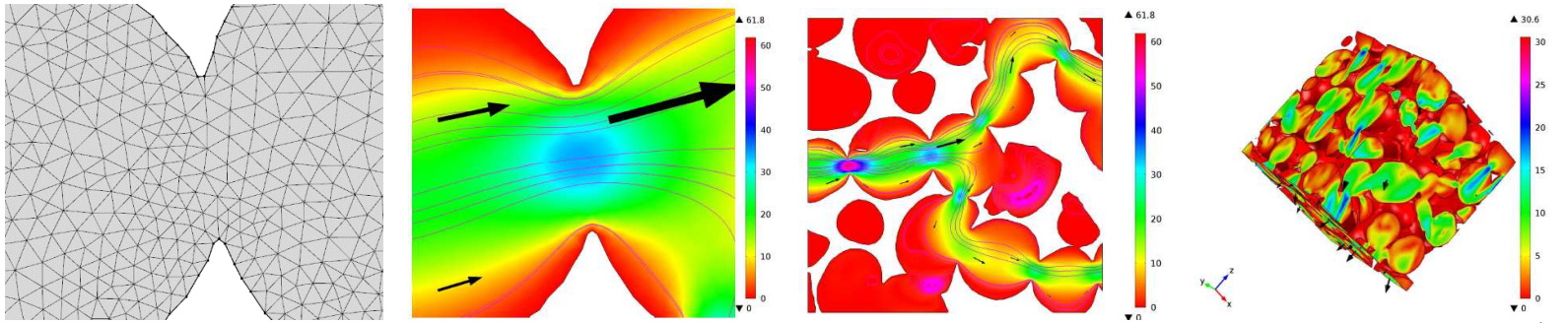


Fig 4.6A. Mesh structure and streamline velocity plots for Y1 structure at 5x res/6.75Lmin and 1.3 Growth rate for a superficial inlet velocity of 2.369 m.s^{-1} [*Numerical scales unit for the legends measured in m.s^{-1}].*

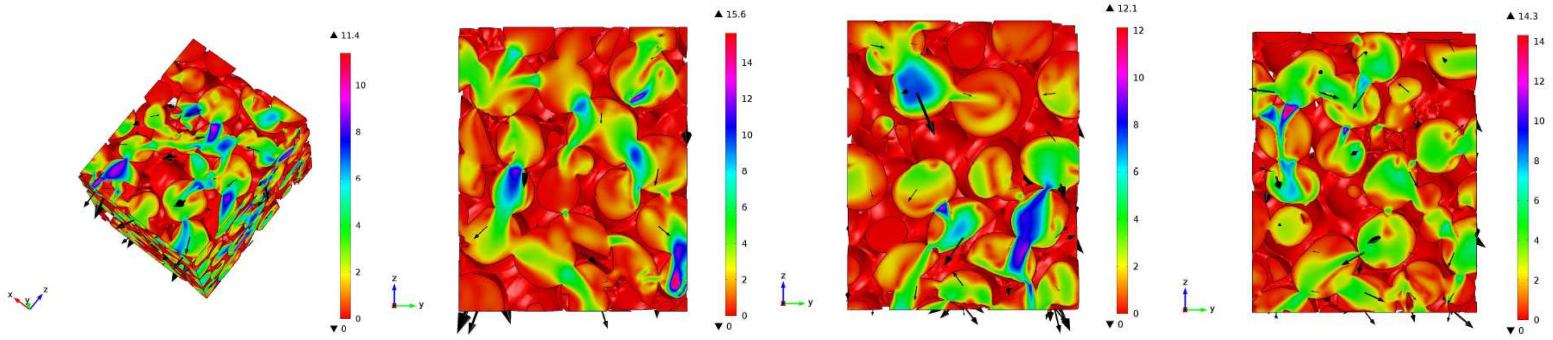


Fig 4.7A. (Left-right), 3D velocity profile plots and 2D (YZ, ¼, ½ & ¾) section of computed airflow across foam structure Y1 at 1.0 m.s^{-1} superficial inlet velocity (pore inlet velocity, v_p, in this case, is 1.418m/s calculated using the foam porosity, 70.5%) [*Numerical scales unit for the legends measured in m.s^{-1}].*

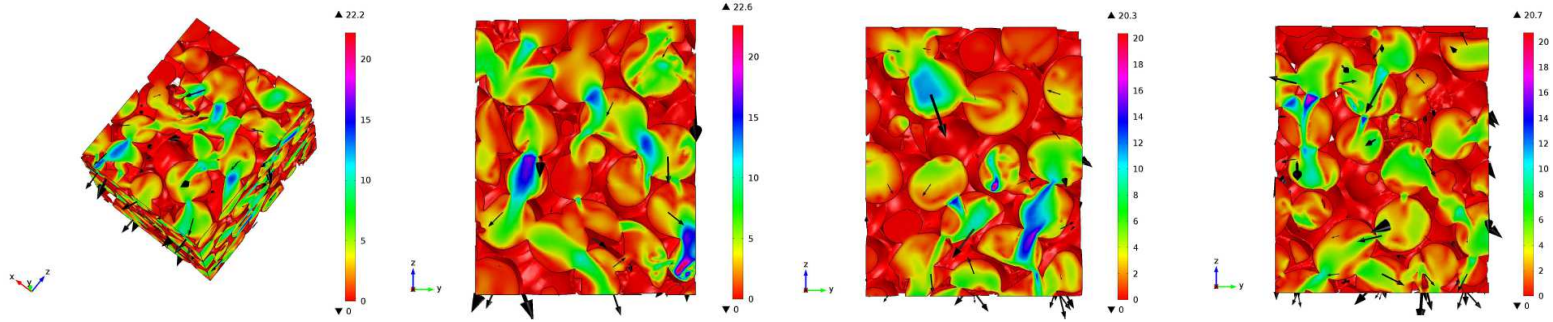


Fig 4.8A. (Left-right), 3D velocity profile plots and 2D (YZ, ¼, ½ & ¾) section of computed airflow across foam structure Y1 at 1.516 m.s^{-1} superficial inlet velocity (pore inlet velocity, v_p, in this case, is 2.150m/s calculated using the foam porosity, 70.5%) [*Numerical scales unit for the legends measured in m.s^{-1}].*

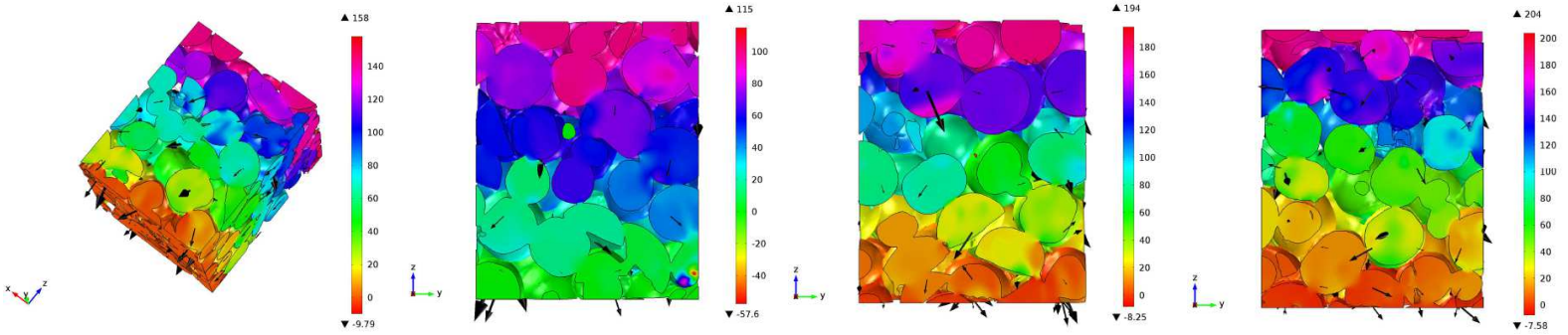


Fig 4.9A. (Left-right), 3D pressure profile plots and 2D (YZ, ¼, ½ & ¾) section of computed airflow across foam structure Y1 at 1.0m.s^{-1} superficial inlet velocity (pore inlet velocity, v_p, in this case, is 1.418m/s calculated using the foam porosity, 70.5%) [*Numerical scales unit for the legends measured in Pa]*.

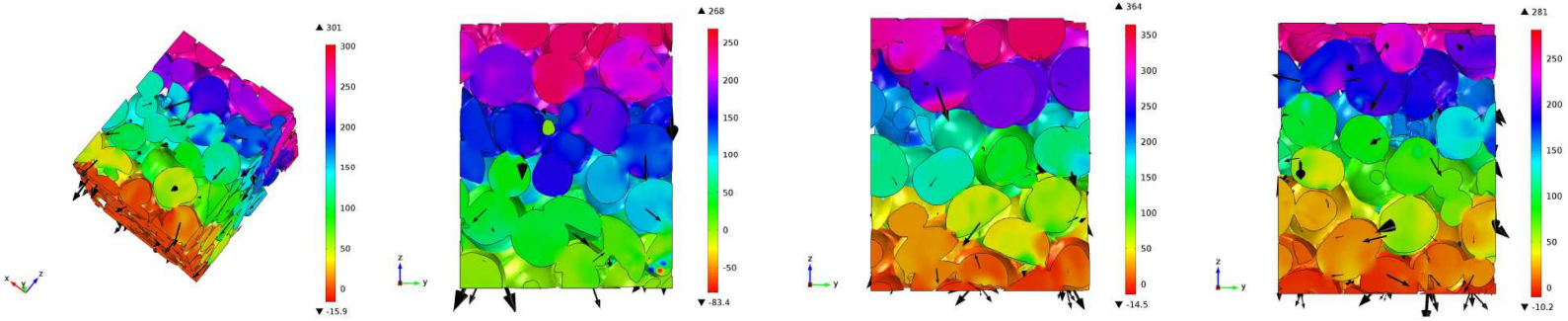


Fig 4.10A. (Left-right), 3D pressure profile plots and 2D (YZ, ¼, ½ & ¾) section of computed airflow across foam structure Y1 at 1.516m.s^{-1} superficial inlet velocity (pore inlet velocity, v_p, in this case, is 2.150m/s calculated using the foam porosity, 70.5%) [*Numerical scales unit for the legends measured in Pa]*.

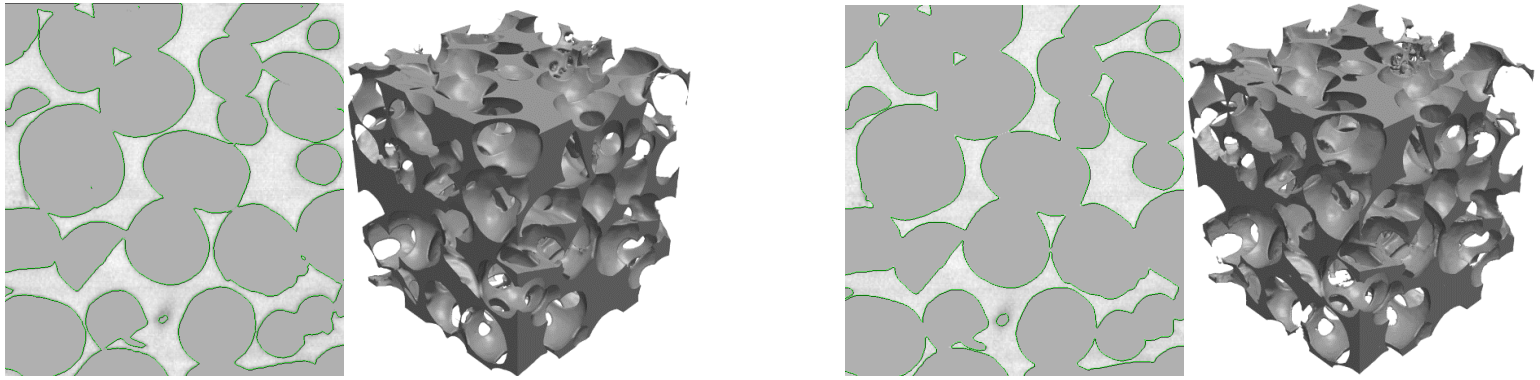


Fig 4.11A. A 2D contour fluid phase and 3D RVE structural phase of Y1 structure for (Left) no fluid phase dilation and (Right) 1-pixel addition to the fluid phase.

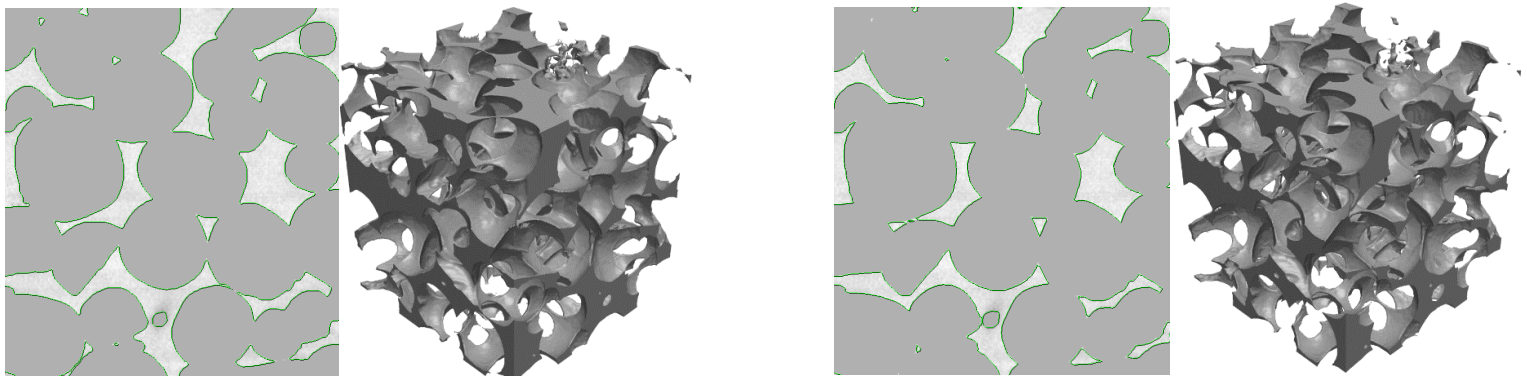


Fig 4.12A. A 2D contour fluid phase and 3D RVE structural phase of Y1 structure for (Left) 2-pixel addition and (Right) 3-pixel addition to the fluid phase.

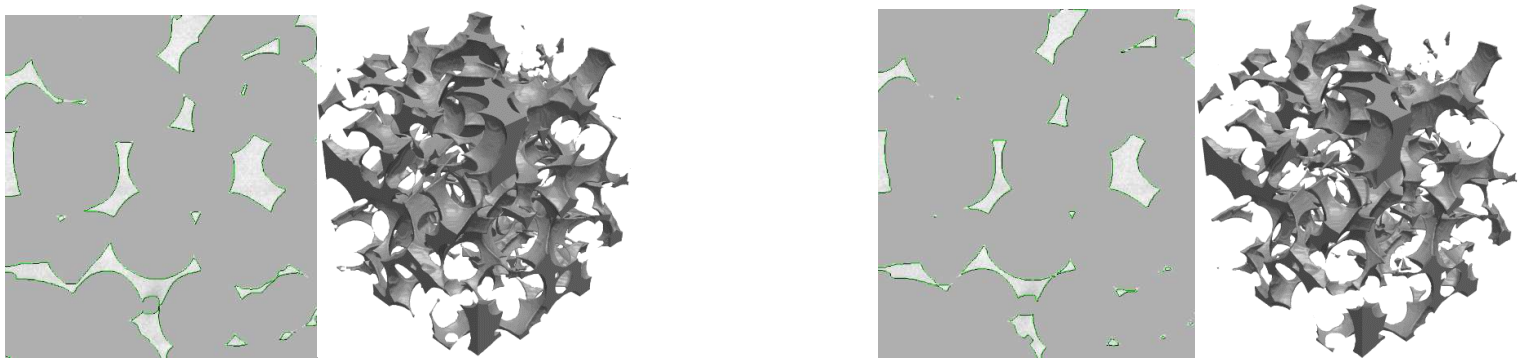


Fig 4.13A. A 2D contour fluid phase and 3D RVE structural phase of Y1 structure for (Left) 3-pixel addition and (Right) 4-pixel addition to the fluid phase.

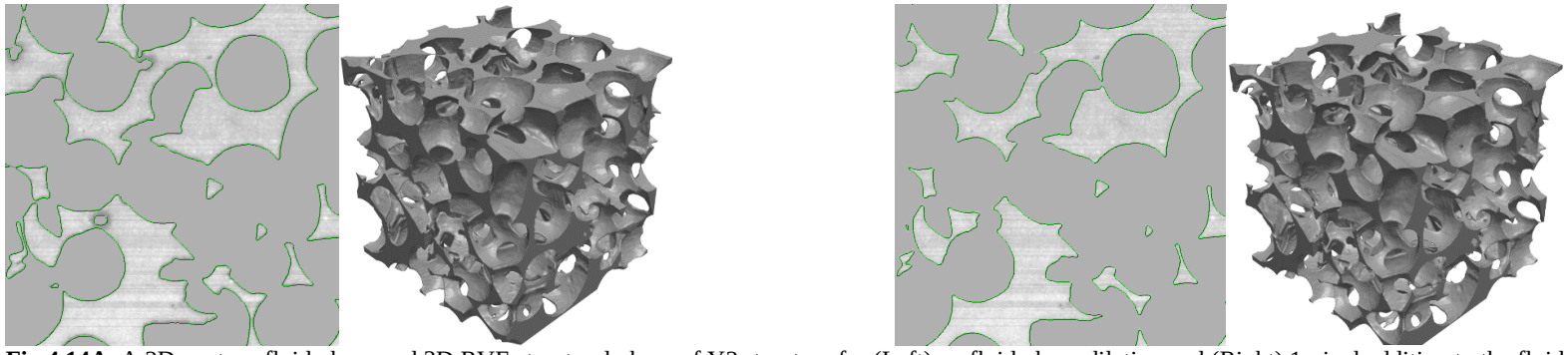


Fig 4.14A. A 2D contour fluid phase and 3D RVE structural phase of Y2 structure for (Left) no fluid phase dilation and (Right) 1-pixel addition to the fluid phase.

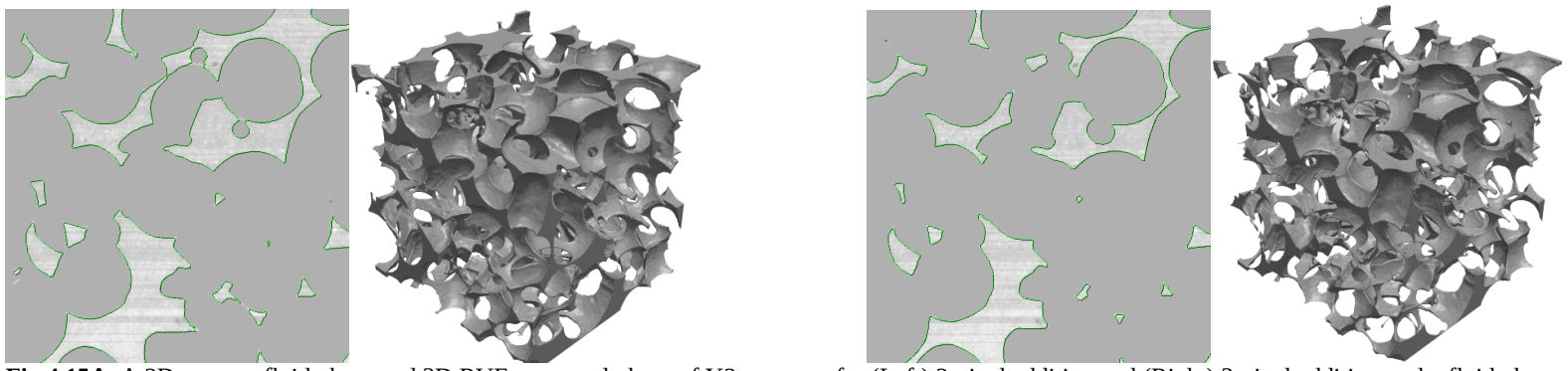


Fig 4.15A. A 2D contour fluid phase and 3D RVE structural phase of Y2 structure for (Left) 2-pixel addition and (Right) 3-pixel addition to the fluid phase.

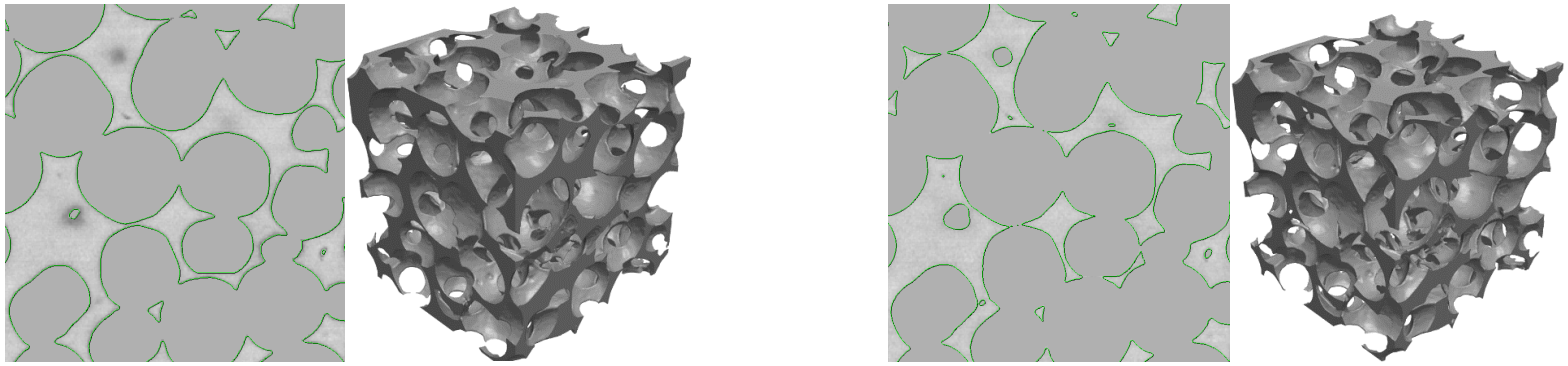


Fig 4.16A. A 2D contour fluid phase and 3D RVE structural phase of Y3 structure for (Left) no fluid phase dilation and (Right) 1-pixel addition to the fluid phase.

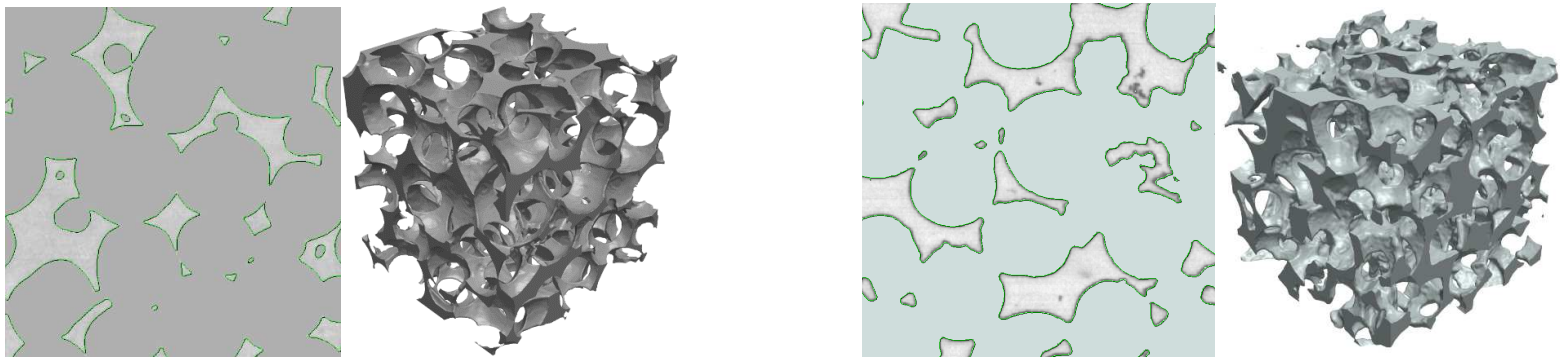


Fig 4.17A. A 2D contour fluid phase and 3D RVE structural phase of (Left) Y3 structure for 2-pixel addition to the RVE fluid phase and (Right) Y4 structure with no fluid phase dilation.

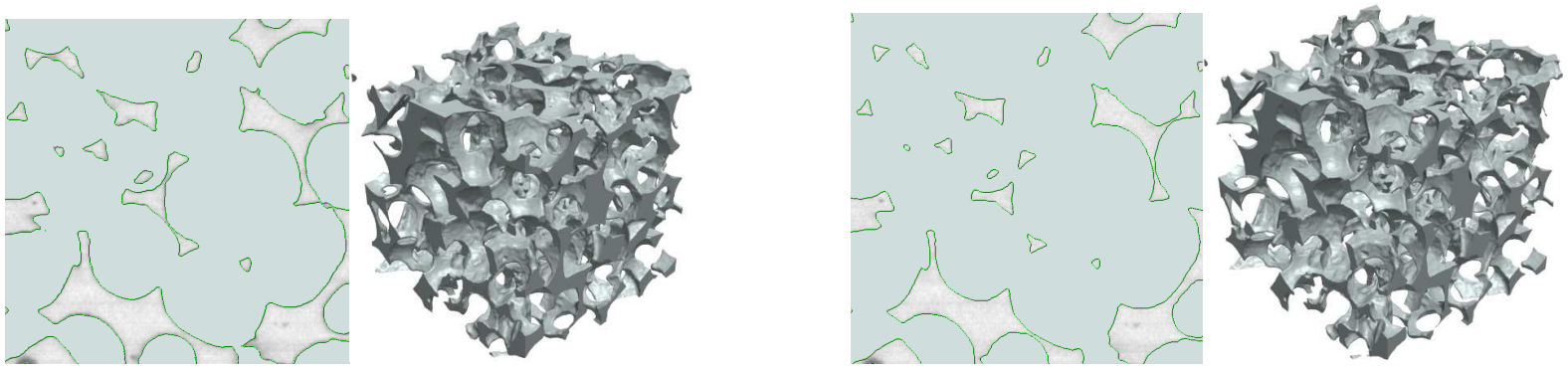


Fig 4.18A. A 2D contour fluid phase and 3D RVE structural phase of Y4 structure for (Left) 1-pixel addition and (Right) 2-pixel addition to the fluid phase.

APPENDIX II: IMAGES, TABLES, AND FIGURES ON SOUND ABSORPTION BEHAVIOUR OF POROUS STRUCTURES

Table 5.1A. Tabular representation of the measured (Lu & He, 2000) and simulated (current) sound absorption coefficient at 500, 1000 and 1600Hz for a 20mm thick hardbacked and airgap aluminium foam structures with spherical cells.

		Measured and simulated absorption coefficient					
		500Hz		1000Hz		1600Hz	
Samples	Cavity	Measured	Simulated	Measured	Simulated	Measured	Simulated
A	Hard backed and 20mm thick for each sample	0.14	0.13	0.54	0.46	0.84	0.89
B		0.19	0.10	0.28	0.28	0.70	0.74
C		0.22	0.07	0.29	0.16	0.67	0.45
d		0.13	0.08	0.22	0.19	0.52	0.55
f		0.11	0.08	0.31	0.23	0.78	0.68
ae		0.40	0.49	0.91	0.89	0.88	0.68
ea		0.48	0.33	0.74	0.99	0.69	0.77
bd		0.34	0.37	0.98	1.00	0.78	0.61
db		0.31	0.30	0.94	0.99	0.89	0.66
ba		0.51	0.46	0.75	0.94	0.70	0.66
da		0.47	0.36	0.75	1.00	0.79	0.71
a+10mm	Behind the sample	0.37	0.32	0.80	0.88	0.79	0.85
a+25mm		0.62	0.65	0.75	0.87	0.63	0.64
a+10mm	Between two 10mm thick	0.35	0.25	0.79	0.80	0.87	0.98
a+25mm		0.62	0.50	0.88	0.99	0.82	0.84

Table 5.2A. Tabular representation of predicted (Lu & He, 2000) and simulated (current) noise reduction coefficient and absorption peak for a 20mm thick hardbacked aluminium foam structures with spherical cells.

	Measured			Predicted (Current)	Predicted (Lu & He, 2000)		Predicted (Current)	
Samples	Ø (%)	Dw (μm)	Dp (μm)	$k_0/10^{-09}m^2$	*NRC*	*Ap*	*NRC*	*Ap*
a1	59.84	100	999	0.045	0.220	0.450	0.280	0.641
a2	59.84	200	999	0.431	0.419	0.851	0.395	0.960
a3	59.84	300	999	1.624	0.359	0.997	0.327	1.000
a4	59.84	500	999	8.630	0.270	0.841	0.179	0.848
a5	59.84	300	500	3.912	0.252	0.900	0.248	0.958
a6	59.84	300	1000	1.622	0.359	0.997	0.327	1.000
a7	59.84	300	1500	0.969	0.399	0.977	0.363	0.998
a8	59.84	300	2000	0.673	0.406	0.900	0.381	0.996
a9	59.84	300	3000	0.402	0.420	0.680	0.396	0.951
a10	50.00	300	999	1.134	0.361	0.999	0.340	0.995
a11	60.00	300	999	1.633	0.359	0.997	0.327	1.000
a12	70.00	300	999	2.222	0.346	0.978	0.292	0.986

Table 5.3A. Structural parameters and acoustic properties of DEM monosized (1, 2 & 3mm) spherical structures.

DEM structures-capillary radii (μm)	D_w (mm)	Dp (mm)	$\sigma_{FB}=S_F/V_B$ (mm^{-1})	Ø	τ	∧ (μm)	$\bar{\kappa}$ (μm)	*DEM* k_0 m^2	DEM σ ($Pa.s/m^2$)	*THEO* k_0 m^2	*Ap*	*NRC*	*SAA*
DU1-10	0.175	1.02	6.434	66.994	1.770	98.722	541.298	4.61E-10	39490.24	0.33E-10	0.968	0.396	0.605
DU1-30	0.270	1.02	5.992	67.508	1.763	171.641	574.065	1.41E-09	12911.35	1.39E-09	0.974	0.338	0.514
DU1-45	0.313	1.02	5.705	68.169	1.754	216.624	595.993	2.28E-09	7984.65	2.29E-09	0.912	0.296	0.449
DU1-80	0.375	1.02	5.052	70.458	1.721	289.531	651.014	4.29E-09	4243.59	4.42E-09	0.792	0.233	0.359
DU2-10	0.274	2.04	3.347	66.319	1.780	161.182	1041.887	1.21E-09	15045.45	0.58E-09	0.988	0.349	0.531
DU2-30	0.421	2.04	3.246	66.439	1.778	228.571	1073.830	2.44E-09	7461.07	2.39E-09	0.908	0.291	0.440
DU2-45	0.492	2.04	3.158	66.631	1.776	300.290	1098.688	4.23E-09	4303.78	3.98E-09	0.809	0.240	0.365
DU2-80	0.605	2.04	2.979	67.306	1.766	406.185	1150.634	7.86E-09	2316.16	7.97E-09	0.678	0.184	0.286
DU3-10	0.370	3.06	2.180	66.440	1.778	334.633	1569.498	5.23E-09	3480.88	0.93E-09	0.768	0.220	0.337
DU3-30	0.557	3.06	2.065	68.662	1.747	373.924	1620.394	6.87E-09	2649.93	3.79E-09	0.702	0.194	0.300
DU3-45	0.645	3.06	2.039	68.707	1.746	436.237	1638.553	9.36E-09	1944.98	6.13E-09	0.638	0.168	0.264
DU3-80	0.797	3.06	1.961	68.934	1.743	558.116	1690.320	1.54E-08	1182.14	1.23E-08	0.537	0.133	0.212

Table 5.4A. Structural parameters and acoustic properties of DEM mixed-sized (S-S and L-L) spherical structures.

DEM structures-% add of S - S	D_w (mm)	Dp (mm)	S_F/V_B (mm^{-1})	Ø	τ	∧ (um)	$\bar{\kappa}$ (um)	k_0 m^2	σ ($Pa.s/m^2$)	*Ap*	*NRC*	*SAA*
DU(L-L)-0%	0.283	2.270	2.999	63.435	1.820	154.054	1176.633	1.03E-09	17606.383	0.995	0.358	0.543
DN(L-S)-6.25%	0.224	1.142	3.093	67.995	1.756	172.495	1102.295	1.44E-09	12642.712	0.972	0.336	0.511
DN(L-S)-12.50%	0.199	0.866	3.385	70.554	1.720	184.042	1024.923	1.74E-09	10479.797	0.945	0.319	0.487
DN(L-S)-18.25%	0.186	0.854	3.612	71.586	1.705	175.070	885.629	1.61E-09	11314.783	0.953	0.326	0.498
DN(L-S)-25.00%	0.178	0.831	3.818	73.950	1.670	167.800	828.650	1.56E-09	11678.061	0.954	0.327	0.501
DN(L-S)-31.20%	0.172	0.807	4.096	73.810	1.672	169.712	777.353	1.59E-09	11452.459	0.952	0.326	0.499
DN(L-S)-37.50%	0.167	0.792	4.351	73.362	1.678	168.649	739.271	1.55E-09	11714.763	0.956	0.328	0.502
DN(L-S)-50.00%	0.161	0.779	5.487	73.310	1.679	152.436	604.581	1.27E-09	14355.908	0.975	0.345	0.529
DU(S-S)-100%	0.149	0.752	7.983	65.884	1.786	71.843	449.343	2.38E-10	76491.597	0.857	0.400	0.591

Table 5.5A. Structural and acoustic parameters of porous structures with spherical cells (X, Y and Z) characterized using CT images and DEM.

Samples	Ø	D_w (mm)	Dp (mm)	σ_{FB} (mm^{-1})	τ	r_w/r_p	^ (µm)	⍰ (µm)	k_0 m^2	*Ap*	*NRC*	*SAA*
µCT-Y1	70.526	0.650	2.225	2.540	1.720	0.292	513.216	1327.827	1.35E-08	0.555	0.140	0.222
µCT-Y2	72.563	0.720	2.215	2.518	1.690	0.325	564.095	1325.059	1.71E-08	0.504	0.123	0.196
µCT-Y3	75.205	0.741	2.273	2.407	1.651	0.326	562.304	1372.941	1.80E-08	0.486	0.118	0.187
µCT-Y4	78.397	0.899	2.226	2.054	1.601	0.404	739.261	1576.613	3.34E-08	0.371	0.085	0.135
DEM-Y1	71.752	0.617	2.327	2.475	1.702	0.265	483.284	1344.584	1.23E-08	0.571	0.145	0.229
DEM-Y2/3	74.736	0.731	2.373	2.229	1.658	0.308	582.304	1482.851	1.91E-08	0.476	0.115	0.183
DEM-Y4	78.246	0.892	2.406	1.921	1.604	0.371	752.223	1660.122	3.45E-08	0.366	0.084	0.133
µCT-X1	72.053	0.275	1.213	4.588	1.698	0.227	285.031	759.841	4.31E-09	0.787	0.231	0.357
µCT-Z1	75.243	0.732	2.774	2.245	1.650	0.264	621.645	1423.585	2.20E-08	0.449	0.107	0.170

Table 5.6A. Structural and acoustic properties of "bottleneck-type" porous structures for window to pore ratio for 0.15, 0.30 and 0.45, pore diameter sizes between 200 and 3000µm and porosities, 56, 68 and 80%.

Samples	Ø (%)	τ	rw/rp	rp (mm)	k_0 m^2	Ap	*f*peak (Hz)	*NRC*	*SAA*	*rw µm*
A1	56	1.9198	0.15	0.1	5.89E-12	0.288	6500	0.1071	0.1309	15
A12	56	1.9198	0.15	0.5	1.47E-10	0.711	1700	0.3581	0.5125	75
A2	56	1.9198	0.15	0.7	2.89E-10	0.873	1800	0.3694	0.5608	105
A21	56	1.9198	0.15	0.9	4.77E-10	0.954	1800	0.3663	0.5640	135
A22	56	1.9198	0.15	1.1	7.13E-10	0.991	1900	0.3586	0.5479	165
A23	56	1.9198	0.15	1.3	9.96E-10	0.996	2000	0.3478	0.5238	195
A3	56	1.9198	0.15	1.5	1.33E-09	0.992	2000	0.3349	0.4973	225
B1	80	1.5743	0.15	0.1	1.20E-11	0.437	6500	0.1756	0.2120	15
B11	80	1.5743	0.15	0.3	1.08E-10	0.816	6500	0.4006	0.5286	45
B12	80	1.5743	0.15	0.5	3.01E-10	0.929	2100	0.4271	0.6323	75
B2	80	1.5743	0.15	0.7	5.89E-10	0.997	2200	0.3983	0.6102	105
B21	80	1.5743	0.15	0.9	9.74E-10	0.989	2400	0.3633	0.5593	135
B3	80	1.5743	0.15	1.5	2.70E-09	0.853	2500	0.2683	0.4115	225

C1	68	1.7551	0.15	0.1	8.69E-12	0.365	6500	0.1406	0.1709	15
C12	68	1.7551	0.15	0.5	2.17E-10	0.840	1800	0.4045	0.5909	75
C2	68	1.7551	0.15	0.7	4.26E-10	0.961	2000	0.3994	0.6090	105
C21	68	1.7551	0.15	0.9	7.04E-10	0.997	2100	0.3819	0.5854	135
C22	68	1.7551	0.15	1.1	1.05E-09	0.994	2100	0.3594	0.5485	165
C3	68	1.7551	0.15	1.5	1.95E-09	0.936	2200	0.3102	0.4708	225
D1	56	1.9198	0.45	0.1	2.14E-10	0.809	1700	0.3673	0.5457	45
D2	56	1.9198	0.45	0.7	1.05E-08	0.851	6500	0.1819	0.2611	315
D3	56	1.9198	0.45	1.5	4.81E-08	0.533	6500	0.0922	0.1367	675
E1	80	1.5743	0.45	0.1	4.37E-10	0.979	2200	0.4140	0.6278	45
E2	80	1.5743	0.45	0.7	2.14E-08	0.438	2800	0.1054	0.1647	315
E3	80	1.5743	0.45	1.5	9.83E-08	0.228	2800	0.0492	0.0778	675
F1	68	1.7551	0.45	0.1	3.16E-10	0.918	1900	0.4046	0.6086	45
F2	68	1.7551	0.45	0.7	1.55E-08	0.540	2400	0.1340	0.2126	315
F3	68	1.7551	0.45	1.5	7.10E-08	0.292	2500	0.0635	0.1045	675
G1	56	1.9198	0.30	0.1	5.68E-11	0.613	6500	0.2936	0.3770	30
G11	56	1.9198	0.30	0.3	5.11E-10	0.961	1800	0.3653	0.5623	90
G12	56	1.9198	0.30	0.5	1.42E-09	0.989	2000	0.3313	0.4902	150
G2	56	1.9198	0.30	0.7	2.78E-09	0.995	6400	0.2869	0.4133	210
G3	56	1.9198	0.30	1.5	1.28E-08	0.813	6500	0.1676	0.2413	450
H1	80	1.5743	0.30	0.1	1.16E-10	0.824	6500	0.4058	0.5403	30
H11	80	1.5743	0.30	0.3	1.04E-09	0.985	2400	0.3580	0.5511	90
H2	80	1.5743	0.30	0.7	5.68E-09	0.702	2600	0.1978	0.3046	210
H3	80	1.5743	0.30	1.5	2.61E-08	0.405	2800	0.0955	0.1496	450
I1	68	1.7551	0.30	0.1	8.38E-11	0.724	6500	0.3557	0.4655	30
I11	68	1.7551	0.30	0.3	7.54E-10	0.999	2100	0.3786	0.5801	90
I2	68	1.7551	0.30	0.7	4.11E-09	0.810	2300	0.2404	0.3678	210
I3	68	1.7551	0.30	1.5	1.89E-08	0.502	2400	0.1219	0.1945	450
DU1-10	66.994	1.7700	0.172	0.501	4.61E-10	0.968	2000	0.396	0.6047	86

Table 5.7A. Tabular representation of macroscopic data of actual eroded and dilated DEM structural phase for 1, 2 and 3mm.

DEM structures-capillary radii (um)	D_w (mm)	Dp (mm)	σ_{FB} (mm^{-1})	Ø	τ	r_w/r_p	k_0 m^2	∧ (μm)	$\bar{\pi}$ (μm)	*Ap*	*NRC*	*SAA*
DU1-10	0.175	1.020	6.434	66.994	1.770	0.172	4.61E-10	98.722	541.298	0.957	0.359	0.600
DU1-30	0.270	1.020	5.992	67.508	1.763	0.265	1.41E-09	171.641	574.065	0.974	0.338	0.514
DU1-45	0.313	1.020	5.705	68.169	1.754	0.307	2.28E-09	216.624	595.993	0.912	0.296	0.449
DU1-80	0.375	1.020	5.052	70.458	1.721	0.368	4.29E-09	289.531	651.014	0.792	0.233	0.359
DU1-E1	0.280	1.037	5.655	72.073	1.697	0.270	1.47E-09	166.423	587.979	0.962	0.333	0.510
DU1-E2	0.366	1.060	4.876	76.757	1.627	0.345	3.41E-09	240.456	648.379	0.819	0.249	0.383
DU1-E3	0.472	1.080	4.229	81.010	1.559	0.437	6.90E-09	325.903	734.902	0.658	0.181	0.278
DU1-E4	0.569	1.097	3.553	84.852	1.493	0.518	1.03E-08	380.711	815.992	0.562	0.148	0.225
DU1-E5	0.631	1.112	2.912	88.199	1.429	0.567	1.51E-08	442.480	916.627	0.476	0.122	0.182
DU1-D1	0.139	0.985	6.950	61.963	1.840	0.141	2.18E-10	71.968	518.779	0.828	0.388	0.571
DU1-D2	0.096	0.958	7.469	57.184	1.905	0.100	1.06E-10	53.151	499.049	0.654	0.346	0.476
DU2-10	0.274	2.040	3.347	66.319	1.780	0.134	1.21E-09	161.181	1041.887	0.988	0.349	0.531
DU2-30	0.421	2.040	3.246	66.439	1.778	0.207	2.44E-09	228.571	1073.830	0.908	0.291	0.440
DU2-45	0.492	2.040	3.158	66.631	1.776	0.241	4.23E-09	300.290	1098.688	0.809	0.240	0.365
DU2-80	0.605	2.040	2.979	67.306	1.766	0.296	7.86E-09	406.185	1150.634	0.678	0.184	0.286
DU2-E1	0.420	2.073	2.882	71.547	1.705	0.203	6.03E-09	339.071	1151.191	0.720	0.201	0.312
DU2-E2	0.543	2.119	2.482	76.328	1.633	0.256	1.37E-08	470.861	1268.855	0.534	0.134	0.210
DU2-E3	0.653	2.159	2.031	80.749	1.563	0.302	2.57E-08	616.078	1446.580	0.406	0.096	0.150
DU2-E4	0.731	2.194	1.709	84.670	1.496	0.333	3.97E-08	734.368	1602.956	0.328	0.076	0.117
DU2-E5	0.791	2.225	1.394	88.089	1.432	0.356	5.87E-08	873.617	1798.909	0.269	0.063	0.093
DU2-D1	0.196	1.968	3.629	61.097	1.852	0.100	5.09E-10	111.101	999.942	0.971	0.380	0.583
DU2-D2	0.136	1.913	3.906	56.159	1.919	0.071	2.17E-10	77.016	964.881	0.813	0.368	0.548
DU3-10	0.370	3.060	2.180	66.440	1.778	0.121	5.23E-09	334.634	1569.498	0.768	0.220	0.337
DU3-30	0.557	3.060	2.065	68.662	1.747	0.182	6.87E-09	373.924	1620.394	0.702	0.194	0.300
DU3-45	0.645	3.060	2.039	68.707	1.746	0.211	9.36E-09	436.237	1638.553	0.638	0.168	0.264
DU3-80	0.797	3.060	1.961	68.934	1.743	0.260	1.54E-08	558.116	1690.320	0.537	0.133	0.212
DU3-E1	0.742	3.137	1.791	73.651	1.674	0.236	2.07E-08	613.520	1778.329	0.464	0.111	0.178
DU3-E2	1.100	3.199	1.472	78.312	1.602	0.344	4.70E-08	877.154	2024.315	0.321	0.072	0.114

DU3-E3	1.308	3.253	1.253	82.506	1.534	0.402	7.18E-08	1033.282	2233.417	0.258	0.057	0.089
DU3-E4	1.472	3.300	1.043	86.236	1.467	0.446	1.08E-07	1212.425	2489.852	0.208	0.046	0.070
DU3-E5	1.599	3.339	0.842	89.450	1.404	0.479	1.61E-07	1421.923	2803.614	0.168	0.038	0.056
DU3-D1	0.265	2.992	2.246	63.655	1.817	0.089	3.75E-09	292.626	1546.862	0.842	0.255	0.382
DU3-D2	0.184	2.915	2.430	58.771	1.884	0.063	1.99E-09	225.883	1482.278	0.953	0.312	0.459
DU1-80	0.375	1.029	5.052	70.458	1.721	0.364	4.29E-09	289.531	651.014	0.792	0.233	0.359
DU18-D1	0.347	1.008	5.582	66.313	1.780	0.344	3.30E-09	266.201	612.161	0.855	0.263	0.399
DU18-D2	0.304	0.984	6.102	62.175	1.837	0.309	2.51E-09	243.591	579.789	0.911	0.292	0.435



Fig 5.1A. A 2D fluid phase model contour and 3D structural phase of DEM virtual structure of 1mm pore sizes and capillary radius of 10μm for a (left) No structural erosion, DU1-10, and (right) 1-pixel, DU1-E1, removed from the structural phase.

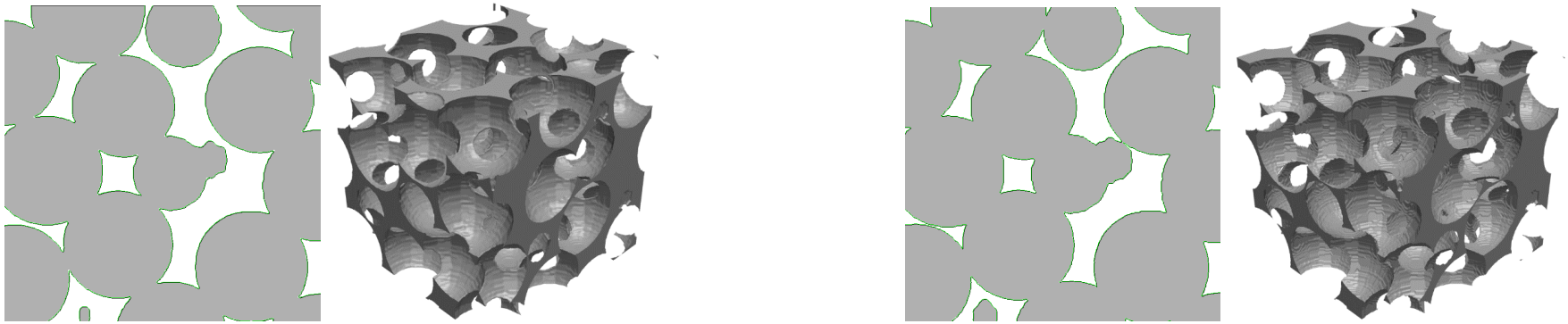


Fig 5.2A. A 2D fluid phase model contour and 3D structural phase of DEM virtual structure of 1mm pore sizes and capillary radius of 10µm for a (left) 2-pixel, DU1-E2, and (right) 3-pixel, DU1-E3, removed from the structural phase.

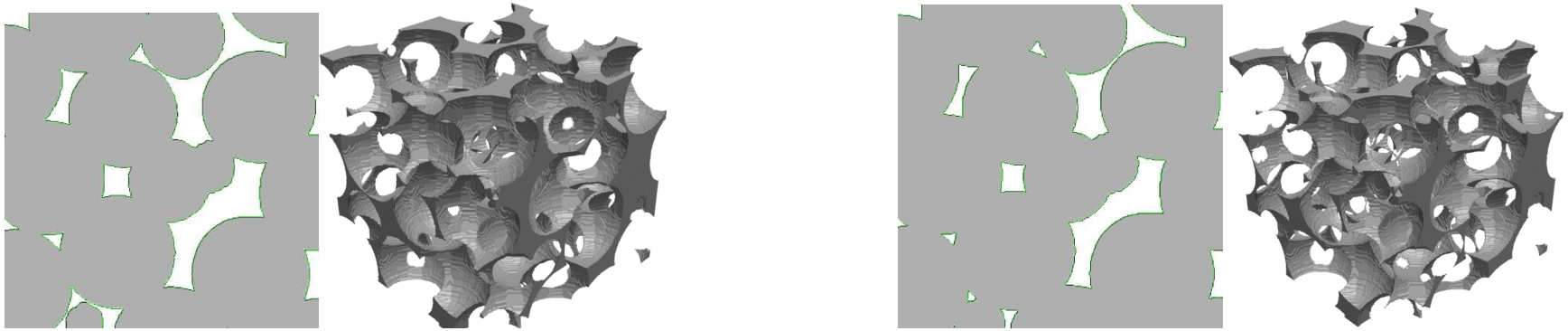


Fig 5.3A. A 2D fluid phase model contour and 3D structural phase of DEM virtual structure of 1mm pore sizes and capillary radius of 10µm for a (left) 4-pixel, DU1-E4, and (right) 5-pixel, DU1-E5, removed from the structural phase.

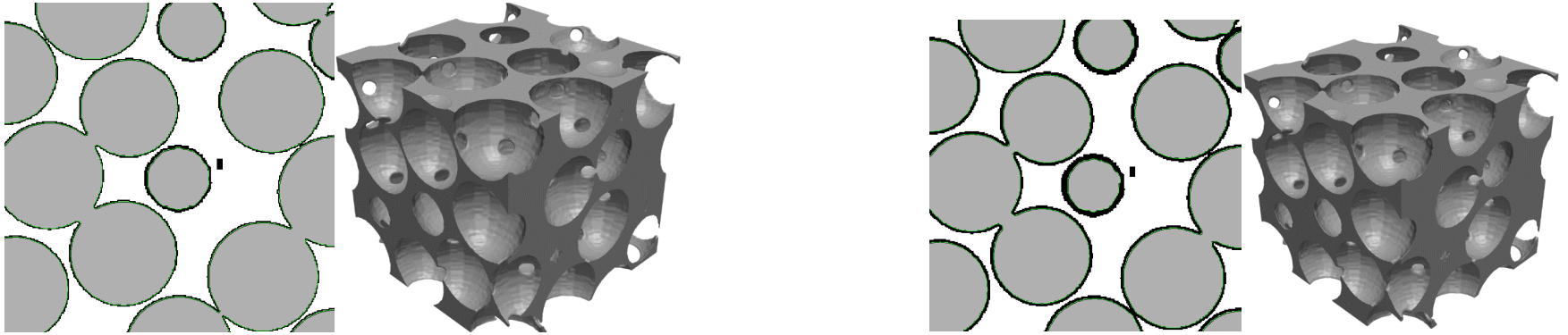


Fig 5.4A. A 2D fluid phase model contour and 3D structural phase of DEM virtual structure of 1mm pore sizes and capillary radius of 10µm for a (left) 1-pixel, DU1-D1, and (right) 2-pixel, DU1-D2, added to the structural phase.



Fig 5.5A. A 2D fluid phase model contour and 3D structural phase of DEM virtual structure of 2mm pore sizes and capillary radius of 10µm for a (left) No structural erosion, DU2-10, and (right) 1-pixel, DU2-E1, removed from the structural phase.



Fig 5.6A. A 2D fluid phase model contour and 3D structural phase of DEM virtual structure of 2mm pore sizes and capillary radius of 10µm for a (left) 2-pixel, DU2-E2, and (right) 3-pixel, DU2-E3, removed from the structural phase.



Fig 5.7A. A 2D fluid phase model contour and 3D structural phase of DEM virtual structure of 2mm pore sizes and capillary radius of 10µm for a (left) 4-pixel, DU2-E4, and (right) 5-pixel, DU2-E5, removed from the structural phase.



Fig 5.8A. A 2D fluid phase model contour and 3D structural phase of DEM virtual structure of 2mm pore sizes and capillary radius of 10μm for a (left) 1-pixel, DU2-D1, and (right) 2-pixel, DU2-D2, added to the structural phase.



Fig 5.9A. A 2D fluid phase model contour and 3D structural phase of DEM virtual structure of 3mm pore sizes and capillary radius of 10μm for a (left) No structural erosion, DU3-10, and (right) 1-pixel, DU3-E1, removed from the structural phase.



Fig 5.10A. A 2D fluid phase model contour and 3D structural phase of DEM virtual structure of 3mm pore sizes and capillary radius of 10µm for a (left) 2-pixel, DU3-E2, and (right) 3-pixel, DU3-E3, removed from the structural phase.



Fig 5.11A. A 2D fluid phase model contour and 3D structural phase of DEM virtual structure of 3mm pore sizes and capillary radius of 10µm for a (left) 4-pixel, DU3-E4, and (right) 5-pixel, DU3-E5, removed from the structural phase.

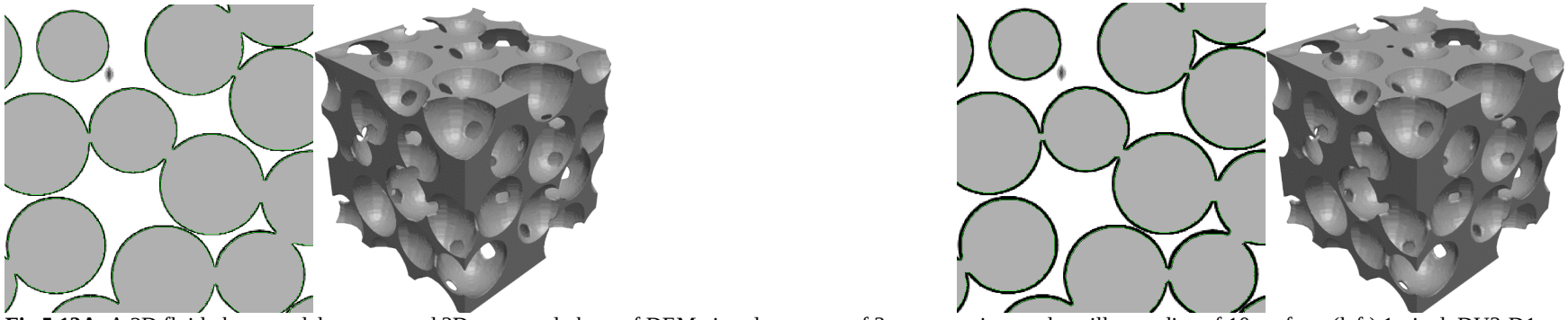


Fig 5.12A. A 2D fluid phase model contour and 3D structural phase of DEM virtual structure of 3mm pore sizes and capillary radius of 10µm for a (left) 1-pixel, DU3-D1, and (right) 2-pixel, DU3-D2, added to the structural phase.

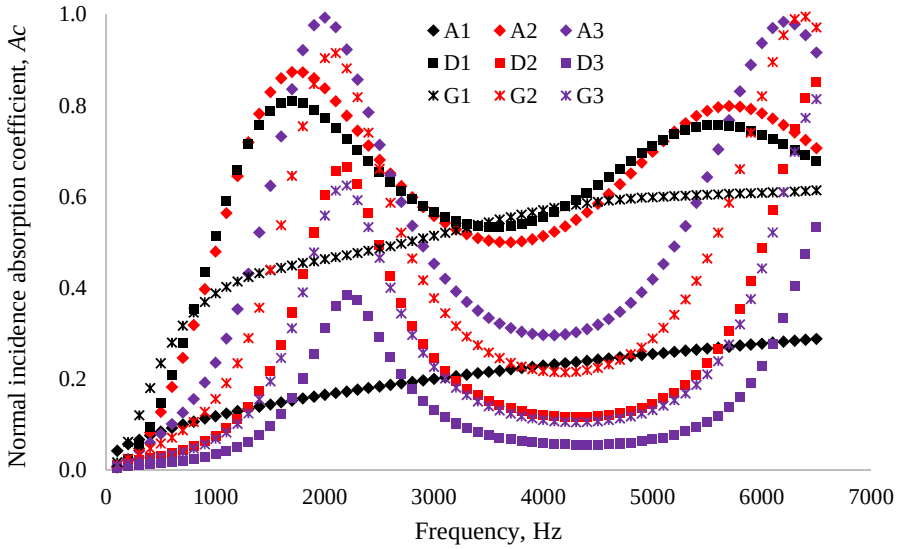


Fig 5.13A. Plots of normal incidence absorption coefficient against frequency (Hz) for structures with constant porosity (56%), different pore sizes (rp=100, 700 and 1500µm) and three different windows to pore ratio (rw/rp=0.15, 0.45 and 0.30).

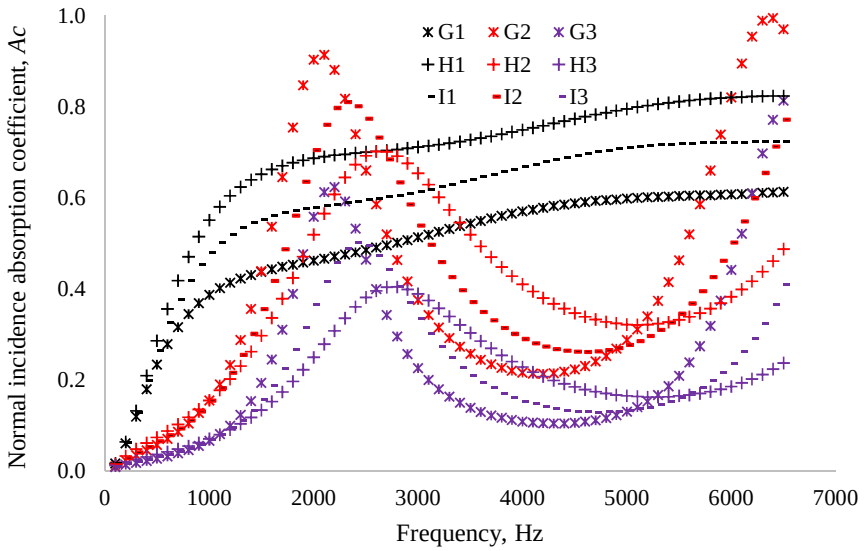


Fig 5.14A. Plots of normal incidence absorption coefficient against frequency (Hz) for structures with constant window to pore ratio (rw/rp-0.30), for different pore sizes rp=100, 700 and 1500µm) and for different porosities (Ø=56, 68 & 80%).

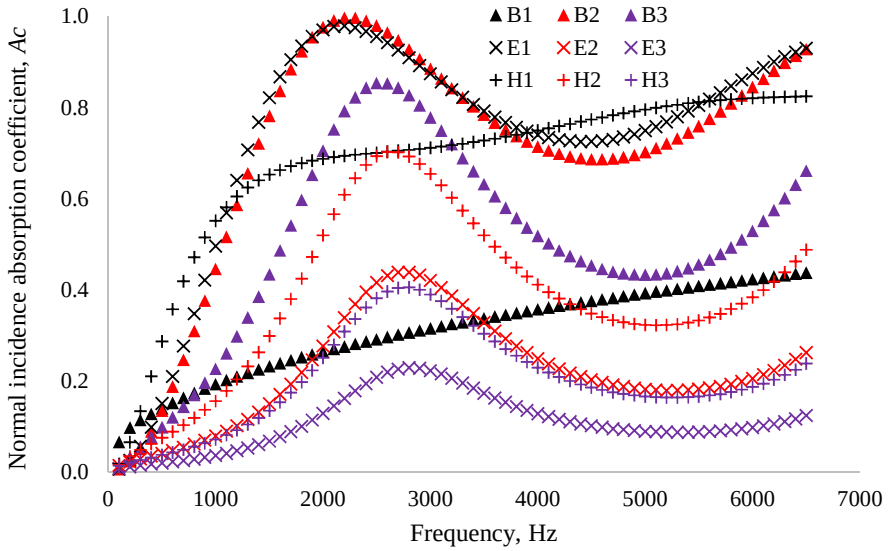


Fig 5.15A. Plots of normal incidence absorption coefficient against frequency (Hz) for structures with constant porosity (80%), different pore sizes (rp=100, 700 and 1500µm) and three different windows to pore ratio (rw/rp=0.15, 0.45 and 0.30).

APPENDIX III: KOZENY CONSTANT OF SPHERICAL STRUCTURES GENERATED BY SPHERE-PACKING MODELS

As part of the appendices, we look to computationally explore the possibility of using the sphere packed structures to flow through packed beds which are an inverse representation of metal foam structure. The aim is to understand the benefit of the virtual structures to the accurate prediction of Kozeny constant spherical packed structures and make a comparison with established facts available in the literature.

Summary

The study presents a novel approach to Kozeny constant of near-spherical packed beds from two-dimensional images obtained from discrete element method (DEM) simulation packing of spheres for the virtual description of the porous packed beds. A Three-dimensional representative elemental volume (RVE) of the porous microstructure with uniform particle sizes 1 - 3mm were restored from 2D slices of DEM images with a cubic strut length three times the average pore size. Particles and fluid volume preservation were resolved to utilize smart mask smoothing at iteration number of 10 for the de trop noise within the microstructure. The modeled values agree reasonably well with an analytical Blake-Kozeny (BK) model within an established Kozeny-constant (K) of 4.5-5.1. K value of 4.62 is proposed for BK equation which shows reasonable agreement with modeled values and measured data on polydispersed packed beds in the literature.

Keywords: Porous media; Permeability; Kozeny-Constant.

The flow of fluids through porous media is of great interest in many fields. These include water flow through rocks, petroleum recovery processes, sound absorption and metallurgical processing. For laminar flow, the well-established Darcy equation relates the flow rate per unit area ($\frac{Q}{A}$) of fluid through a porous medium under a defined pressure drop per unit length $|\nabla p|$ [2] and [4]. The two are related through the viscosity (η) of the fluid and the permeability of the porous medium. This inter-relationship is given in Equation 1

$$\frac{Q}{A} = -\frac{k_o}{\eta}|\nabla p| \quad \text{and} \quad k_o = \frac{D_S^2}{B_k}\left(\frac{\emptyset^3}{(1-\emptyset)^2}\right) \qquad 1$$

The permeability is a key term describing the flow behaviour within the porous medium. The Blake-Kozeny equation, shown in Equation 1 [16] defines the permeability of a packed bed of spheres as a function of the porosity or void space (Ø), particle size *(D_s)*, and the Kozeny constant B_k [9]. The complex nature of the porous medium makes the Kozeny constant, K, difficult to determine. K value of 5.0 proposed by Kozeny, 1927 is universally untrue and K values ranging from 4.5 to 5.1 have been proposed [8]. It is clear that accurate determination of K is imperative for the precise determination of k_o.

Several computational approaches on the determination of Kozeny constant of flow through packed beds have been done but accurate value of this constant for flow developed across spherical packed beds using discrete element method porescale approach has not been studied. Examples of these computational works involving determination of Kozeny constant in literature are cross flow and staggered square cylinder [6], soil sample and random spheres [10], random

packings constructed with square-shaped particles [12], spatially correlated porous media [21], Fibers [1], Square rods, cubes and cylinder [17 & 18], Foam [11], Blocks [5], spherical particles & blocks [22]. In the mainstream, the work of Liu and Hwang, 2012 [15] proposed the Kozeny – constant for fibrous porous materials whilst the work by Ozgumus, Mobedi & Ozkol, 2014 [19] put forward the Kozeny – constant for rectangular rods. This study compares computational fluid dynamic (CFD) simulations for laminar flow of water through packed beds of spheres and compares predictions for the permeability with those from the Blake - Kozeny equation. The study then extends the analysis to polydisperse systems.

Discrete element method (DEM) has been used to simulate the packing of 1, 2 and 3mm diameter spheres in a cylindrical vessel, a schematic of which is shown in Fig 1. The details of this method are published in [14]. The packing density was controlled by varying the value of the inter-particle friction, achieving packing densities between 0.55 and 0.67, consistent with those for loose and dense random packing of monosized spheres. Position and size data were exported to MATLAB^{TM} which was used to create serial 2D sections at prescribed intervals at a resolution of 300dpi. A two and three-dimensional images of packed spheres (2mm) are presented in Fig 2a. The 2D image slices were restored to a 3D volume (Fig 2b). Accurate preservation of the particle size and fluid volume were achieved by optimizing the smart mask smoothing process in the ScanIP module of Simpleware^{TM}. A representative volume element (RVE) was determined by measuring the volume fraction as a function of test volume size, at a number of test regions (Fig 2c and 2d). The volume

fractions of the test regions converged to within 33 - 45% of the bulk value for a test volume that was 3x the particle size.

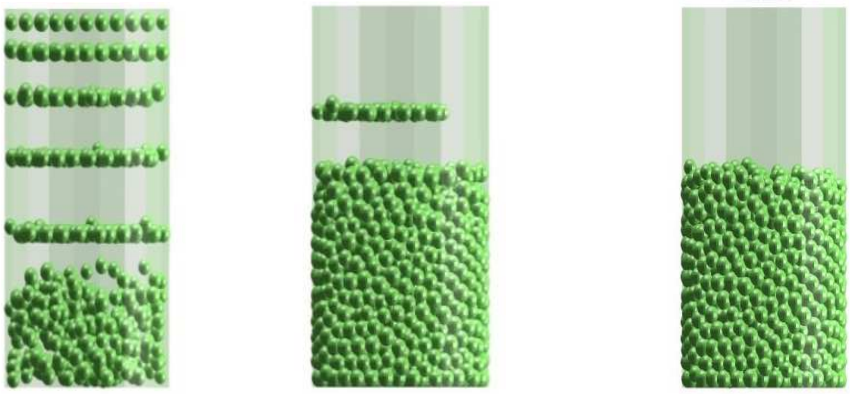


Fig 1: DEM simulation of the filling of a 35mm diameter vessel with mono – sized beads (Langston & Kennedy, 2014).

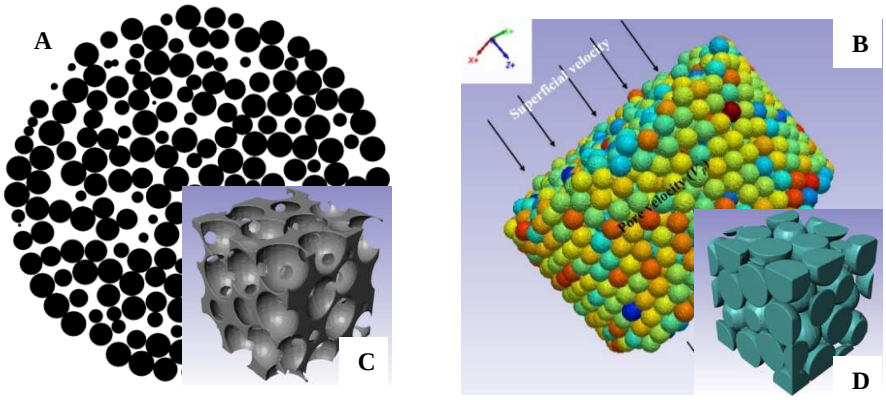


Fig 2. (A) Two-dimensional (2D) horizontal slice (B) three-dimensional (3D) volume of DEM monosized packed spheres (C) RVE Fluid domain and (D) RVE structural domain representative matrices of the virtual macroporous structures (DEM) obtained using sphere-packing models.

A high density hexahedral/quadratic tetrahedral mesh (HQTM, known as FE-Grid in Simpleware) was used as a benchmark (Fig 3) which creates over 25 million cells with a recorded minimum edge length less than 14μm. Fig 3(left) shows a 2D section of the FE grid (HQTM) meshed structure, indicating a hexahedral mesh on the fluid dominated region and a tetrahedral mesh on the re-entrant edges. Simpleware +FLOW module solves the Navier-Stokes equation

at fluid velocities consistent with laminar flow in the Darcy regime. An impermeable side wall boundary condition was imposed and the permeability in the height, Z, direction was determined. Fig 3(right) presents a three-dimensional fluid phase velocity streamlines plot obtained from solving the impermeable side walls Stokes equation in the FLOW solver of Simpleware.

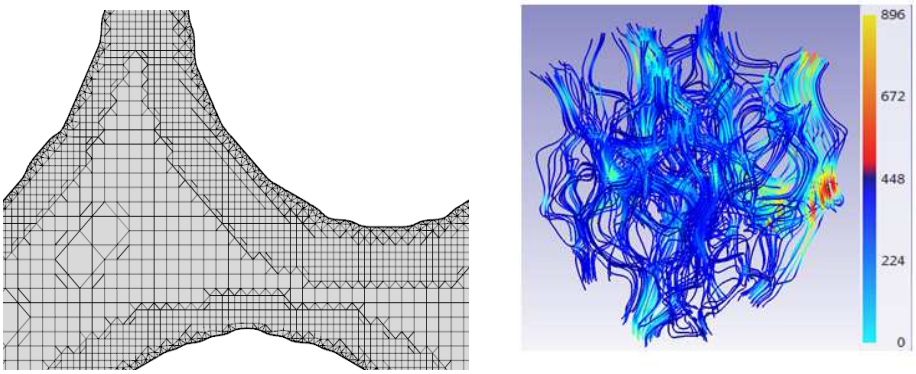


Fig 3. A two-dimensional image of the HQTM (left) and 3D velocity streamline plot (right).

The highly dense mesh structure looks extremely computationally expensive on resolving in a commercial CFD software requiring high memory usage and longer computational time. The Flow+ solver in Simpleware, however, avoids the use of quadratic elements for the velocity and linear element for pressure computation, instead of using linear element for both, making computation faster and using less memory. Studies have shown that the HQTM holds greater promise in terms of accuracy and useful for finite element and finite volume than the LTM, but the LTM is quite useful when properly optimized [3] and [20]. However, the mesh dependence study was thus used to quantify the likely trade-off between mesh element number and accuracy (compared with the FE grid mesh) in resolving the representative structure in a 64 – bit (32GB RAM and 3.7GHz) PC specification. For this study, a sensible optimization study adopting

the linear tetrahedral mesh (LTM) (Fig 5) was used on an RVE for 2mm spheres with a void space of 42.9%.

Tables 1 and 2 present the change in the permeability ratio (the computed permeability to the baseline obtained from the FE grid simulation) as a function of mesh geometry, and the computational time for the solution. The optimization process was carried out by varying the minimum and maximum edge lengths as multiples of the resolution of the original 2D stack images (1 pixel = 22 um). A sensible balance of computational efficiency (being mindful of reducing the element count to below 3 million cells for ease of use in CFD packages) and accuracy was identified by a minimum and maximum edge length 2.5x and 3x the resolution respectively (Fig 4 left). For a mesh with 2.2 million cells, the permeability is 95.6% of that for the FE grid model ($6.37*10^{-09}$ m^2). In the case of laminar flow, having small elements at the particle surfaces yields very little improvement in modelling accuracy for a large penalty in mesh density. Coarsening the mesh on the surfaces (Fig 4 right), were velocity is already assumed to be zero (no slip) is imperative to reduce the mesh density as well as the computational cost. The relationship between the permeability for the optimized linear tetrahedral mesh (LTM) and highly discretized FE grid hexahedral/quadratic tetrahedral meshes (HQTM) are shown in Fig 5 (ball points) giving a consistent, 6% lower value for the optimized LTM mesh.

Table 1. Data for constant growth rate, variation in Lmax and Lmin = resolution

L_{max} (mm)	Permeability / $10^{-09}m^2$	Mesh density /10^{06}	Permeability ratio	Growth rate	Homogenisation time (s)
10.0x	5.42	1.1211	0.85	1.30	152
9.0x	5.44	1.1269	0.85	1.30	159
6.0x	5.68	1.2624	0.89	1.30	176
4.0x	5.99	1.8906	0.94	1.30	302
3.0x	**6.14**	**2.9670**	**0.96**	**1.30**	**535**
2.0x	6.29	8.5742	0.99	1.30	2065

Table 2. Data for constant growth rate, variation in minimum Lmin and Lmax = 3x resolution

L_{max} (mm)	Permeability / $10^{-09}m^2$	Mesh density /10^{06}	Permeability ratio	Growth rate	Homogenisation time (s)
2.5x	6.11	2.190	0.956	1.30	346
2.0x	6.20	2.288	0.960	1.30	395
1.5x	6.31	2.764	0.963	1.30	469
1.0x	6.31	2.967	0.964	1.30	555

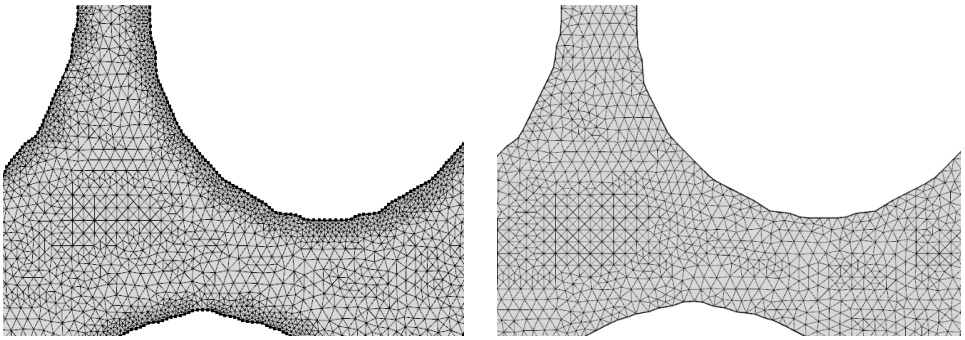


Fig 4: Two dimensional images of LTM meshed structures.

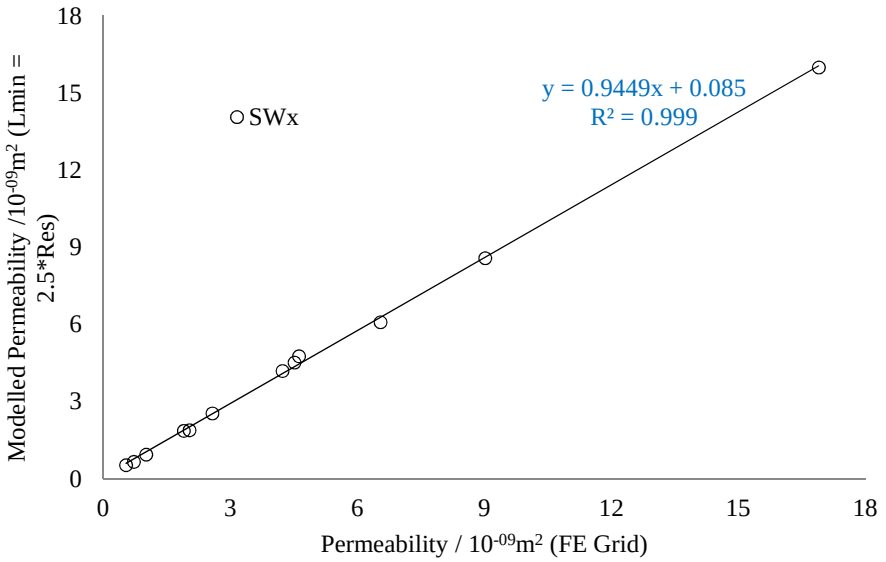


Fig 5. CFD Modelled permeabilities for the optimized LTM against the HQTM mesh structure.

The optimized LTM mesh structure was exported to COMSOL Multiphysics 5.2^{TM} (CMx) for solving. The low-velocity incompressible Navier-Stokes

equation, velocity inlet, zero pressure outlet, no-slip wall and symmetrical boundary condition of side faces were solved on the fluid domain of the micro–geometrical structure. A homogenization time in the range of 500 and 600s was recorded for CMx computation for each pressure drop whilst that of Simpleware FLOW direct computation of permeability is limited 300-500s. Using COMSOL, the pressure drop was calculated for laminar flow of water (velocities between 0-100mm/s) corresponding to pore diameter Reynolds (Re_D) numbers between 0-110, 0-220 and 0-330 for 1, 2 and 3mm pore size structures respectively. The permeabilities at Darcy regime were obtained for $Re_D<1.0$, typically, flow velocities less than $0.1mm.s^{-1}$ in this case, as prescribed by Lage, Krueger & Narasimham, 2005 and then determined by fitting the pressure-velocity to Darcy equation as opposed to direct computation of permeability for different boundary conditions in Simpleware +FLOW module. Table 3 shows the permeabilities (At Darcy regime) for packed beds with 1-3mm spheres for porosities between 0.33 and 0.45. Also, the permeabilities and Form drag for all regime of laminar flow was computed by fitting the pressure-velocity data into Darcy-Dupuit-Forchheimer model suggested in [23 & 24]. A two-dimensional image of surface-arrow velocity plots for flow through ($50mm.s^{-1}$ pore inlet velocity) the interstices of a 1 and 3mm monosized (33% void space or packing fraction) particles packed beds are shown in Fig 6. This clearly shows that the size of the particle and void spaces within the packed porous beds often dictates the flow of fluid (water) through it. A large particle sized (3mm) virtually packed beds the much higher void spaces within the beds which eventually influences more fluid through it whilst the lowest sized particle (1mm) confers to higher

pressure and low permeability (in order of $10^{-10}m^2$) through it which is often the case of realistic flow packed beds (Fig 6).

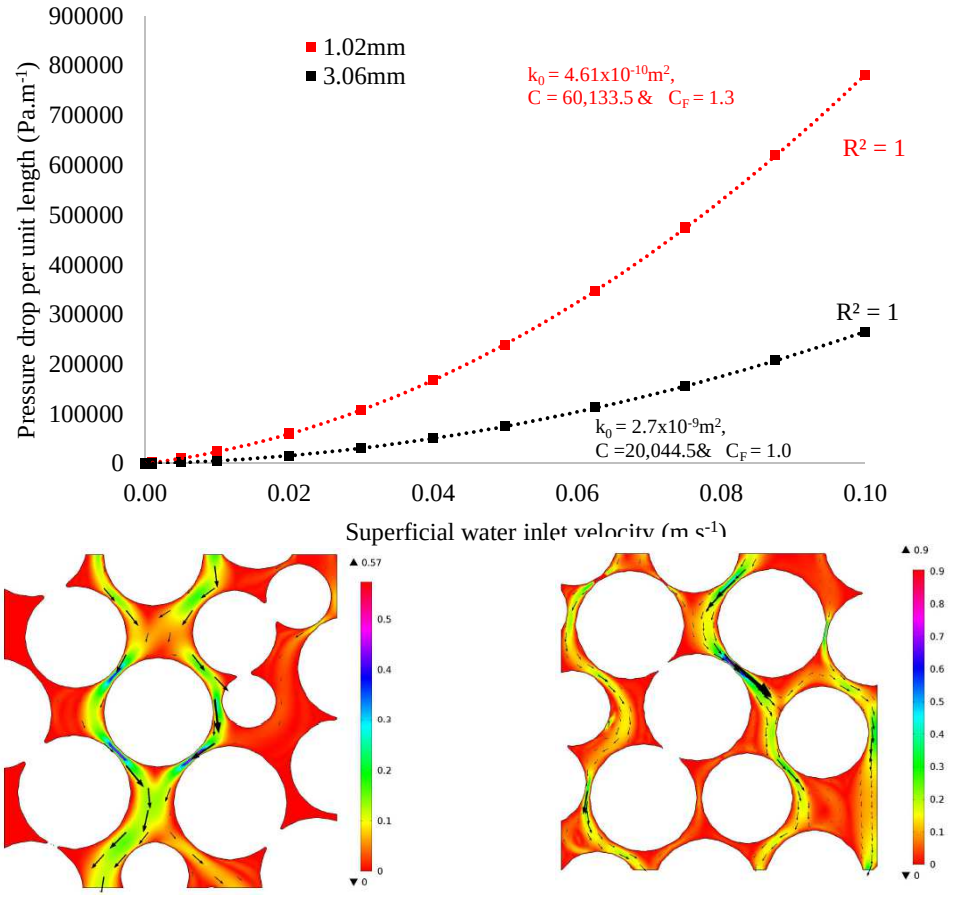


Fig 6. Top, is the plots of pressure drop per unit length ($Pa.m^{-1}$) against superficial velocity for laminar flow of fluid through a 1.02mm and 3.06mm mean pore sized virtually packed structures and bottom, is the 2D images of the velocity streamlines (cubic structural thickness 3mm to the bottom left, and 9mm, to the bottom right) at $50mm.s^{-1}$ pore inlet velocity.

The computed values of permeabilities at Darcy regime using FE grid mesh (Hexahedral/Quadratic tetrahedral mesh) vary on average, less than 1% and are 5% higher than those for the linear tetrahedral mesh structure resolved in Multiphysics (CMx) and Simpleware (SWx) respectively. Using Eq 1, the value of K (Kozeny constant) was determined by plotting the modeled permeability against $\frac{D_S^2}{1}\left(\frac{\emptyset^3}{(1-\emptyset)^2}\right)$ with a slope of $\frac{1}{B_k}$ = $6.0x10^{-3}$ and a Kozeny constant of 4.62 was achieved which lies in the region of K value (4.5-5.1) available in the

literature [8]. Fig 8 (left) plots CFD modeled data (points) and Blake Kozeny predictions (lines) of the absolute permeability against void fraction. The modeled values agree well with that obtained from the BK model. The proposed value of K (4.62) was used to predict measured [7] permeability data of spherical beds for the polydispersed packed spherical particles (0.794 – 7.94mm) and cubes presented in Fig 8 (right) and Table 3 (last page). This shows better prediction by, on an average, less than 15% gradient difference when compared with that of the K value of 5.0 (more than 31% gradient difference) in literature [13].

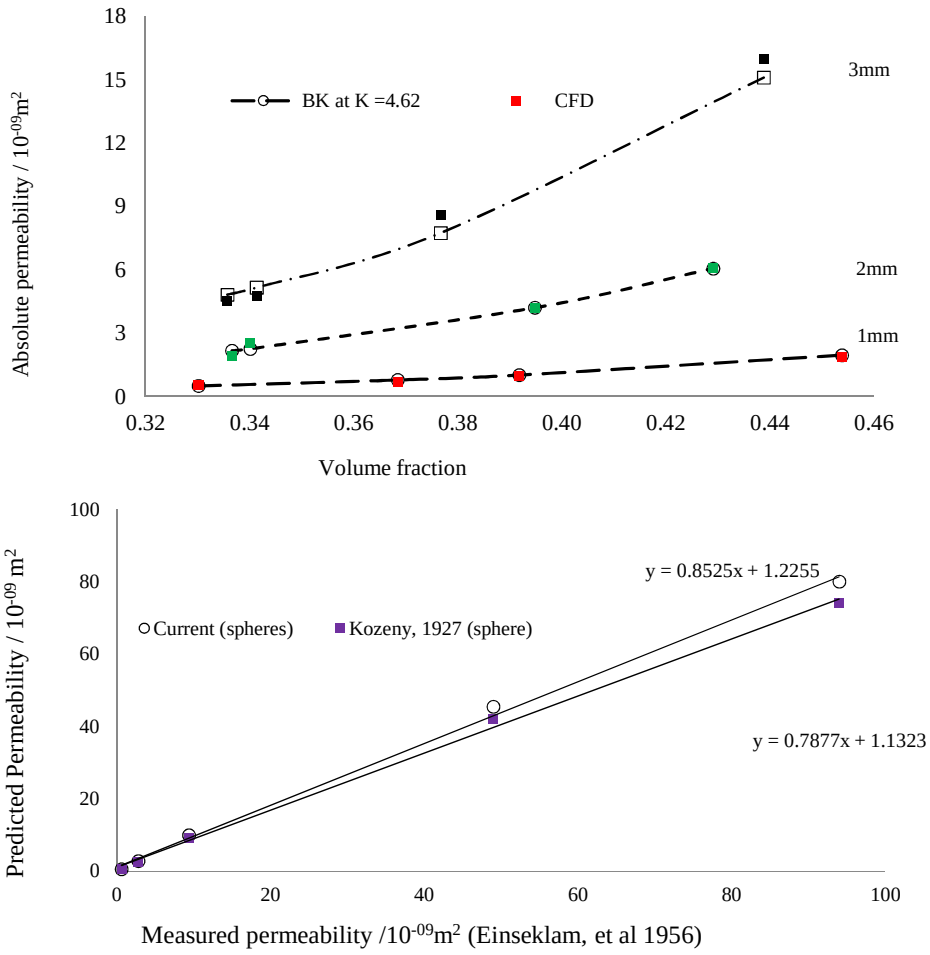


Fig 8: Top, is the plots of CFD modelled and theoretical values of permeability against void fraction and to the bottom, is the theoretical permeability value against against measured permeability.

In conclusion, a study on the numerical simulation of fluid flow through computer-generated structures at Darcy regime has been investigated utilizing discrete element modelling (DEM) simulated packing of spherical beads. DEM has been used to create randomly-packed beds of monosized spherical beads with different packing fractions. DEM data have been used to create 3D volumes for simulation of 1D laminar flow using Simpleware software combined with a flow solver. Discretization and mesh dependent study were carried out to make the problem mesh independent by specifying a growth rate of 1.3. For sphere diameters in the range of 1-3 mm and void fractions in the range of 0.3-0.5, the agreement between the permeabilities of modeled structures and predictions from the Blake – Kozeny model is good when the Kozeny constant, K, is 4.62.

Acknowledgments: AO would like to acknowledge the University of Nottingham for the Dean of Engineering Research Scholarship for International Excellence and Simpleware Ltd and B&W Group for the provision of the licenses and technical support.

Table 3. Measured and predicted permeability data.

	Ds (mm)	Specific surface area (m^2/m^3)	Packing fraction (Ø)	Measured Permeability (m^2) Einseklam, et al 1956	Predicted Permeability (m^2) Kozeny, 1927	Predicted Permeability (m^2) Nakayama et al, 2007	Predicted Permeability (m^2) current
Spheres	0.7940	7600	0.393	6.20E-10	5.770E-10	3.037E-10	6.244E-10
	1.5880	3759	0.405	2.80E-09	2.629E-09	1.384E-09	2.845E-09
	3.1750	1895	0.393	9.40E-09	9.226E-09	4.856E-09	9.985E-09
	6.3500	948	0.405	4.90E-08	4.203E-08	2.212E-08	4.549E-08
	7.9400	756	0.416	9.40E-08	7.393E-08	3.891E-08	8.001E-08
Cubes	3.1750	1860	0.190	4.60E-10	5.855E-10	3.081E-10	6.336E-10
	3.1750	1860	0.425	1.50E-08	1.300E-08	6.844E-09	1.407E-08
	6.3500	1078	0.318	1.40E-08	1.549E-08	8.151E-09	1.676E-08
	6.3500	1078	0.455	6.90E-08	7.104E-08	3.739E-08	7.689E-08